

AD-A162 100

MIXED MODE I AND II FULLY PLASTIC CRACK GROWTH FROM
SIMULATED WELD DEFECTS(U) MASSACHUSETTS INST OF TECH
CAMBRIDGE DEPT OF MECHANICAL ENGIN.. G A KARDOMATERS

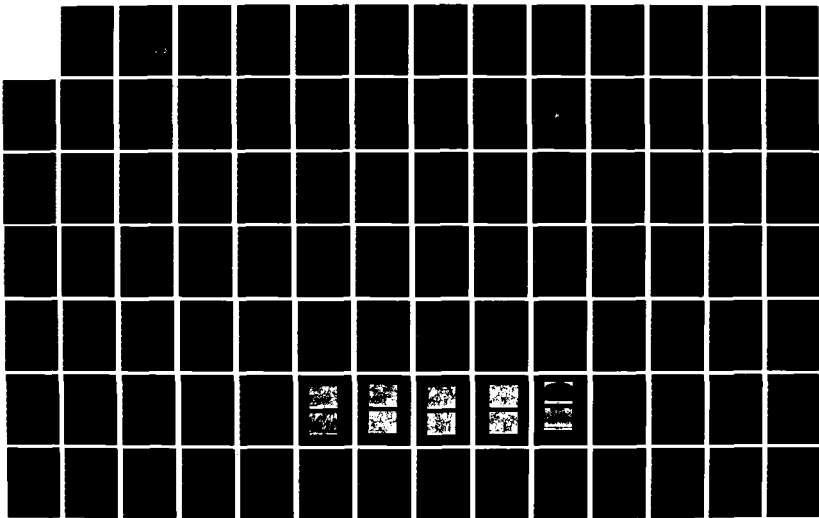
1/3

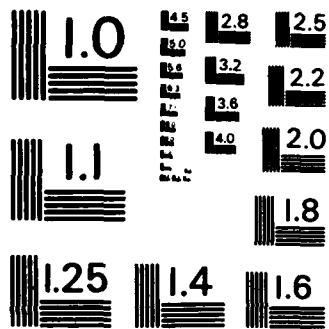
UNCLASSIFIED

23 OCT 85 N00014-82-K-0025

F/G 13/8

NL





MICROCOPY RESOLUTION TEST CHART
NATIONAL BUREAU OF STANDARDS-1963-A

AD-A162 108

3

Technical Report N00014-B2-K-0025 P00002 TR02

MIXED MODE I AND II FULLY PLASTIC CRACK GROWTH FROM SIMULATED WELD DEFECTS

George A. Kardomateas, now at
Engineering Mechanics, RMB 256, (313) 575-3043
General Motors Research Laboratory
Warren, Michigan 48090-9055

Unlimited Distribution

23 October 1985

Technical Report.

Frank A. McClintock, Principal Investigator
Room 1-304, (617) 253-2219
Department of Mechanical Engineering
Massachusetts Institute of Technology
Cambridge, MA 02139

DTIC
EXECTE
DEC 06 1985
S D

Prepared for
OFFICE OF NAVAL RESEARCH
Solids Mechanics Program, Mechanics Division
Scientific Officer: Dr. Yapa Rajapakse
Code 432S (202) 696-4306
800 N. Quincy Street
Arlington, VA 22217

DISTRIBUTION STATEMENT A
Approved for public release;
Distribution Unlimited

DTIC FILE COPY

REPORT DOCUMENTATION PAGE		READ INSTRUCTIONS BEFORE COMPLETING FORM
1. REPORT NUMBER N00014-82-K-0025 P00002-TR02	2. GOVT ACCESSION NO. H162108	3. RECIPIENT'S CATALOG NUMBER
4. TITLE (and Subtitle) MIXED MODE I AND II FULLY PLASTIC CRACK GROWTH FROM SIMULATED WELD DEFECTS		5. TYPE OF REPORT & PERIOD COVERED Technical Report 23 October 1985
7. AUTHOR(s) George A. Kardomateas (now at Eng. Mech.) RMB 256 General Motors Research Lab. Warren, Michigan 48090-9055		6. PERFORMING ORG. REPORT NUMBER
9. PERFORMING ORGANIZATION NAME AND ADDRESS Department of Mechanical Engineering Massachusetts Institute of Technology Cambridge, MA 02139		8. CONTRACT OR GRANT NUMBER(s) N00014-82-K-0025 P00002
11. CONTROLLING OFFICE NAME AND ADDRESS Office of Naval Research Solid Mechanics Program, Mech. Div. Code 432S		10. PROGRAM ELEMENT, PROJECT, TASK AREA & WORK UNIT NUMBERS
14. MONITORING AGENCY NAME & ADDRESS (if different from Controlling Office)		12. REPORT DATE 23 October 1985
		13. NUMBER OF PAGES 206
		15. SECURITY CLASS. (of this report) Unclassified
		15a. DECLASSIFICATION/DOWNGRADING SCHEDULE
16. DISTRIBUTION STATEMENT (of this Report) Distribution Unlimited		
17. DISTRIBUTION STATEMENT (of the abstract entered in Block 20, if different from Report)		
18. SUPPLEMENTARY NOTES PhD thesis, September 1985 Frank A. McClintock, Supervisor Department of Mechanical Engineering Massachusetts Institute of Technology		
19. KEY WORDS (Continue on reverse side if necessary and identify by block number) Steels 1018, HY-80, HY-100, and A36; 5086-Hill Aluminum, asymmetric , weld defect, shear band , mixed Mode I and II , oblique, strain hardening, fully plastic, limit load, ductile fracture, J-integral, crack initiation, crack tip displacement, crack growth ductility, crack opening angle, tearing modulus,		
20. ABSTRACT (Continue on reverse side if necessary and identify by block number) In symmetric specimens, the crack advances into the relatively undamaged region between two plastic shear zones. A crack near a weld or shoulder, loaded into the plastic range, may have only a single shear band, along which the crack grows in prestrained and damaged material with less ductility than the usual symmetrical configurations. A crack ductility can be defined as the minimum displacement per unit crack growth. A low crack ductility requires higher stiffness of the surrounding structure		

DD FORM 1473
1 JAN 73

EDITION OF 1 NOV 68 IS OBSOLETE

S N 0102-LF-014-6601

19 (cont.) tearing modulus, fracture-stable design,

tearing modulus, fracture-stable design, fractography, shear lip, experiments, theory

20 (cont.)

for fracture-stable design. Tests of six alloys showed that, for the low hardening alloys, the crack ductility in the asymmetric case is less than a third that of the symmetric. In the higher hardening alloys the crack ductility in the asymmetric case is smaller by a factor of 1.2 at most. A noteworthy result is the presence of a Mode I opening component even with asymmetry, as is shown by the far field displacement vector being more than 45° from the transverse direction. The crack direction is less than 45° , indicating the effect of triaxiality on cracking.

A macro mechanical model for crack advance by combined fracture and sliding off along two slip planes gives the independent physical parameters (cracking and two shear directions, relative amounts of cracking and shearing) in terms of the observable quantities of the macroscopic fracture (flank angles, flank lengths, back angle). This two slip-plane model admits a Mode I opening component and describes, based on an idealization of underlying physical mechanisms, the development of deformation in ductile crack growth for both the symmetric and asymmetric specimens. A finite element study of the asymmetric specimens gave a crack direction within two degrees and a far field displacement vector at initiation within three degrees of that experimentally found. Stress and strain fields indicate the presence of a Mode I component. Early growth, studied by successive removal of the most damaged element, resulted in crack growth rate for the lower hardening case about twice that of the higher hardening one. Finally, a logarithmic tensile singularity in the mean stress was found for rigid-plastic flow past a growing crack of finite angle with rigid flanks under combined shear and tension. The tensile singularity predicts yielding of the crack flanks.

**MIXED MODE I AND II FULLY
PLASTIC CRACK GROWTH
FROM
SIMULATED WELD DEFECTS**

by

GEORGE A. KARDOMATEAS

Diploma, Ethnikon Metsovion Polytechnion, Greece (1981)
M.Sc., Massachusetts Institute of Technology (1982)

SUBMITTED TO THE DEPARTMENT OF MECHANICAL
ENGINEERING IN PARTIAL FULFILLMENT OF THE
REQUIREMENTS FOR THE DEGREE OF

DOCTOR OF PHILOSOPHY

at the

MASSACHUSETTS INSTITUTE OF TECHNOLOGY

September 1985

Copyright © 1985 Massachusetts Institute of Technology

Signature of Author *George Kardomateas*
Department of Mechanical Engineering
September 10, 1985

Certified by *Frank A. McClintock*
Frank A. McClintock
Thesis Supervisor

Accepted by *Ain A. Sonin*
Ain A. Sonin
Chairman, Departmental Graduate Committee

Mixed Mode I and II Fully Plastic Crack
Growth From Simulated Weld Defects

by

GEORGE A. KARDONATEAS

Submitted to the Department of Mechanical Engineering on September 10, 1985
in partial fulfillment of the requirements for the degree of Doctor of
Philosophy

Abstract

In symmetric specimens the crack advances into the relatively undamaged region between two plastic shear zones. A crack near a weld or shoulder, loaded into the plastic range, may have only a single shear band, along which the crack grows into prestrained and damaged material with less ductility than the usual symmetrical configurations. A crack ductility can be defined as the minimum displacement per unit crack growth. A low crack ductility requires higher stiffness of the surrounding structure for fracture-stable design. Tests of six alloys showed that, for the low-hardening alloys, the crack ductility in the asymmetric case is less than a third that of the symmetric. In the higher hardening alloys the crack ductility in the asymmetric case is smaller by a factor of 1.2 at most. A noteworthy result is the presence of a Mode I opening component even with asymmetry, as is shown by the far field displacement vector being more than 45° from the transverse direction. The crack direction is less than 45° , indicating the effect of triaxiality on cracking.

A macro-mechanical model for crack advance by combined fracture and sliding off along two slip planes gives the independent physical parameters (cracking and two shear directions, relative amounts of cracking and shearing) in terms of the observable quantities of the macroscopic fracture (flank angles, flank lengths, back angle). This two slip plane model admits a Mode I opening component and describes, based on an idealization of underlying physical mechanisms, the development of deformation in ductile crack growth for both the symmetric and asymmetric specimens. A finite element study of the asymmetric specimens gave a crack direction within two degrees and a far field displacement vector at initiation within three degrees of that experimentally found. Stress and strain fields indicate the presence of a Mode I component. Early growth, studied by successive removal of the most damaged element, resulted in crack growth rate for the lower hardening case about twice that of the higher hardening one. Finally, a logarithmic tensile singularity in the mean normal stress was found for rigid-plastic flow past a growing crack of finite angle with rigid flanks under combined shear and tension. The tensile singularity predicts yielding of the crack flanks.

Thesis Supervisor: Frank A. McClintock

Title: Professor of Mechanical Engineering

ACKNOWLEDGEMENTS

I would like to express my deep gratitude to Professor Frank McClintock for his advice and interest in my research and to the Office of Naval Research for sponsoring the project under Contract N0014-82K-0025.

Having finished my student years I would like to thank my earlier teachers from the National Technical University of Athens for providing me with an excellent scientific background.

Accession For	
NTIS CRA&I	<input checked="" type="checkbox"/>
DTIC TAB	<input type="checkbox"/>
Unannounced	<input type="checkbox"/>
Justification	
By	
Distribution/	
Availability Codes	
Dist	Avail and/or Special
A-1	

3

TABLE OF CONTENTS

	Page
Abstract	2
CHAPTER ONE: Introduction	5
CHAPTER TWO: Directional Effects in Fully Plastic Crack Growth near a Shear Band	8
CHAPTER THREE: Experimental Study	31
CHAPTER FOUR: Shear-band Characterization	82
CHAPTER FIVE: Finite Element Investigation of Plane Strain Asymmetric Fully Plastic Specimens.	107
CHAPTER SIX: On the Fully Plastic Flow Past a Growing Asymmetric Crack and its Relation to Machining Mechanics.	127
CHAPTER SEVEN: The Asymmetric (Mixed Mode I and II) Fracture - overview	149
Appendix A - Experimental Techniques.	177
Appendix B - Mesh Generator.	187

CHAPTER ONE

INTRODUCTION

In symmetric singly grooved unconstrained tensile specimens the crack advances into the relatively undamaged region between two symmetric shear zones. An asymmetry, introduced through a weld fillet or a harder, heat-affected zone or a shoulder on one side of the crack suppresses one of the two slip lines that would appear in a symmetrical specimen. This is likely to give asymmetric cracking along the remaining active slip line, with less ductility because the crack is advancing into prestrained and pre-damaged material. A reduced ductility requires higher stiffness of the surroundings for fracture-stable design.

Near the tip of the growing crack, strain hardening will cause the deformation field to fan out. For power law creep or deformation theory plasticity and a stationary crack, the asymptotic stress and strain distribution may be found from the extended by Shih [1] HRR [2,3] solutions for the general mixed mode I and II case. Notice, however, that such a superposition of stationary singularities does not take into account the hardening of the material left behind the growing crack. Indeed, the stress and strain fields near the tips of growing cracks in ductile materials are known to differ from the stress and strain state around stationary cracks in the same materials as is shown from asymptotic solutions [4,5,6] supplemented through finite element calculations [7,8].

McClintock and Slocum [9] developed a formulation for the accumulation of damage directly ahead of an asymmetric crack, based on strain increments adapted from Shih's [1] analysis. The crack was assumed to follow the center of the 45° shear band. It was found that the crack growth per unit displacement increases

approximately as the logarithm of the total crack advance per inclusion spacing ρ and varies inversely as the critical fracture strain γ_c . Little effect of strain hardening on the growth rate was found.

The objective of the current study is to investigate through experimental, analytical and numerical work, the ductility of asymmetric, fully plastic, unconstrained configurations. First, the approximate pure Mode II incremental solution [9] is extended to admit a crack growing at an angle to the shear band. This deviation from the shear band is expected from the higher triaxiality. Far field displacement is assumed again to be parallel to the shear band. Next, tests results on symmetric and asymmetric specimens of six alloys are presented. A method for quantifying and representing the ductility is suggested. A macromechanical model of crack growth by combined fracture on one plane and sliding off along two others describes, for this idealization of the physical mechanisms, the ductile crack growth for both the asymmetric and symmetric specimens. To account for the effect of the finite width of the shear band and study the stress and strain fields at initiation, a finite element investigation is undertaken. Early growth is also studied by successive element removal. Finally, a stream function technique is used to investigate whether rigid-plastic strain hardening flow past a growing crack of finite angle with rigid flanks can be sustained. The last chapter contains an overview of the results and summarizes the conclusions. It also contains recommendations for further research.

REFERENCES

1. Shih C.F. "Small Scale Yielding Analysis of Mixed Mode Plane Strain Crack Problems", *Fracture Analysis, ASTM STP 560*, Am.Soc.Test.Mat., Philadelphia, 187-210 (1974).
2. Hutchinson J.W. "Singular behaviour at the end of a tensile crack in a

- hardening material", *J. Mech. Phys. Sol.*, 16, 13-31 (1968).
3. Rice J.R. and Rosengren G.F. "Plane Strain Deformation near a crack tip in a power-law hardening material", *J. Mech. Phys. Sol.*, 16, 1-12 (1968).
 4. Rice J.R. "Elastic-Plastic Crack Growth" in *Mechanics of Solids*, Pergamon Press, Oxford, pp.539-562 (1982).
 5. Amazigo J.C. and Hutchinson J.W. "Crack tip fields in steady crack growth with linear strain-hardening" *J. Mech. Phys. Sol.*, 25, pp.81-97 (1977).
 6. Slepyan L.I. "Deformation at the edge of a growing crack", *Mekhanika Tverdogo Tela*, Vol. 8, No. 4, pp. 139-148 (1973).
 7. Parks D.M., Lam P.S. and McMeeking R.M. "Some effects of inelastic constitutive models on crack tip fields in steady quasistatic growth", in *Advances in Fracture Research*, D. Francois et al. eds, pp. 2607-2633, Pergamon (1981).
 8. Rice J.R., Drugan J.W. and Sham T.L. "Elastic-Plastic Analysis of Growing Cracks" *ASTM STP 700*, pp. 189-221 (1980).
 9. McClintock F.A. and Slocum A.H. "Predicting Fully Plastic Mode II Crack Growth from an Asymmetric Defect", *Int.J.Fract.Mechanics*, 27, 49-62 (1985).

CHAPTER TWO

DIRECTIONAL EFFECTS IN FULLY PLASTIC
CRACK GROWTH NEAR A SHEAR BAND.

TABLE OF SYMBOLS

F_t	hole growth ratio
$I_{1/n}$ (n, M^P)	dimensionless parameter
J	J-integral
k	shear yield
M^P	mixity parameter (eq. 2)
n	strain hardening exponent
T_j	traction vector
U	far field displacement (along shear band)
W	work per unit volume
σ	mean normal stress
σ_1	flow stress at unit strain
ϕ	angle between crack and shear band
η	damage
Δc	increment of crack advance
γ	principal shear strain
τ	principal shear strain
ρ	mean inclusion spacing
$\tilde{\sigma}_{ij}$	angular stress functions
$\tilde{\epsilon}_{ij}$	angular strain functions
\tilde{u}_i	angular displacement functions

ABSTRACT

Welds, shoulders, or other asymmetries may eliminate one of the shear bands of symmetrically cracked parts and thus give crack propagation through pre-damaged material, instead of through the relatively unstrained region between the two plastic shear zones of the symmetric case. Previous work is extended to include sites at several angles ahead of the crack. Far field displacement is assumed to take place parallel to the shear band. Strain increments are approximated from the mixed mode, power-law elastic solution for a stationary crack and used with a

fracture criterion for hole growth in shear bands to predict the direction and rate of crack growth. The crack is assumed to advance in the direction that requires the minimum far field displacement to reach critical damage. For a shear band at 45° the crack progresses at 21° - 30° from the transverse (depending on strain hardening), indicating the effect of higher triaxiality. The crack growth rate is about 6-15% higher than if the directional effects are neglected. Lower strain-hardening results in a 5% higher rate of crack advance per unit displacement, a higher fracture strain, and the final crack orientation being closer to the 45° shear band.

INTRODUCTION

Most fracture tests use symmetric specimens. The crack advances into relatively undamaged material between two shear bands. This will not happen if one of the bands is eliminated due to a weld bead, or a harder heat-affected zone, for example (Fig. 1). A fatigue crack or other defect near such an asymmetry will tend to advance along the remaining shear band through highly strained material. Lower ductility is thus expected. An example of lowered ductility in asymmetric flow is the formation of a shear lip at the end of an ordinary cup and cone fracture in a tensile test.

McClintock and Slocum [1] developed an approximate formulation for the accumulation of damage ahead of the crack in a power-law strain hardening material, by using the strain and displacement fields derived by Shih [2] for a stationary mixed-mode crack and the McClintock, Kaplan, and Berg [3] criterion for fracture by hole growth. It was assumed that the crack advances directly along the shear band. Preliminary experiments, however, have indicated that the crack actually advances at an angle from the shear band which reflects the effect of the

higher triaxiality on one side.

In the following we modify the Pure Mode II [1] solution by considering several sites around the crack tip. The far field displacement is again assumed to be parallel to the shear band and the strain increments to follow Shih's [2] mixed mode stationary crack fields. The accumulated damage from initiation and prior growth is calculated and the necessary far-field displacement for critical damage is found for each site. The crack is assumed to advance in the direction requiring the least far-field displacement.

ANALYSIS

1. Crack initiation. A nonlinear elastic solution for the small scale yielding of mixed Modes I and II stationary crack problems was developed by Shih [2]. The material was assumed to be power-law hardening according to the relation between equivalent stress and strain:

$$\sigma = \sigma_1 \epsilon^n, \quad (1)$$

where σ_1 is the flow strength at unit strain and n is the strain hardening exponent. Shih [2] introduced a Mode I mixity parameter M^P , defined in terms of the near field stresses by

$$M^P = \frac{2}{\pi} \tan^{-1} \left| \lim_{r \rightarrow 0} \frac{\sigma_{\theta\theta}(r, \theta=0)}{\sigma_{r\theta}(r, \theta=0)} \right|. \quad (2)$$

The mixity parameter varies from 0 for pure Mode II to 1 for pure Mode

I. McClintock [4] restated the dominant singularity governing the behavior of the stresses, strains and displacements (for large plastic strains) in terms of the J integral as

$$\frac{\sigma_{ij}}{\sigma_1} = \left[\frac{J}{\sigma_1 r I_{1/n}(n, MP)} \right]^{n/(n+1)} \bar{\sigma}_{ij}(\theta, MP, n),$$

$$\epsilon_{ij} = \left[\frac{J}{\sigma_1 r I_{1/n}(n, MP)} \right]^{1/(n+1)} \bar{\epsilon}_{ij}(\theta, MP, n), \quad (3)$$

$$\frac{u_i}{r} = \left[\frac{J}{\sigma_1 r I_{1/n}(n, MP)} \right]^{1/(n+1)} \bar{u}_i(\theta, MP, n).$$

The J integral is defined (x_1 axis along crack) as

$$J = \int W dx_2 - T_j \frac{\partial u_j}{\partial x_1} ds.$$

where T_j is the traction vector, u_j is the displacement vector, and W is the work per unit volume. For a single shear band, J can be evaluated in terms of the shear strength k , the far field relative displacement U and the angle ϕ between crack and shear band (Fig. 2) by

$$J = \frac{kU}{\cos\phi}. \quad (4)$$

The dimensionless functions $\bar{\sigma}_{ij}(\theta, MP, n)$, $\bar{\epsilon}_{ij}(\theta, MP, n)$ and $I_{1/n}(n, MP)$ have been numerically determined by Shih [2] for $n=1/3$ and $n=1/13$. The dimensionless functions $\bar{u}_i(\theta, MP, n)$ are derived in the Appendix from the strain functions and are shown in Fig. 3 for $n=1/13$ and $MP=0.5$.

Assume that currently the shear band forms an angle ϕ with a recent average crack direction to be defined below. With the crack not advancing along the shear band, there is no longer pure Mode II. When the relative far-field displacement is assumed to be parallel to a single narrow shear band, as is valid in the non-hardening limit, and that direction is assumed to be the same as the local relative displacement across the flanks, the mixity parameter can be determined from the angular

functions ($\bar{\cdot}$) of the displacement field relative to $\theta = -\pi$ since, from Fig. 2,

$$\tan \phi = \frac{u_\theta}{u_r} = \frac{\bar{u}_\theta(\pi, M^P, n)}{\bar{u}_r(\pi, M^P, n)}. \quad (5)$$

Fig. 4 shows the resulting variation of the mixity parameter with the angle ϕ for $n=1/13$. Thus, the angle ϕ determines the angular stress and strain functions and hence the local stress and strain for a given J through (3). The angular functions turn out to affect the fracture criterion through the triaxiality and the shear strain, as follows. The mean normal stress for plane incompressible flow is

$$\sigma = \frac{\sigma_{rr} + \sigma_{\theta\theta}}{2}. \quad (6)$$

The triaxiality σ/τ used in the fracture criterion is given in terms of the dimensionless principal shear stress $\bar{\tau}$, defined by

$$\bar{\tau} = \left[\bar{\sigma}_{r\theta}^2 + \left(\frac{\bar{\sigma}_{rr} - \bar{\sigma}_{\theta\theta}}{2} \right)^2 \right]^{1/2}, \quad (7)$$

by

$$\sigma/\tau = \frac{\bar{\sigma}_{rr} + \bar{\sigma}_{\theta\theta}}{2\bar{\tau}}. \quad (8)$$

The angular variation of this triaxiality, σ/τ , is shown in Fig. 5 for $n=1/13$. Note that the triaxiality is highest for negative values of θ for all cases except pure Mode I. This is the primary reason for exploring the directional effects.

Similarly, the dimensionless principal shear strain $\bar{\gamma}$ can be expressed for the plane incompressible case as:

$$\bar{\gamma} = 2 \left[\bar{\epsilon}_{r\theta}^2 + \left(\frac{\bar{\epsilon}_{rr} - \bar{\epsilon}_{\theta\theta}}{2} \right)^2 \right]^{1/2} = 2 \sqrt{\bar{\epsilon}_{r\theta}^2 + \bar{\epsilon}_{rr}^2}. \quad (9)$$

Introducing (4) into the first of (3) and solving for the displacement gives the far-field displacement U in terms of the principal shear strain γ at any point in the near

field:

$$U = \frac{\sigma_1}{\Delta} I_{1,n}(n, M^P) r \cos \phi (\gamma/\tilde{\gamma})^{n+1}. \quad (10)$$

The critical displacement for crack initiation occurs when the fracture strain is reached at the point (ρ, θ) where ρ is a fracture process zone size (e.g. the mean inclusion spacing). The fracture strain is found by using the fracture criterion of McClintock, Kaplan and Berg [3] by which it is postulated that fracture due to micro-void coalescence occurs when the "damage", η , reaches unity. The damage is expressed in terms of a hole growth ratio F_t , the principal shear strain γ and the triaxiality σ/τ :

$$\eta = \frac{1}{\ln F_t} \left[\ln \sqrt{1+\gamma^2} + \frac{\gamma}{2(1-n)} \sinh\left(\frac{(1-n)\sigma}{\tau}\right) \right]. \quad (11)$$

The above damage equation is associated with growth of cylindrical holes. Alternatively one might use, for example, the eqs for growth of spherical holes in nonhardening material (Rice and Tracey, [5]).

A Newton-Raphson technique is used to solve (10) and (11) at $r=\rho$ for the critical far-field displacements for initiation in a number of directions. The actual initial direction is that which minimizes the required displacement. Once the initiation displacement U_i for the critical strain at the point (ρ, θ_c) is known, the strain at all other points can be found by re-arranging (10):

$$\gamma = \left[\frac{kU_i}{r \sigma_1 I_{1,n}(n, M^P) \cos \phi} \right]^{1/(n+1)} \tilde{\gamma}. \quad (12)$$

2. Crack growth. After initial growth by Δc , further growth requires reaching the critical damage at some new site ρ from the current crack tip. The damage at each site is that from crack initiation plus those for any following crack growth

increments. The strain to bring the damage to unity is found by differentiating (11) to find the damage increments in terms of the strain increment and the strain itself:

$$d\eta = \frac{1}{\ln F_t} \left[\frac{\gamma}{1+\gamma^2} + \frac{1}{2(1-n)} \frac{\sinh \frac{(1-n)\sigma}{\tau}}{\tau} \right] d\gamma. \quad (13)$$

In the absence of an incremental strain-hardening solution for a growing crack, we follow McClintock and Slocum [1] and approximate the strain increment in terms of the far-field displacement increment by differentiating and rearranging (10) (this is strictly valid only for non-linear elasticity):

$$d\gamma = \frac{k\tilde{\gamma}}{(n+1)\sigma_1 I_1(n, M^P) r \cos \phi} (\tilde{\gamma}/\gamma)^n dU. \quad (14)$$

The damage at any point in front of the growing crack is given by the sum of the damage due to crack initiation, as found from (12) and (11), and all of the damage increments from prior crack growth, as found from (13) and (14), with r taken to be the distance from the prior crack tip to the point in question, and ϕ the prior angle between crack and shear band.

The necessary increment in damage for fracture is $\delta\eta=1-\eta$. The corresponding strain increment can be found from (13):

$$\delta\gamma = (1-\eta) \ln F_t / \left[\frac{\gamma}{1+\gamma^2} + \frac{1}{2(1-n)} \frac{\sinh \frac{(1-n)\sigma}{\tau}}{\tau} \right]. \quad (15)$$

The necessary increment in far-field displacement to cause this strain increment can then be found from (14):

$$\delta U = (n+1) \frac{\sigma_1 I_1(n, M^P) \rho \cos \phi}{\tilde{\gamma} k} (\gamma/\tilde{\gamma})^n \delta\gamma. \quad (16)$$

The crack will advance in the direction ϕ which requires the least far field displacement to reach critical damage, not necessarily toward the most severely

i.e. the angle between crack and shear band is smaller and the triaxiality is smaller.

(5) For the low strain hardening $n=1/13$, increasing ϕ_0 gave smaller initiation displacements and strains and larger initial crack growth rates (dc/du).

(6) Strains and triaxialities during growth are relatively insensitive to the initial angle between crack and shear band.

(7) For both strain hardening exponents and all the angles ϕ_0 , the final average angle between crack and shear band ϕ_{avg} after growth by $c/\rho=100$ was between 23° and 32° from the shear band. The Mode I mixity corresponding to the final crack orientation was also within a correspondingly narrow range for each of the strain hardening exponents.

(8) These rigid-plastic results do not predict instability (infinite crack advance per unit far field displacement). Instability could, however, arise from the compliance of the surrounding structure.

SUMMARY OF CONCLUSIONS

A part containing a crack near a weld or a shoulder, loaded into the plastic range, can give an asymmetric shear band extending from the crack tip. The resulting crack propagation into previously damaged material gives less ductility than the typical symmetric case. A previous incremental solution for crack growth using Shih's asymptotic fields for a stationary crack in nonlinear elastic material is extended to account for the effect of triaxial stress in advancing a crack at an angle to the shear band. Far field displacement is assumed to take place along the shear band. Cracking is assumed to occur at the site around the crack tip that needs the least far field displacement for critical damage. For a 45° shear band, it is found that the crack does not advance along the shear band but at an angle of about 21° from the transverse under a higher triaxiality. The crack growth rate is higher by

about 6-15% (the larger increase with less hardening) than if the directional effects are neglected and the crack is assumed to progress along the shear band. A higher strain hardening decreases slightly (about 5%) the crack growth rate and the final angle from the transverse of the growing crack. Strains and triaxiality during growth are not sensitive to the initial angle between the crack and the shear band.

REFERENCES

1. McClintock F.A. and Slocum A.H., "Predicting fully plastic Mode II crack growth from an asymmetric defect", *Int.J.Fract.Mechanics*, 27, 49-62 (1985)
2. Shih C.F., "Small scale yielding analysis of mixed mode plane strain crack problems", *Fracture Analysis, ASTM STP 560*, Am.Soc.Test.Mat., Philadelphia, 187-210 (1974).
3. McClintock F.A., Kaplan S.M. and Berg C.A.(1966), "Ductile fracture by hole growth in shear bands", *Int.J.Fract.Mech.*, 2, 614-627 (1966).
4. McClintock F.A., "Plasticity aspects of fracture", in "Fracture", edited by H. Liebowitz (1971)
5. Rice J.R. and Tracey D.M. (1969) "On the ductile enlargement of voids in triaxial stress fields", *J.Mech.Phys.Sol.*, 17, 201-217.

TABLE 1

Comparison of numerical and approximate pure Mode II solutions

ϕ_0	Numerical				Approx. Mode II	
	0^0		45^0		0^0	
n	1/13	1/3	1/13	1/3	1/13	1/3
u_i/ρ	0.92	0.81	0.79	0.82	1.07	1.25
$\Delta c/\Delta u$	5.90	5.57	5.95	5.64	5.06	5.28

Appendix - Displacement Functions

The displacement functions u_i are determined from the strain functions for the plane strain considered here. The radial displacement u_r may be found from the radial strain

$$\epsilon_{rr} = \frac{\partial u_r}{\partial r}, \quad (17)$$

so

$$u_r = \int_0^r \epsilon_{rr} dr + u_r(0, \theta). \quad (18)$$

For zero rigid-body translation at $r=0$, $u_r(0, \theta)=0$. Eliminating ϵ_{rr} with (3) and integrating gives

$$\frac{u_r}{r} = \left[\frac{J}{\sigma_1 r I_{1/n}(n, MP)} \right]^{1/(n+1)} \left(\frac{n+1}{n} \right) \tilde{\epsilon}_{rr}. \quad (19)$$

Using the displacement equation (3) gives the radial displacement function \tilde{u}_r relative to that at $\theta=-\pi$:

$$\tilde{u}_r(\theta, MP, n) = \frac{n+1}{n} (\tilde{\epsilon}_{rr}(\theta, MP, n) - \tilde{\epsilon}_{rr}(-\pi, MP, n)). \quad (20)$$

The tangential displacement function u_θ is determined from

$$\epsilon_{\theta\theta} = \frac{1}{r} u_r + \frac{1}{r} \frac{\partial u_\theta}{\partial \theta} \quad (21)$$

as

$$u_\theta = \int_{-\pi}^{\theta} (r \epsilon_{\theta\theta} - u_r) d\theta + f(r). \quad (22)$$

Noting that $\epsilon_{\theta\theta} = -\epsilon_{rr}$ for plane strain incompressibility and using (3) with (20) gives the tangential displacement:

$$\frac{u_\theta}{r} = - \left[\frac{J}{\sigma_1 r I_{1/n}(n, MP)} \right]^{1/(n+1)} \left(\frac{2n+1}{n} \right) \int_{-\pi}^{\theta} \tilde{\epsilon}_{rr} d\theta + f(r)/r. \quad (23)$$

With respect to the displacement at $\theta=-\pi$, $f(r)=0$. By using (3) we can thus find the dimensionless tangential displacement function relative to the displacement at $\theta=-\pi$, in terms of the dimensionless strain function $\tilde{\epsilon}_{rr}$:

$$\bar{u}_{\theta}(\theta, M^p, n) = \frac{2n+1}{n} \int_{-\pi}^{\theta} \tilde{\epsilon}_{rr}(\theta, M^p, n) d\theta. \quad (24)$$

As an example, the displacement functions for $n=1/13$, $M^p=0.50$, determined numerically by (24), (20) are given in Fig. 3.

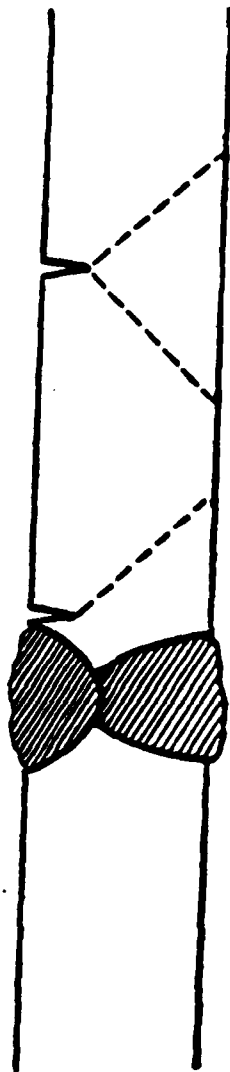


Fig. 1 Asymmetric crack from a defect near a weld. the syanetric case is shown above

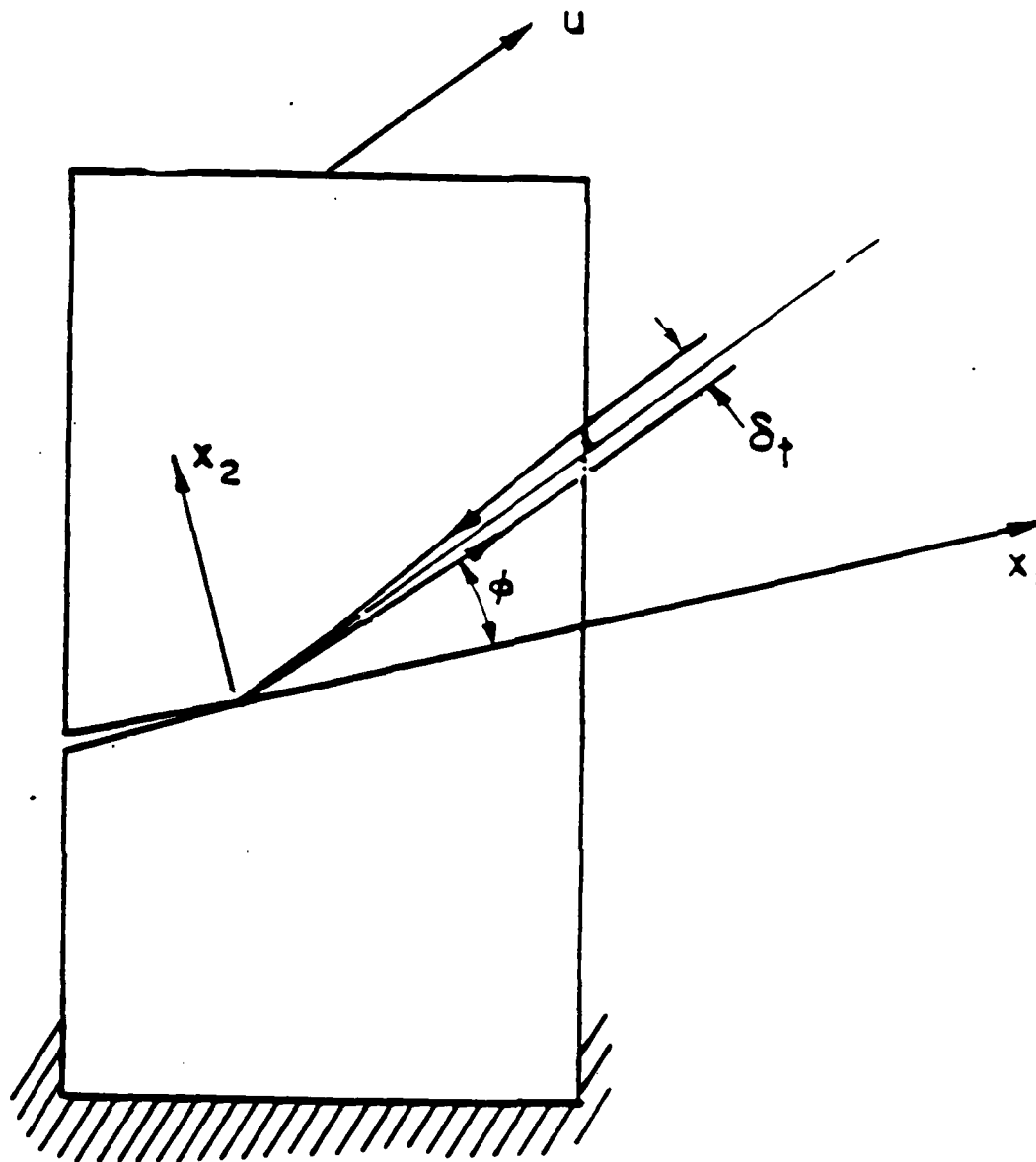


Fig. 2 J-integral parameters.

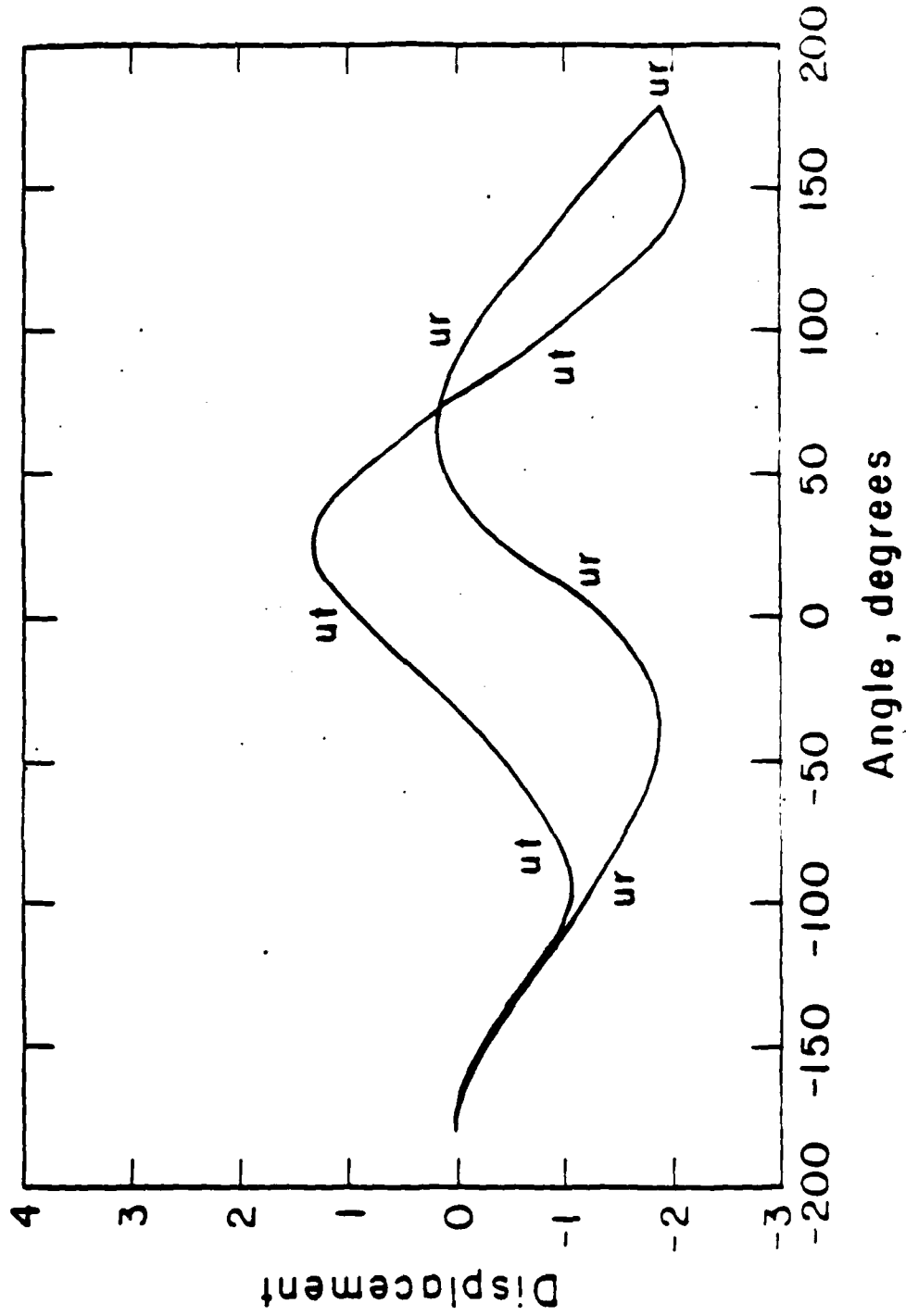


Fig 3 Angular variation of the radial and tangential near tip dimensionless displacement functions for plane strain with $n=1/13$ and $M^2=0.5$

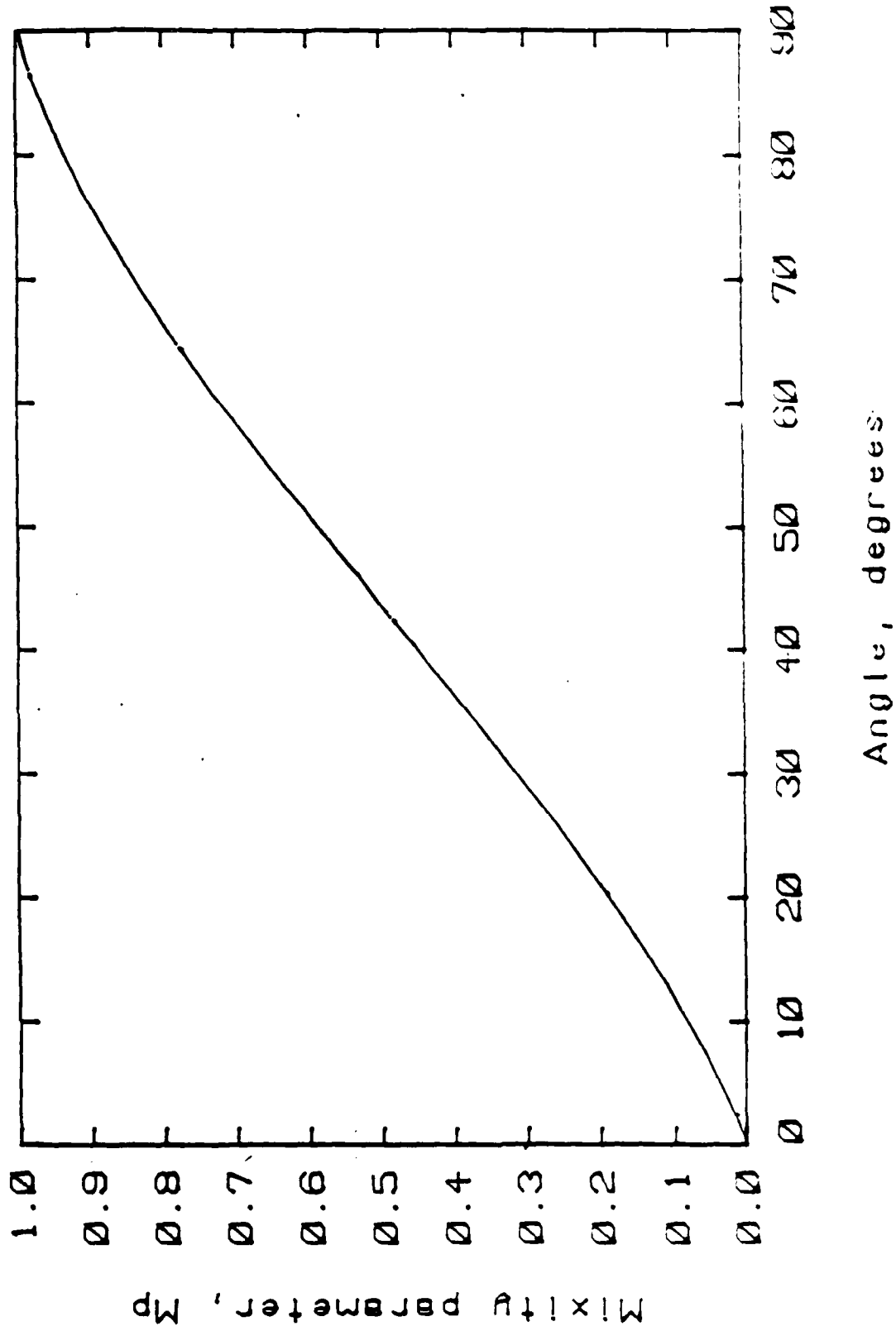


Fig 4 Mode I mixity parameter M_p as a function of the crack-shear band angle ϕ .

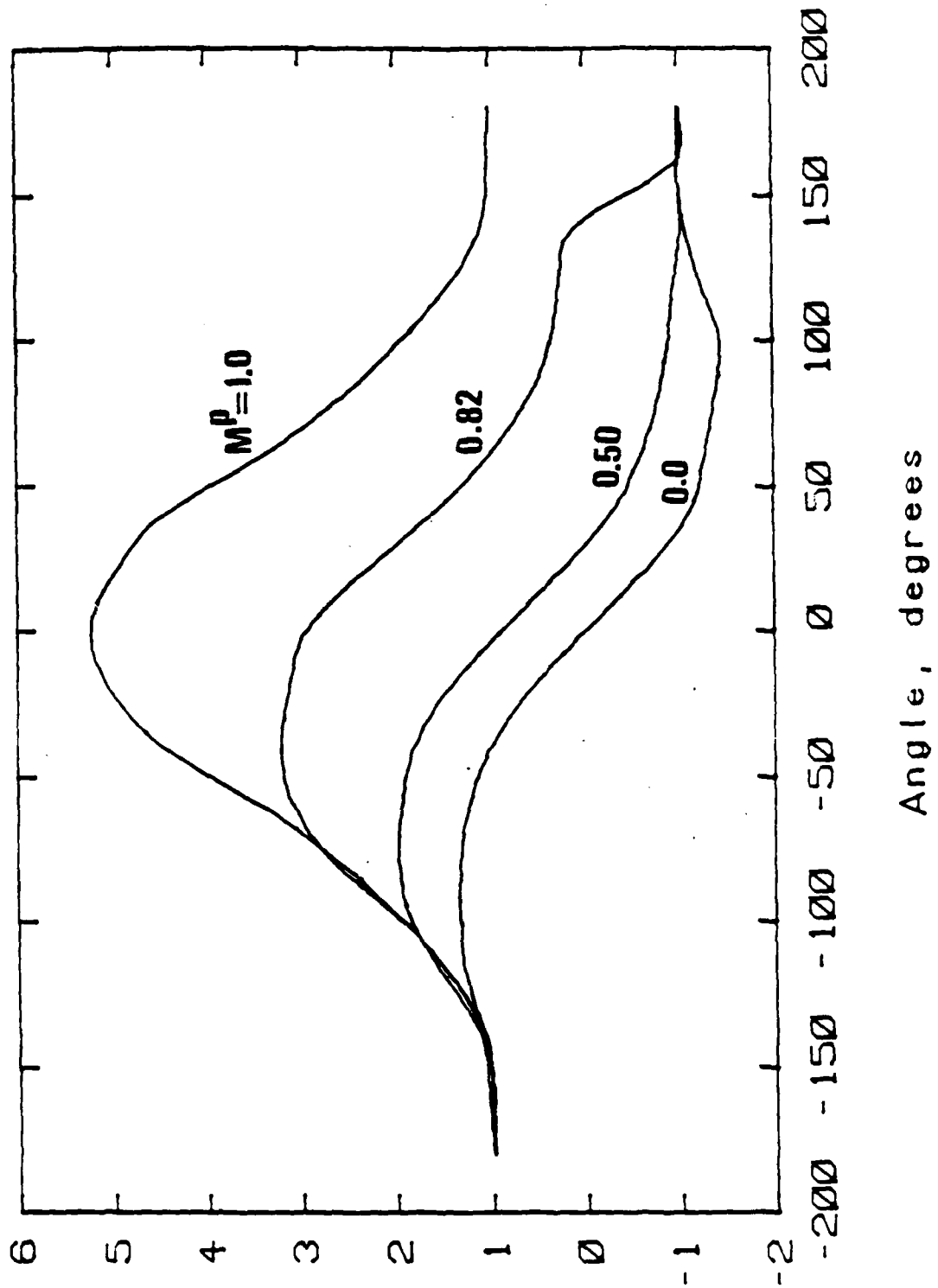


Fig 5 Angular variation of the triaxiality σ/τ for plane strain with $n=1/13$ and mixity $M^P = 0, 0.5, 0.82, 1.0$

A t t e c h n i c a l

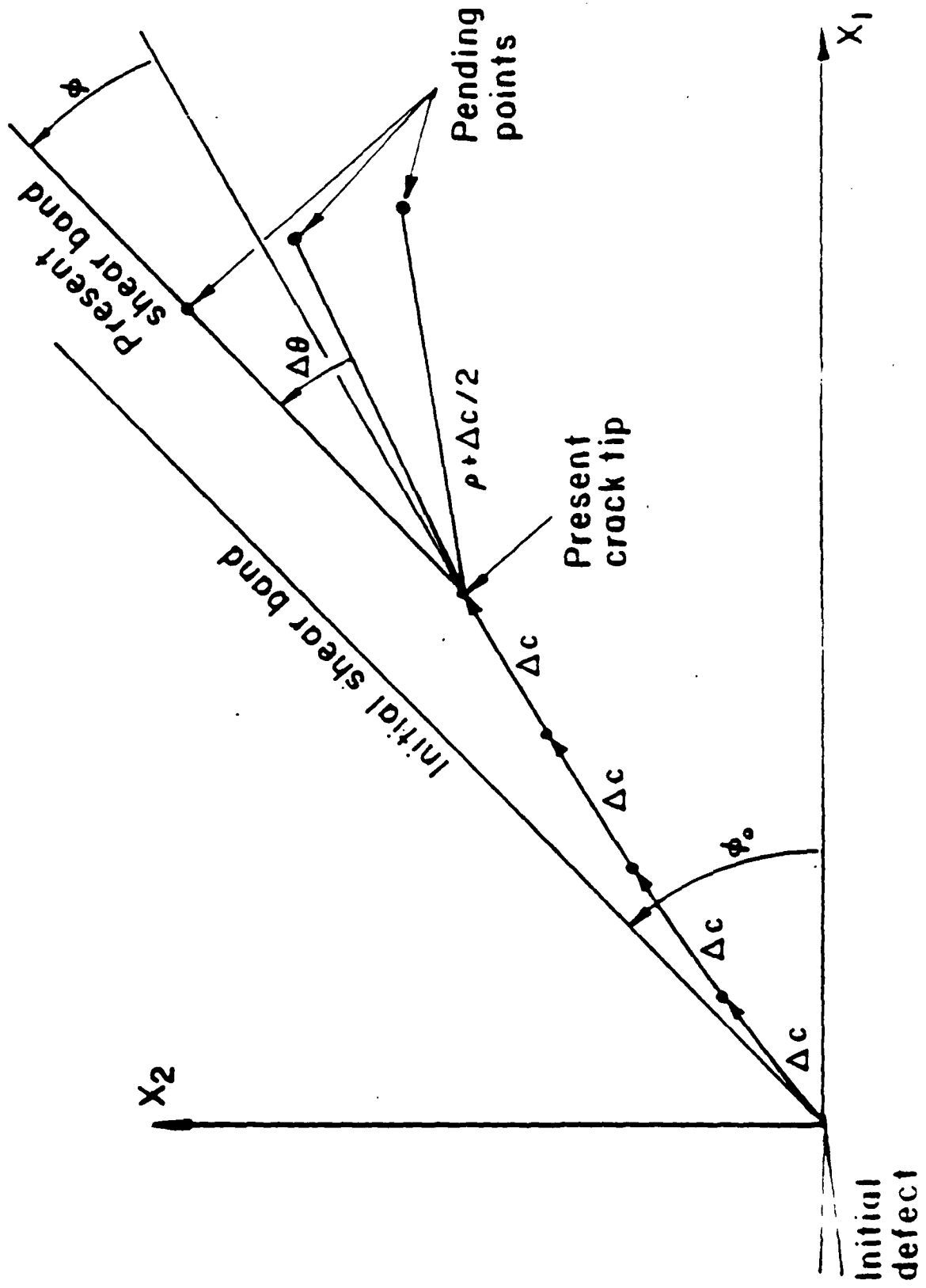
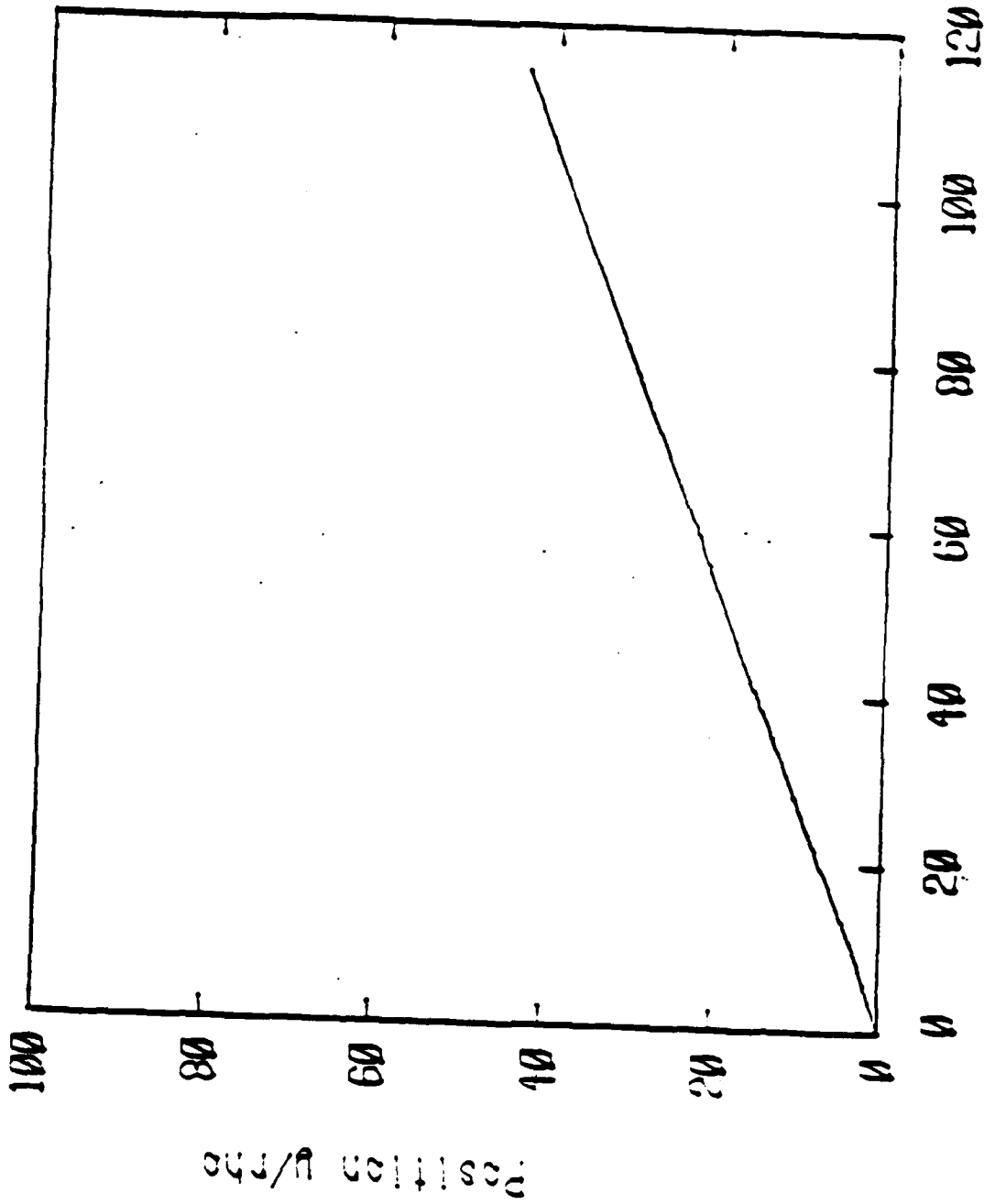
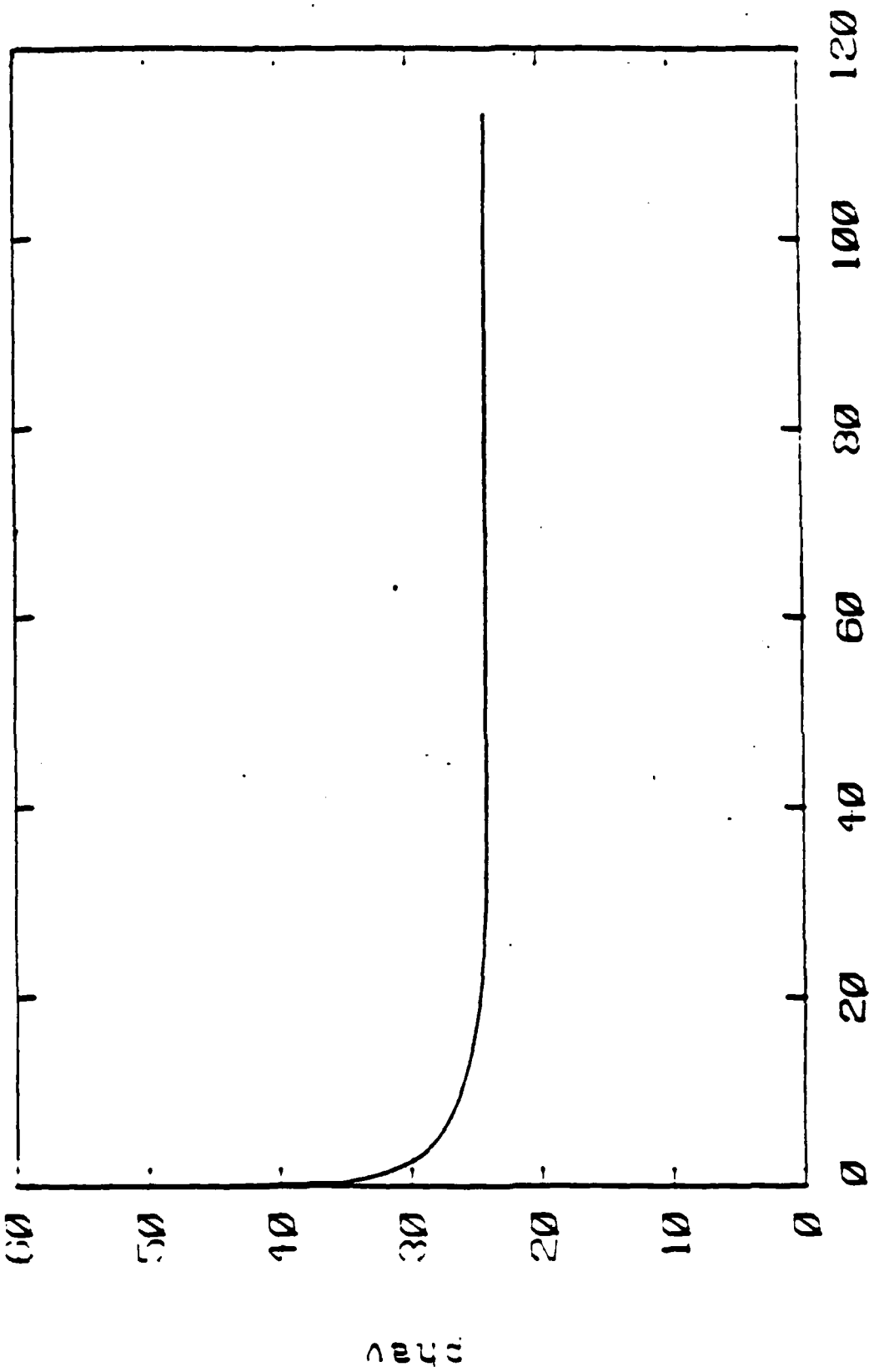


Fig. 6 Incremental crack growth



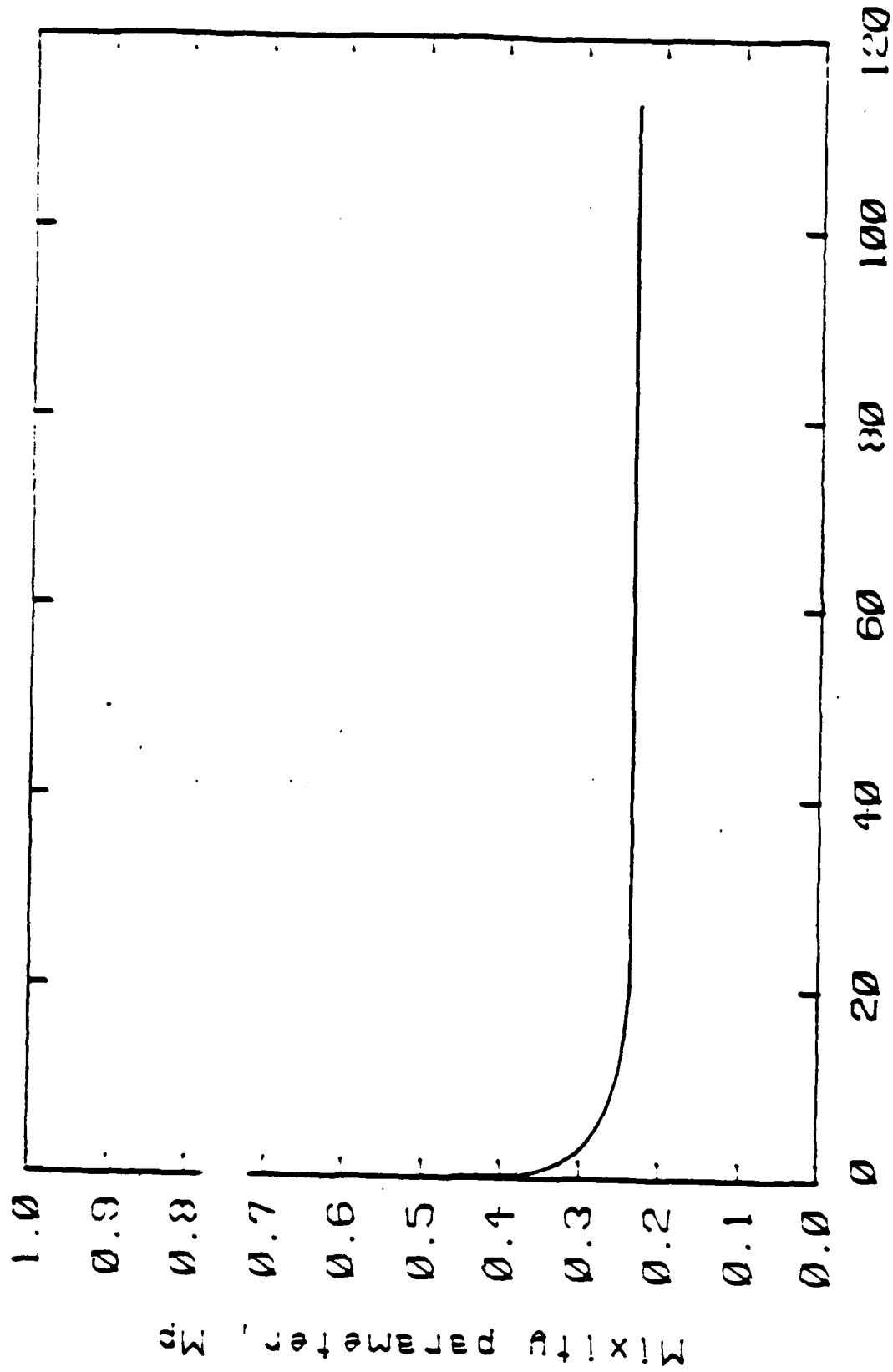
Position x/rho , $n=1/13$, $dc/rho=1/8$

Fig 7 Growing crack path for an initial crack-shear band angle $\phi_0=45^\circ$



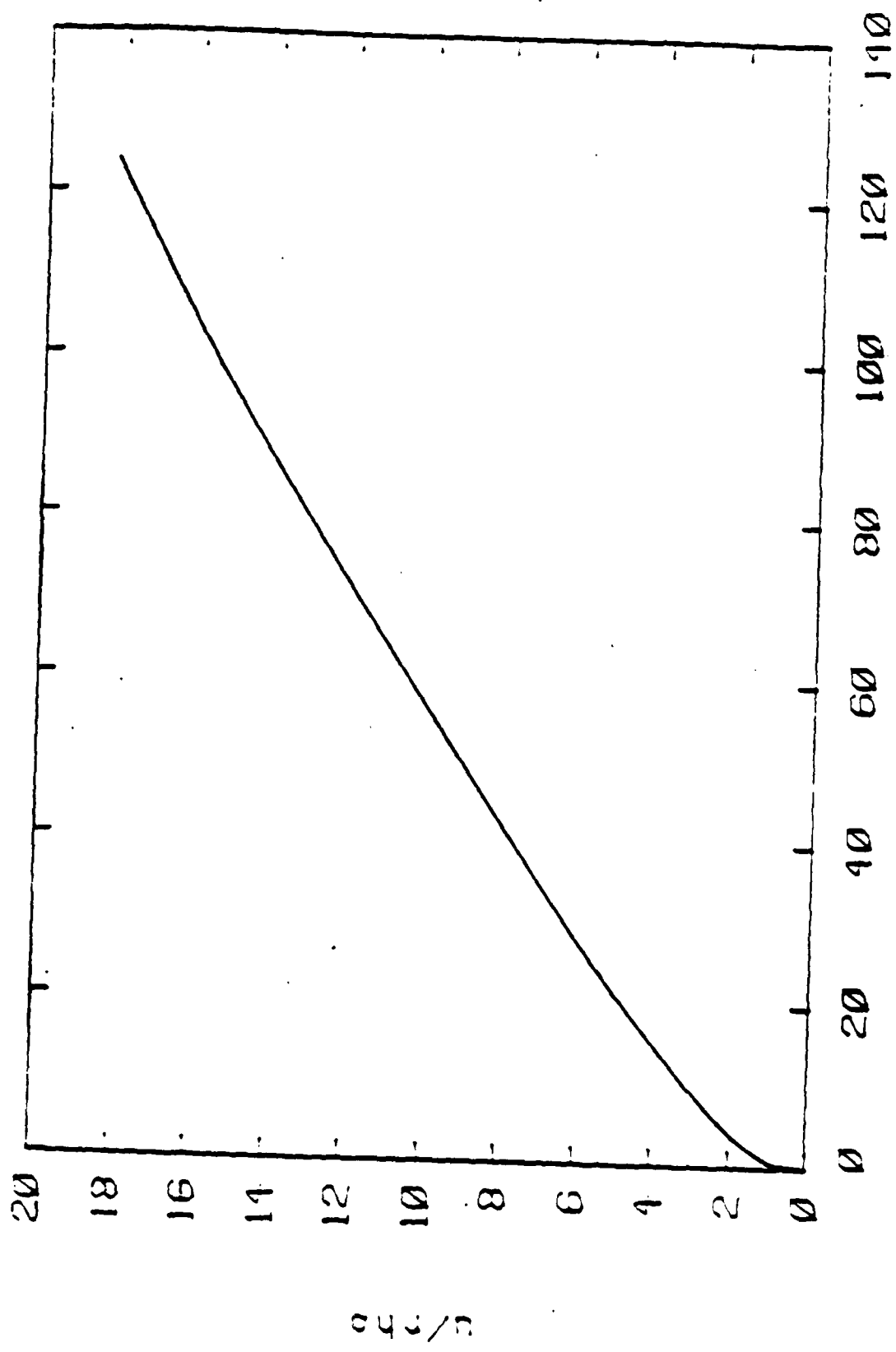
$x/\rho = 0.5$, $n = 1/13$, $d_c/\rho = 0.5$

Fig. 8 Average crack-shear band angle vs. projected crack advance



Position x/ρ , $n=1/13$, $d_c/\rho h_0=0.5$

Fig 9 Mode I mixity M^P vs. projected crack advance.



$c/\rho h_0, n = 1/13, d_c/\rho h_0 = 0.5$

Fig 10 Far-field displacement vs crack growth.

CHAPTER THREE
EXPERIMENTAL STUDY

TABLE OF SYMBOLS

D_{ext}	minimum extension rate (eq. 10)
D_g	crack ductility (eq. 3)
E	modulus of elasticity
F_L	load factor (eq. 12)
J	J-integral
k	shear yield
l_0	initial ligament
n	strain hardening exponent
P_{nom}	nominal load
T.S.	tensile strength
T	tearing modulus
T^*	eq. 8
T^*_{asym}	eq. 9
T^*_{sym}	
u_i	initiation displacement
u_g	growth displacement
\vec{v}_g	total displacement vector
\vec{v}_1	growth displacement vector
w	specimen width
σ_y	yield strength
ρ	mean inclusion spacing
σ_1	flow stress at unit strain
ϕ	displacement vector angle from transverse
γ_c	fracture strain
ω	crack opening angle
θ_c	crack direction from transverse.

ABSTRACT

Most fracture tests use symmetric specimens, with the crack advancing into the relatively undamaged region between two plastic shear zones. However, a crack near a weld or shoulder, loaded into the plastic range, may have only a single shear band, along which the crack grows into prestrained and damaged material with less

ductility than the usual symmetrical configurations. An experimental study on six alloys shows that while the crack initiation displacements are similar, the growth displacement is much less for the asymmetrical specimens, especially with less hardening. Indeed, for the low-hardening alloys ($n \approx 0.1$) the crack growth ductility, defined as the minimum displacement per unit ligament reduction, is less in the asymmetric case than the symmetric by a factor of three. In the higher hardening alloys the crack growth ductility is less in the asymmetric case by a factor of 1.2 at most. Triaxiality on one side of the asymmetric shear crack diverts it from 45° to 38° - 41° from the transverse direction, the larger angles with smaller strain hardening. In addition, the far field displacement vector is more axial than the 45° line, at 51° to 63° from transverse, suggesting a Mode I component even with asymmetry.

INTRODUCTION

For fracture-stable structures it is important not only that fully plastic conditions be attained before fracture, but also that the load does not fall off too rapidly during crack growth. Flow fields such as Fig. 1, in which the far-field deformation consists of a single shear band, may arise in practice due to the constraint of weld material. These specimens may exhibit less ductility than the symmetric ones, because the crack is advancing into pre-strained and damaged material, rather than into the new material encountered by a crack advancing between two symmetrical shear bands. Being able to predict such increased crack growth can have useful applications in the design, inspection and maintenance of pressure vessels and ships.

Near the tip of the growing crack, strain hardening will cause the deformation

field to fan out. For power law creep or deformation theory plasticity, the stress and strain in the neighborhood of a stationary crack may be found from Shih's [1] mixed mode solutions. More realistically, a corresponding, fully-plastic, incremental plasticity solution should be obtained for a growing crack, taking into account the hardening of the material left behind the growing crack. McClintock and Slocum [2] developed a formulation for the accumulation of damage directly ahead of an asymmetric crack, based on strain increments adapted from Shih's [1] analysis for stationary cracks in a power law material. The crack was assumed to follow the center of the 45° shear band. It was found that the crack growth per unit displacement increases approximately as the logarithm of the total crack advance per inclusion spacing ρ and varies inversely as the critical fracture strain γ_c . To correct for triaxial effects, several sites around the current crack tip were considered in chapter 2. The damage at each site due to crack initiation and prior growth was determined and then the necessary increment in far field displacement was found for each site. The crack was assumed to advance in the direction requiring the least displacement. This numerical investigation resulted in growth directions not along the 45° shear band but at a smaller angle from the transverse depending on the hardening and the initial crack-shear band angle, and lower ductility by 6-15% (larger decrease with less hardening) than with growth along the shear band.

A test with pure shear (Mode II) loading was carried out by Chant et al. [3] of high hardening carbon manganese steel (B.S. 1501-151-430A, Y.S.=329 MN/m², T.S.=490 MN/m²). Small specimens were subjected to both Mode II and Mode I testing but the ductility, measured by dJ/da , was practically the same although the microscopic features for the pure shear specimens are different than those observed in the Mode I specimens. The objective of the current study is to present experimental evidence on the ductility of asymmetric crack configurations.

EXPERIMENTAL PROCEDURES

Material. Tests were performed on six alloys with the mechanical properties listed in Table 1. True stress-true plastic strain curves (Figs. 2a,b) for these alloys were obtained using standard 6.35 mm. dia. specimens with 25.4 mm. gage length. It is convenient to represent a curve of equivalent stress $\bar{\sigma}$ vs. equivalent plastic strain $\bar{\epsilon}^p$ by:

$$\bar{\sigma} = \sigma_1(\epsilon_0 + \bar{\epsilon}^p)^n, \quad (1)$$

where σ_1 , ϵ_0 and n are three constants that were determined from the flow strengths at yield point, $\epsilon=0.125$ and $\epsilon=0.250$, and are given in Table 2. The lower hardening alloys are the 1018 cold finished steel, HY-80 and HY-100 steels ($n \approx 0.10$) and the higher hardening alloys are the 1018 normalized and A36 hot rolled steels ($n \approx 0.24$). The 5086-H111 aluminum is between these two groups.

Test Method. From 12.7 mm. dia. round bars of each alloy, seven specimens were first machined as shown in Fig. 3a, with side grooves to ensure a straight fatigue pre-crack approximately 1.3 mm deep. For the four asymmetric specimens (Fig. 3b), further side grooves were machined at 40° from the transverse direction. This corresponded to the crack direction found in preliminary tests and served to reduce 3-dimensional effects. For the three symmetric specimens, since the crack grows by alternating shear at $\pm 45^\circ$, orthogonal triangles were machined, as shown in Fig. 3c.

Stability of the tests turned out to be an important consideration due to the high crack growth rate expected in the asymmetric case. Thus short specimens, stiff adapters, and locknuts were used. The tensile tests were performed on an MTS 50

metric ton testing machine with resulting compliances of 2.3×10^{-6} , 4.6×10^{-6} , 1.08×10^{-6} mm/N for the steel specimens, the adapters, and the machine respectively. The axial and transverse displacements across the notch were plotted continuously.

A typical plot of load vs. axial displacement is shown in Fig. 4; the breakthrough point is when the fracture first breaks through the back surface, with some shear lips remaining on the sides. The displacement during crack initiation and growth, u_i and u_g , are found from the drawings of the crack path. The topographies of the fracture surfaces were thus subsequently plotted using a metallurgical microscope with a travelling stage. The horizontal and vertical coordinates of the travelling stage are recorded with two linear potentiometers; several points are obtained to give an impression of the surface profile of the broken specimens. A typical microscope plot, as in Fig. 5, consists of the 60° notch, the fatigue crack (with some amount of deformation, $\vec{v}_1 - \vec{v}_2$), an initiation zone which shows some blunting, and a growth zone. The initiation displacement is $\vec{v}_1 - \vec{v}_g$. These quantities were also checked against the data from the load-extension curves. In addition, fracture profiles were used to obtain the angular quantities such as the crack opening angle, ω , the lower and upper flank angles, θ_l and θ_u , and the orientation of the total displacement vector, ϕ , in the asymmetric case.

RESULTS

Initiation Displacement. Stable tests were obtained except for the lower hardening alloys, which were unstable for less than 20% of the falling part of the load-displacement curve. The results of the tests are summarized in Table 3. An idealized initiation displacement, u_i^I/l_0 , can be defined as the extension between the initial elastic loading and the steepest unloading parts of the load-displacement curve

at maximum load, normalized with the initial ligament l_0 (Fig. 4). This quantity, given in the first row of the table, is a convenient measure of initiation and can be compared with the the initiation displacement u_i , measured from the fracture surface profiles after complete separation. The normalized crack initiation displacement u_i/l_0 , does not appreciably differ between the asymmetric and symmetric configurations. It is, however, dependent on the strain hardening, being for the higher hardening alloys two to four times that of the lower hardening ones.

Ductility. For a measure of the crack growth resistance, the crack ductility, D_g , is defined as the minimum displacement, du_c , per unit projected ligament reduction, dl . Thinning of the ligament from the far side in fully plastic flow makes the reduction in ligament rather than crack advance more appropriate for describing load drop. The displacement du_c is associated with the crack opening stretch and consists of the gauge displacement du and the elastic unloading du_{unl} (Fig. 4):

$$du_c = du + du_{unl} \quad (2)$$

The ligament reduction can be approximated from the relative load drop and thus we can define:

$$D_g = \left(\frac{du_c/l_0}{dP/P_{max}} \right)_{min} \simeq \left(\frac{du_c}{dl} \right)_{min} \quad (3)$$

From Fig. 6, this is also related to the crack opening angle by

$$D_g \simeq (COA)/\cos^2\theta_c, \quad (4)$$

where θ_c is the crack orientation. In addition, the above defined quantity is the normalized compliance requirement for fracture-stable design:

$$\text{Compliance of surrounding} < D_g l_0 / P_{max} \quad (5)$$

The crack ductility, given in the second row, is smaller for the asymmetric case by a factor ranging from 3.4 for the lower hardening HY100 to 1.1 for the higher hardening A36 hot rolled steel. Notice that in the lower hardening alloys 1018 CF, HY-80, HY-100 steel the factor by which the ductility is reduced is larger than three which shows also that these alloys have much larger stiffness requirements for stability. A comparison of D_g among the alloys reveals that, in the asymmetric case, the crack growth rate in the lower hardening alloys is about 2 times larger than in the higher hardening alloys. In the symmetric case, on the contrary, the crack growth rate is practically insensitive to strain hardening.

The third row is a parameter analogous to the "tearing modulus" T of Paris et al. [4] defined in terms of the yield or tensile strength σ_0 , the modulus E and the J-integral by:

$$T = \frac{E}{\sigma_0^2} \frac{dJ}{dc} \quad (6)$$

To approximate the J-integral, consider the simple case of the far-field displacement taking place along a single shear band [2] and express it in terms of the shear strength, k , and the displacement along the band $u\sqrt{2}$,

$$J = ku\sqrt{2}, \quad (7)$$

and thus define a parameter, T^* , analogous to the tearing modulus T , which allows comparing the ductility of alloys of different strength. In terms of the tensile strength T.S. $\simeq k\sqrt{3}$, by:

$$T^*_{\text{asym}} = \left(\frac{E/\sqrt{3}}{\text{(T.S.)}} \right) D_g \quad (8)$$

In the symmetric case the expression for the J-integral, $J=2ku$ [5] leads to an analogous to (8) expression.

$$T_{\text{sym}}^* = \left(\frac{2E/\sqrt{3}}{\text{(T.S.)}} \right) D_g \quad (9)$$

T_{asym}^* is about 3 times larger for the higher hardening alloys, as is shown in Table 3.

The load-displacement curve of Fig. 4 can be described in terms of the initial elastic compliance, the idealized initiation displacement u_i^I , and the minimum gauge displacement per unit crack advance (steepest slope of the falling part), D_{ext} , given by

$$D_{\text{ext}} = \left(\frac{du/l_0}{dP/P_{\text{max}}} \right)_{\text{min}} \simeq \left(\frac{du}{dl} \right)_{\text{min}} \quad (10)$$

This definition includes the effect of the compliance in the shoulders and is thus smaller than D_g . Results for 25 mm gauge length are given in the fourth row of Table 3.

Growth Displacement. The growth displacement until the fracture breaks through the back of the specimen, u_g , can be found from the fracture surface profiles. The normalized displacements during crack growth, u_g/l_0 is more than 3 times larger in the symmetric than the asymmetric specimens for the lower hardening alloys but only about 18% larger for the higher hardening A36 HR steel. It is also larger by about a factor of two in the higher hardening relative to that of the low hardening alloys.

The far-field displacement vector angle from the transverse in the asymmetric case, defined from the slope of the transverse-axial displacement curves, is found to be greater than 45° and larger initially in the lower hardening alloys. As the crack grows the displacement vector becomes less axial (Fig. 7a). The final orientation θ_c , measured after fracture from the microscope plots (Fig. 5) is between 53° and 63° ,

larger for the higher hardening case. The fact that the axial component of the displacement is larger than the transverse one suggests a Mode I mixity of the local plastic flow.

Crack direction. In the symmetric specimens the crack runs within ten degrees of horizontal except for shear lips near the ends of the cracks. In the lower hardening alloys, even with the symmetric geometry, the fracture turned often into the asymmetric mode, the fracture advancing close to the 45^0 slip plane or, in some cases, half of the cross section following the one and the other half following the other slip plane. In the asymmetric specimens the crack progresses at an angle of about 38^0 - 41^0 from the transverse. This smaller than 45^0 angle was expected from the higher triaxiality. In the lower strain hardening alloys the crack grows closer to the 45^0 band, at 40^0 - 41^0 from the transverse and in the higher hardening alloys at 38^0 - 39^0 (Table 3). Finally more blunting occurred with the higher hardening alloys and in the symmetric case.

Load. To summarize the load performance, a parameter dealing with the maximum load will be defined. The nominal load-carrying ability is simply the tensile strength multiplied by the net area at the end of the fatigue crack (and corrected by the plane strain factor). In terms of the initial ligament l_0 , the width w , and the tensile strength T.S.,

$$P_{\text{nom}} = l_0 w (\text{T.S.}) (2/\sqrt{3}) . \quad (11)$$

A load factor F_L can be defined in terms of the actual maximum load P_{max} as:

$$F_L = P_{\text{max}}/P_{\text{nom}} . \quad (12)$$

Table 3 also contains the load factors. They are in general larger in the symmetric

case, where the overall deformation is bigger, and in the higher hardening alloys.

The normalized load-normalized displacement (and transverse-axial displacement for the asymmetric case) curves, obtained for the lower hardening HY-100 steel and higher hardening A36 HR steel for both the asymmetric and symmetric case are shown in Figs. 7a, 7b, 8a and 8b. For the HY-100 steel, notice the sharp increase in the slope of the falling part of the load-displacement curve of the asymmetric case relative to that of the symmetric; this is not the case in the A36 HR steel. The microscope plots for these alloys are shown in Figs. 9a, 9b 10a and 10b. In the HY-100 steel, notice the large reduction in the crack opening angle of the asymmetric case relative to that of the symmetric, whereas in the A36 steel the difference in the crack opening angle between the two geometries is not appreciable.

Size effects. To investigate size effects, tests were performed in 38.1 mm. dia. specimens of 5086-H111 aluminum and the results were compared with those from the 12.7 mm. specimens. Table 4 summarizes the results Comparing with the data given in Table 3 for the smaller 5086-H111 specimens, we conclude that the ductility and the normalized growth displacement is only 4% smaller for the larger specimens and the load factor is slightly larger. Notice that the size effects that were predicted in [2] are associated with a transient behavior (increasing crack advance per unit far field displacement).

Marking the crack front. In the large 38.1 mm dia. 5086-H111 aluminum specimens, the crack front was marked by imposing unloading-loading cycles at selected points during crack advance. The spacing of these fatigue marks was measured with a stereo microscope at about 50x. The corresponding displacements were then obtained from the load-displacement curves. In this manner, points on the

c-u curve can be accurately determined. Figure 11a and 11b show the load-displacement curves and in Figure 12 the corresponding crack growth-displacement data.

Comparing with theoretical formulations. An approximate formulation for the accumulation of damage ahead of an asymmetric crack, based on strain increments following a power law relationship was presented by McClintock and Slocum [2]. The crack was assumed to progress along the 45° shear band (pure Mode II) with the far field displacement along the shear band. The initiation displacement was expressed by:

$$u_i = \frac{\sigma_1}{k} I_{1/n} \rho \left(\frac{\gamma_c}{2\epsilon} \right)^{n+1}, \quad (13)$$

where γ_c is the fracture strain, k is the shear strength, $\epsilon = 0.88$ for the assumed pure Mode II and $I_{1/n} = 0.72-0.83$ for $n = 0.1-0.2$. The initiation displacement is thus of the order of the inclusion spacing (0.010 mm), much smaller than the one found experimentally. This discrepancy is due to the blunting that occurs during crack initiation. For a quasi-steady growth, the crack advance per unit displacement was practically insensitive to the strain hardening exponent n and was found:

$$\frac{d(u/u_i)}{d(c/\rho)} = \frac{n+1}{\ln[(c-c_i)/\rho + \exp(n+1)]}. \quad (14)$$

The above formula, for a mean inclusion spacing $\rho = .01$ mm and growth by the ligament length of $l_0 = 2.54$ mm, gives $du/dc \approx 0.200$, which is closer to the test data for the higher hardening alloys. Equation (14) underestimates the crack growth rate in the lower hardening alloys by a factor of two. For the size effects, predicted in [2], use the mean inclusion spacing of about 10 microns and find the ratio of the crack growth rate for the large 38.1 mm specimens (initial ligament $l_0 = 7.62$ mm) to that of the small 12.7 mm (initial ligament $l_0 = 2.54$ mm) ones as

$$\frac{(dc/du)_{\text{large}}}{(dc/du)_{\text{small}}} = \frac{\ln[(c-c_i)/\rho]_{\text{large}}}{\ln[(c-c_i)/\rho]_{\text{small}}} = \frac{\ln 762}{\ln 254} = 1.20 .$$

Thus the resulting from the integration of stationary crack fields [2] increasing crack advance per unit displacement (associated with the strain distribution flattening out in front of the crack at a decreasing rate) leads to larger size effects than those experimentally observed. Notice, however, that a solution based on a superposition of stationary singularities does not take into account the hardening of the material left behind the growing crack. More realistically, a corresponding fully-plastic, incremental plasticity solution should be obtained for a growing mixed mode crack.

To study the directional effects, an incremental solution was developed in chapter 2. The far field displacement was again assumed to be along the shear band. At the initiation and at each growth step several sites around the current crack tip were considered and the crack was assumed to advance to the direction requiring the least far-field displacement to reach critical damage. The program predicted that a smaller strain-hardening coefficient would cause the crack to grow closer to the shear band and this was confirmed from the experimental results. It also gave 6-15% higher crack growth rates (the larger increase with less hardening) than the pure Mode II [2] solution and thus closer to the experimental findings. The effect of strain hardening was very small, although it was correctly found that a lower strain hardening increases the crack growth rate. The 45° shear band gave however a crack angle of 21° from the transverse. The experimentally found angle of approximately 40° from the transverse can be obtained by assuming a 65° shear band. Notice however that the displacement vector angles (Table 3) suggest that we cannot assume the far-field displacement taking place along a 45° shear band as this model did.

CONCLUSIONS

In asymmetrical configurations with only a single shear band, (which can occur with cracks near welds for example), the crack progresses into prestrained material instead of the new material between the two shear bands of the symmetric case. Experiments on six alloys have shown that the resulting reduction in ductility is primarily dependent on the strain hardening exponent. In the lower hardening alloys the crack ductility, defined as the minimum displacement per unit ligament reduction, in the asymmetric case is less than a third that of the symmetric one but in the higher hardening alloys the reduction is no more than 20%. The high crack growth rate of the asymmetric configuration leads also to correspondingly higher stiffness requirements for fracture-stable design. The initiation displacement is not much different and a fair amount of blunting was observed during initiation for both cases. The crack growth direction is 38° - 41° from the transverse (instead of 45°) as expected from triaxiality, the higher angles with the smaller strain hardening. The displacement vector is at about 51° - 63° from the transverse. Angles greater than 45° suggest a Mode I component, even with asymmetry.

REFERENCES

1. Shih C.F. "Small Scale Yielding Analysis of Mixed Mode Plane Strain Crack Problems", *Fracture Analysis, ASTM STP 560*, Am.Soc.Test.Mat., Philadelphia, 187-210 (1974).
2. McClintock F.A. and Slocum A.H. "Predicting Fully Plastic Mode II Crack Growth from an Asymmetric Defect", *Int.J.Fract.Mechanics*, 27, 49-62 (1985).
3. Chant M., Green G., Whatmough I.J., Williams D.C. "The first large shear specimen test" General Electricity Generating Board Report No. SSW/SSD/0250/R/83, Job No. 01-95 (1983).
4. Paris P.C., Tada H., Zahoor A., and Ernst H. "A Treatment of the Subject of Tearing Instability" U.S. Nuclear Regulatory Commission Report NUREG-0311 (1977).
5. McClintock F.A. "Plasticity Aspects of Fracture", *Fracture, Vol.3*, edited by H. Liebowitz, Academic Press, New York, pp. 47-225 (1971).
6. Carter W.T. "Incremental solution of Asymmetric Crack Growth along a single Fully Plastic Shear Band", S.M. Thesis, Department of Mechanical Engineering, M.I.T. (1983).

TABLE 1

Ambient temperature mechanical properties of the six alloys tested.

Alloy	Yield strength	Tensile Strength (T.S.)	Hardness HBN	Reduction in area
	MN/m ²	MN/m ²	kgf/mm ²	Percent
1018 steel cold finished 0.15-0.20% C, 0.60-0.90% Mn	586	600	157	49.3
1018 steel normalized at 1700 ⁰ F in argon flow	321	355	101	61.7
A36 steel hot rolled 0.29% C max, 0.60-0.90% Mn	281	348	105	61.1
HY80 steel 0.18% C, 2-3.25% Ni, 0.10-0.40% Mn, 0.15-0.35% Si	587	692	175	69.9
HY100 steel 0.20% C, 2.25-3.50% Ni, 0.10-0.40% Mn, 0.15-0.35% Si	693	772	195	68.6
5086-H111 aluminum 4% Mg, 0.4% Mn, 0.15% Cr	210	264	70	45.8

TABLE 2

Stress-strain equation parameters.

Alloy	σ_1 MN/m ²	ϵ_0	n
1018 steel cold finished	796	0.05152	0.10
1018 steel normalized	818	0.01718	0.23
A36 steel hot rolled	697	0.02628	0.24
HY80 steel	1107	0.00702	0.12
HY100 steel	1180	0.00488	0.10
5086-H111 aluminum	589	0.00554	0.19

TABLE 3 - TEST RESULTS (Ligament $l_0=2.54$ mm)

Alloy	1018 CF	HY80	HY100	1018 norm.	A36 HR	5086-H111
INITIATION						
Idealized initiation displacement, u_i^I/l_0 (Fig. 4)						
Sym	0.072	0.108	0.083	0.348	0.172	0.179
Asym	0.073	0.110	0.100	0.252	0.206	0.161
DUCTILITY MEASURES						
Crack Growth Ductility, D_g , eq. (3), $\simeq (du_c/d)_{\min}$						
Sym	0.233	0.320	0.354	0.258	0.192	0.166
Asym	0.072	0.096	0.105	0.215	0.181	0.108
Modified Tearing Modulus, T^* , eqs. (8), (9), $\propto (E/T.S.)D_g$						
Sym	90.9	107.9	103.8	144.3	108.8	43.6
Asym	14.1	16.2	15.8	57.6	51.3	14.2
Min. extension rate, D_{ext} , eq. (10), $\simeq (du/d)_{\min}$ (25mm gauge length)						
Sym	0.199	0.285	0.299	0.237	0.165	0.120
Asym	0.046	0.060	0.061	0.195	0.154	0.083
DISPLACEMENTS from fracture profiles, Fig. 5						
Initiation Displ., u_i/l_0						
Sym	0.021	0.051	0.051	0.214	0.080	0.079
Asym	0.033	0.072	0.052	0.152	0.110	0.073
Growth Displ., u_g/l_0						
Sym	0.262	0.362	0.404	0.317	0.254	0.278
Asym	0.084	0.115	0.125	0.230	0.216	0.138
Displacement vector angle, ϕ						
Sym			($\approx 90^\circ$)			
Asym	51°	55°	55°	63°	61°	56°
CRACK DIRECTION, $\theta_c = (\theta_u + \theta_l)/2$ (Fig. 5)						
Sym			($\approx 0^\circ$)			
Asym	41°	40°	40°	38°	38°	40°
LOAD FACTOR, $F_L = P_{\max}/l_0 w(T.S.) (2/\sqrt{3})$						
Sym	1.02	1.16	1.15	1.29	1.21	1.19
Asym	0.88	1.05	1.06	1.15	1.20	1.12

TABLE 4 - RESULTS FROM LARGE SPECIMENS (Ligament $l_0=7.62$ mm)

Alloy	5086-H111 Aluminum
INITIATION	
Idealized initiation displacement, u_i^I/l_0	
Sym	0.081
Asym	0.072
DUCTILITY MEASURES	
Crack Ductility, D_g	
Sym	0.165
Asym	0.105
Modified Tearing, Modulus, T^*	
Sym	43.4
Asym	13.8
Min. extension rate, D_{ext} , for 25 mm gauge length	
Sym	0.118
Asym	0.080
DISPLACEMENTS from fracture profiles	
Initiation Displ., u_i/l_0	
Sym	0.026
Asym	0.024
Growth Displ., u_g/l_0	
Sym	0.280
Asym	0.133
Displacement vector angle, ϕ	
Sym	($\approx 90^\circ$)
Asym	57°
CRACK DIRECTION, θ_c	
Sym	($\approx 0^\circ$)
Asym	40°
LOAD FACTOR, F_L	
Sym	1.21
Asym	1.18

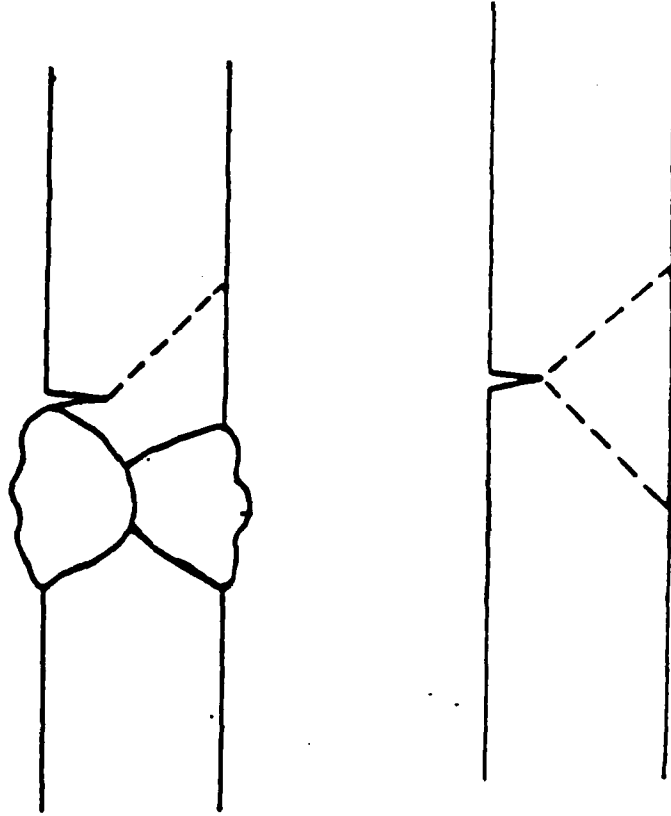


Figure 1. Asymmetric and Symmetric shear from cracks.

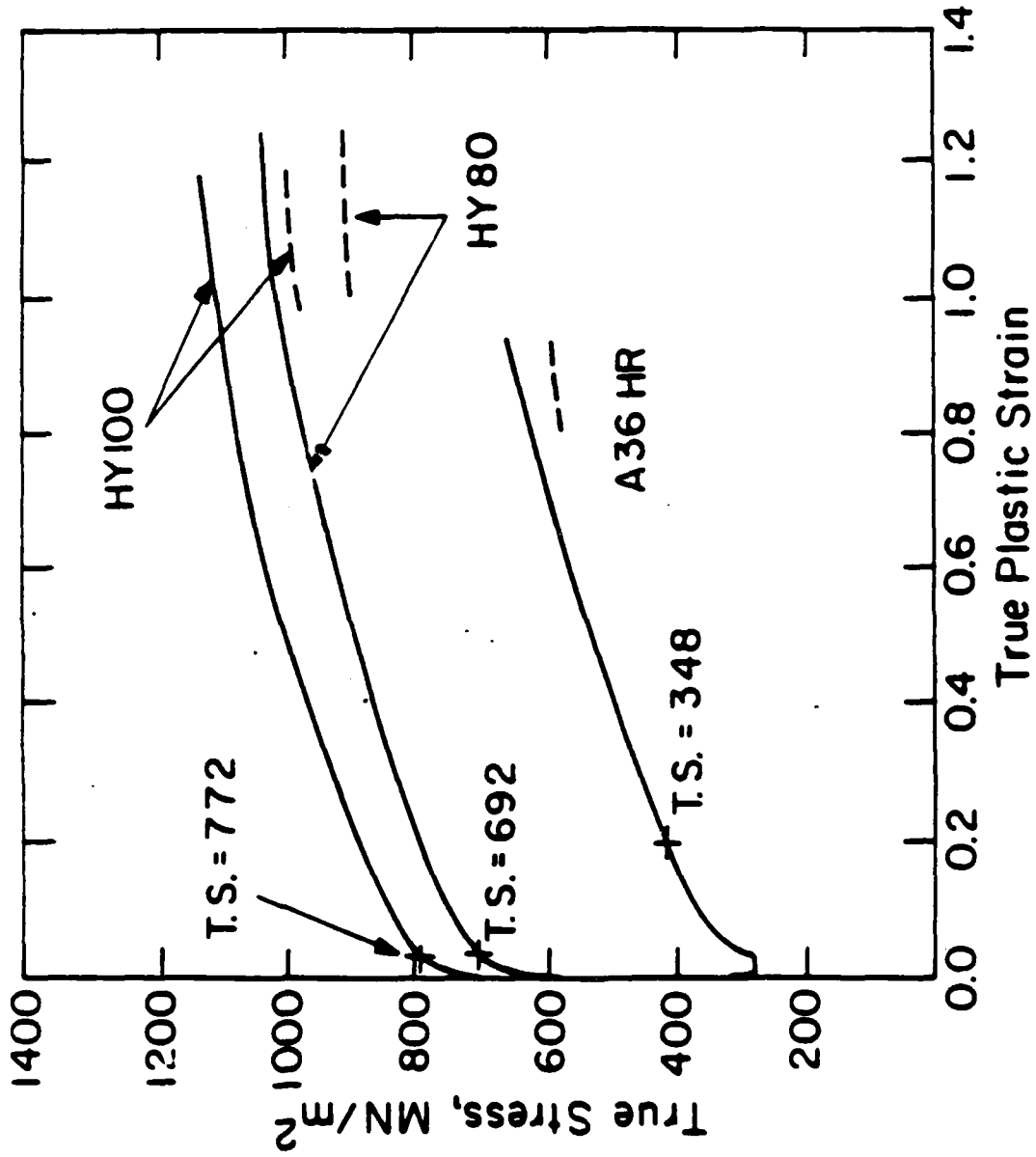


Figure 2a. True Stress- True Plastic Strain for HY-80, HY-100 and A36 Hot Rolled Steel. Dashed lines indicate Bridgman necking correction from the semiempirical relations.

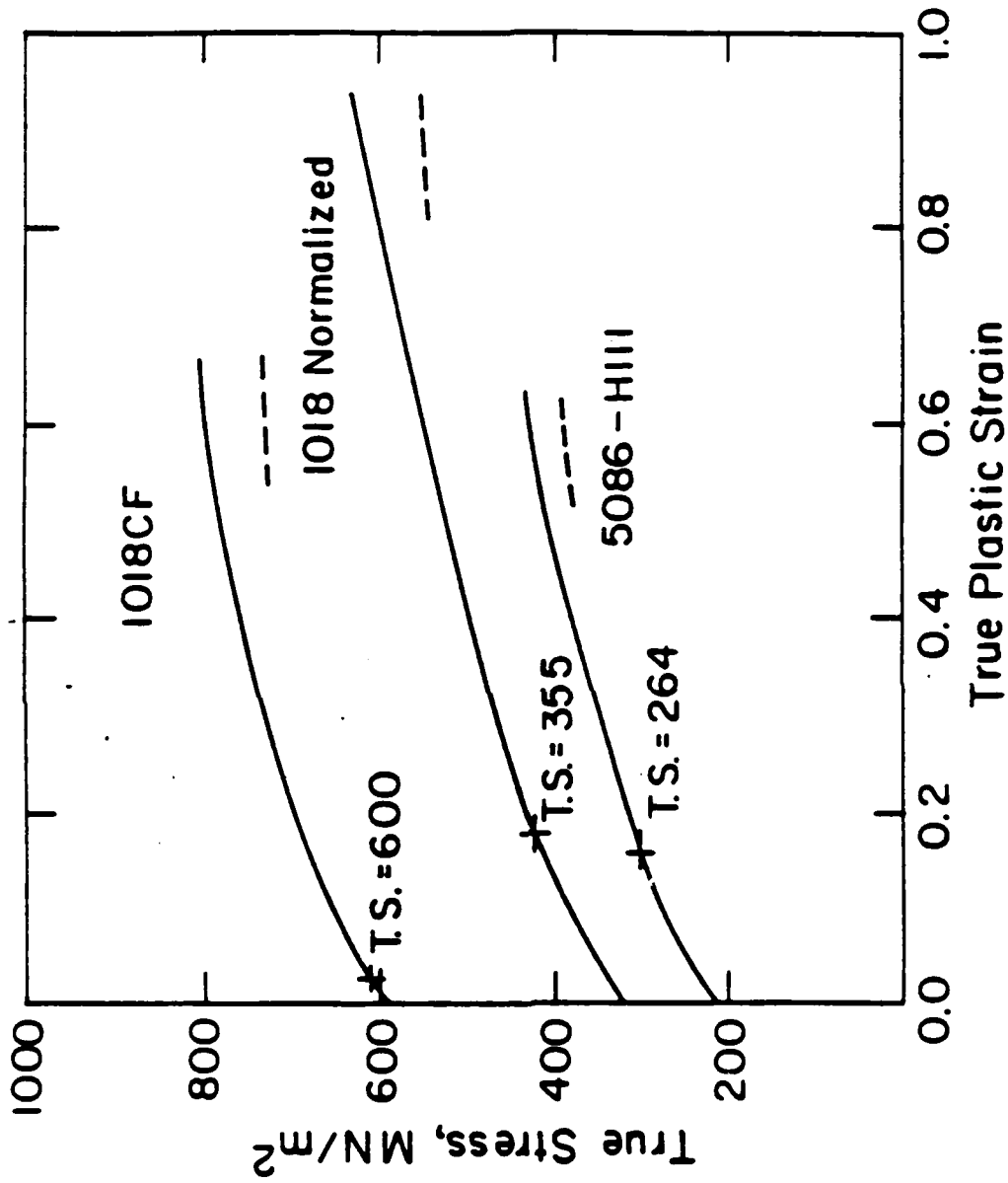


Figure 2b. True Stress- True Plastic Strain for 1018 Cold Finished, 1018 Normalized Steel and 5086-H111 Aluminum. Dashed lines indicate Bridgman necking correction from the semiempirical relations.

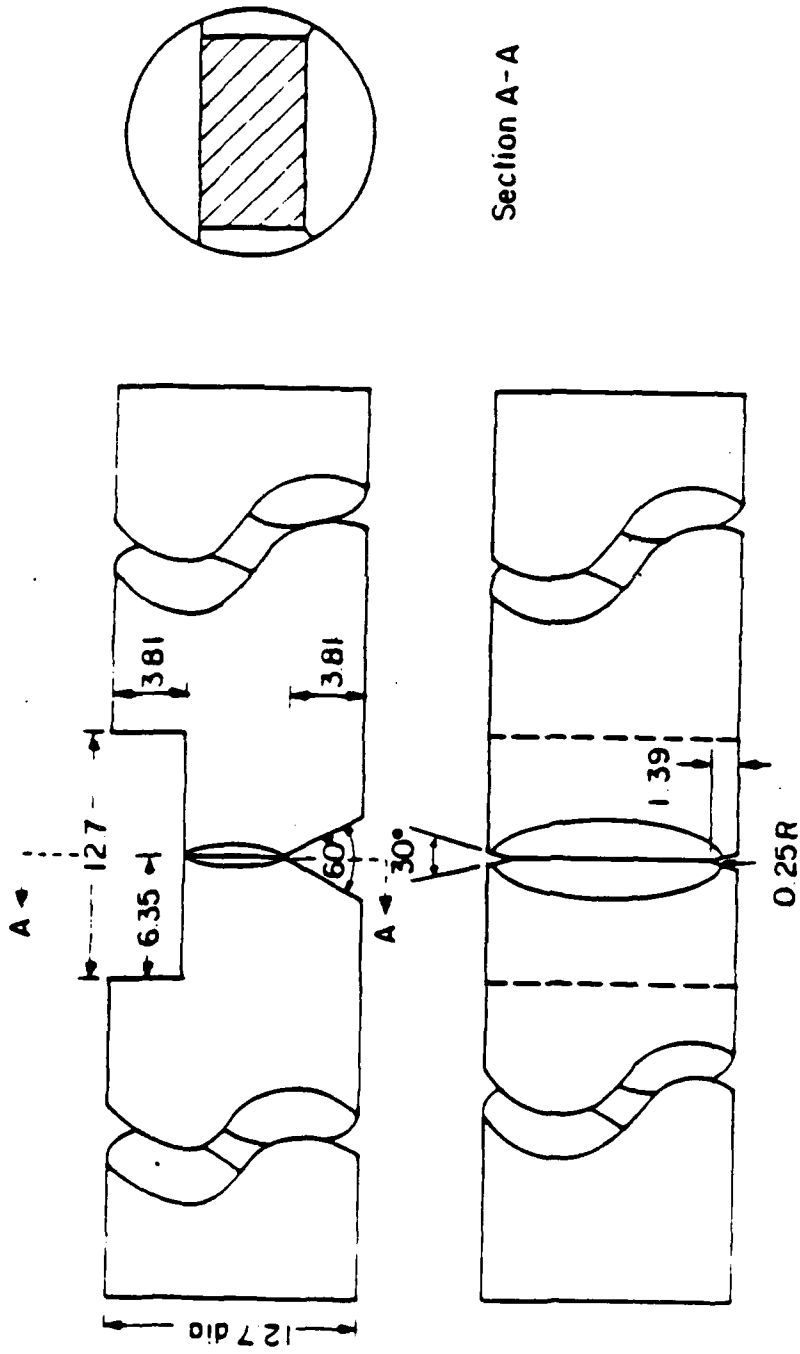
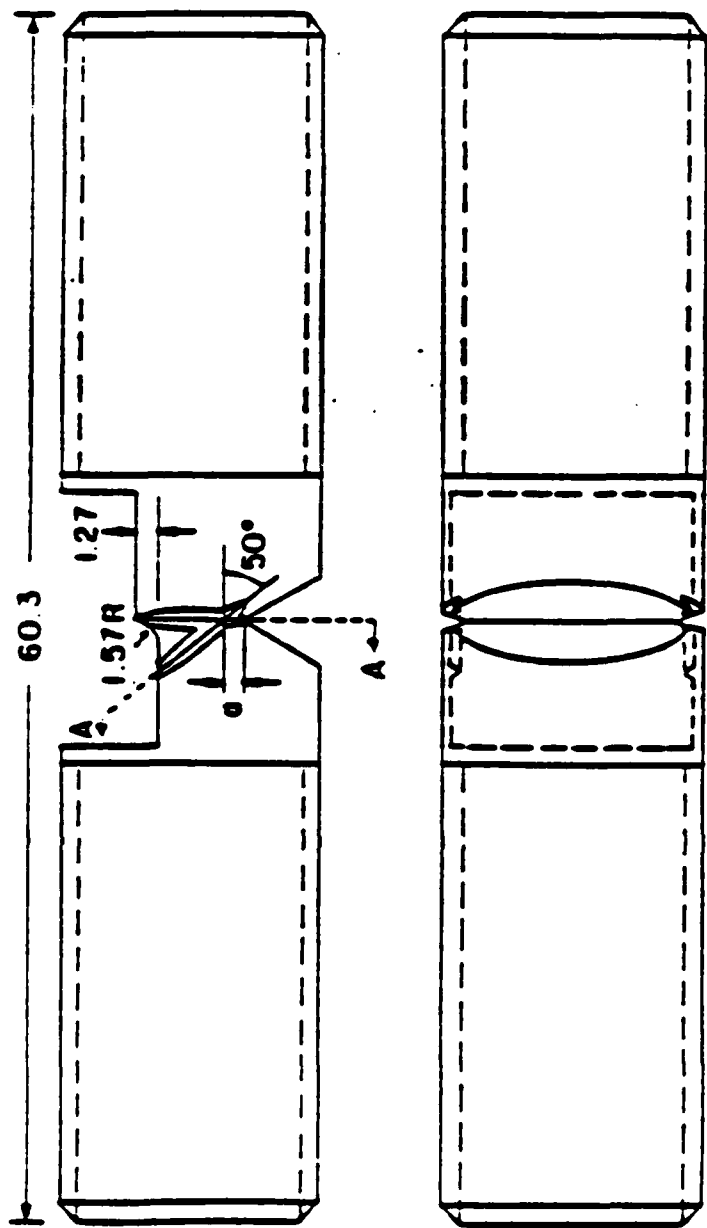


Figure 3a. Machining for precracking of the Specimens.



Section A-A

Figure 3b Second Machining (after fatigue precracking) for the Asymmetric Specimens: a is the fatigue crack.

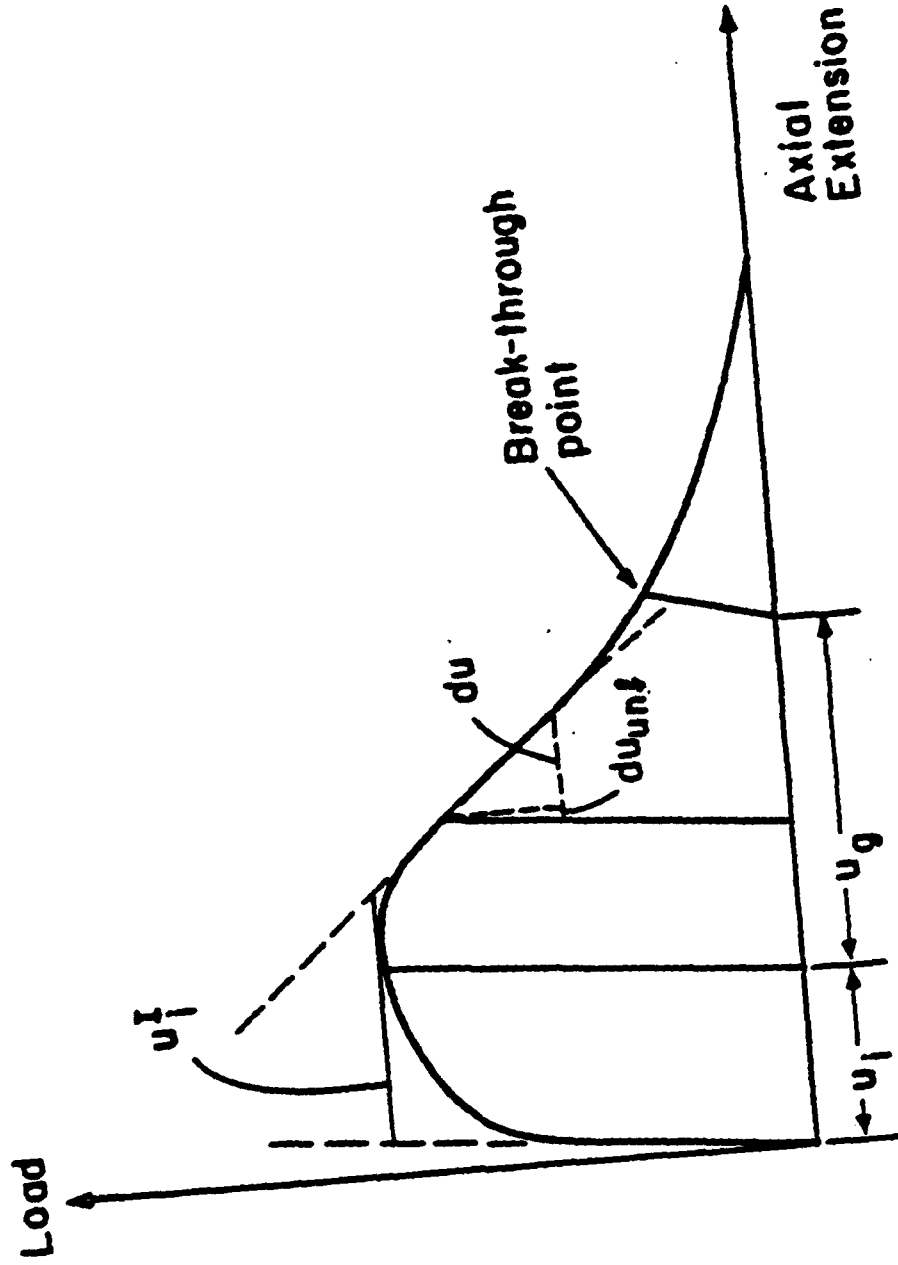


Figure 4. Schematic of the load vs axial gauge-point displacement curve. The displacements u_g and u_1 are measured after fracture.

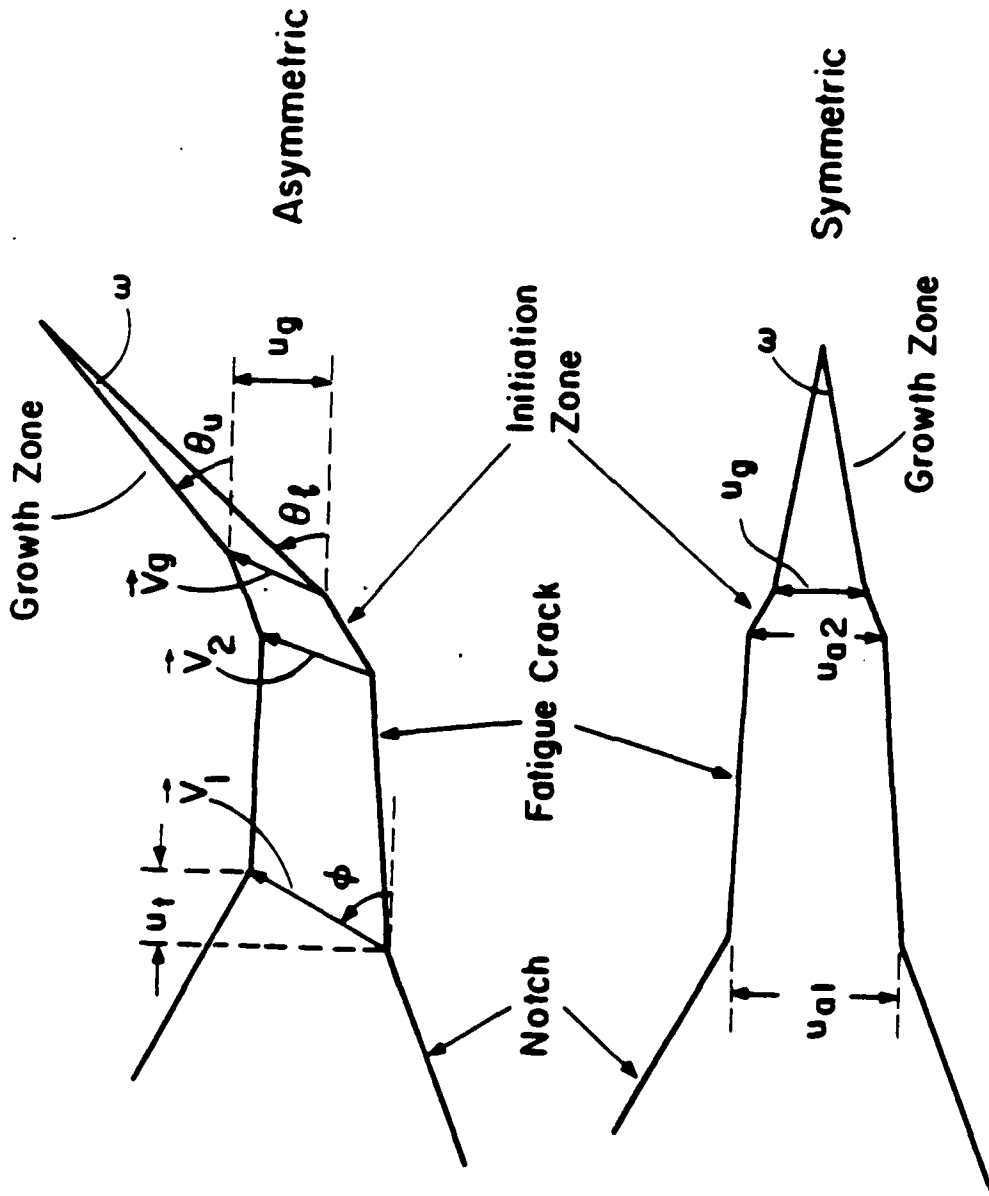


Figure 5. Schematic of the Fracture Surface Profile for the Asymmetric and Symmetric cases.

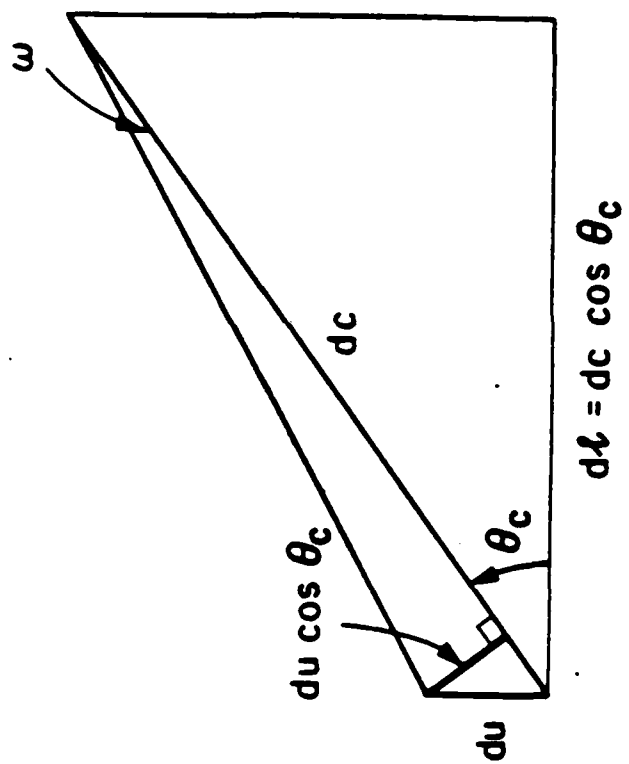


Figure 6. Deriving the relation between the crack opening angle and the crack growth rate.

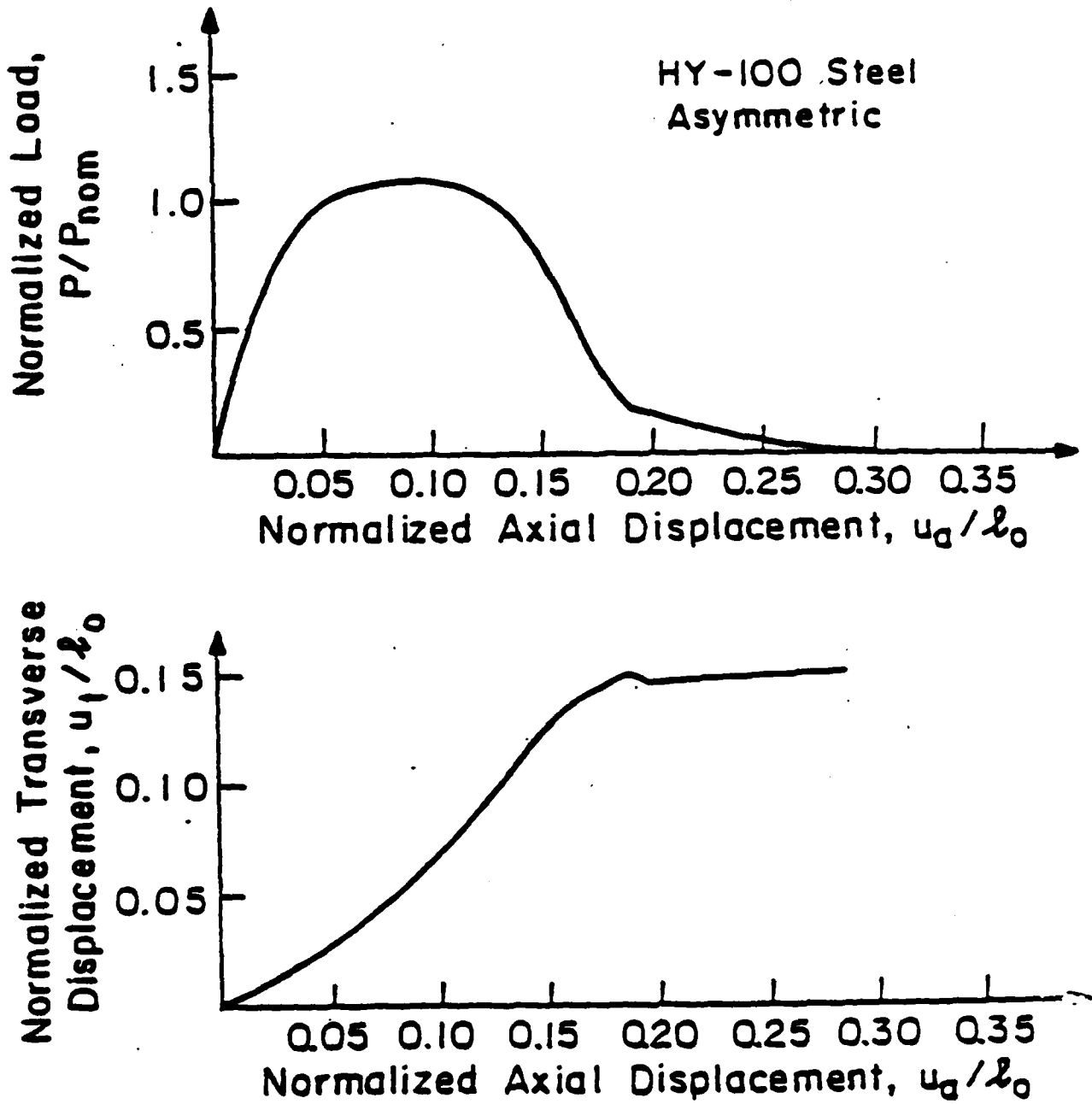


Figure 7a. Test Data for the HY-100 Steel Asymmetric Specimens.

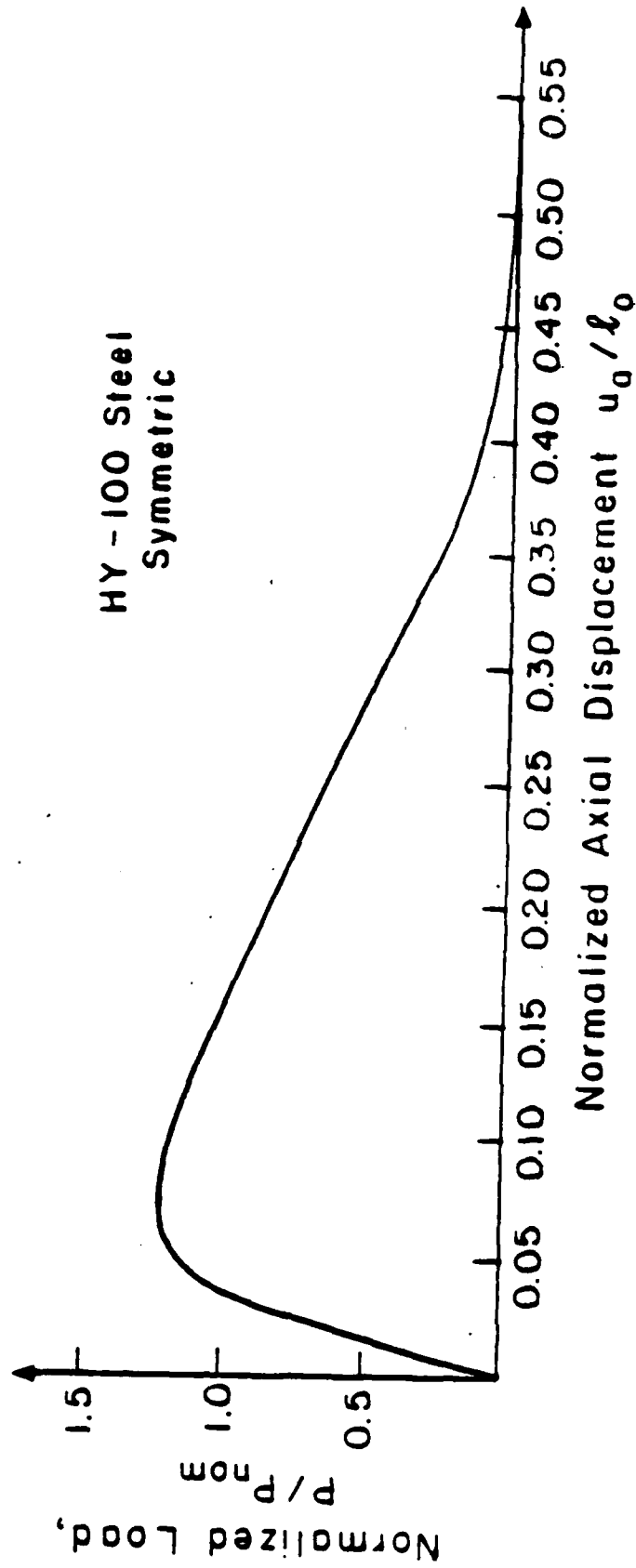


Figure 7b. Test Data for the HY-100 Steel Symmetric Specimens.

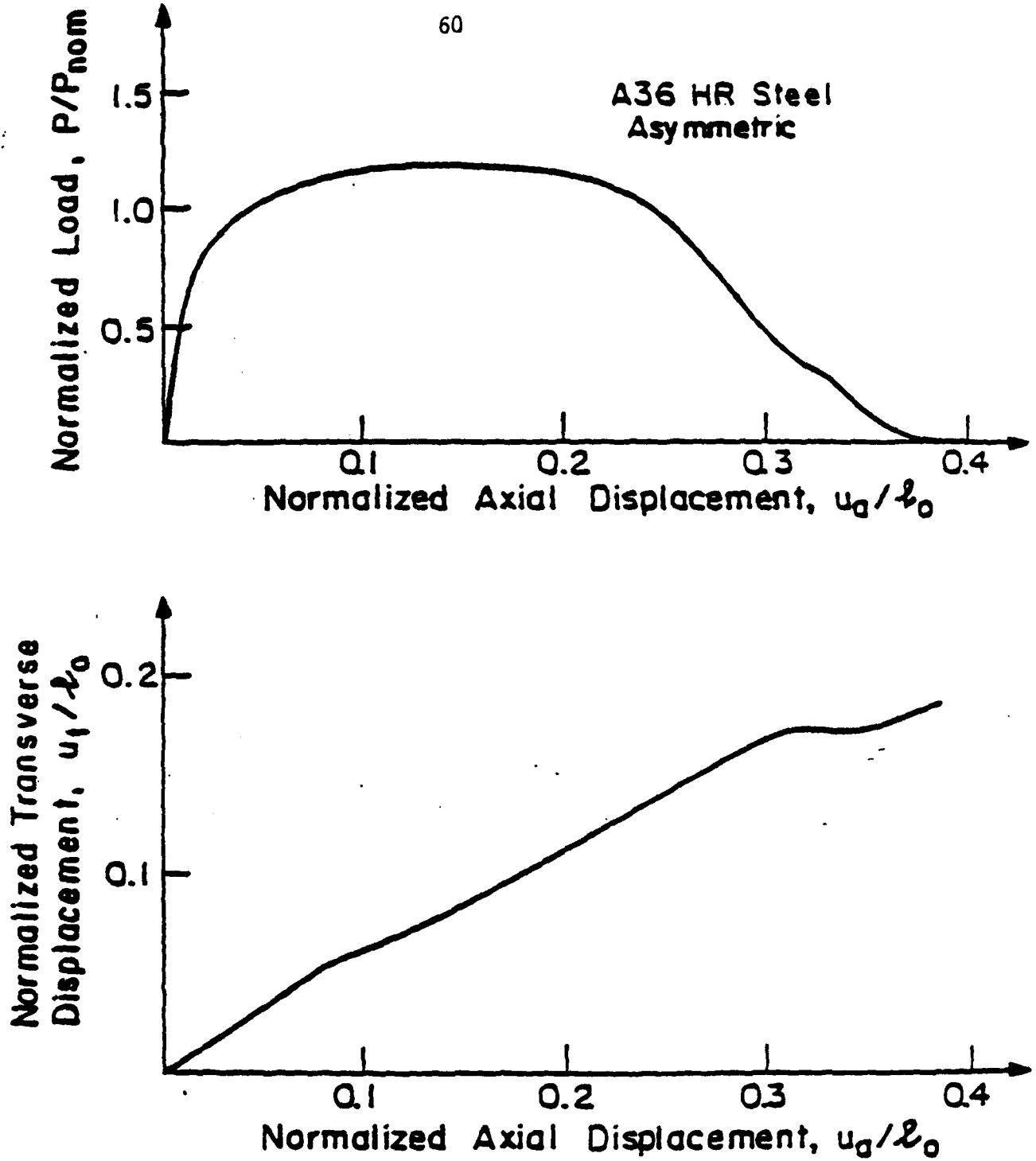


Figure 8a. Test Data for the A36 Hot Rolled Steel Asymmetric Specimens.

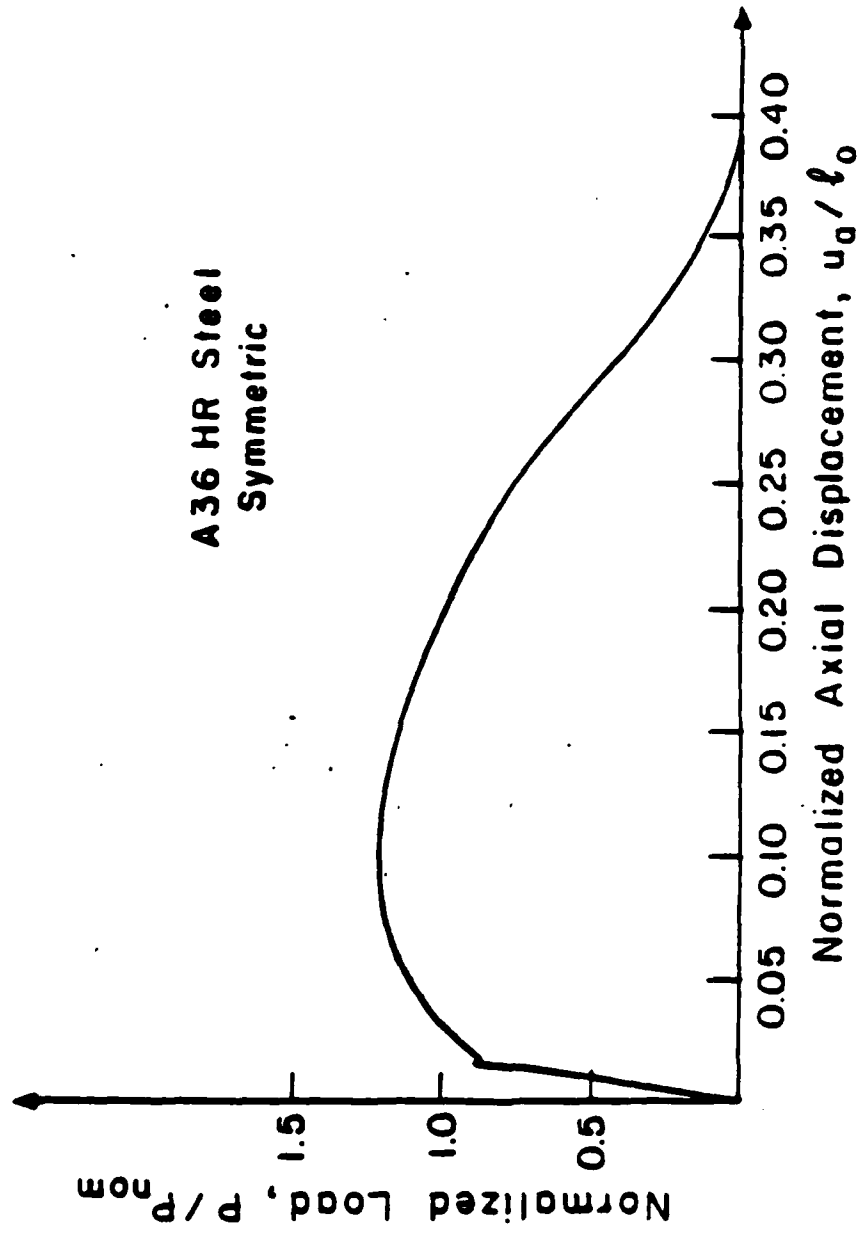


Figure 8b. Test Data for the A36 Hot Rolled Steel Symmetric Specimens.

HY-100 Steel Asymmetric

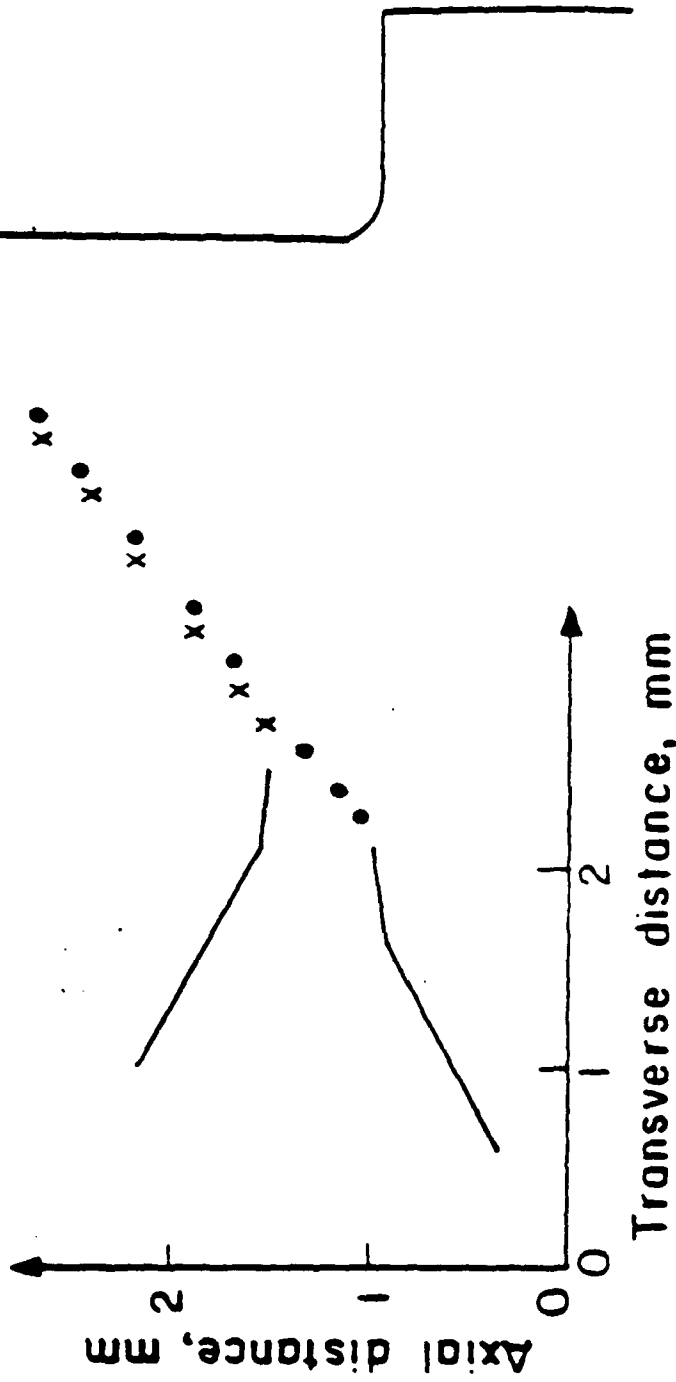


Figure 1a Fracture Surface Profile for the HY-100 Steel Asymmetric Specimens

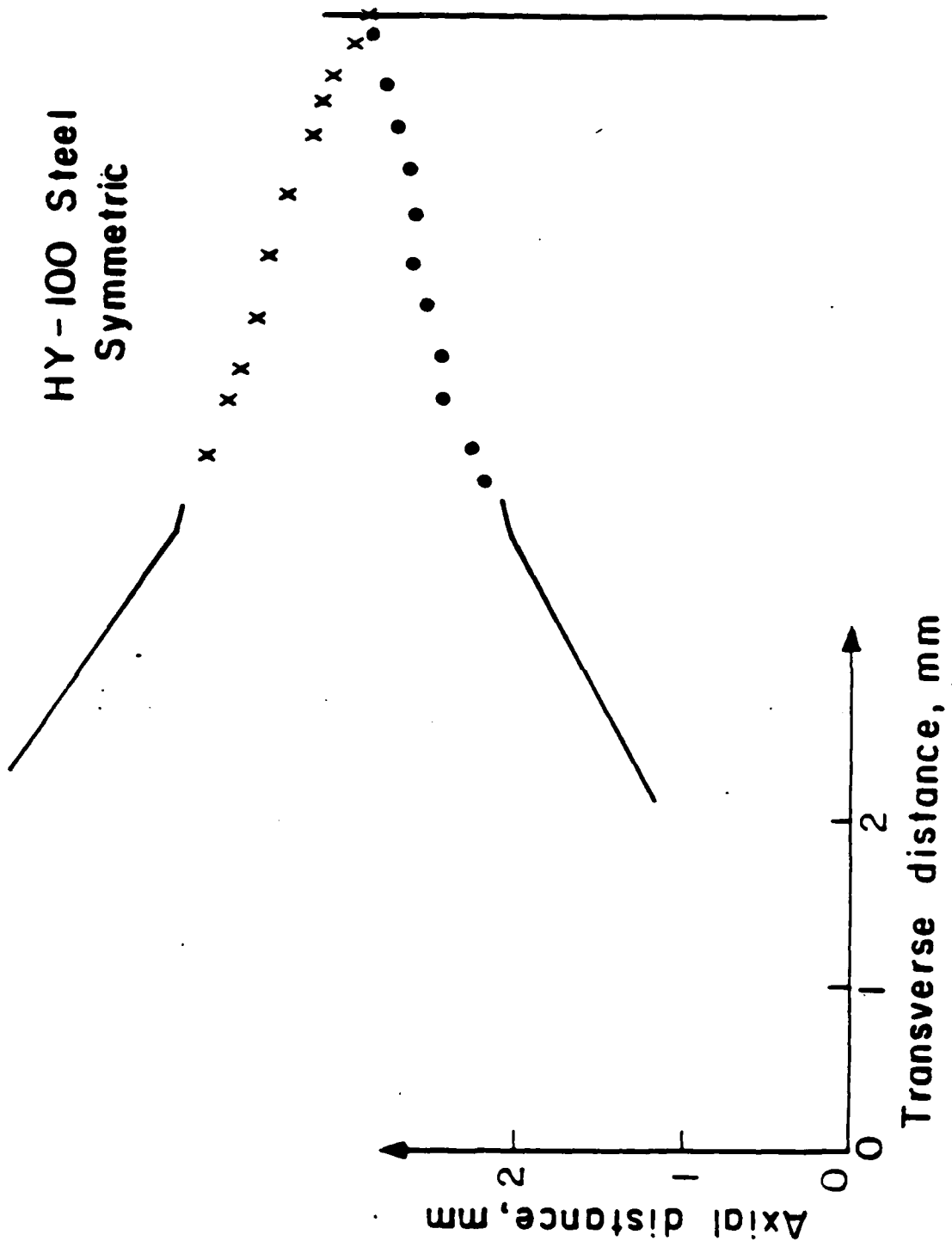


Figure 9b Fracture Surface Profile for the HY-100 Steel Symmetric Specimens.

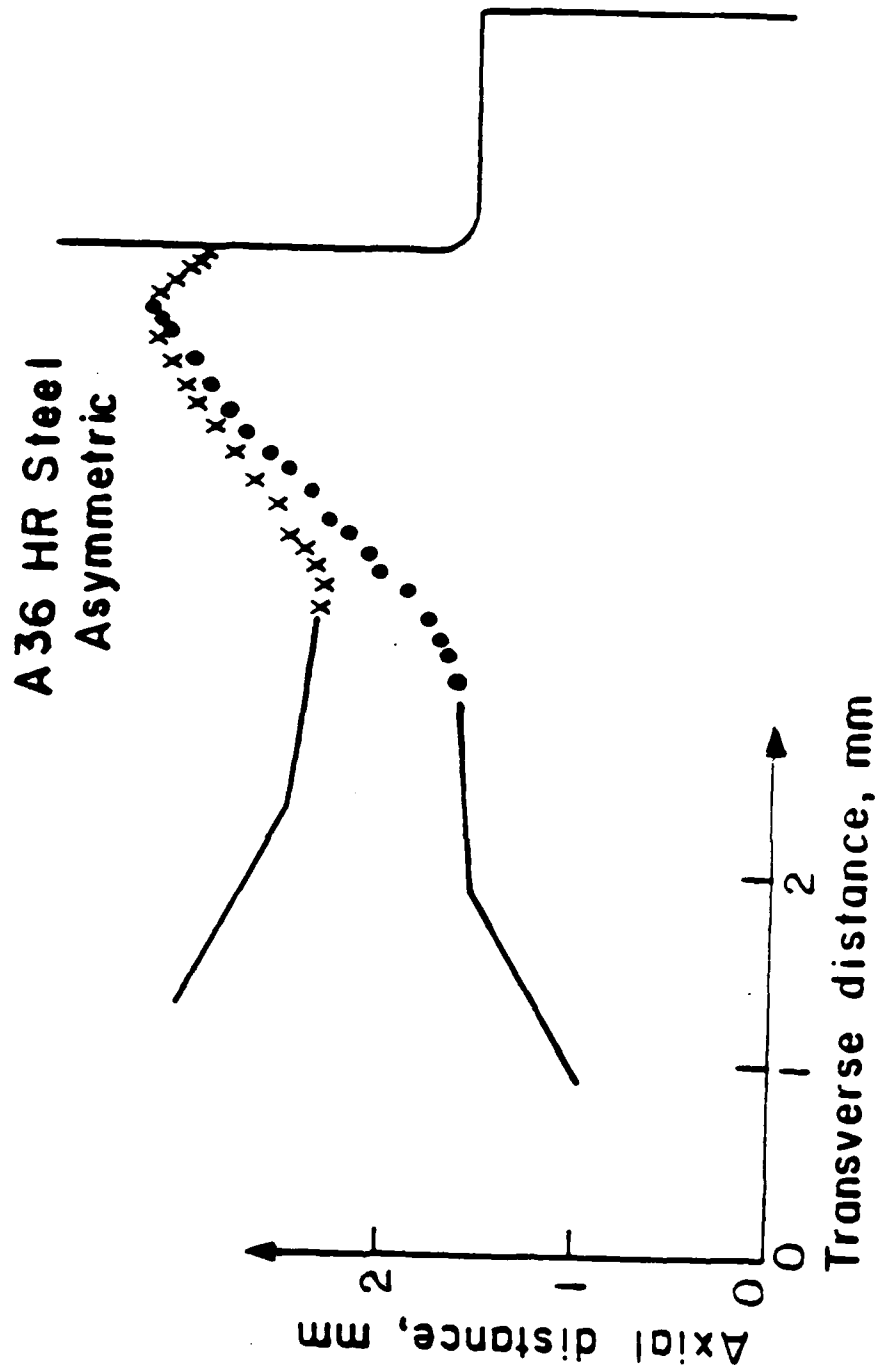


Figure 10a Fracture Surface Profile for the A36 Hot Rolled Steel Asymmetric Specimens

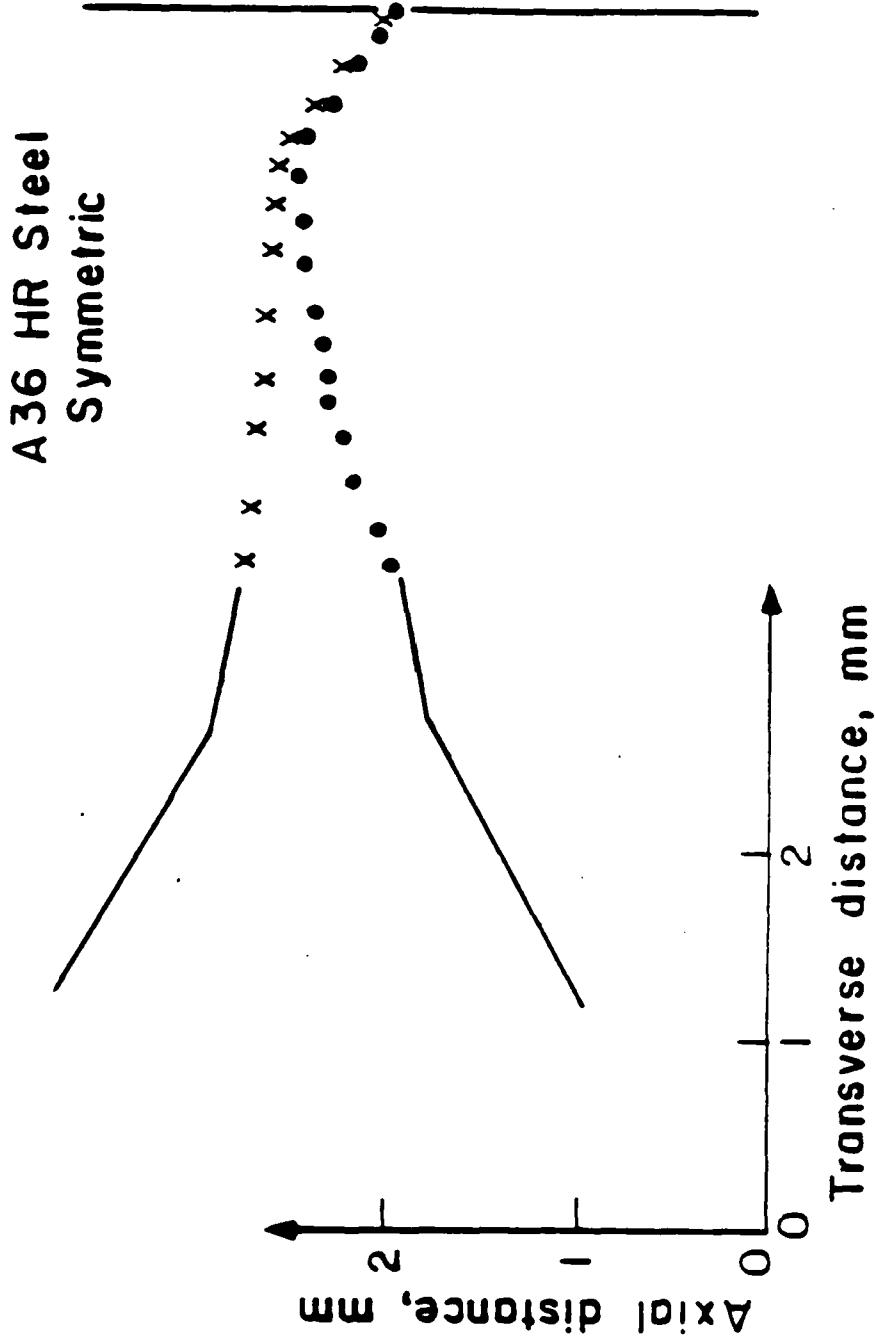


Figure 10b Fracture Surface Profile for the A36 Hot Rolled Steel Symmetric Specimens

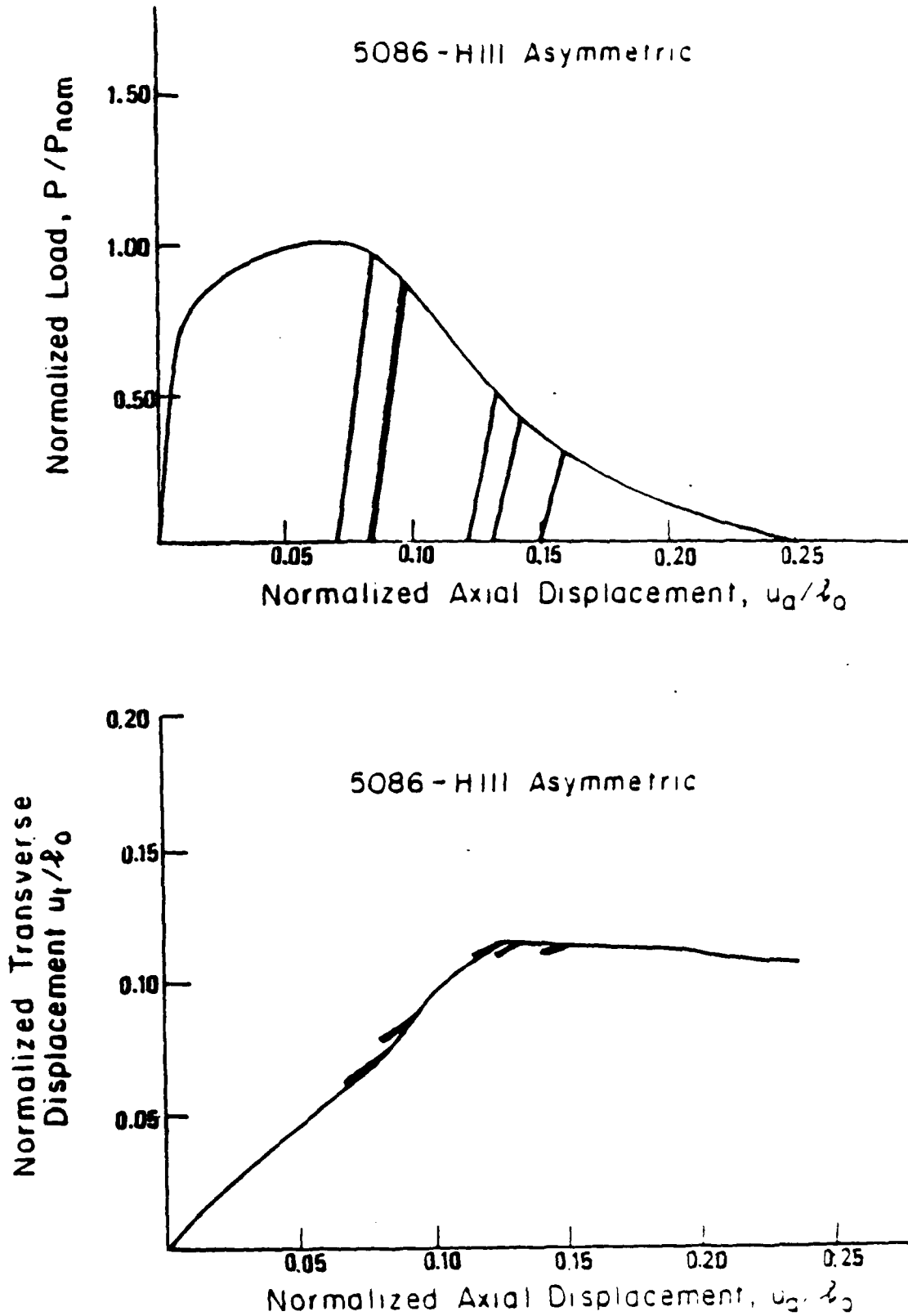


Figure 11a. Test Data for the 38.1 mm dia. 5086-H111 asymmetric specimens showing the unloading-loading points for marking the crack front.

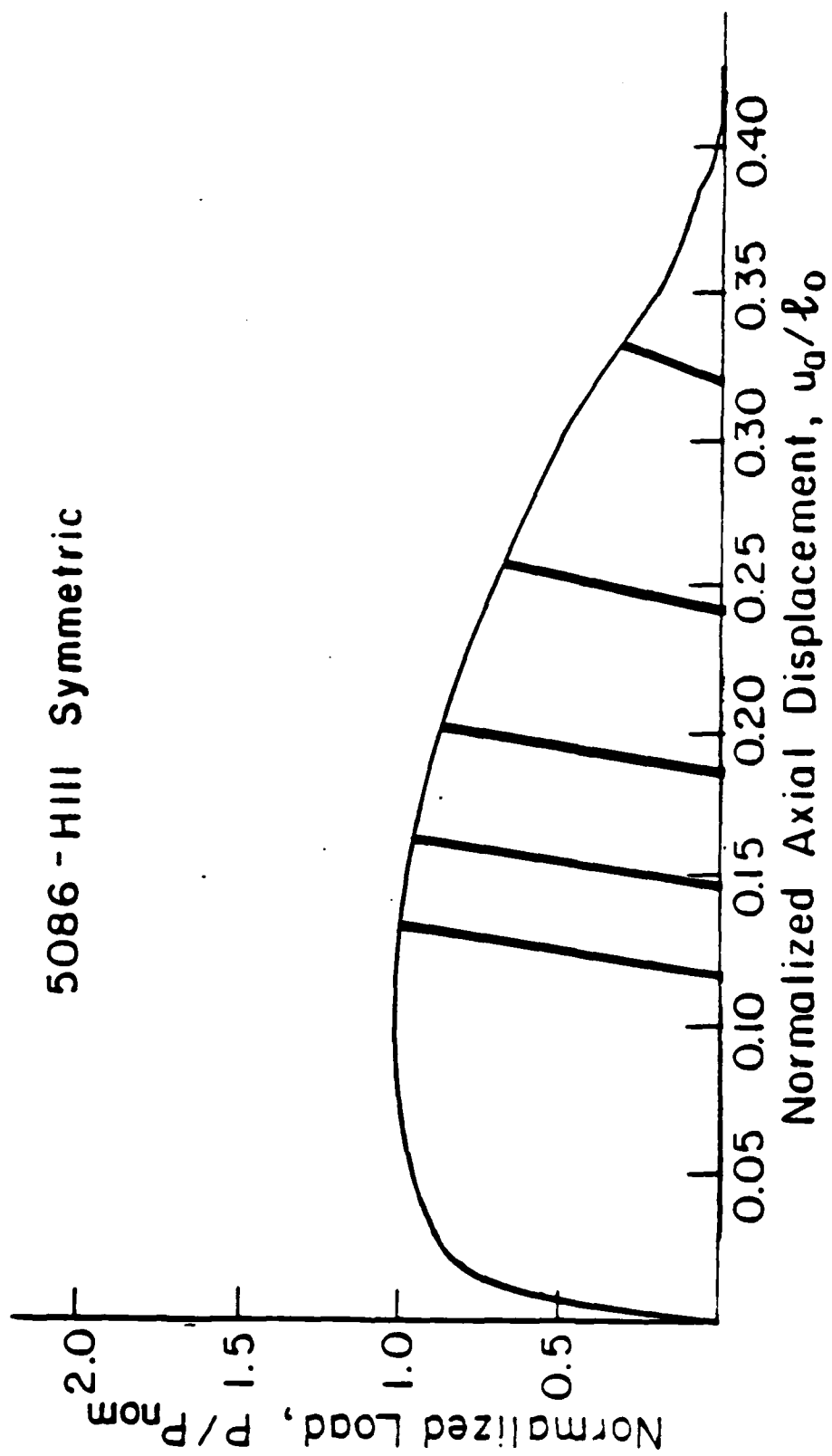


Figure 11b. Test Data for the 38.1 mm dia. 5086-H111 symmetric specimens showing the unloading-loading points for marking the crack front.

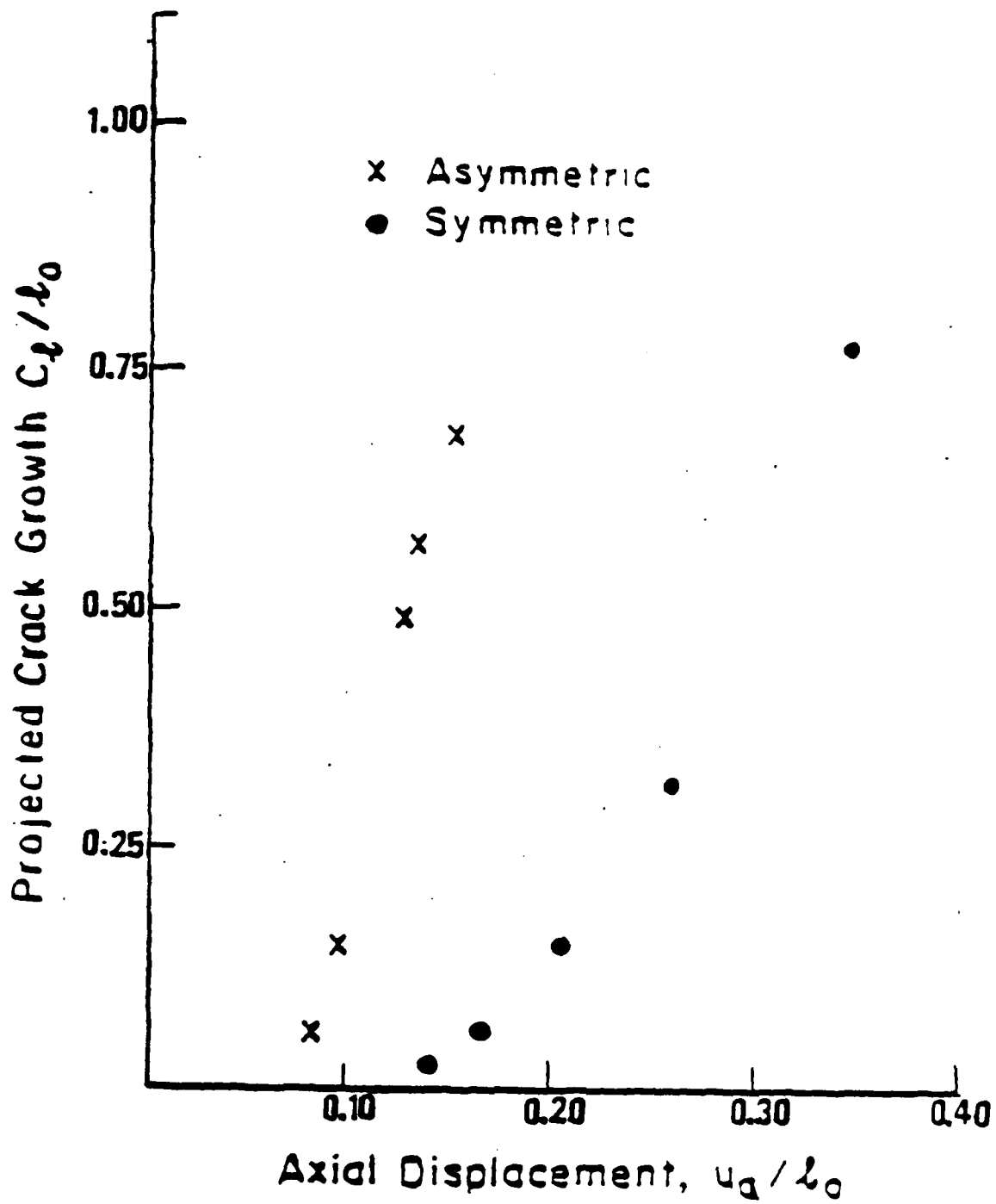


Figure 12. Crack advance-displacement data for the specimens of Figs. 11a, 11b. The fatigue marks provided the crack positions.

APPENDIX

FRACTOGRAPHIC OBSERVATIONS IN ASYMMETRIC AND SYMMETRIC FULLY PLASTIC SPECIMENS.

Observations of ductile fracture suggest that it results from a multi-step process initiated by the cracking of inclusions or the separation of inclusion-metal interfaces, followed by void growth and coalescence. The coalescence has been observed to occur on a plane of high shear stress, giving elongated dimples form, or on a plane normal to the direction of maximum tensile stress, giving equiaxed dimples [1]. Furthermore, fracture surfaces have been studied to identify and classify the characteristic surface markings that are produced by the deformation mechanisms [2].

Tests on symmetric and asymmetric specimens were performed on six alloys for which X-ray spectrography gave the predominant inclusions: 1018 cold finished steel with Si-bearing inclusions, 1018 steel normalized at 1700⁰, A36 hot rolled steel with MnS inclusions, HY80 steel with Al-bearing inclusions, HY100 steel with MnS inclusions and 5086-H111 aluminum with Fe-bearing inclusions. These alloys can be separated into the lower hardening ones (1018 cold finished, HY80 and HY100 steel) and the higher hardening ones (A36 hot rolled, 1018 normalized steel). In this work the microscopic features of the fracture surface for the two geometries are quantitatively compared.

In general, for a given crack tip opening displacement, the amount of crack extension can be separated into two components: a sliding off component and a fracture component. To quantify the ductility, as observed from the fractographs, an "apparent crack ductility", D_{AC} , observed fractographically, can be defined as

the ratio of that part of the projected crack area exposed by pure plastic flow to the total projected area, including that exposed by fracture. For instance, with n parabolic dimple markings per unit area, each having tip radius r , the apparent crack ductility may be found by assuming that the area πr^2 of each parabola opens up before arrival of the crack front, and the balance of the surface is formed by sliding off. Then $D_{AC} = 1 - n\pi r^2$. Due to the difficulty in measuring these quantities, only rough approximations for D_{AC} can be obtained. Table 1 shows these approximate findings (estimated from the lower flank fractographs, surface normal to the beam) for the lower hardening HY100 steel and the higher hardening 1018 normalized steel from the asymmetric and symmetric specimens which are more ductile. These results are another manifestation of the fact that higher hardening alloys are more ductile than the lower hardening ones in the asymmetric configuration but almost equally ductile in the symmetric one.

TABLE 1 - Apparent Crack Ductility D_{AC}

HY-100 steel Asymmetric	0.51
HY-100 steel Symmetric	0.64
1018 normalized steel Asymmetric	0.68
1018 normalized steel Symmetric	0.67

Fig. 1 shows micrographs of the upper and lower flanks for 5086-H111 aluminum with different degrees of void formation and shearing. Fracture is more "shear type" in the lower flank, indicating a larger sliding off component in the crack extension. This suggests a macro-mechanical model for crack growth by combined void growth and sliding off, where the lower flank slides off along the upper slip plane and the upper flank slides off along the lower slip plane by a smaller amount. Thus the lower flank consists of a larger amount of "sheared" material

than the upper.

A qualitative understanding of the differences in ductility from the fractographs can be obtained by comparing in Fig. 2, the micrograph for the less ductile HY100 asymmetric specimen with the corresponding one for the more ductile higher hardening 1018 normalized steel (larger and less elongated voids).

To compare the symmetric and asymmetric cases, consider Fig. 3 which shows micrographs of the low-hardening 1018 cold finished asymmetric and symmetric specimens. This alloy shows a substantial reduction in ductility in the asymmetric configuration. In the asymmetric case the fracture is more the "shear type" with voids elongated in the direction of crack growth; in the symmetric case the fracture is more the "normal type" with equiaxed voids. In the high-hardening A36 hot rolled steel, with small differences in the ductility between the asymmetric and the symmetric cases, the corresponding micrographs (Fig. 4) are not much different: the fracture in the asymmetric case is almost as much the "normal type" as in the symmetric case.

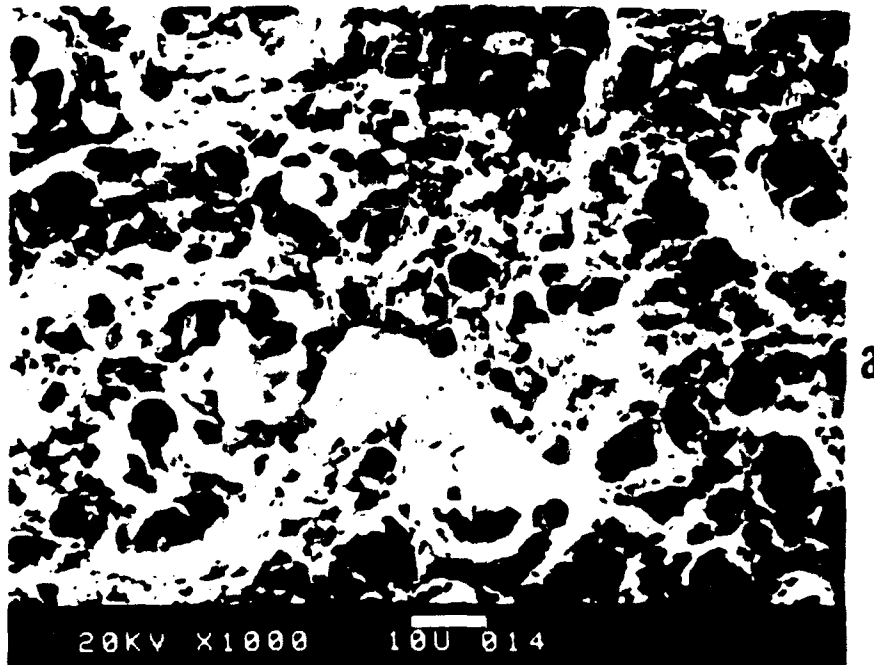
"Zig-zagging" of the fracture surface is a characteristic of some symmetric specimens, where two slip planes are active and the crack grows by alternating shear. Fig. 5 shows this for the 5086-H111 aluminum. The wavy (zig-zag) region followed the fatigue precrack. In the end the fracture turned into a shear lip. Symmetric specimens in the lower hardening alloys often turned into asymmetric ones, following only one slip plane. In some instances, half of the specimen followed the $+45^{\circ}$ slip plane and half the -45° plane.

In conclusion, fractographic observation of deformation during crack extension

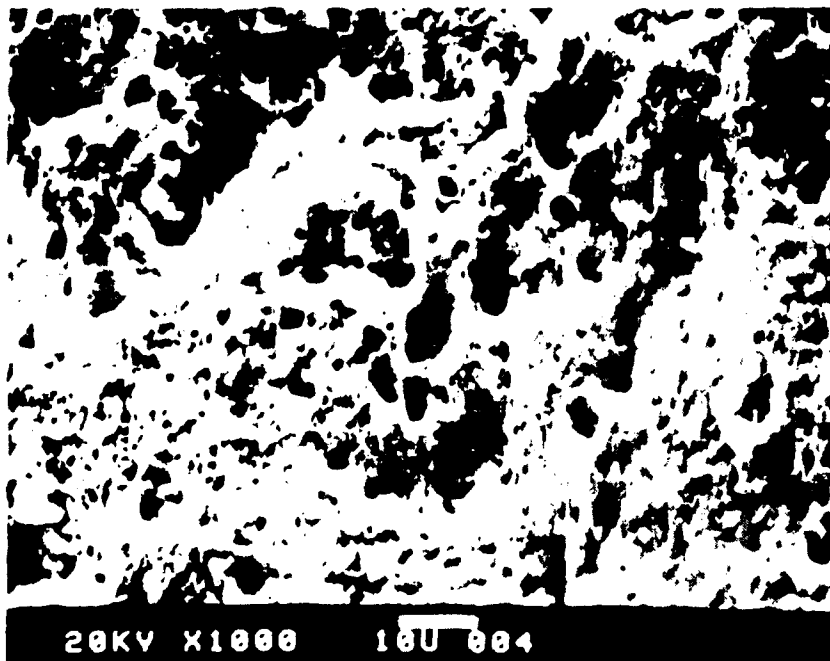
in the asymmetric specimens suggests a mechanism by fracture followed by a different amount of sliding off in the two flanks. The usual symmetric case suggests alternating shear and fracture and in some cases the macroscopic surface is characterized by zig-zagging. Noteworthy features in the asymmetric specimens are the "shear type" fracture, more evident in the lower hardening alloys and a larger amount of sliding off in the lower flank. The symmetric specimens, with the larger ductility, show in turn the "normal type" fracture with more equiaxed voids than the corresponding asymmetric specimens.

REFERENCES

1. Hayden H.W. and Floreen S. "Observations of Localized Deformation During Ductile Fracture", *Acta Met.*, 17, pp. 213-224 (1969).
2. Beachem C.D. and Meyn D.A. "Fracture by Microscopic Plastic Deformation Processes", ASTM STP 436, Am. Soc. Test. Mat., pp. 59-88 (1968).



a



b

Figure 1 Fracture surface of 5086-H111 aluminum asymmetric specimen showing the difference between the two flanks
(a) Upper flank, (b) Lower flank with more shearing

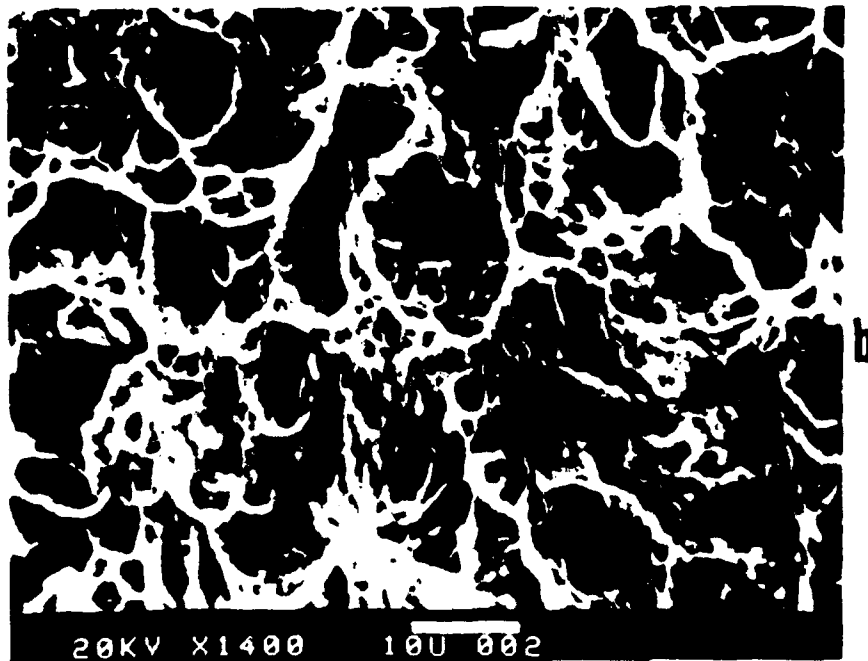
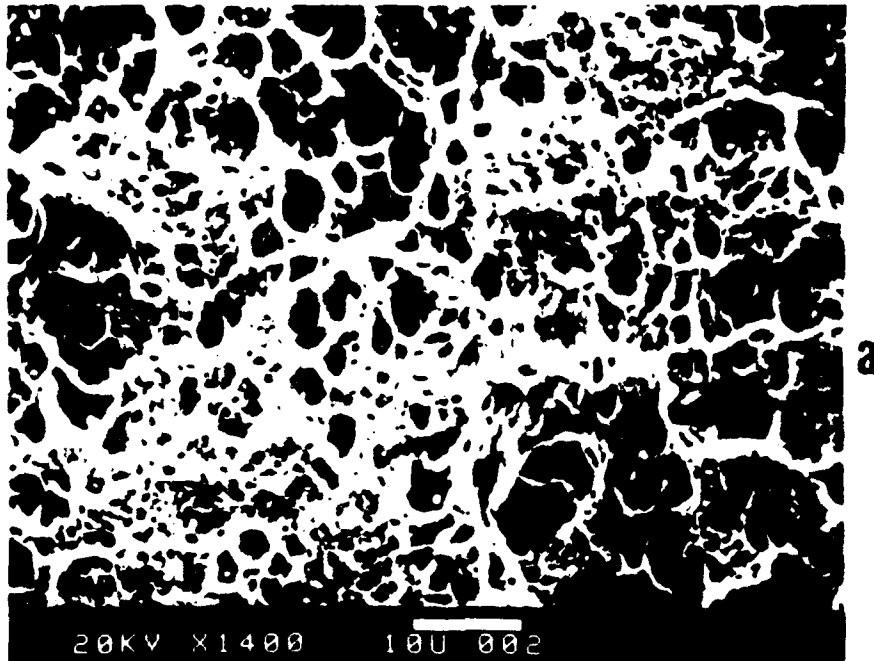


Figure 2. Fracture surface of the upper flank of asymmetric specimens in
(a) HY-100 steel (lower hardening, less ductile)
(b) 1018 normalized steel (higher hardening, more ductile).

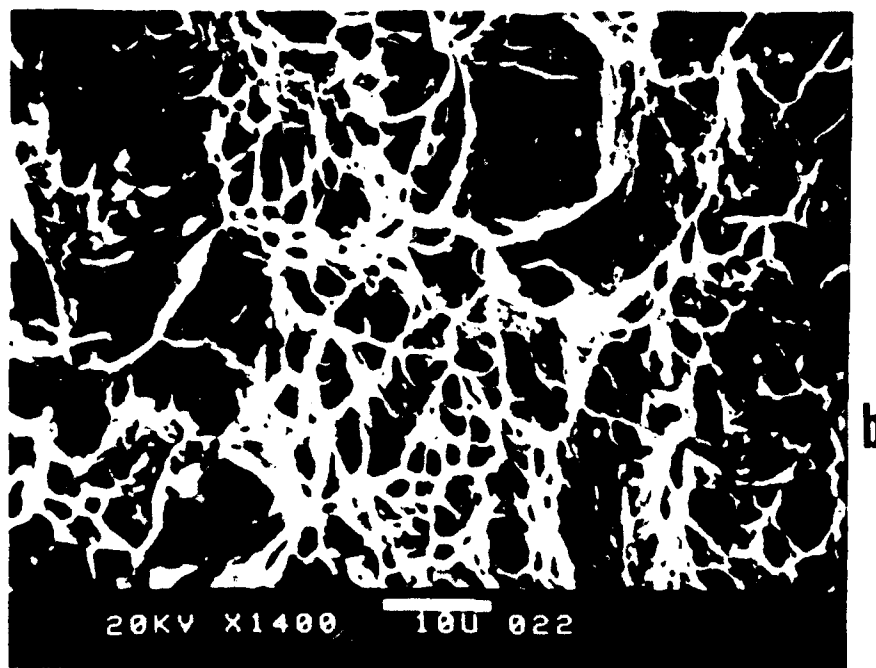
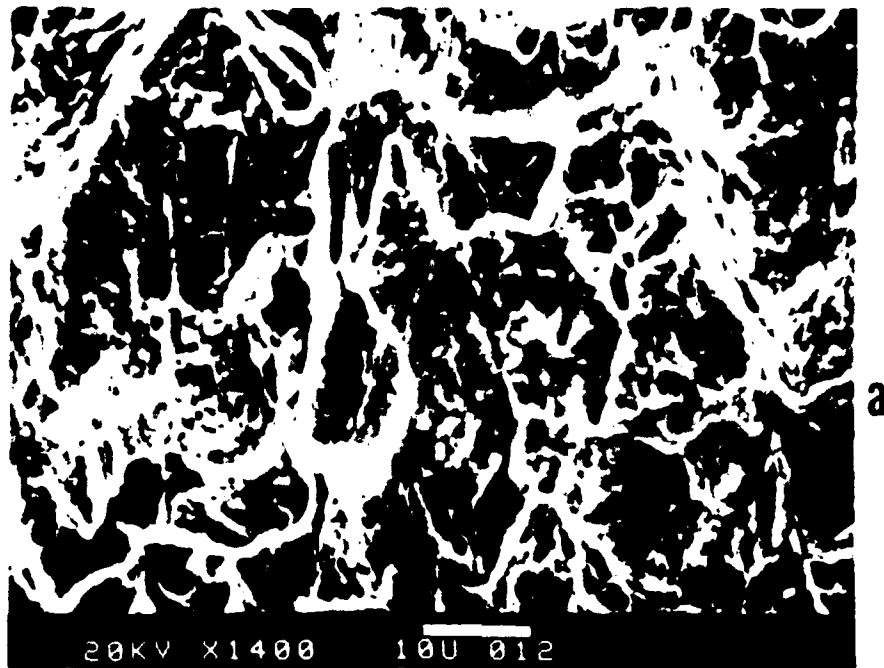


Figure 3 Fracture surface of 1018 cold finished steel (lower hardening alloy). (a) Asymmetric, (b) Symmetric. Distinctly more "shear type" fracture in the asymmetric, less ductile case

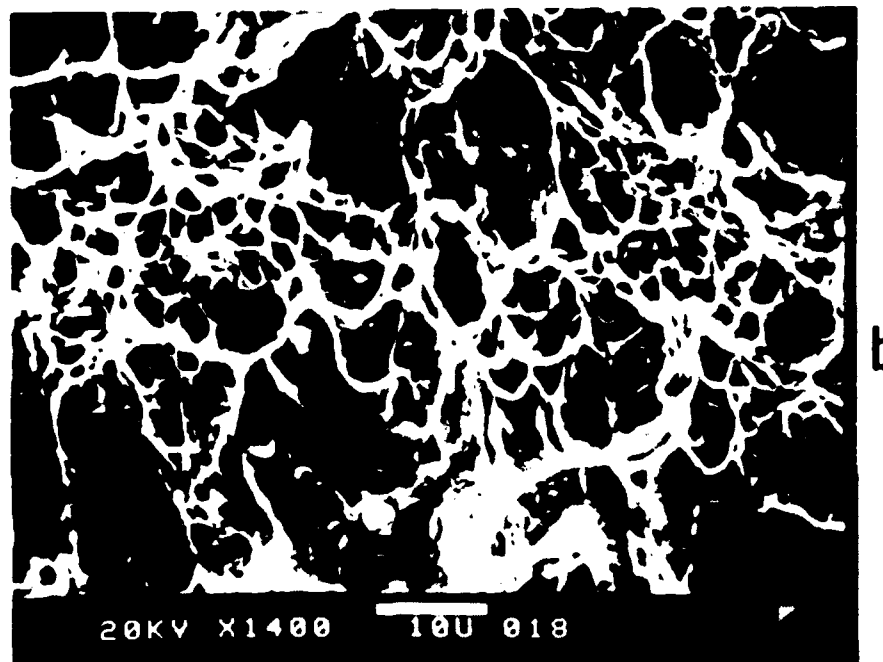
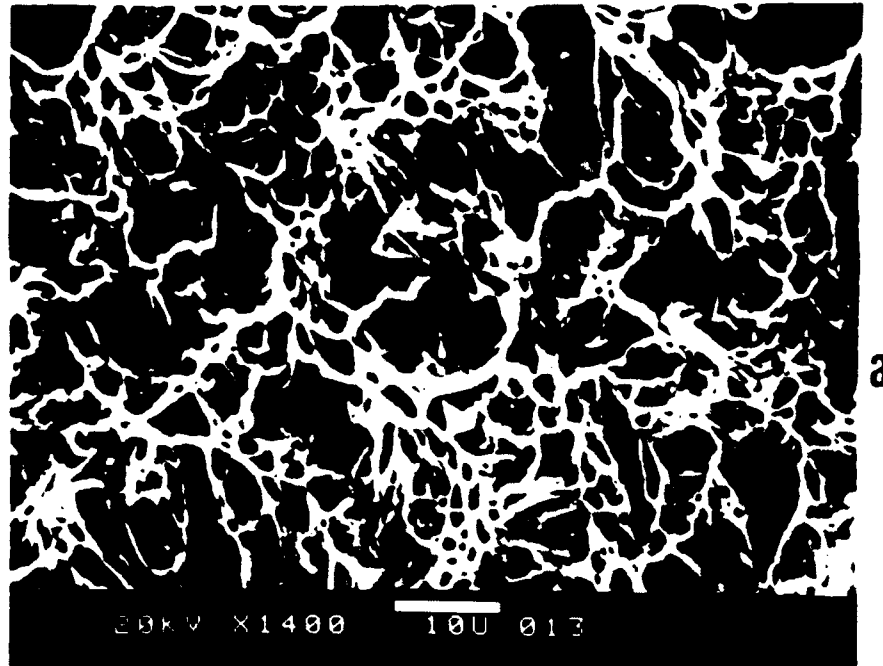


Figure 4 Fracture surface of A36 hot rolled steel (higher hardening alloy). (a) Asymmetric. (b) Symmetric, without appreciable difference Both cases have almost the same ductility

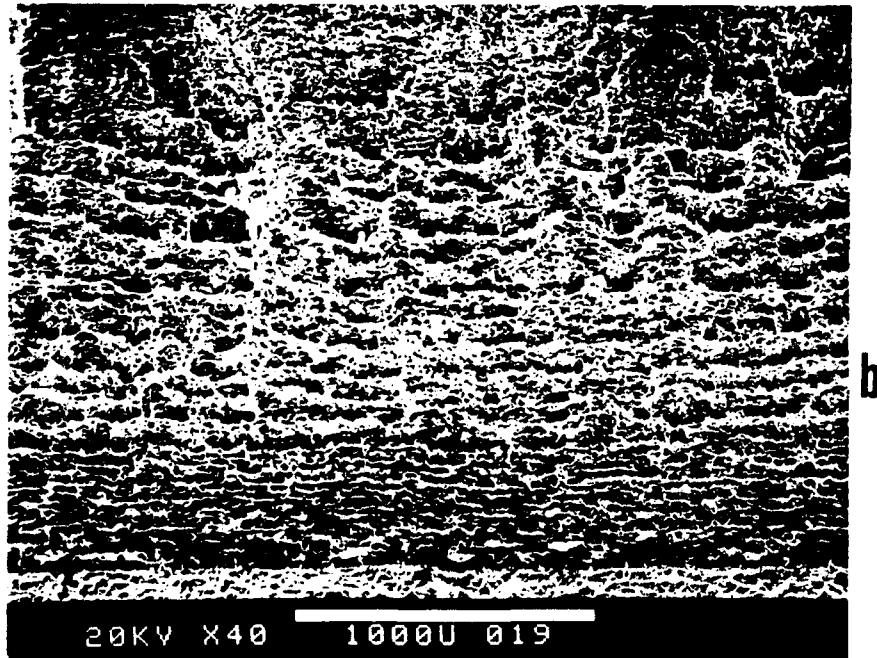
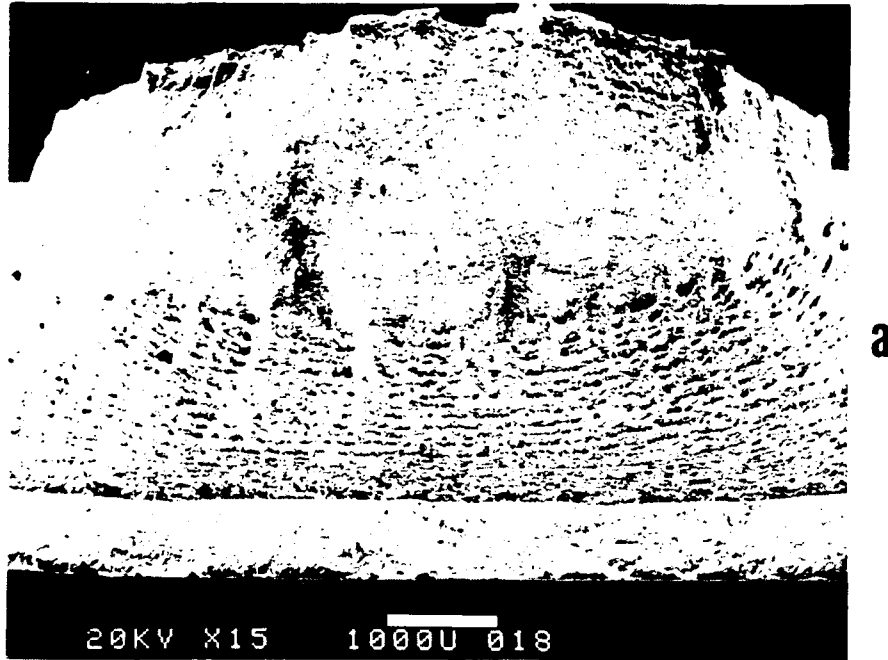


Figure 5 Fracture surface of 5086-H111 aluminum symmetric specimen showing the macroscopic roughness of the specimen After the fatigue crack a "wavy" region [shown better in (b)] and finally a shear lip at the end

APPENDIX

ON FRACTURE CHARACTERIZATION

In this section the concepts that are commonly used in characterizing fracture are discussed.

Growth Resistance. Representing ductile crack propagation has been based on the introduction of $d(\text{COD})/da$ [1,2,3] and the tearing modulus T or dJ/da concept [4]. In general, past work has implied that the results are all characterized by a common triaxiality (or are independent of it) whereas in fact both $d(\text{COD})/da$ and T should depend on triaxiality, since both cleavage and hole growth do. Analogous to the above measures of growth resistance are the previously defined crack ductility $D_g = du_c^p/dl$ or gauge displacement per unit reduction in ligament $D_{\text{ext}} = du/dl$, and the modified tearing modulus T^* to include asymmetric cracks. Table 1 gives some values of $d(\text{COD})/da$ and T for some common tests. They can be compared with the much lower values of about 0.010 for D_g and 0.060 for D_{ext} and of about 15 for T^* found in the asymmetric low hardening tests. Symmetric tests, on the other hand, show values of D_g and D_{ext} close to those in Table 1. It may also be that an asymmetry, introduced in the bending specimens could result in values of $d(\text{COD})/da$ below those of the symmetric bending specimens.

J-controlled growth. In large-scale yielding the HRR singularity is embedded in a plastic zone that extends throughout the remaining ligament. J-control depends on material and crack geometry (McMeeking and Parks [7]). The finite element study of the asymmetric specimens showed that stress and strain fields are consistent with the HRR singularity at initiation. The COA (crack opening angle) concept has also been alternatively used to characterize growth. Shih [1] in his experimental study found that the COA appears to be constant over a larger range of growth than the

tearing modulus. Instead of dJ/da , Shih [1] suggested characterizing growth by COA. A condition in terms of a tearing modulus T_δ based on the COA ($=d\delta/da$):

$$T_\delta = \frac{d\delta}{da} \frac{E}{\sigma_0} \gg 1$$

In other words the COA, $d\delta/da$, must be large compared to the yield strain, σ_0/E . In similar fashion, the tearing modulus T should be much larger than unity. How large T or T_δ must be for a J-controlled or COA controlled growth is yet to be explored. COA's of more than 10^0 - 20^0 , were reported in the COA-controlled tests in [1].

Stability. Stability depends again on triaxiality and geometry. Paris et al. [5] developed instability relations for fully-plastic (nonhardening) conditions including some common test piece configurations. For example, in the double edge cracked strip in tension the imposed constraint leads to a critical value of T for instability six times that in the center cracked strip in tension. In the expression for the 3-point bending case the remaining ligament size, l , comes into the instability criterion, so that if l is small enough in the first place the situation remains stable throughout.

In conclusion, single-test characterization of crack propagation can apply only if crack extension occurs in a certain mode and configuration. Instead of a single parameter representation like $d(COD)/da$, a set of $d(COD)/da$, each referring to a certain mode and triaxiality, could conceivably describe adequately the material resistance in crack propagation. For instance, asymmetric (mixed mode I and II) fully plastic configurations in low hardening alloys have been found less ductile than the corresponding symmetric singly grooved unconstrained tensile specimens. Extended work could involve studying the effect of triaxiality by performing constrained asymmetric tests. For example, tensile testing on doubly-grooved specimens with the asymmetry introduced through varying notch angles and

positions; or wedge-splitting of a doubly grooved specimen; or ductile fracture under asymmetric bending with the asymmetry introduced not only by specimen geometry but also through shear loading.

REFERENCES

1. Shih C.F., deLorenzi H.G., Andrews W.R. "Studies on Crack Initiation and Stable Crack Growth", *Elastic-Plastic Fracture, ASTM STP 668*, pp. 65-120 (1979).
2. Dawes M.G. "Elastic-Plastic Fracture Toughness Based on COD and J-Contour Integral Concepts", *Elastic-Plastic Fracture, ASTM STP 668*, pp. 307-333 (1979).
3. Chipperfield C.G., Knott J.F. and Smith R.F. "Critical Crack Opening Displacement in Low Strength Steels", Third Intern. Congress on Fracture, Munich, April 1973, paper I-233 (1973).
4. Paris P.C., Tada H., Ernst H. and Zahoor A. "Initial Experimental Investigation of Tearing Instability Theory", *Elastic-Plastic Fracture, ASTM STP 668*, pp. 251-265 (1979).
5. Paris P.C., Tada H., Ernst H. and Zahoor A. "The Theory of Instability of the Tearing Mode of Elastic-Plastic Crack Growth" *Elastic-Plastic Fracture, ASTM STP 668*, pp. 5-36 (1979)
6. Green A.P. and Hundy B.B, *J.Mech.Phys.Sol.*, 4, pp. 128-144 (1956).
7. McMeeking R.M. and Parks D.M. "On Criteria for J-Dominance of Crack-Tip Fields in Large-Scale Yielding", *Elastic-Plastic Fracture, ASTM STP 668*, pp. 175-194 (1979).
8. Hutchinson J.W. and Paris P.C. "Stability Analysis of J-Controlled Crack Growth" *Elastic-Plastic Fracture, ASTM STP 668*, pp. 37-64 (1979).

TABLE 1
d(COD)/da and T for some common tests

Material	Test	d(COD)/da	T	Ref.
A533B steel Y.S. = 443 MPa T.S. = 574 MPa	compact tension 4T	0.205		[1]
ASTM A471 rotor steel Y.S. = 931 MN/m ² T.S. = 1022 MN/m ²	3-point bend 8 x 1 x 0.5 in Notched and Fatigue precracked, a/w = 0.502		36.1	[4]
Free-cutting Mild steel	3-point bend fatigue precracked	0.300		[3]
BS 4360 Grade 50 steel Y.S. = 359 MN/m ² T.S. = 526 MN/m ²	3-point single edge notch bend	0.250		[2]
Asymmetric and Symmetric tensile tests.				
1018 CF steel Y.S. = 586 MN/m ² T.S. = 612 MN/m ²	Asymmetric	0.072 (0.046)*		
	Symmetric	0.233 (0.199)		
HY80 steel Y.S. = 587 MN/m ² T.S. = 708 MN/m ²	Asymmetric	0.096 (0.060)		
	Symmetric	0.320 (0.285)		

* values in parentheses are based on gauge extension

CHAPTER FOUR

SHEAR-BAND CHARACTERIZATION OF MIXED
MODE I AND II FULLY PLASTIC CRACK GROWTH

TABLE OF SYMBOLS

f	amount of fracture
s_l	amount of slip along lower slip plane
s_u	amount of slip along upper slip plane
θ_f	fracture plane
θ_{sl}	lower slip plane
θ_{su}	upper slip plane
χ	fracture parameter ($=f/s_u$)
ξ	shearing parameter ($=s_l/s_u$)
l_l	projected lower flank length
l_u	projected upper flank length
l_0	initial ligament
θ_u	upper flank angle from transverse
θ_l	lower flank angle from transverse
ω	crack opening angle
u_y	axial displacement
ϕ	displacement vector angle from transverse
β_u	upper back angle
β_l	lower back angle
γ_u	strain for upper shearing
γ_l	strain for lower shearing

ABSTRACT

Asymmetric fully plastic specimens give higher crack growth rates and thus smaller deformation to fracture than the corresponding symmetric specimens. A macro-mechanical model of crack growth by combined fracture on one plane and sliding off along two others describes, for this idealization of the physical mechanisms, the ductile crack growth for the general mixed mode I, II case. The analysis allows determining the independent physical parameters (shear and cracking

directions, relative amounts of cracking and shearing) in terms of the observable quantities of the macroscopic fracture (flank angles, flank lengths, back angle).

INTRODUCTION

In studying fracture there is a need for understanding and characterizing the deformation and crack growth in the fully plastic range for both the usual symmetric case and for the asymmetric case shown in Fig. 1. The asymmetric configuration may occur near welds due to the constraint of a heat-affected zone or due to some geometric asymmetry, such as near-by shoulders. These cracks exhibit less ductility than symmetric ones, because the crack is advancing into prestrained and damaged material rather than into the new material encountered by a crack advancing between two symmetric shear bands.

The nonhardening rigid plastic flow field of Fig. 1b consists of a single slip line at 45° . Strain hardening, however, causes the deformation field to fan out. It also leads to adding a Mode I component, as suggested by the direction of the far field displacement being more axial than 45° . To account for the presence of the Mode I component and the spreading out of the deformation in the more general asymmetric case we assume two slip planes at arbitrary angles.

Crack growth is a mixture of sliding off and fracture. In the general case it may be idealized by assuming cycles of first sliding off on the upper slip plane, then on the lower, and finally fracture on possibly a third (Fig. 2). The combination of cracking and sliding off gives the two new surfaces of the macro fracture. These define the crack opening angle and the crack direction. In the symmetric case the two slip planes and the fracture are symmetric. These ideas will now be developed

quantitatively, giving a description of the mixed mode ductile crack growth based on an idealization of the underlying physical mechanisms. The single-band pure Mode II asymmetric and the pure Mode I symmetric behavior can be obtained as limiting cases.

ANALYSIS

Consider lower and upper slip planes at angles θ_{sl} and θ_{su} (Fig. 2). The upper crack flank is formed by sliding off along the lower slip plane through a distance s_l at θ_{sl} , combined with fracture over a distance f at an angle θ_f . The lower flank is formed by sliding off along the upper slip plane at θ_{su} and the fracture f at θ_f . A cracking parameter $\chi=f/s_u$ and a shearing parameter $\xi=s_l/s_u$ can be defined. As independent physical variables consider the cracking and shearing parameters χ and ξ , the fracture angle θ_f and the slip angles θ_{sl} , θ_{su} . The limiting case of Mode I, with two symmetric slip lines corresponds to $\theta_f=0$, $\theta_{su}=-\theta_{sl}$, $s_l=s_u$ and the limiting Mode II case of slip on a single plane corresponds to $s_l=0$.

Observable quantities that allow solving for the above physical variables turn out to be the angles between the faces of the crack and the transverse direction θ_u , θ_l , the transverse components of the crack flank lengths after complete separation, normalized with the initial ligament, l_u/l_0 , l_l/l_0 , and the angle that the deformed upper back surface makes to the load axis, β_u (Fig. 3). Other dependent variables of interest are the crack opening angle (COA), the total axial displacement per initial ligament u_y/l_0 , the orientation of the displacement vector ϕ , and the angle that the deformed lower back surface makes to the load axis β_l (Fig. 3). These can be deduced from the analysis and observed from the tests, except for the lower back angle which is suppressed by the shoulder.

The orientations of the crack flanks θ_u and θ_l from the transverse direction can be found from Fig. 1:

$$\theta_l = \tan^{-1} \frac{f \sin \theta_f + s_u \sin \theta_{su}}{f \cos \theta_f + s_u \cos \theta_{su}} = \tan^{-1} \frac{\chi \sin \theta_f + \sin \theta_{su}}{\chi \cos \theta_f + \cos \theta_{su}}, \quad (1)$$

$$\theta_u = \tan^{-1} \frac{f \sin \theta_f + s_l \sin \theta_{sl}}{f \cos \theta_f + s_l \cos \theta_{sl}} = \tan^{-1} \frac{\chi \sin \theta_f + \xi \sin \theta_{sl}}{\chi \cos \theta_f + \xi \cos \theta_{sl}}. \quad (2)$$

The crack opening angle is

$$\text{COA} = \omega = \theta_l - \theta_u, \quad (3)$$

Fig. 4 shows the crack opening angle as a function of χ and ξ with the slip angle difference $\theta_{su} - \theta_{sl}$ as a parameter. An increasing cracking ratio $\chi = f/s_u$ or shearing ratio $\xi = s_l/s_u$ leads to a decreasing COA (notice that the COA is more sensitive to χ than ξ). A larger slip angle difference, $\theta_{su} - \theta_{sl}$, leads to a larger COA. Large slip angle differences represent spreading out of the deformation and can simulate the effect of a high strain hardening exponent which has been found experimentally to result in a bigger crack opening angle.

The original ligament thickness, l_0 , projected onto the transverse direction, is reduced to zero by the cracking f and by the sliding off s_l and s_u (Fig. 2):

$$l_0 = f \cos \theta_f + s_u \cos \theta_{su} + s_l \cos \theta_{sl}. \quad (4)$$

The corresponding axial extension is

$$u_y = s_u \sin \theta_{su} - s_l \sin \theta_{sl}. \quad (5)$$

From (4) and (5) the deformation ratio, defined as the total axial displacement per initial ligament, which is a measure of the ductility, is found to be

$$\frac{u_y}{l_0} = \frac{\sin\theta_{su} - \xi \sin\theta_{sl}}{\chi \cos\theta_f + \cos\theta_{su} + \xi \cos\theta_{sl}} \quad (6)$$

The deformation ratio behaves as the COA, being higher for a lower χ or ξ and smaller for a larger slip angle difference $\theta_{su} - \theta_{sl}$. Fig. 5 shows an example of variation of u_y/l_0 .

An expression for the flank lengths is desirable because the final projected flank lengths per initial ligament can be measured. The projected upper and lower flank lengths, l_u and l_l are given by

$$l_u = f \cos\theta_f + s_l \cos\theta_{sl} \quad (7)$$

$$l_l = f \cos\theta_f + s_u \cos\theta_{su} \quad (8)$$

Using (4) and substituting the expressions for the cracking and shearing ratios χ and ξ gives

$$\frac{l_u}{l_0} = \frac{\chi \cos\theta_f + \xi \cos\theta_{sl}}{\chi \cos\theta_f + \xi \cos\theta_{sl} + \cos\theta_{su}} \quad (9)$$

$$\frac{l_l}{l_0} = \frac{\chi \cos\theta_f + \cos\theta_{su}}{\chi \cos\theta_f + \xi \cos\theta_{sl} + \cos\theta_{su}} \quad (10)$$

The lower flank ratio l_l/l_0 decreases with an increasing shearing parameter ξ in contrast to the upper flank ratio l_u/l_0 which increases (Fig. 6). The amount by which the upper back surface is drawn in, projected along the transverse, is (Fig. 2)

$$t_u = s_u \cos\theta_{su} \quad (11)$$

A "thinning" ratio for the upper surface, t_u/l_0 , can be defined in terms of the independent parameters by noting that

$$t_u/l_0 = 1 - l_u/l_0. \quad (12)$$

For the lower surface similarly,

$$t_l/l_0 = 1 - l_l/l_0. \quad (13)$$

Of interest is also the orientation of the displacement vector from the transverse, ϕ . In terms of the flank lengths and angles, it can be found from

$$\phi = \tan^{-1} \frac{(l_l/l_0) \tan \theta_l - (l_u/l_0) \tan \theta_u}{(l_l/l_0) - (l_u/l_0)}. \quad (14)$$

The back angle, defined as the angle that the deformed back surface makes to the load axis, can be observed macroscopically. For the upper slip line from Fig. 2

$$\beta_u = \tan^{-1} \frac{ds_u \cos \theta_{su}}{[df \sin(\theta_{su} - \theta_f) + ds_l \sin(\theta_{su} - \theta_{sl})] / \cos \theta_{su} + ds_u \sin \theta_{su}}. \quad (15)$$

Substituting the expressions for the cracking and shearing ratios we can write

$$\beta_u = \tan^{-1} \frac{\cos \theta_{su}}{\chi(\cos \theta_f \tan \theta_{su} - \sin \theta_f) + \xi(\cos \theta_{sl} \tan \theta_{su} - \sin \theta_{sl}) + \sin \theta_{su}}. \quad (16)$$

Similarly for the lower surface

$$\beta_l = \tan^{-1} \frac{ds_l \cos \theta_{sl}}{[df \sin(\theta_{sl} \theta_f) + ds_u \sin(\theta_{sl} \theta_{su})] / \cos \theta_{sl} + ds_l \sin \theta_{sl}}, \quad (17)$$

or

$$\beta_l = \tan^{-1} \frac{\xi \cos \theta_{sl}}{\chi(\cos \theta_f \tan \theta_{sl} - \sin \theta_f) + (\cos \theta_{su} \tan \theta_{sl} - \sin \theta_{su}) + \xi \sin \theta_{sl}}. \quad (18)$$

There are five independent macroscopically observable parameters: the flank angles θ_u , θ_l , the projected flank lengths per initial ligament, l_u/l_0 , l_l/l_0 , and the back angle β_u . Equations (1) for θ_u , (2) for θ_l , (9) for l_u/l_0 , (10) for l_l/l_0 , and (16) for β_u give the corresponding physical variables χ , ξ , θ_f , θ_{sl} , θ_{su} , as described in the Appendix.

Finally, an expression for the shear strain can also be found. It can be expressed in terms of the slip and the normal separation between corresponding slip planes. For the upper shear band, s_u ,

$$\begin{aligned}\gamma_u &= s_u / [f \sin(\theta_{su}-\theta_f) + s_l \sin(\theta_{su}-\theta_{sl})] = \\ &= 1 / [\chi \sin(\theta_{su}-\theta_f) + \xi \sin(\theta_{su}-\theta_{sl})].\end{aligned}\quad (19)$$

Similarly, for the lower shearing, s_l ,

$$\begin{aligned}\gamma_l &= s_l / [f \sin(\theta_{sl}-\theta_f) + s_u \sin(\theta_{sl}-\theta_{su})] = \\ &= \xi / [\chi \sin(\theta_{sl}-\theta_f) + \sin(\theta_{sl}-\theta_{su})].\end{aligned}\quad (20)$$

APPLICATION TO TESTS

Tests were performed on 12.7 mm dia. round bars of six alloys: 1018 cold finished, 1018 normalized, A36 hot rolled, HY-80 and HY-100 steel and 5086-H111 aluminum in both the asymmetric and symmetric configurations. The alloys tested can be grouped into the lower hardening ones (1018 cold finished, HY-80 and HY-100) and the higher hardening ones (A36 hot rolled, 1018 normalized). The lower hardening alloys exhibited a significantly lower ductility in the asymmetric configuration than the symmetric; the higher hardening alloys showed only a small reduction. The profiles of the fracture surface and the deformed back surface were plotted with a travelling stage microscope to obtain the flank lengths, the flank angles, the back angle, the displacement to separation and the orientation of the displacement vector.

To apply the above model to the tests, the projected crack length ratios l_u/l_0 , l_l/l_0 for the upper and lower flanks and the flank angles θ_u , θ_l were measured from

the profiles of the fracture surface. In addition the back angle for the upper surface β_u was measured from the microscope plots of the back surface. The projected length ratios depend on the strain hardening exponent, being smaller for a higher strain hardening. These quantities were used in equations (1), (2), (9), (10), (16) to yield the cracking parameter $\chi=f/s_u$, the shearing parameter $\xi=s_l/s_u$, the slip angles θ_{sl} and θ_{su} and the fracture angle θ_f . The axial displacement u_y/l_0 and the orientation of the displacement vector ϕ can also be obtained and compared with the test data. Results are shown in the tables at the end of this chapter. For the asymmetric specimens the shearing ratio ξ is found to be about 0.5 indicating shearing in lower flank about twice that in upper flank. SEM fractographs have confirmed that the lower flank shows indeed more "shear type" fracture than the upper one (chapter three). The slip angle difference $\theta_{sl}-\theta_{su}$ is a measure of the spreading out of deformation and is found to be 4^0-6^0 in the high hardening alloys as opposed to 1^0-2^0 in the low hardening ones. The cracking ratio χ is a measure of the relative amount of fracture and sliding off and allows defining an comparing with the 'apparent crack ductility', D_{AC} , as the sliding off to total area. Thus,

$$\text{In upper flank } D_{AC,u} = s_l/(f+s_l) = 1/(\chi/\xi+1)$$

$$\text{In lower flank } D_{AC,l} = s_u/(f+s_u) = 1/(\chi+1)$$

A smaller cracking ratio means higher ductility. In the low hardening alloys the cracking ratio χ is smaller in the symmetric case, whereas in the higher hardening alloys it is about the same in both the symmetric and asymmetric configurations. The cracking ratio χ in the higher hardening asymmetric specimens is also smaller than that of the low hardening asymmetric ones.

The Mode I symmetric case corresponds to the limit of $\theta_{sl}=-\theta_{su}$, $\theta_f=0$, and

$\xi = s_l/s_u = 1$. Results are also shown in the tables at the end of the chapter. The projected flank ratio $l_u/l_0 = l_l/l_0$ and the flank orientation $\theta_l = -\theta_u$ were measured to give the cracking ratio χ and the slip angle θ_s . As dependent variables, the displacement to separation u_y/l_0 , and the back angle $\beta_u = -\beta_l$ can be found. The displacement is more than twice that of the asymmetric case in the lower hardening HY-100 steel. Fig. 7 shows the variation of the deformation ratio u_y/l_0 and the crack opening angle ω vs. the cracking parameter χ with $\theta_s = \theta_{su} = -\theta_{sl}$ as a parameter.

CONCLUSIONS

In asymmetrical, singly grooved, fully plastic tensile specimens the crack progresses into pre-strained material. This results in less ductility than in symmetrical specimens where the crack grows into new material between two shear bands. A macro-mechanical model for crack advance by sliding off along two slip planes and fracture in the asymmetric specimens gives the independent parameters (shear and cracking directions, relative amounts of cracking and shearing) in terms of the observable quantities of the macroscopic fracture (flank angles, flank lengths, back angle). This two slip plane model accounts for the presence of a Mode I component (far field displacement more axial than 45°) that was experimentally confirmed in the asymmetric case. Higher hardening alloys are found to exhibit more thinning of the ligament (hence smaller projected length ratios), a larger slip angle difference, indicating more fanning out of the deformation and a bigger sliding off component. The analysis, based on an idealization of underlying physical mechanisms, describes the deformation that leads to a larger crack opening angle and displacement to separation in the higher hardening asymmetric specimens relative to the lower hardening ones as well as the symmetric specimens relative to

the asymmetric ones.

REFERENCES

1. Shih, C.F. "Small scale Yielding Analysis of Mixed Mode Plane-Strain Crack Problems", *Fracture Analysis*, ASTM STP 560, Am. Soc. Test. Mat., Philadelphia, pp. 187-210 (1974).
2. McClintock F.A. and Slocum A. H. "Predicting Fully Plastic Mode II Crack Growth from an Asymmetric Defect", *Int.J.Fract.Mech.*, 27, 49-62 (1985).
3. McClintock F.A. "Plasticity Aspects of Fracture", *Fracture*, vol. 3, edited by I. Liebowitz, Academic Press, New York, pp.47-225 (1971).
4. Slepyan L.I. "Growing Crack During Plane Deformation of an Elastic-Plastic Body", *Mekhanika Tverdogo Tela*, Vol. 9, no. 1, pp. 57-67 (1974).

APPENDIX

The problem is to determine χ , ξ , θ_f , θ_{sl} , θ_{su} from the observable quantities θ_p , θ_u , l_f/l_0 , l_u/l_0 , β_u . The relevant equations are summarized:

$$\theta_f = \tan^{-1} \frac{\chi \sin \theta_f + \sin \theta_{su}}{\chi \cos \theta_f + \cos \theta_{su}}, \quad (21)$$

$$\theta_u = \tan^{-1} \frac{\chi \sin \theta_f + \xi \sin \theta_{sl}}{\chi \cos \theta_f + \xi \cos \theta_{sl}}, \quad (22)$$

$$\frac{l_f}{l_0} = \frac{\chi \cos \theta_f + \cos \theta_{su}}{\chi \cos \theta_f + \xi \cos \theta_{sl}}, \quad (23)$$

$$\frac{l_u}{l_0} = \frac{\chi \cos \theta_f + \xi \cos \theta_{sl} + \cos \theta_{su}}{\chi \cos \theta_f + \xi \cos \theta_{sl}}, \quad (24)$$

$$\beta_u = \tan^{-1} \frac{\cos \theta_{su}}{\chi(\cos \theta_f \tan \theta_{su} - \sin \theta_f) + \xi(\cos \theta_{sl} \tan \theta_{su} - \sin \theta_{sl}) + \sin \theta_{su}}. \quad (25)$$

For convenience define the upper thinning ratio from (24)

$$t_u/l_0 = 1 - l_u/l_0 = \frac{\cos \theta_{su}}{\chi \cos \theta_f + \xi \cos \theta_{sl} + \cos \theta_{su}}. \quad (26)$$

Dividing Eqs (21)-(25) by $\cos \theta_{su}$ leaves them in terms of four parameters, (A, B, C, D defined in the following) plus $\tan \theta_{su}$ that can be solved from the observed variables.

The first is found by dividing (23) by (26):

$$A \equiv \frac{\chi \cos \theta_f}{\cos \theta_{su}} = l_f/t_u - 1. \quad (27)$$

Dividing (23) by (24) and introducing A from (27) gives

$$B \equiv \frac{\xi \cos \theta_{sl}}{\cos \theta_{su}} = (l_u/l_f)(A+1) - A. \quad (28)$$

Introducing (27) into (21) and rearranging,

$$C \equiv \frac{\chi \sin \theta_f}{\cos \theta_{su}} = (\tan \theta_f)(A+1) - \tan \theta_{su}. \quad (29)$$

Now introduce (27), (28), and (29) into (22)

$$D \equiv \frac{\xi \sin \theta_{sl}}{\cos \theta_{su}} = (\tan \theta_u)(A+B) - C . \quad (30)$$

From (25) and the above definitions of A,B,C,D,

$$\tan \beta_u = 1 / [(A+B+1) \tan \theta_{su} - (C+D)] . \quad (31)$$

From (30) C+D of (31) is given in terms of observed variables. Solve for θ_{su}

$$\tan \theta_{su} = \frac{1 + (A+B) \tan \beta_u \tan \theta_u}{(A+B+1) \tan \beta_u} . \quad (32)$$

Having found θ_{su} , find C from (29) and D from (30). Now find θ_f from (27) and (29)

$$\tan \theta_f = C/A , \quad (33)$$

and θ_{sl} from (28) and (30):

$$\tan \theta_{sl} = D/B . \quad (34)$$

Then χ is determined from (27) by using the already determined values of θ_{su} in (32) and of θ_f in (33)

$$\chi = A \cos \theta_{su} / \cos \theta_f , \quad (35)$$

and similarly ξ is found from (28) by using the values of θ_{su} from (32) and θ_{sl} from (34)

$$\xi = B \cos \theta_{su} / \cos \theta_{sl} . \quad (36)$$

TABLE 1
Deformation of singly-grooved
asymmetrical specimens

Alloy:	HY-100 steel (low hardening, $n=0.10$)		1018 normalized (high hardening, $n=0.24$)	
<u>Observations</u>				
Projected upper flank ratio, l_u/l_0	0.820		0.750	
Projected lower flank ratio, l_l/l_0	0.900		0.870	
Upper flank angle, θ_u	39^0		36^0	
Lower flank angle, θ_l	41^0		42^0	
Upper back angle, β_u	14^0		13^0	
<u>Corresponding slip and fracture parameters</u>				
Slip angle θ_{sl}	53^0		52^0	
Slip angle θ_{su}	54^0		58^0	
Cracking angle θ_f	37^0		31^0	
Cracking parameter χ	2.912		1.518	
Shearing parameter ξ	0.536		0.445	
<u>Dependent variables</u>	deduced	gauge	deduced	gauge
Growth Displ. ratio, u_y/l_0	0.118	0.115	0.238	0.230
Growth displ. vector angle from transverse	56^0	54^0	60^0	60^0

TABLE 2
Deformation of singly-grooved
symmetrical specimens

Assumed $\theta_s = \theta_{su} = -\theta_{sl}$, $\xi = s_l/s_u = 1$, $\theta_f = 0^0$.

Alloy	HY-100 steel		1018 normalized	
<u>Observations</u>				
Projected flank ratio, $l_u/l_0 = l_l/l_0$	0.780		0.740	
Flank angle, $\theta_l = -\theta_u$	14 ⁰		12 ⁰	
<u>Corresponding parameters</u>				
Slip angle θ_s	41 ⁰		31 ⁰	
Cracking parameter, χ	1.907		1.579	
<u>Dependent variables</u>	deduced	observed	deduced	observed
Growth Displ. ratio, u_y/l_0	0.390	0.404	0.315	0.317
Back angle, β_u	12 ⁰	13 ⁰	19 ⁰	15 ⁰

AD-A162 108

MIXED MODE I AND II FULLY PLASTIC CRACK GROWTH FROM
SIMULATED WELD DEFECTS(U) MASSACHUSETTS INST OF TECH
CAMBRIDGE DEPT OF MECHANICAL ENGIN. G A KARDOMATERS

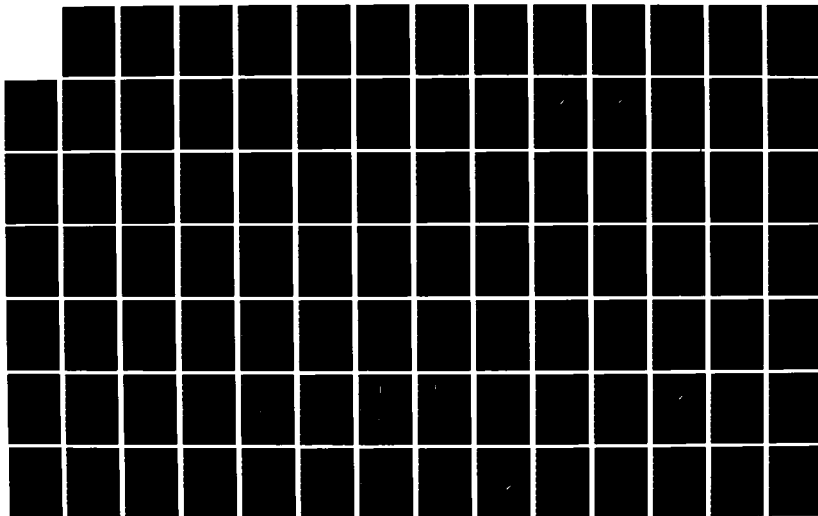
2/3

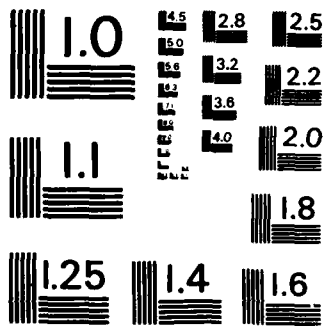
UNCLASSIFIED

23 OCT 85 N00014-82-K-0025

F/O 13/8

NL





MICROCOPY RESOLUTION TEST CHART
NATIONAL BUREAU OF STANDARDS-1963-A

Deformation of singly-grooved
asymmetrical specimens

Alloy:	1018 CF steel		HY-80 Steel	
<u>Observations</u>				
Projected upper flank ratio, l_u/l_0	0.890		0.850	
Projected lower flank ratio, l_l/l_0	0.960		0.930	
Upper flank angle, θ_u	40^0		39^0	
Lower flank angle, θ_l	41^0		41^0	
Upper back angle, β_u	13^0		12^0	
<u>Corresponding slip and fracture parameters</u>				
Slip angle θ_{sl}	50^0		52^0	
Slip angle θ_{su}	51^0		54^0	
Cracking angle θ_f	39^0		38^0	
Cracking parameter χ	6.335		3.822	
Shearing parameter ξ	0.354		0.440	
<u>Dependent variables</u>	deduced	gauge	deduced	gauge
Growth Displ. ratio, u_y/l_0	0.088	0.084	0.120	0.115
Growth displ. vector angle from transverse	51^0	52^0	56^0	54^0

Deformation of singly-grooved
symmetrical specimens

Assumed $\theta_s = \theta_{su} = -\theta_{sl}$, $\xi = s_l/s_u = 1$, $\theta_f = 0^0$.

Alloy: 1018 CF steel HY-80 steel

Observations

Projected flank ratio, $l_u/l_0 = l_l/l_0$ 0.820 0.800

Flank angle, $\theta_l = -\theta_u$ 9^0 13^0

Corresponding parameters

Slip angle θ_s 36^0 43^0

Cracking parameter, χ 2.883 2.204

Dependent variables deduced observed deduced observed

Growth Displ. ratio, u_y/l_0 0.260 0.262 0.369 0.362

Back angle, β_u 12^0 12^0 10^0 12^0

Deformation of singly-grooved
asymmetrical specimens

Alloy:	A36 hot rolled steel		5086-H111 aluminum	
<u>Observations</u>				
Projected upper flank ratio, l_u/l_0	0.770		0.810	
Projected lower flank ratio, l_l/l_0	0.890		0.900	
Upper flank angle, θ_u	36^0		41^0	
Lower flank angle, θ_l	41^0		39^0	
Upper back angle, β_u	13^0		16^0	
<u>Corresponding slip and fracture parameters</u>				
Slip angle θ_{sl}	53^0		51^0	
Slip angle θ_{su}	57^0		53^0	
Cracking angle θ_f	32^0		37^0	
Cracking parameter χ	1.834		2.821	
Shearing parameter ξ	0.425		0.507	
<u>Dependent variables</u>	deduced	gauge	deduced	gauge
Growth Displ. ratio, u_y/l_0	0.214	0.216	0.126	0.138
Growth displ. vector angle from transverse	61^0	60^0	55^0	56^0

Deformation of singly-grooved
symmetrical specimens

Assumed $\theta_s = \theta_{su} = -\theta_{sl}$, $\xi = s_l/s_u = 1$, $\theta_f = 0^0$.

Alloy: A36 hot rolled steel 5086-H111 aluminum

Observations

Projected flank ratio, $l_u/l_0 = l_l/l_0$ 0.780 0.760

Flank angle, $\theta_l = -\theta_u$ 10^0 10^0

Corresponding parameters

Slip angle θ_s 32^0 29^0

Cracking parameter, χ 2.158 1.892

Dependent variables deduced observed deduced observed

Growth Displ. ratio, u_y/l_0 0.275 0.254 0.263 0.278

Back angle, β_u 16^0 15^0 19^0 16^0

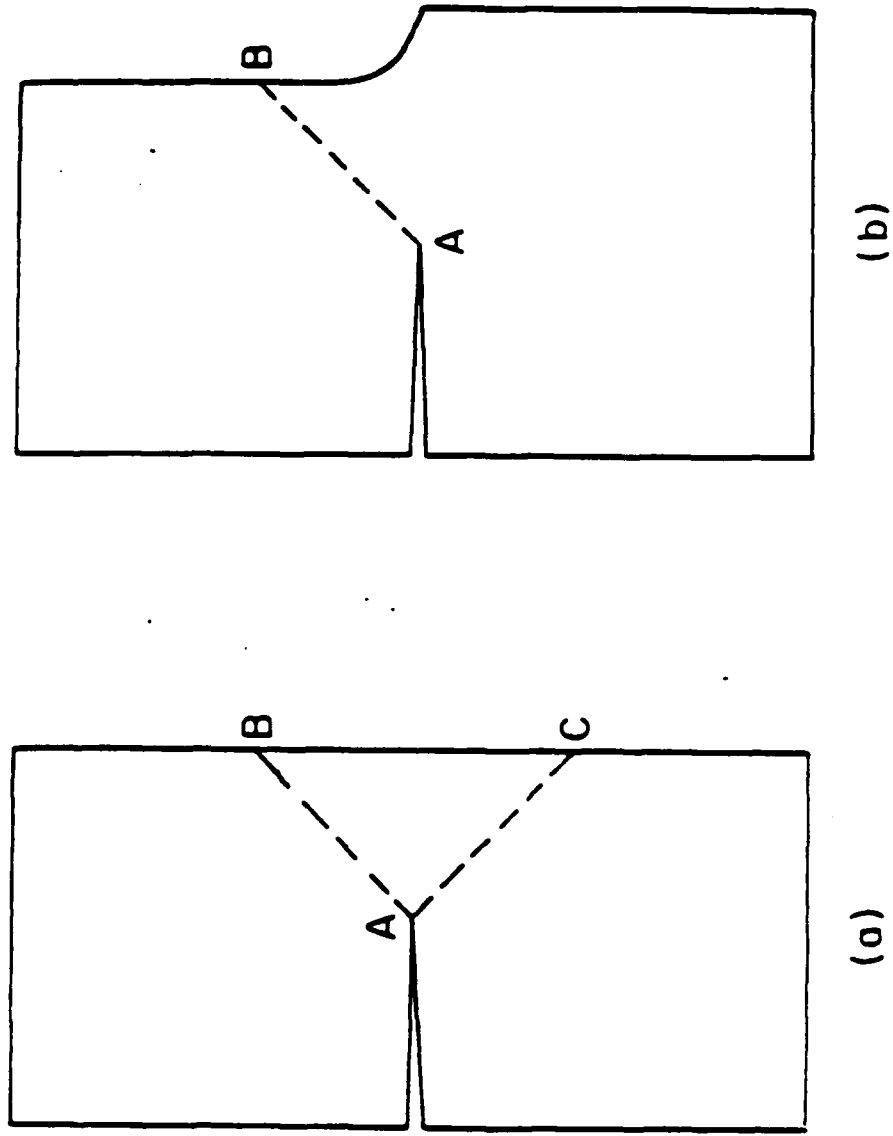


Figure 1 Symmetric (a) and Asymmetric (b) shear from cracks

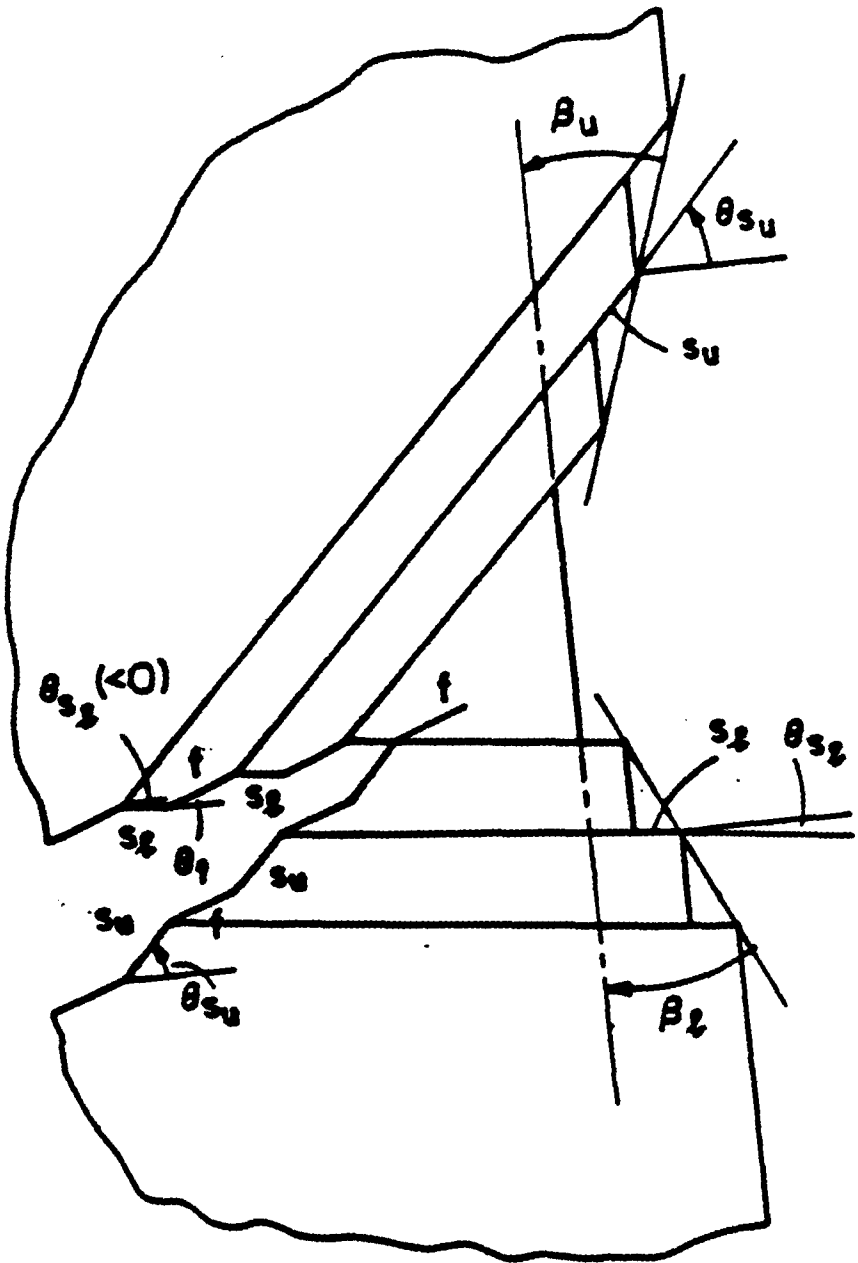


Figure 2. Development of deformation for the two-slip plane model

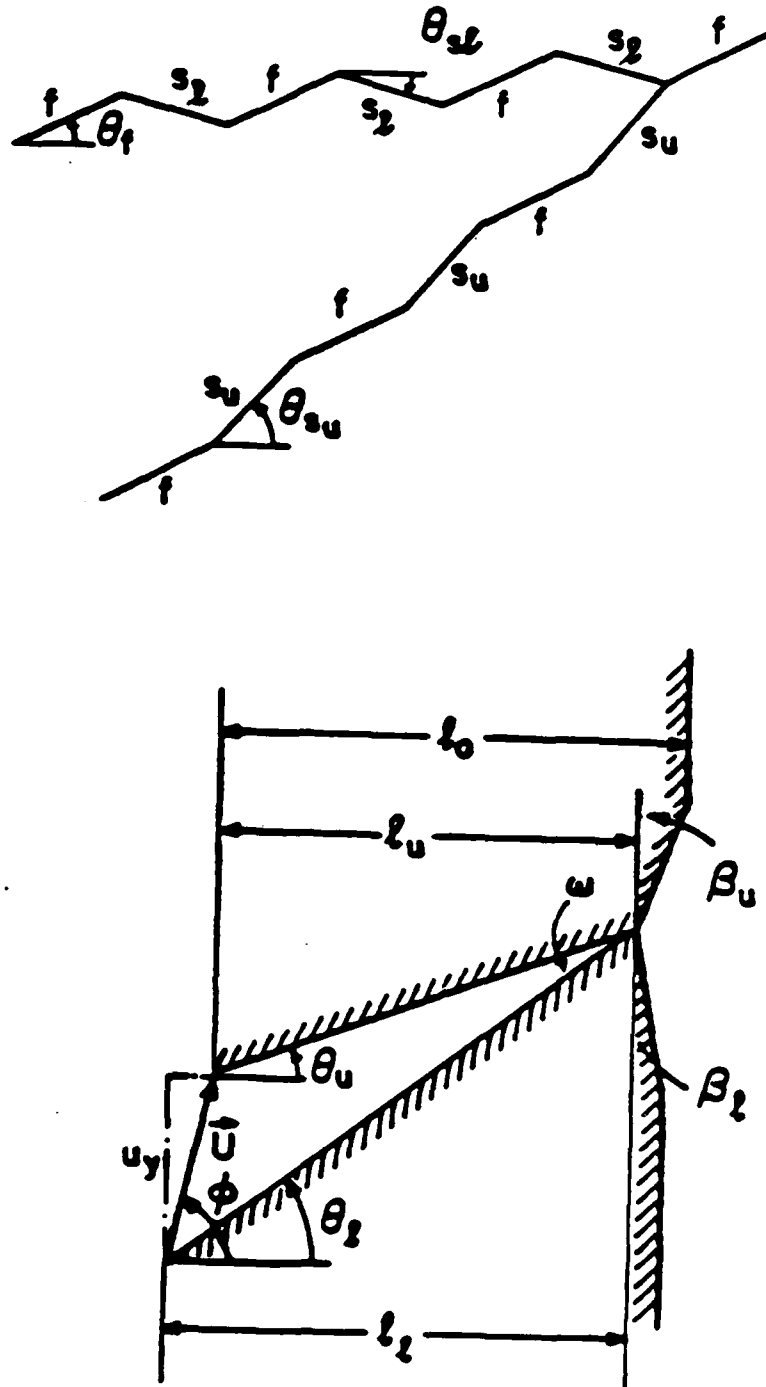


Figure 3. Micro- and Macroscopic geometry

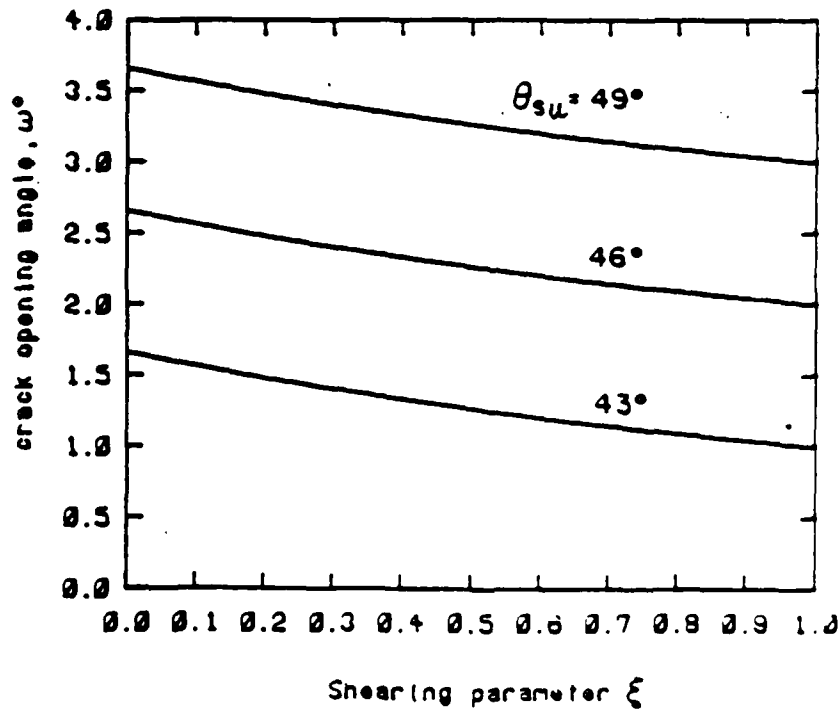
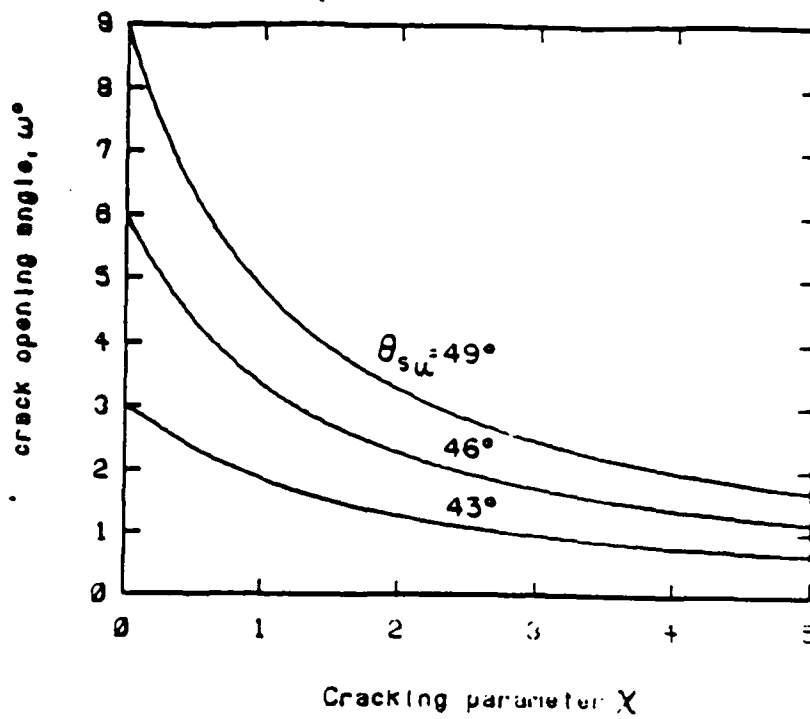


Figure 4. Crack opening angle as a function of the cracking parameter χ for $\xi=s_f/s_u=0.5$, and the shearing parameter ξ for $\chi=f/s_u=2.0$. In both cases $\theta_f=38^\circ$ and $\theta_{s_f}=40^\circ$.

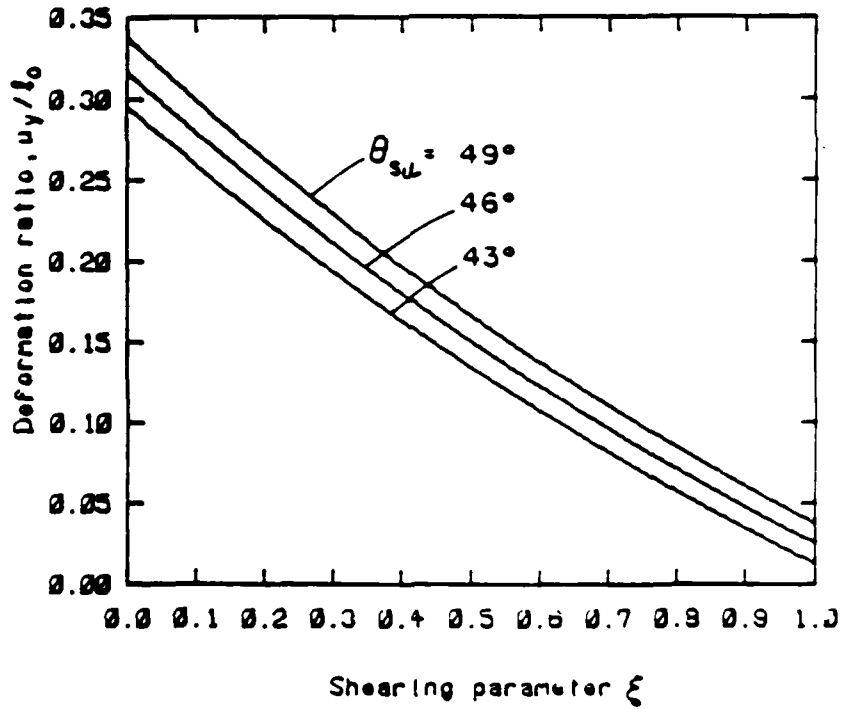
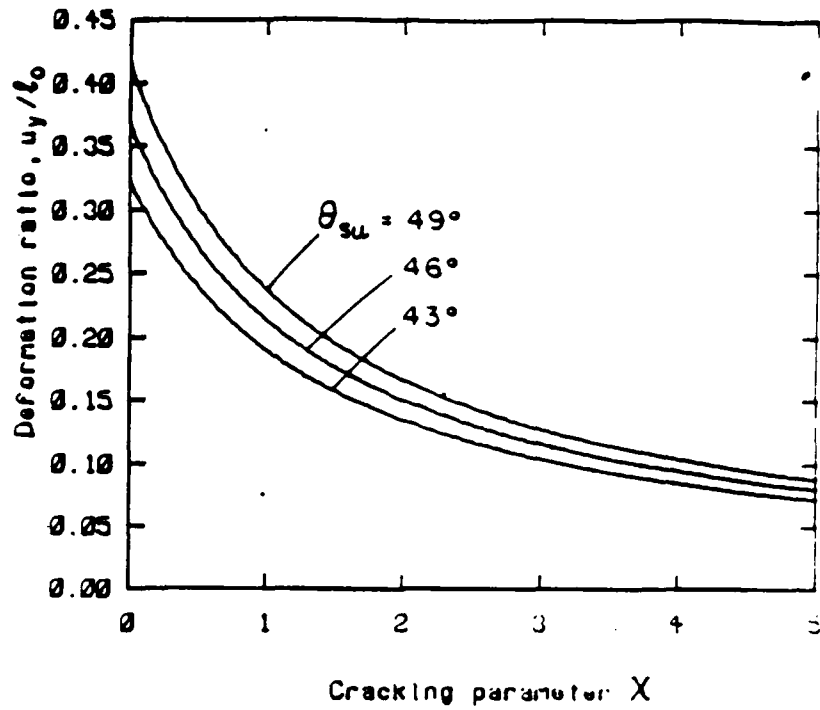


Figure 5. Deformation ratio as a function of the cracking parameter χ for $\xi = s_f/s_u = 0.5$, and the shearing parameter ξ for $\chi = f/s_u = 2.0$. In both cases $\theta_f = 38^\circ$ and $\theta_{su} = 40^\circ$.

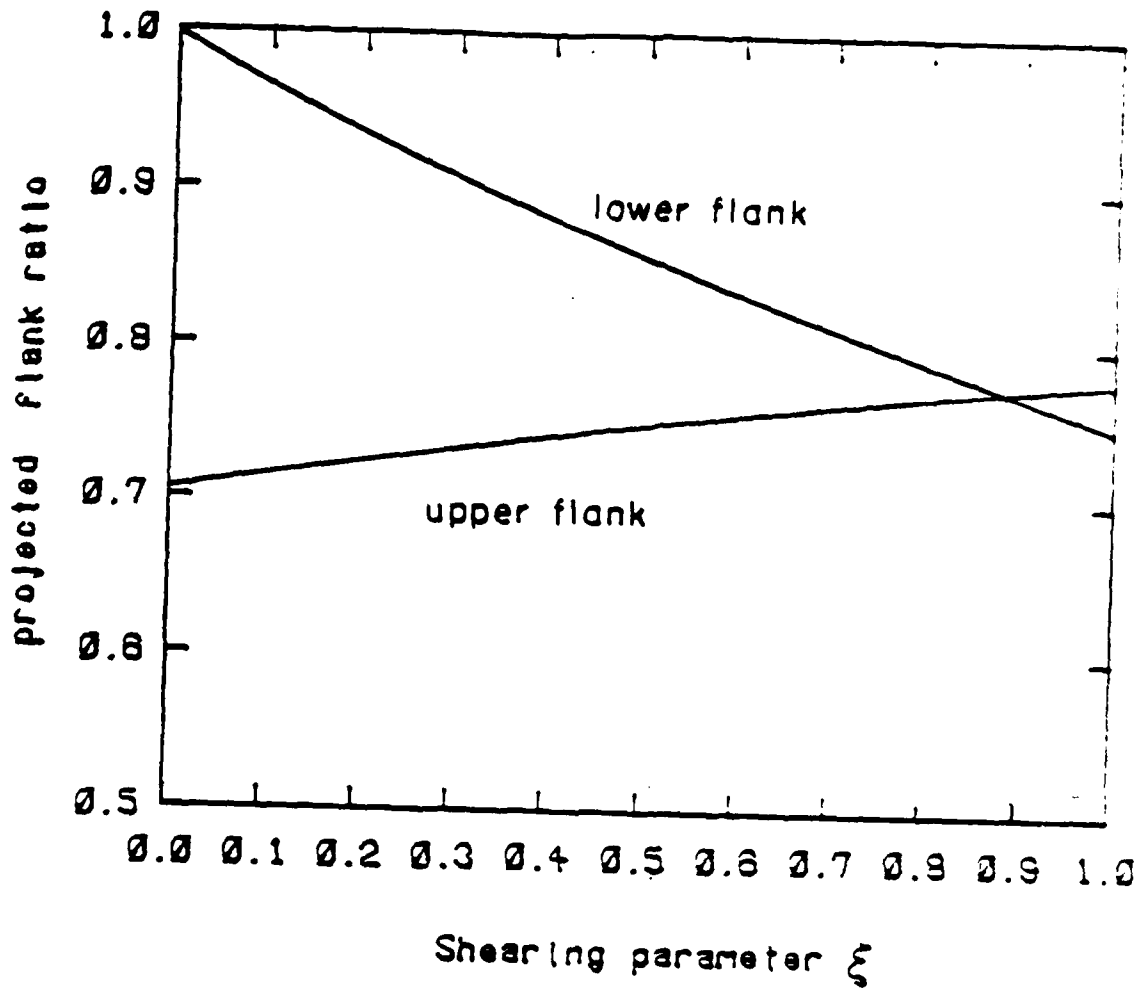


Figure 6. Projected lower and upper flank ratio as a function of the shearing parameter ξ for $\chi=f/s_y=2.0$, $\theta_l=38^\circ$, $\theta_{sl}=40^\circ$ and $\theta_{su}=49^\circ$.

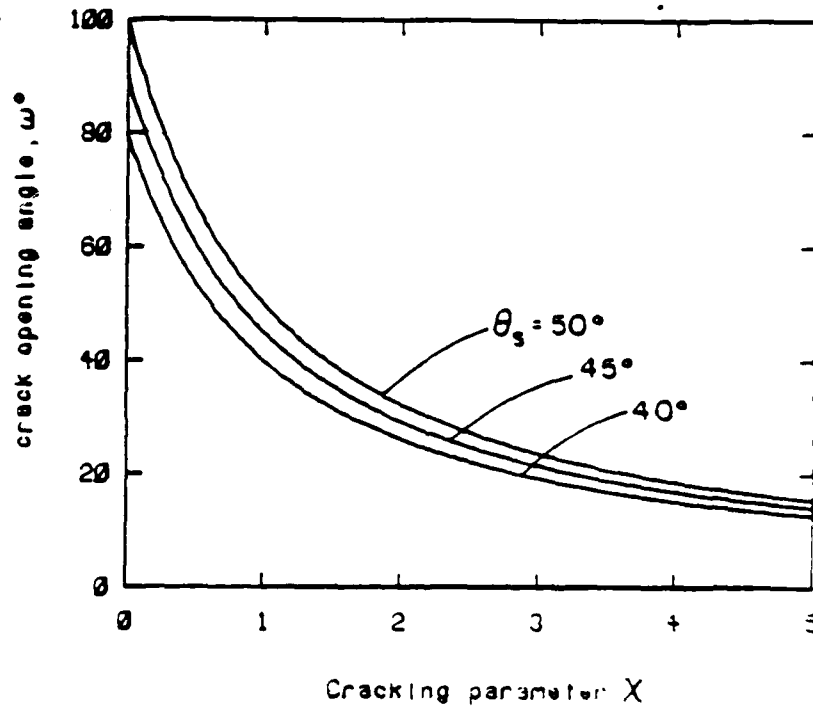
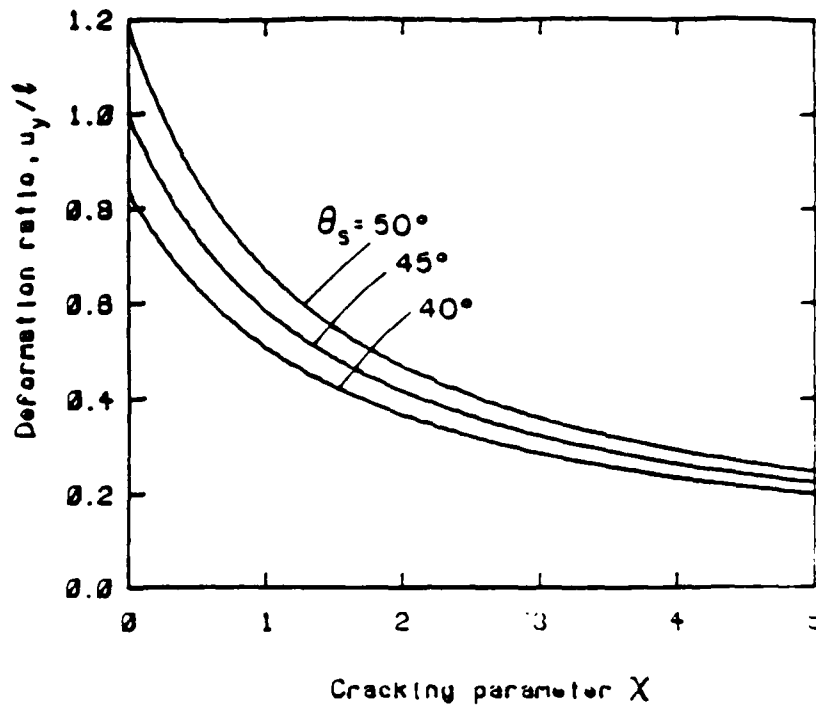


Figure 7. Deformation ratio and crack opening angle as a function of the cracking parameter χ for the limiting Mode I symmetric case. $\theta_f = 0$, $\xi = s_f/s_u = 1$, $\theta_s = \theta_{su} = -\theta_{sl}$.

CHAPTER FIVE

FINITE ELEMENT INVESTIGATION OF PLANE
STRAIN ASYMMETRIC FULLY PLASTIC SPECIMENS

TABLE OF SYMBOLS

n	strain hardening exponent
σ_1	flow stress at unit strain
η	damage (eq. 3)
σ	mean normal stress
γ	principal shear strain
τ	principal shear stress
σ_{eq}	equivalent stress
ϵ_{eq}	equivalent strain
θ_c	critical orientation
ρ	mean inclusion spacing
ϕ	displacement vector angle from transverse
U_y	axial component of far field displacement vector
U_x	transverse component of far field displacement vector
M^p	mixity parameter (eq. 4)
u_y	axial component of relative crack tip displacement ($=u_x^+ - u_x^-$)
u_x	transverse component of relative crack tip displacement ($=u_x^+ - u_x^-$)

ABSTRACT

Crack initiation and early growth in asymmetric, fully plastic, plane strain configurations in power-law hardening materials is investigated numerically via the finite element method. In such asymmetric configurations a single shear band is present instead of the two shear bands of the symmetric case. Results for two strain hardening exponents, $n=0.12$ and $n=0.24$, indicate that cracking occurs at an angle of 39° - 43° from the transverse, smaller than 45° due to the higher triaxiality. The direction of cracking is closer to 45° for lower strain hardening exponents and is

within 2^0 of those experimentally found. The stress and strain field is consistent with the power law singularity of the HRR fields. The far field displacement vector is not along the shear band but at about 68^0-70^0 from the transverse at initiation, indicating the presence of a Mode I component. Early growth, studied by successive removal of elements reaching unit damage, results in crack growth per unit displacement for the lower hardening case about twice that of the higher hardening one.

INTRODUCTION

Asymmetric plane strain specimens have been used to study crack growth along a single shear band. Such cases may occur when a weld fillet or a harder heat-affected zone on one side of the crack suppresses the other shear zone that would appear in a symmetric specimen. Based on Shih's extension to mixed mode [1] of the HRR [2,3] fields, McClintock and Slocum [4] developed an approximate formulation for the accumulation of damage directly ahead of an asymmetric crack. The crack was assumed to follow the center of a 45^0 shear band and the far-field displacement was assumed to be parallel to the shear band. It was found that the initiation displacement was of the order of the fracture process zone size ρ . To study the directional effects, several sites around the current crack tip were considered in chapter two and the crack was assumed to advance to the direction requiring the least far field displacement for critical damage. The far field displacement vector was again assumed to be at 45^0 from the transverse. Both these solutions found only little effect of strain hardening on the crack growth rate. However, tests have shown that the far field displacement vector is not at 45^0 but more axial, at an angle of about 60^0 from the transverse. In addition, a lower strain hardening exponent n was found to increase the crack growth rate dramatically. Strain hardening causes the

deformation field to fan out. The effect of the finite width of the shear band can be captured with a finite element investigation. In the following the finite element method is used to study crack initiation and early growth in fully plastic plane strain asymmetric specimens.

TECHNIQUE

The finite element grid used is indicated in Fig. 1, with the details of the refined mesh for the first circle around the crack tip shown in Fig. 2. An increased element concentration near the 45° line is used to account for the high strain gradients there. Angular spacings of 3.75° for four sectors, 7.5° for two sectors, 15° for four sectors and 30° for nine sectors are used. Minimum radial size for the 3.75° elements is $\rho=0.01$ mm, the approximate value for the mean inclusion spacing. The radial size ratio was $s=1.155$ for the 3.75° sectors becoming s^2 for the 7.5° sectors, s^4 for the 15° and s^8 for the 30° sectors. The net ligament of the specimen is $l_0=2.55$ mm. 8-node plane strain isoparametric elements are used. The mesh consisted of a total of 207 elements with 722 nodes and 1444 degrees of freedom. The nodes at the bottom were on rollers with the center node pinned. An axial displacement with zero shear traction was applied at the nodes of the upper end. The analysis was carried on a Data General computer available at M.I.T. and the general purpose finite element code ABAQUS [5] was used.

The mesh was checked by comparing the theoretical strain distribution for the elastic and the low hardening $n=1/13$ HRR [2,3] fields with the linear variation of strains within the 8-node elements. The radial variation in strain showed a maximum deviation of 15% from the elastic solution for the first element around the tip. For the HRR $n=1/13$ solution the deviation was 33%, dropping to 5.6% for the

second element. The angular distribution in $\epsilon_{r\theta}$ showed a maximum deviation of 8% from the HRR for the 30° sectors. In addition, a circular portion of the finite element mesh with 16 radially elements at the finest sectors was tested by imposing Mode I HRR displacement boundary conditions. The HRR singularity in $\epsilon_{r\theta}$ was reproduced with no more than 5% deviation in all elements except the first one, where the maximum deviation was 14% at the first integration point.

The material is modeled as isotropic power-law hardening: the stress σ is given in terms of the plastic strain ϵ^P , the flow stress at unit strain σ_1 , a strain hardening exponent n , and a pre-strain ϵ_0 by

$$\sigma = \sigma_1(\epsilon_0 + \epsilon^P)^n . \quad (1)$$

Two cases were considered, $n=0.24$, $\sigma_1=826 \text{ MN/m}^2$, yield strength $Y=333 \text{ MN/m}^2$ and $n=0.12$, $\sigma_1=909 \text{ MN/m}^2$, $Y=435 \text{ MN/m}^2$.

The fracture criterion of McClintock, Kaplan and Berg [6] is used, by which it is postulated that fracture due to micro-void coalescence occurs when a quantity η , named "damage", reaches a critical value of unity. The damage is expressed in terms of a hole growth ratio F_t , the principal shear strain γ , and the triaxiality (defined as the ratio of the mean normal stress σ to principal shear strain τ). In terms of the equivalent stress and strain,

$$\tau = \sigma_{eq}/\sqrt{3}, \quad \gamma = \epsilon_{eq}\sqrt{3} . \quad (2)$$

The damage is:

$$\eta = \frac{1}{\ln F_t} \left[\ln \sqrt{1+\gamma^2} + \frac{\gamma}{2(1-n)} \sinh\left(\frac{(1-n)\sigma}{\tau}\right) \right] . \quad (3)$$

The critical displacement for growth initiation occurs when the damage becomes

unity at a point (ρ, θ_c) where ρ is the fracture process zone size and θ_c is the critical orientation. To study the first steps of crack growth, successive elements were removed as they reached a damage of unity.

RESULTS AND DISCUSSION

The axial displacement, at the upper end, U_y , was gradually increased and the damage from (3) was calculated at each site around the tip. Cracking occurs when the fracture criterion of $\eta=1$ is first satisfied.

The initiation conditions (critical orientation from the transverse, θ_c , critical strain γ_c , critical triaxiality σ/τ , far-field displacement u_i/ρ) are shown in Table 1. The crack tip initiation displacement is of the order of the mean inclusion spacing as was also found by McClintock and Slocum [4] and in chapter 2. The critical orientation of $39-43^\circ$ from the transverse and the far field displacement vector orientation of about $68-70^\circ$ at initiation can be compared with the values of $38-41^\circ$ for the crack direction and $58^\circ-69^\circ$ for the displacement vector at initiation from tests. The lower hardening $n=0.12$ case results in fracture closer to the shear band, as found experimentally.

For a crack at $\theta=0^\circ$, a Mode I mixity parameter M^P was introduced by Shih [1], defined in terms of the near field stresses by

$$M^P = \frac{2}{\pi} \tan^{-1} \left| \lim_{r \rightarrow 0} \frac{\sigma_{\theta\theta}(r, \theta=0)}{\sigma_{r\theta}(r, \theta=0)} \right| \quad (4)$$

The mixity parameter varies from 0 for pure Mode II to 1 for pure Mode I. This parameter can be referred to either the initial crack direction $\theta=0^\circ$ or the final (critical) one $\theta=\theta_c$, giving values as shown in Table 1. Notice that the above definition of the Mode I mixity is with respect to both shearing and crack advance at

$\theta=0$, for both the limiting cases $M^P=0$ or 1. In the problem at hand, pure Mode I is crack advance along the line $\theta=0$ (corresponding to the symmetric case) and pure Mode II would be relative deformation and crack advance along the 45° shear band. Alternatively, for experiments and finite element studies, a definition of a Mode I mixity in terms of the displacement field is helpful:

$$M_I^* = \frac{2}{\pi} \tan^{-1} \left| \lim_{r \rightarrow 0} \frac{u_\theta(r, \pi) - u_\theta(r, -\pi)}{u_r(r, \pi) - u_r(r, -\pi)} \right| \quad (5)$$

Values for this parameter are also shown in Table 1. Notice that for the non-hardening rigid plastic pure Mode II limit with a single slip line at $\theta=45^\circ$, $M_I^*=0.5$ for the crack at $\theta=0^\circ$ but $M_I^*=0$ for the crack at $\theta=45^\circ$.

Fig. 3a shows the angular variation of the $\sigma_{r\theta}$ stress component. The curve is consistent with the Shih's [1] curves and has a maximum near $\theta=65^\circ$. This compares with the case $M^P=1$, $n=1/13$ which has a maximum at an angle near 97° and the $M^P=1$, $n=1/3$ case with a maximum near 88° whereas the case of $M^P=0$ has a maximum $\sigma_{r\theta}$ at $\theta=0^\circ$. Furthermore, the maximum for $n=1/13$, $M^P=0.82$ is near 55° and for $n=1/3$, $M^P=0.79$ is near 40° [1]. The θ -variation of $\epsilon_{r\theta}$ is shown in Figs. 3b, 3c. Of the two peaks in $\epsilon_{r\theta}$, the one for positive θ is the dominant the other peak tending to vanish during growth when the Mode I mixity is reduced (Fig. 3d).

The radial variation of the equivalent strain for $n=0.12$ (along the critical orientation) is shown in Fig. 4. The asymptotic solution for power-law hardening materials yield singularities in the stress and strain of the form $r^{-n/(n+1)}$ and $r^{-1/(n+1)}$, respectively. The agreement between the theoretical curve and the finite element results is within 5%.

Fig. 5 shows the axial displacement of the upper flank relative to the lower

flank at the initiation point. The components of the relative displacement of the crack tip $u_x(x=0, y=0)$ and $u_y(x=0, y=0)=CTOD$ are included in Table 1. A higher CTOD occurs in the higher hardening case. Figs. 6a and 6b show the angular variation of the near tip displacement field for the two hardening exponents $n=0.24$ and $n=0.12$, along with the nonhardening limit. The far-field displacement (displacement at the upper boundary) components U_x and U_y at the initiation point are also included in Table 1 together with the far field displacement vector orientation from the transverse, ϕ . The value of $\phi=68^\circ$ to 70° , instead of 45° , indicates that we cannot consider the far field displacement taking place parallel to the shear band, as assumed by McClintock and Slocum [4]. We can observe that the displacement vector at initiation is more axial for the lower hardening case with larger M^P . The higher triaxiality for angles smaller than 45° is the main reason for the cracking direction deviating towards the transverse. The triaxiality is smaller for $n=0.24$ because of the smaller Mode I mixity M^P .

Tests have shown that, in the asymmetric case, the lower hardening alloys exhibit a maximum crack growth rate more than twice that of the higher hardening alloys. The finite element mesh of Figure 1 was used to study the early growth. Crack was grown by successive removal of the most heavily damaged element. After initiation and removal of the most damaged element, the far field displacement is further increased until critical damage $\eta=1$ occurs in the next row of elements. At this point the next step of crack growth takes place by removing the critical element. After growth by four steps (1.9% of the ligament) it was found that the average displacement per unit projected crack advance $\Delta u/\Delta l$ is about 88% smaller for the lower hardening $n=0.12$ case than that of the higher hardening $n=0.24$ case (Table 1). Another noteworthy result is that the far field displacement vector U becomes less axial as the crack grows. For the case $n=0.12$, at the end of the fourth

step, the angle of the displacement vector from the transverse is $\phi=67.6^{\circ}$ instead of the initiation value of $\phi=69.5^{\circ}$. Decreasing ϕ angles with crack growth have been experimentally observed (chapter three). During these steps the critical elements were at the same angular sector and no appreciable acceleration of the crack was observed.

CONCLUSIONS

A finite element investigation of fully plastic asymmetric specimens with a single slip band, as might be encountered near a weld, has provided the stress, strain and displacement fields around the tip. Results indicate the presence of a large Mode I component with the far field displacement vector at initiation not along the 45° shear band but at an angle about 67° from the transverse. The initiation conditions were found by using the fracture criterion for hole growth by McClintock Kaplan and Berg [6]. The critical direction was at $39-43^{\circ}$, less than 45° from the transverse, increasing for a lower strain hardening exponent. Displacement to crack initiation is about twice the fracture process zone size. Stress and strain fields are consistent with the solutions for the mixed mode extended HRR fields. Early growth, studied by successive removal of the most damaged element, resulted in crack growth rate for the lower hardening case about twice that of the higher hardening one. The angle of the far-field displacement vector from the transverse was found to be decreasing with crack growth.

REFERENCES

1. Shih C.F. "Small Scale Yielding Analysis of Mixed Mode Plane Strain Crack Problems", *Fracture Analysis, ASTM STP 560*, Am.Soc.Test.Mat., Philadelphia, 187-210 (1974).

2. Hutchinson J.W., "Singular behaviour at the end of a tensile crack in a hardening material", *J. Mech. Phys. Sol.*, 16, 13-31 (1968).
3. Rice J.R. and Rosengren G.F. "Plane Strain Deformation near a crack tip in a power-law hardening material", *J. Mech. Phys. Sol.*, 16, 1-12 (1968).
4. McClintock F.A. and Slocum A.H. "Predicting Fully Plastic Mode II Crack Growth from an Asymmetric Defect", *Int. J. Fract. Mechanics*, 27, 49-62 (1985).
5. ABAQUS from Hibbitt, Karlsson and Sorensen, Inc.
6. McClintock F.A., Kaplan S.M. and Berg C.A. "Ductile Fracture by hole growth in shear bands" *Int. J. Fract. Mech.*, 2, 614-627 (1966).

TABLE 1
Results of the finite element study.

		n = 0.12	n = 0.24
Initiation Conditions			
Critical angle from transverse	θ_c	43.1 ⁰	39.4 ⁰
Far field displ. components	U_y/ρ	2.1	1.8
	U_x/ρ	0.782	0.737
Displacement vector-angle from transverse	ϕ	69.5 ⁰	67.7 ⁰
Displacements at crack tip	$u_x(x=0, y=0)/\rho$	0.134	0.192
	$u_y(x=0, y=0)/\rho$	0.518	0.564
Principal Shear Strain	γ_c	0.246	0.327
Triaxiality	σ/τ	2.18	1.995
Mixity parameter			
Mode I Mixity defined by Shih (based on stresses)	M^P (Shih) (rel. to $\theta=0^0$)	0.936	0.927
	(rel. to $\theta=\theta_c$)	0.717	0.710
Displ. based Mode I Mixity	M_I^*	0.752	0.815
Early Growth			
Far field displ. per projected crack advance (4 steps)	$\Delta u/\Delta l$	0.075	0.143

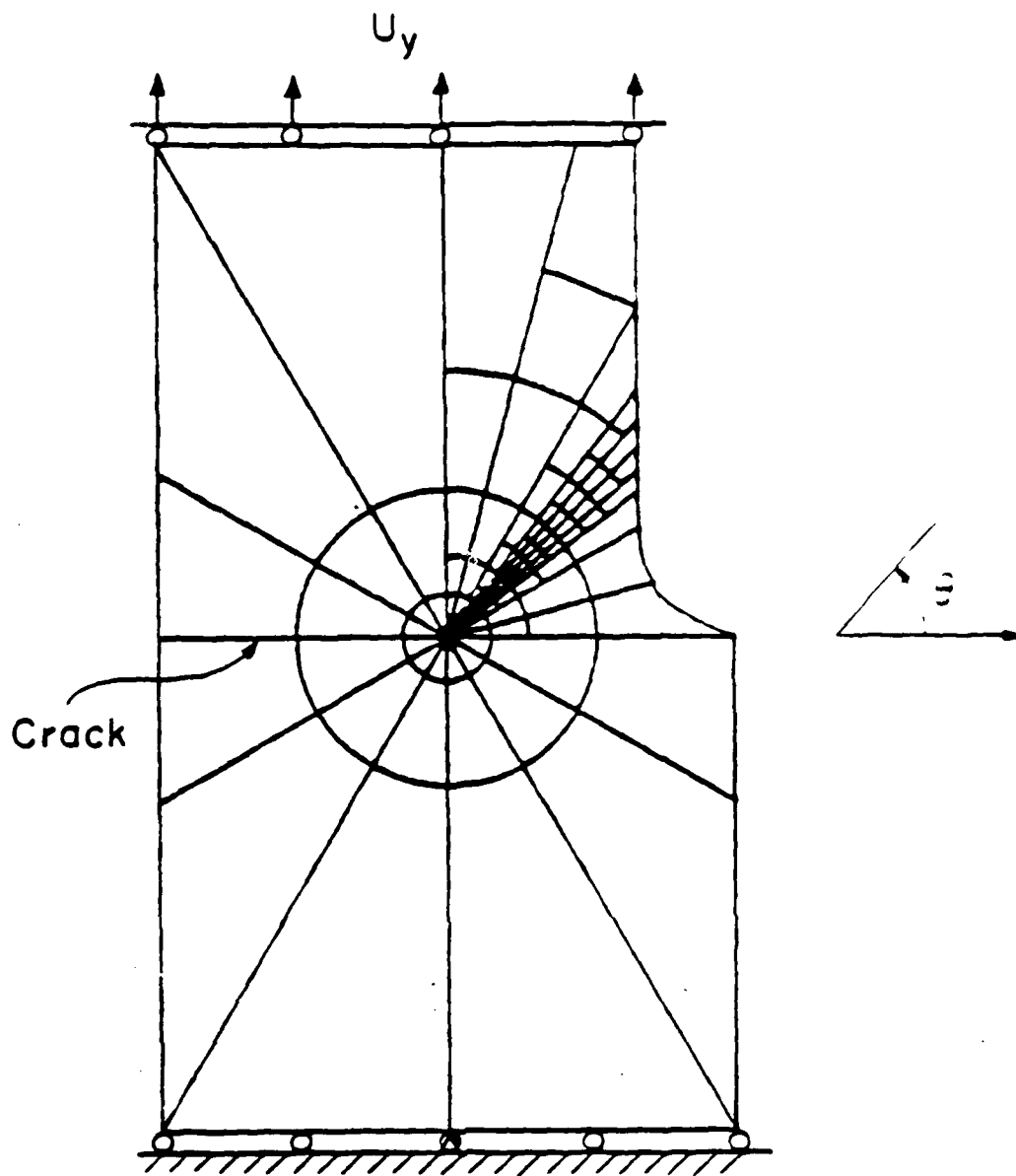


Figure 1. The finite element mesh

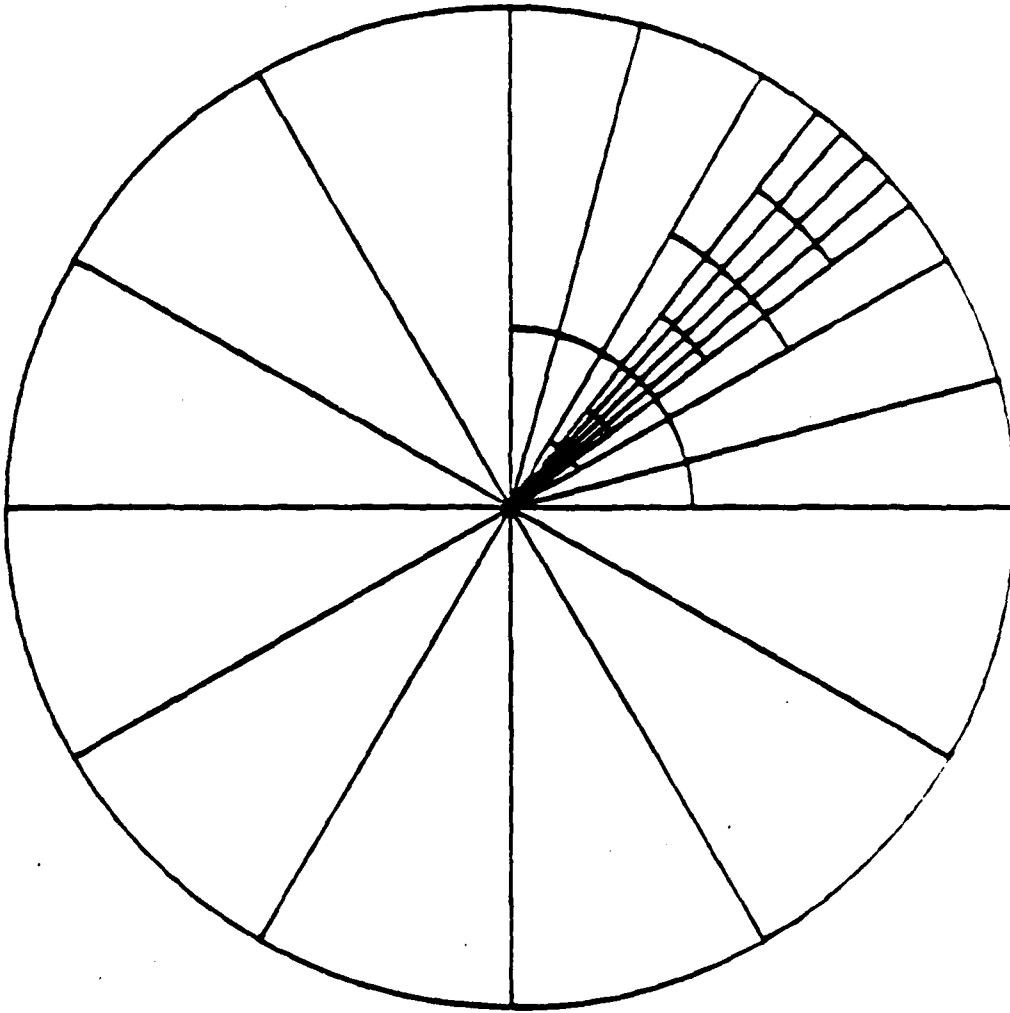


Figure 2. Detail of the finite element mesh around the crack tip

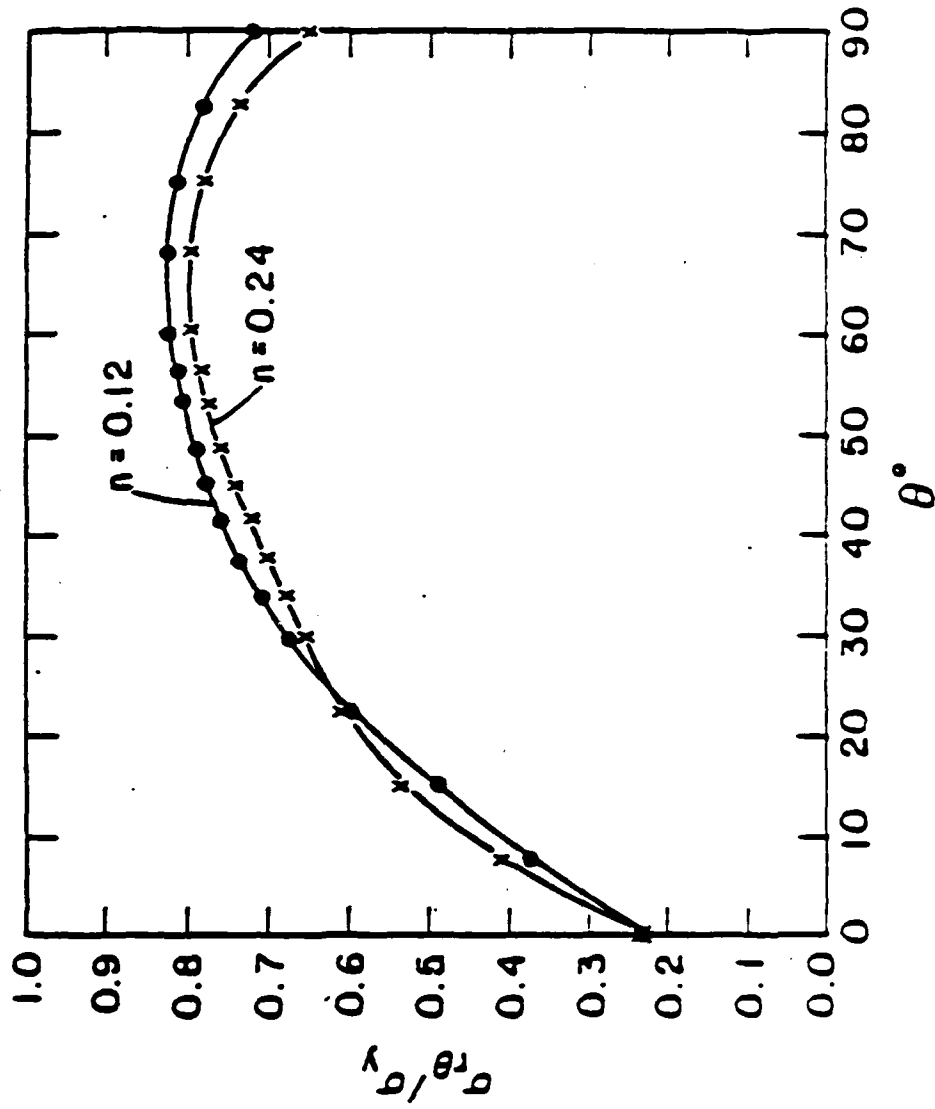


Figure 3a Angular variation of the shear stress $\sigma_{r\theta}$ at initiation (at $r=5\%$ of the ligament)

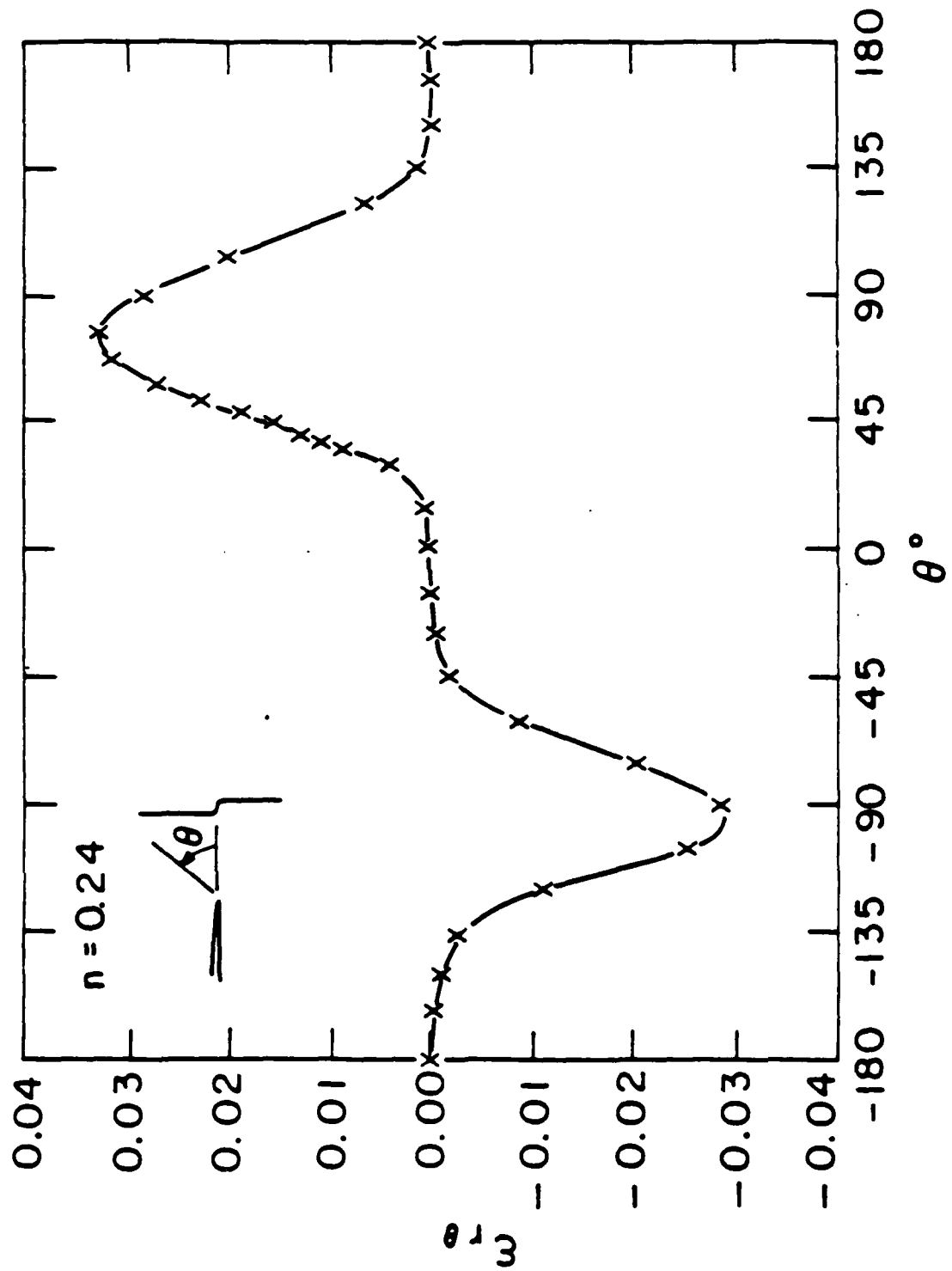


Figure 3b Angular variation of the shear strain $\epsilon_{r\theta}$ at initiation (at $r=5\%$ of the ligament).

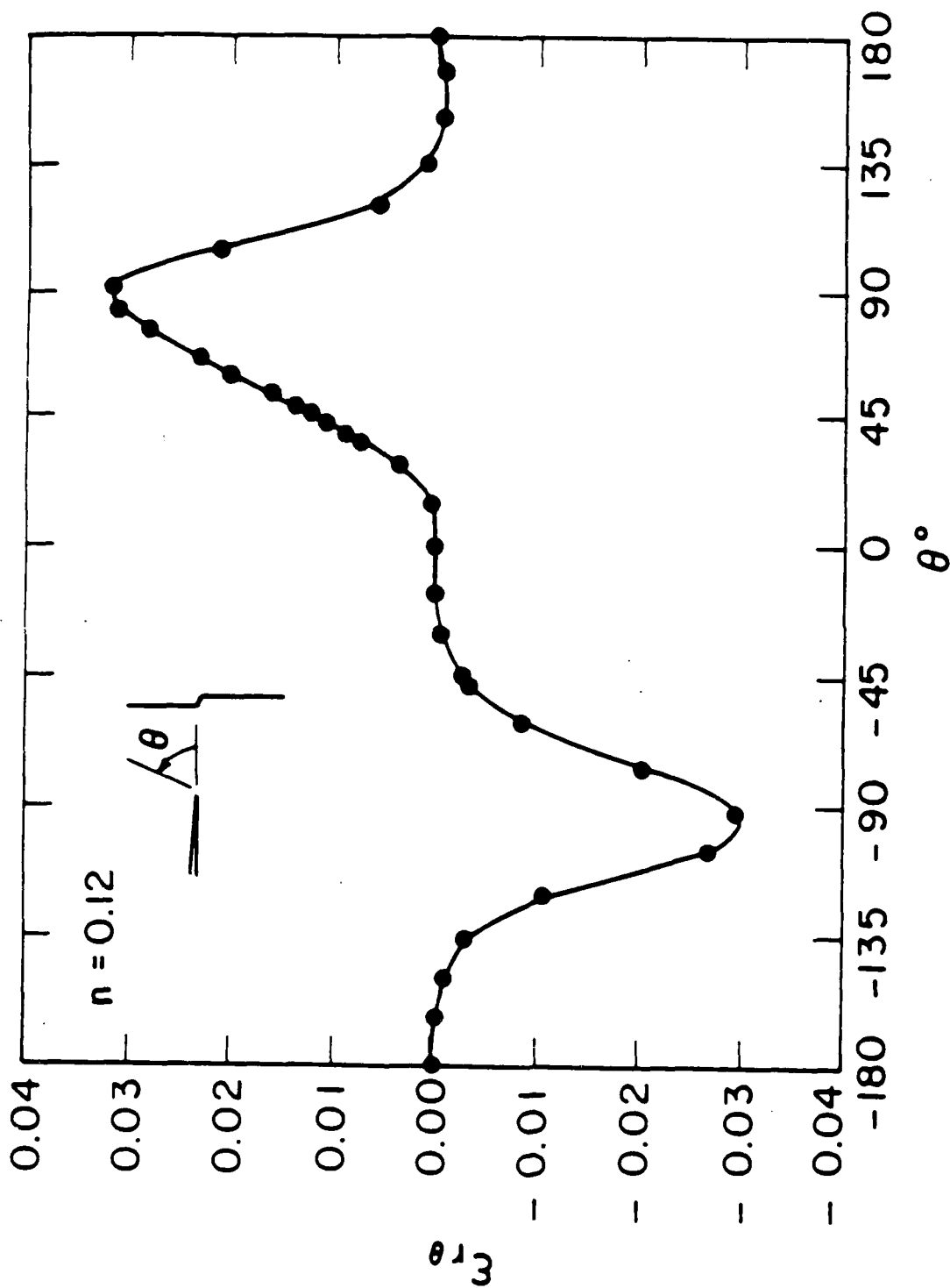


Figure 3c Angular variation of the shear strain $\epsilon_{r\theta}$ at initiation (at $r=5\%$ of the ligament) for $n=0.12$

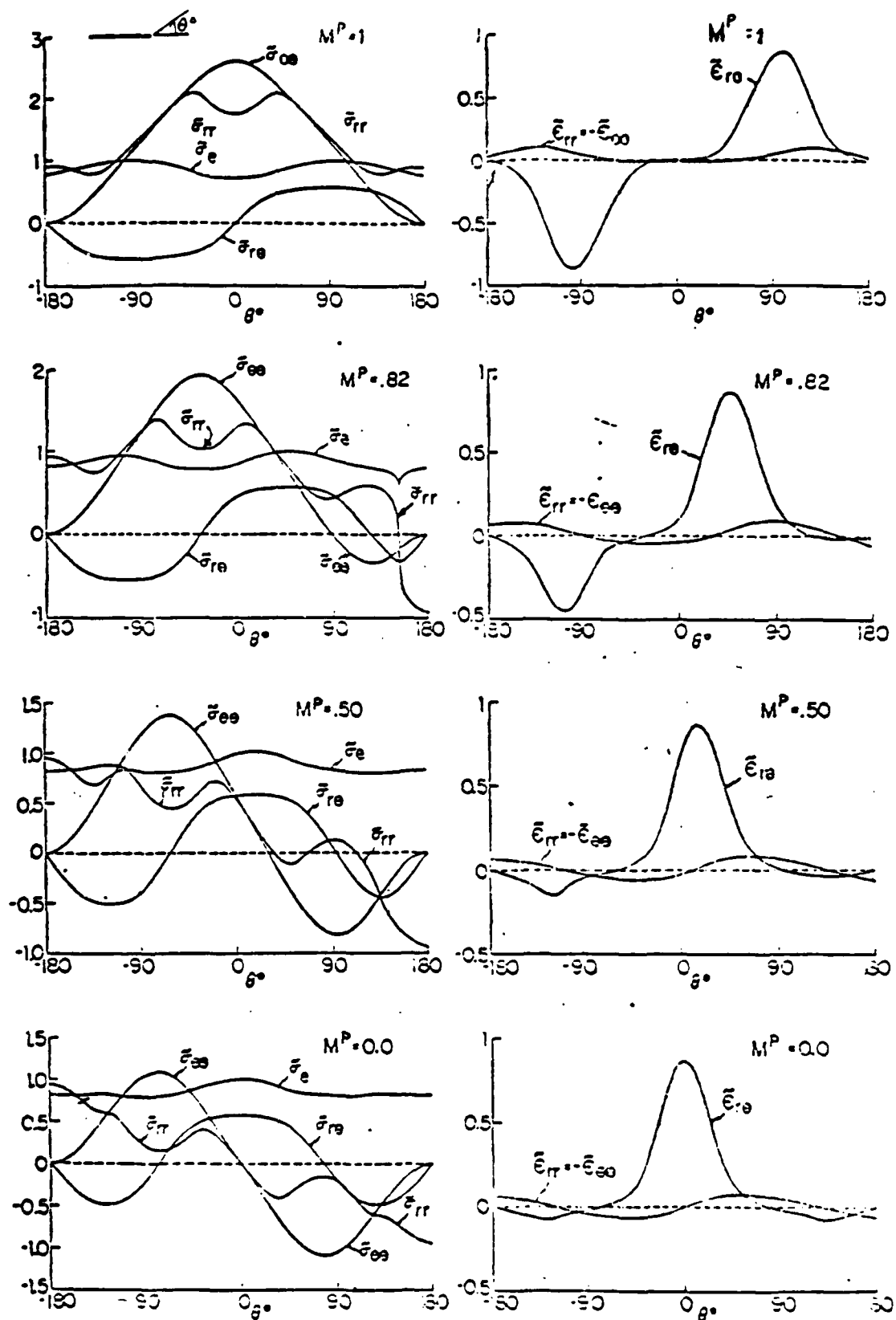


Figure 3d. Angular variation of the stresses and strains for mixed mode, plane strain, $n=1/13$ cracks from Shih [1]

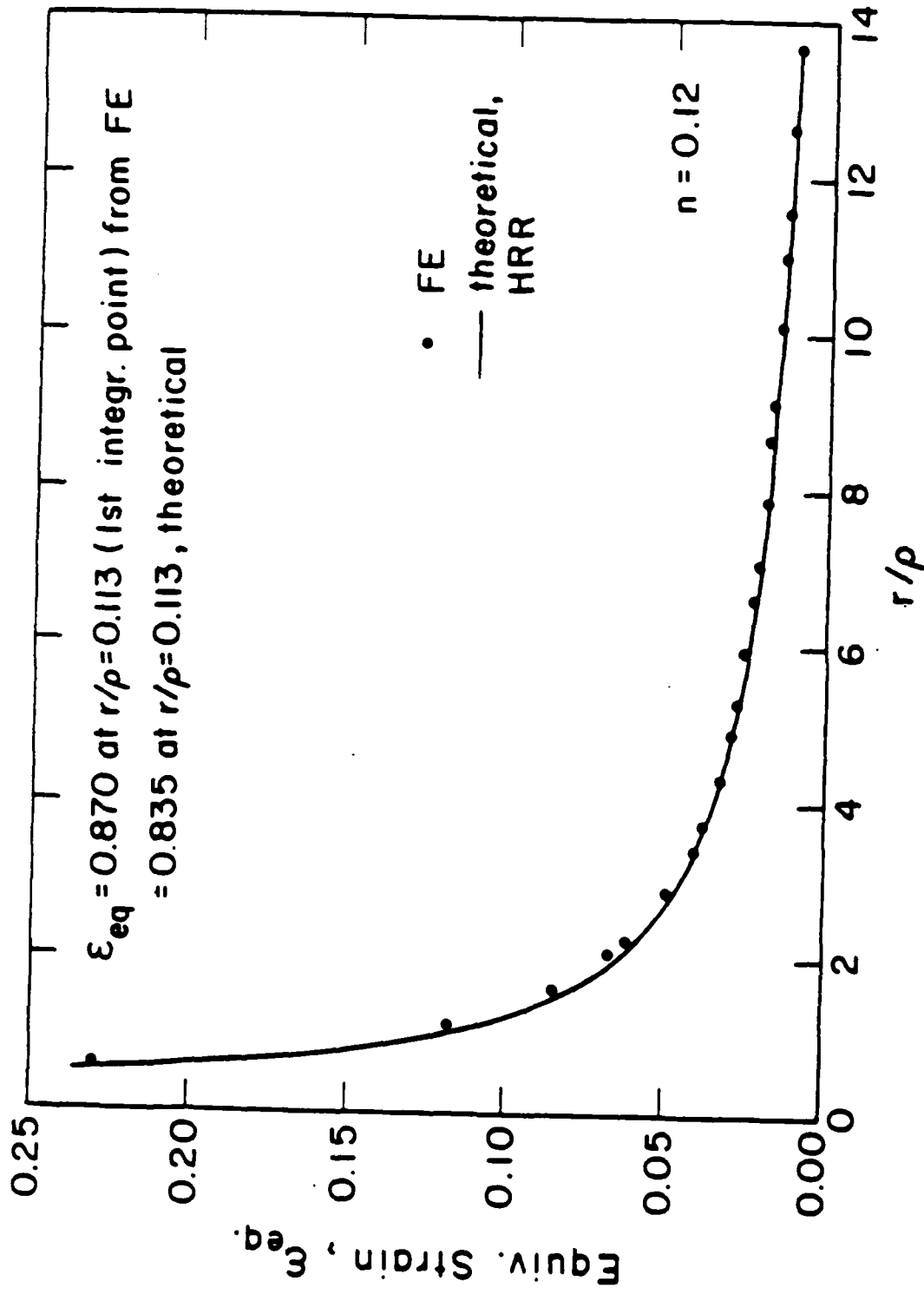


Figure 4 Radial variation of the equivalent plastic strain vs the theoretical one (HRR singularity) at the critical angle

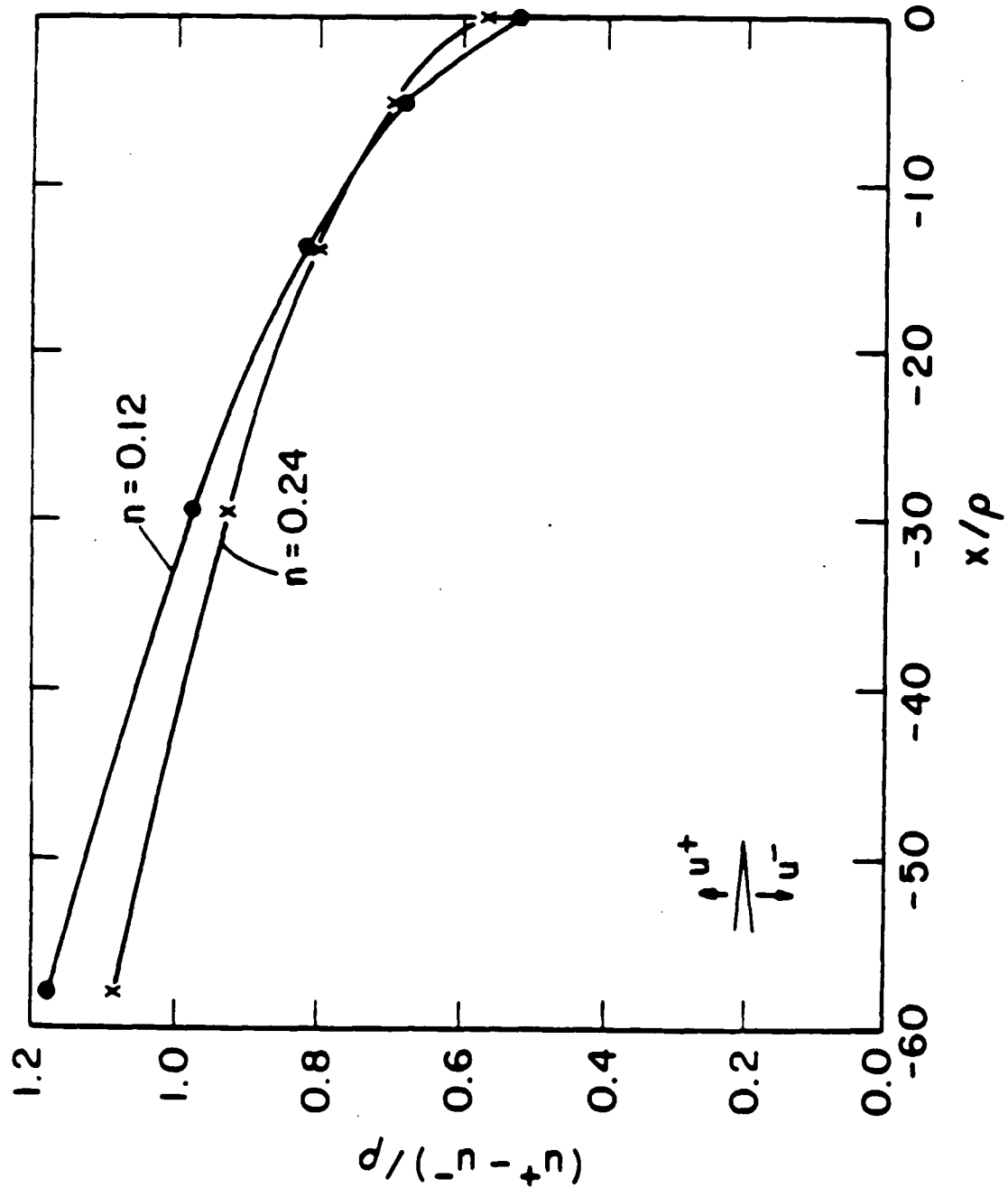


Figure 5 Displacement of the upper crack flank relative to the lower flank

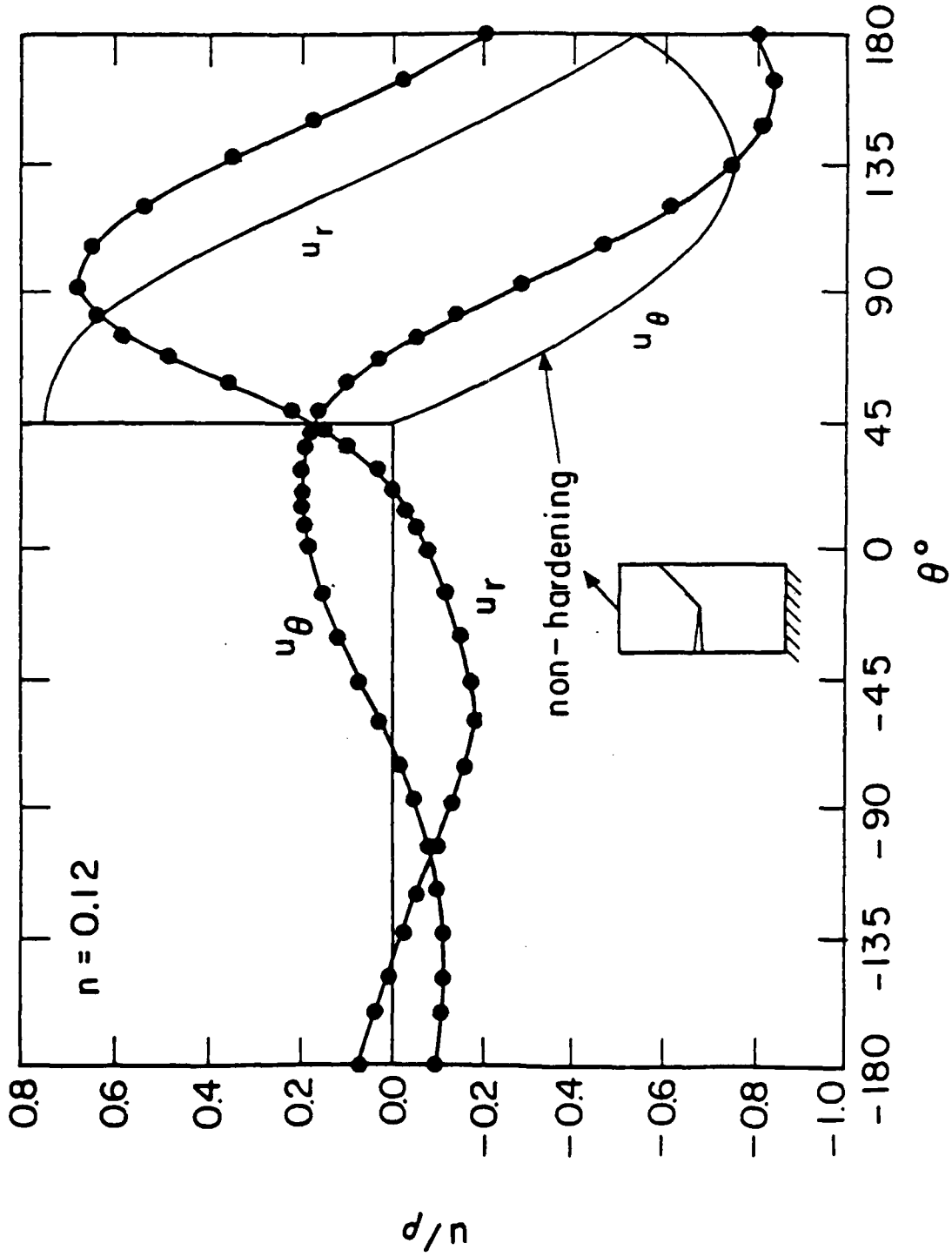


Figure 6b Angular variation of the near tip displacement field (at $r=5\%$ of the ligament) for $n=0.12$.

CHAPTER SIX

ON THE FULLY PLASTIC FLOW PAST A GROWING ASYMMETRIC
CRACK AND ITS RELATION TO MACHINING MECHANICS

TABLE OF SYMBOLS

H	hardening coefficient (eq. 9)
k	eq. 22
ψ	stream function
σ	mean normal stress
$\dot{u}_r, \dot{u}_\theta$	displacement rates
$\dot{\epsilon}_r, \dot{\epsilon}_\theta, \dot{\gamma}_{r,\theta}$	strain rates
$s_r, s_\theta, s_{r,\theta}$	stress deviators
$\bar{\epsilon}$	equivalent strain
$\bar{\sigma}$	equivalent stress
V_l	rigid body velocity at lower flank
V_u	rigid body velocity at upper flank
θ_l	lower boundary of deforming region (Fig. 2a)
θ_u	upper boundary of deforming region (Fig. 2a)
ω	crack opening angle
γ_u	strain at upper boundar
θ_s	"slip angle" (eq. 49)

ABSTRACT

A tensile logarithmic singularity in the mean normal stress is found for steady flow of rigid-plastic, linearly strain-hardening material, with rigid material flowing past straight flanks. For cracks, this indicates that the flanks of the crack tend to deform. For the machining case it explains the tendency for precracking ahead of the tool which contributes to a built-up edge, or the formation of a discontinuous chip. Finally, an approximate analysis of the quasi-steady integral of the stationary crack solution shows a tendency of the crack flanks to form a cusp. The strains for a cusp field would be dominated by the elastic-plastic field which shows instead a

vertical tangent at the crack tip.

INTRODUCTION

Fully plastic flow before fracture is desirable even in structures containing cracks. Such ductility is reduced if plastic flow is limited to one shear band, for example, by a weld (Fig. 1). In such asymmetric mixed mode I and II configurations, the crack accelerates as it advances into pre-strained and damaged material. Further evidence for a lowered ductility in asymmetric cracking is the tendency to form a shear lip at the end of a cup and cone fracture in a tensile test. Non-hardening plasticity gives a shear band of infinitesimal thickness. Strain hardening, however, causes the deformation field to fan out, leaving a finite strain except possibly at the crack tip.

In orthogonal machining the geometry is similar, with the cutting tool progressing steadily below the plastic zone. Here, again due to strain hardening, Christopherson et al. [2] found that the plastic zone fans out over 10^0 - 30^0 , as opposed to the single plane required by the perfectly plastic solid.

STRESS SINGULARITY WITH RIGID FLANKS

Postulate a steady flow past a crack in rigid-plastic, linearly strain hardening material. The mechanics of the problem should determine whether or not the crack tip has a finite angle. Start by assuming a crack of finite angle ω and rigid body velocity of the material flowing along the flanks. To satisfy incompressibility assume a stream function ψ in polar coordinates r and θ . Seek the form of the stream function in the immediate vicinity of the crack tip where the velocities should be

nonzero and finite. In a separable expansion of ψ in the dominant term as $r \rightarrow 0$, $r^s F(\theta)$, the exponent s must be unity since the velocities at the tip are nonzero and finite. Thus,

$$\psi = r F(\theta). \quad (1)$$

The corresponding velocities are

$$\dot{u}_r = -\frac{1}{r} \frac{\partial \psi}{\partial \theta} = F'(\theta), \quad (2)$$

$$\dot{u}_\theta = -\frac{\partial \psi}{\partial r} = -F(\theta). \quad (3)$$

The strain rates are

$$\dot{\epsilon}_r = \frac{\partial \dot{u}_r}{\partial r} = 0 = -\dot{\epsilon}_\theta, \quad (4)$$

$$\dot{\gamma}_{r\theta} = \frac{\partial \dot{u}_\theta}{\partial r} + \frac{1}{r} \frac{\partial \dot{u}_r}{\partial \theta} - \frac{\dot{u}_\theta}{r} = \frac{F''(\theta) + F(\theta)}{r}. \quad (5)$$

Thus the only component of strain is shear. The equivalent strain rate is

$$\bar{\epsilon} = \sqrt{\frac{2}{3} \left[\dot{\epsilon}_r^2 + \dot{\epsilon}_\theta^2 + 2 \left(\frac{\dot{\gamma}_{r\theta}}{2} \right)^2 \right]} = \frac{F''(\theta) + F(\theta)}{\sqrt{3} r}. \quad (6)$$

The stress deviators s_{ij} are found from the stress-strain relations and the equivalent stress $\bar{\sigma}$:

$$\dot{\epsilon}_{ij} = \frac{3}{2} \frac{s_{ij}}{\bar{\sigma}} \bar{\epsilon}. \quad (7)$$

Since $\dot{\epsilon}_r = \dot{\epsilon}_\theta = 0$, from (4),

$$s_r = s_\theta = 0 \text{ and } s_{r\theta} = \bar{\sigma} / \sqrt{3}. \quad (8)$$

Assume the material is rigid-plastic, linearly strain hardening:

$$\bar{\sigma} = Y + H \bar{\epsilon}. \quad (9)$$

The accumulated equivalent strain $\bar{\epsilon}$ is calculated by integration along a streamline, where the time increment is expressed in terms of that required for an element to traverse an increment of angle:

$$\bar{\epsilon} = \int_{-\infty}^t \bar{\epsilon} dt = \int_{\dot{u}_\theta}^{\bar{\epsilon}} r d\theta = - \int_0^\theta \frac{F'' + F}{\sqrt{3} F} d\theta. \quad (10)$$

Thus the equivalent strain is independent of radius. The same holds for the equivalent stress σ , by (9), and also for the shear stress, by (8),

$$s_{r\theta} = s_{r\theta}(\theta). \quad (11)$$

Now turn to the equilibrium equations. In terms of the mean normal stress σ ,

$$\frac{\partial \sigma}{\partial r} + \frac{\partial s_r}{\partial r} + \frac{1}{r} \frac{\partial s_{r\theta}}{\partial \theta} + \frac{s_r - s_\theta}{r} = 0. \quad (12)$$

$$\frac{\partial s_{r\theta}}{\partial r} + \frac{1}{r} \frac{\partial \sigma}{\partial \theta} + \frac{1}{r} \frac{\partial s_\theta}{\partial \theta} + \frac{2s_{r\theta}}{r} = 0. \quad (13)$$

Introducing (8) to eliminate s_r , s_θ , (11) to eliminate $\partial s_{r\theta}/\partial r$, and cross-differentiation to eliminate σ leads to:

$$d^2 s_{r\theta}/d\theta^2 = 0, \text{ from which } ds_{r\theta}/d\theta = \text{const.} = s_{r\theta,\theta}. \quad (14)$$

Now, (12) simplifies with (8), and can be integrated

$$\frac{\partial \sigma}{\partial r} + \frac{1}{r} \frac{ds_{r\theta}}{d\theta} = 0, \quad \sigma = -s_{r\theta,\theta} \ln(r/R) + C(\theta). \quad (15)$$

To find $C(\theta)$, differentiate (13) with respect to θ , and again note $\partial s_{r\theta}/\partial r = 0$ from (11) and $s_\theta = 0$ from (8). Equating the result to the second partial of (15) gives

$$\frac{\partial^2 \sigma}{\partial \theta^2} = -2 \frac{ds_{r\theta}}{d\theta} = \frac{d^2 C(\theta)}{d\theta^2}; \quad C(\theta) = -s_{r\theta,\theta} \theta^2 + C_1 \theta + C_2. \quad (16)$$

Define $\sigma(R,0)$ as the mean normal stress at $\theta=0$ and a convenient radius

R. Equation (15) then becomes:

$$\sigma(r, \theta) - \sigma(R, 0) = -s_{r\theta, \theta}(\ln(r/R) + \theta^2) + C_1 \theta. \quad (17)$$

Thus, the assumption of rigid flanks subtending a finite angle would require that the mean normal stress at the crack tip ($r \rightarrow 0$) have a logarithmic singularity. Let us now complete the study of the field specified by the stream function (1) by applying the boundary conditions and deriving the streamlines.

Two possible flow fields are consistent with the constant rate of shear stress from (14) and the hardening of the material (increase in equivalent stress σ from (8) as it flows along the streamline). The first field, shown in Fig. 2a, is for $s_{r\theta, \theta} > 0$. From (17) this model gives a tensile logarithmic singularity in the mean normal stress as $r \rightarrow 0$, and thus the field will be called "tensile". The second field, shown in Fig. 2b, is for $s_{r\theta, \theta} < 0$. Here the singularity in the mean normal stress is compressive and, accordingly, this field will be called "compressive". A compressive singularity, however, would require strains of order unity or more for fracture. Since such large strains are not actually observed [1], the "compressive" field is not plausible for the growing crack.

Two other conceivable fields can be excluded. A single band being split by the crack (Fig. 2c) would have shear stresses of the same sign, but increasing in magnitude both above and below the line of advance due to increasing strains along a streamline. This change in sign of $s_{r\theta, \theta}$ would give tensile and compressive singularities adjacent to each other, and a discontinuity in normal stress. If the shear in a band being split by the crack were to change sign, on the other hand, there would be an intermediate region below yield, and the band would separate into two, corresponding to those of Figs. 2a,b. In the limit, the Mode I field would be approached.

Thus only the "tensile" field of Fig. 2a remains. From (8) and (9) for positive shearing,

$$\frac{ds_{r\theta}}{d\theta} = \frac{1}{\sqrt{3}} \frac{d\bar{\sigma}}{d\theta} = \frac{1}{\sqrt{3}} H \frac{d\bar{\epsilon}}{d\theta}. \quad (18)$$

(18) and (14) give, with $s_{r\theta,\theta} = \text{const.}$,

$$\frac{d\bar{\epsilon}}{d\theta} = \frac{s_{r\theta,\theta}\sqrt{3}}{H} = \frac{1}{\sqrt{3}} \frac{d\gamma_{r\theta}}{d\theta}. \quad (19)$$

Differentiating (10) gives:

$$\frac{d\bar{\epsilon}}{d\theta} = -\frac{F'' + F}{\sqrt{3} F}. \quad (20)$$

Introducing (19) into (20) gives finally

$$F'' + k^2 F = 0, \quad (21)$$

where

$$k^2 = 1 + \frac{3 s_{r\theta,\theta}}{H} = 1 + \frac{d\gamma_{r\theta}}{d\theta}. \quad (22)$$

The solution of (21) is

$$F(\theta) = A \cos k\theta + B \sin k\theta. \quad (23)$$

Referring to Fig. 2a we denote by V_p , V_u the (rigid body) velocities at the lower and upper boundaries of the deforming region, which are at angles θ_l and θ_u respectively.

Then the boundary conditions are:

at the lower boundary,

$$\dot{u}_r = -V_p \cos \theta_l, \quad \text{and by (2), } F'(\theta_l) = -V_p \cos \theta_l, \quad (24)$$

$$\dot{u}_\theta = V_p \sin \theta_l, \quad \text{and by (3), } F(\theta_l) = -V_p \sin \theta_l; \quad (25)$$

similarly, at the upper boundary,

$$F'(\theta_u) = -V_u \cos(\theta_u + \omega), \quad (26)$$

$$F(\theta_u) = -V_u \sin(\theta_u + \omega). \quad (27)$$

Solving (23)- (27) for ω in terms of θ_p, θ_u gives

$$\omega = \tan^{-1} \left[\frac{P - \tan k \theta_l}{k(1 + P \tan \theta_l)} \right] - \theta_u, \quad (28)$$

where

$$P = \frac{k \tan \theta_l + \tan k \theta_u}{1 - k \tan \theta_l \tan k \theta_u}. \quad (29)$$

Substituting back into the boundary conditions gives

$$\frac{V_u}{V_l} = \frac{k \sin \theta_l \cos k \theta_u + \cos \theta_l \sin k \theta_u}{k \sin(\theta_u + \omega) \cos k \theta_l + \cos(\theta_u + \omega) \sin k \theta_l}, \quad (30)$$

$$\frac{A}{V_l} = \frac{(V_u/V_l) \sin(\theta_u + \omega) \sin k \theta_l - \sin k \theta_u \sin \theta_l}{\sin k(\theta_u - \theta_l)}, \quad (31)$$

$$\frac{B}{V_l} = \frac{\sin \theta_l \cos k \theta_u - (V_u/V_l) \sin(\theta_u + \omega) \cos k \theta_l}{\sin k(\theta_u - \theta_l)}. \quad (32)$$

Assume now a critical strain γ_u at the upper boundary. Then

$$d\gamma_{r,\theta}/d\theta = \gamma_u/(\theta_u - \theta_l), \quad (33)$$

and

$$k^2 = 1 + \frac{\gamma_u}{\theta_u - \theta_l}. \quad (34)$$

The streamlines for a particular example, and the equation for the rotation of elements are given in the Appendix.

According to Hill [7], the infinite mean normal stress by (17) cannot be sustained at the rigid flank and this will lead to plastic yielding. For further insight, turn to the approximate superposition of singularities for stationary cracks.

SUPERPOSITION OF STATIONARY SINGULARITIES

Shih [3] solved the mixed Mode I and II singular fields for the stationary crack field, extending the Mode I field of Hutchinson [4], Rice and Rosengren [5] (HRR). In terms of a stress-strain law of the form $\sigma = \sigma_1 \epsilon^n$, for a far field defined by the path independent integral J with Mode I mixity parameter M^P and the scalar function $I_{1/n}(M^P)$, the displacement and strain components at r, θ for the fully plastic parameters of interest here are (see e.g. McClintock [5]):

$$u_i(r, \theta) = r \left[\frac{J}{\sigma_1 I_{1/n}(M^P) r} \right]^{1/(n+1)} u_i(\theta, 1/n, M^P), \quad (35)$$

$$\epsilon_{ij}(r, \theta) = \left[\frac{J}{\sigma_1 I_{1/n}(M^P) r} \right]^{1/(n+1)} \epsilon_{ij}(\theta, 1/n, M^P). \quad (36)$$

Superposition does not strictly apply to (35) for two reasons: it does not take the convection of hardened material into account and it is a non-linear relation between displacement and J . Qualitative insights may be obtained, however, by assuming, following (35), that the displacement increments vary with radius according to

$$\dot{u}_i \propto r^{n/(n+1)}, \quad (37)$$

and that, correspondingly, the strain rates vary as

$$\dot{\epsilon}_{ij} \propto r^{-1/(n+1)}. \quad (38)$$

For the non-hardening material, $n=0$, (37) correctly indicates displacement rates

independent of radius, which for a growing crack, integrates to displacements increasing linearly away from the tip. For a power law material the displacement rate increases as a fractional root of the distance away from the tip, and its integral gives displacements of the order

$$u_{\theta} = \int \dot{u}_{\theta} dr \propto r^{1+n/(n+1)}, \quad (39)$$

which indicates a cusp.

Correspondingly, integration of the strain rates from (38) with respect to the distance as the material sweeps by the tip of the crack gives strains varying as

$$\epsilon \propto r^{n/(n+1)}. \quad (40)$$

Thus, due to convection, the strains increase continuously behind the crack tip, whereas the stationary Shih solution gave strains that decrease. That is, at any instant during the integration, the material behind the crack is actually harder than assumed for the displacement and strain rates of (37) and (38). Therefore, the above superposition exaggerates any cusp. Furthermore, the nonhardening solution with flank yielding, for bending and tensile doubly grooved specimens gives linear displacement increments which, when integrated, would show an increasing crack opening angle near the crack tip [6]. For example, the normal component of the displacement field at the flank for the doubly grooved specimens and the resulting from integration flank shape is shown in Fig. 3.

For further insight, the relative dominance of the field for a cusp will be considered. Rigid-plastic flow past a cusp-like crack would not exhibit singularities in the strain but, instead, in higher order terms like strain rates, as follows. For no crack tip opening angle, the displacement rates are of the form:

$$\dot{u}_i = O(r^m) + \text{rigid body motion} . \quad (41)$$

The stream function can thus be regarded as being a superposition of steady state rigid body translation of the material past the crack tip and a strain rate singularity:

$$\psi = r^{m+1}F(\theta) - \dot{c}r\sin\theta . \quad (42)$$

Then the velocities are:

$$\dot{u}_r = -\frac{1}{r} \frac{\partial \psi}{\partial r} = r^m F'(\theta) - \dot{c} \cos\theta , \quad (43)$$

$$\dot{u}_\theta = -\frac{\partial \psi}{\partial r} = -(m+1)r^m F(\theta) + \dot{c} \sin\theta . \quad (44)$$

Differentiating the displacement rates would give strain rates, and hence the equivalent strain rate, of the order $O(r^{m-1})$. The accumulated equivalent strain is found by integrating along a streamline, with the time interval to traverse a given angular increment along a streamline expressed in terms of the tangential velocity:

$$\bar{\epsilon} = \int_{\theta}^{\theta} \frac{\bar{\epsilon}}{\dot{u}_\theta} r d\theta . \quad (45)$$

For small r , \dot{u}_θ is of order r^0 from (44) while $\bar{\epsilon}$ is of order r^{m-1} and so the integrand in (45) is of order r^m . Thus

$$\bar{\epsilon}_{,\theta} = O(r^m) , \quad (46)$$

and vanishes for small r (unless $m=0$, which turns out to be the nonhardening case) and the strains are nonsingular. Notice that no stress-strain relationship has been used yet, which means that for any rigid-plastic law the strains are nonsingular for a zero crack opening angle. This field would thus be dominated by any field that exhibits any nonzero crack opening angle. For example the elastic-perfectly plastic field shows logarithmic singularities in the strains but $d\delta/dr$ is unbounded as $r \rightarrow 0$,

giving a vertical tangent at the crack tip [10]. The strains for that field are of the order:

$$\gamma^p = O[\ln(R/r)] + O(r^0) .$$

which goes to infinity for $r \rightarrow 0$, thus dominates the local strain. The large-scale view of a fracture, however, may look like a cusp and since the strains for the cusp field are $O(r^m)$, increasing with r , they may become larger at a sufficiently distant point.

The tendency shown above for flank yielding with any finite opening angle leads to the need for an exact solution of the growing crack, where its shape is unknown and the flank, a part of the deforming boundary, is traction-free. Finally, connecting the steady-state continuum mechanics solution to the micromechanics of hole growth would require a transition to non-steady analysis.

DISCUSSION

In machining, a shear band with an undetermined rigid-plastic boundary breaks through to a free surface. The problem is similar to mixed mode crack growth, except that the deformation is larger. Christopherson et al [2] tried to assess the effect of work hardening in the mechanics of orthogonal machining. By modifying the slip line equations and estimating roughly the magnitude of the added term, they pointed out that, due to hardening, the hydrostatic stress changes from compressive at the free surface to tensile near the tool point. What they found was essentially the qualitative effect of the logarithmic singularity derived above for fully plastic flow. In fact, we can also deduce that, for a certain change in the flow strength between the chip and the parent material, if the deforming region is narrower, the angular change of the shear stress (i.e. $s_{r\theta,\theta}$ in (14)) is bigger and, consequently, the

singularity stronger, in accordance with their observation that the work-hardening effect becomes more pronounced as the plastic zone gets narrower.

It is worth considering now the region of dominance of the logarithmic singularity in mean normal stress that would characterize the flow past rigid flanks. Using typical data $d\bar{\sigma}/d\bar{\epsilon} = H \approx Y$ for 1020 steel and $d\bar{\epsilon}/d\theta \approx 0.8$, gives from (8)

$$s_{r,\theta} = \sqrt{3} \frac{d\bar{\sigma}}{d\bar{\epsilon}} \frac{d\bar{\epsilon}}{d\theta} = \sqrt{3} H \frac{d\bar{\epsilon}}{d\theta} \approx 1.38 Y. \quad (47)$$

From the fully plastic flow field of Prandtl for tension of grooved plane strain specimens (see e.g. McClintock [8]) $\sigma \approx 2.8Y$ and assuming that R is the radius at which $\sigma(r,0)$ changes sign, gives from (17), $r/R \approx 0.1$. The distance R is within the macroscopic scale as is evident from the approximate study for machining field done by Christopherson et al. [9]. According to their slip line theory modified to include hardening the change in the mean normal stress $\Delta\sigma$ from the free surface to a point in the band is roughly estimated in terms of the flow strengths in work-piece and chip, Y_w and Y_c , the distance s from the free surface, and the local width t of the slipband:

$$\Delta\sigma \approx (Y_c - Y_w) s/t\sqrt{3}. \quad (48)$$

In machining mild steel, Y_c may be 40% more than Y_w , so $Y_c - Y_w \approx 0.4k$. Since at the free surface $\sigma \approx -Y/\sqrt{3}$, the mean normal stress becomes positive at about $s/t=3$, which for 10° angular width happens at a radius R approximately 1/3 the total shear band length. Thus the singularity in the mean normal stress dominates in a significant region.

Now that tension has been shown to exist near the tool point, it is possible that brittle (or ductile) fracture may occur at a particular history of stress and this

could give rise to the characteristic fracture running ahead of the tool point and the formation of a built-up edge or a discontinuous chip [9]. In particular, according to the "tensile" field, the maximum strain occurs at the boundary with the chip (upper boundary of the shear band), where cracking could occur. It should be noted, however, that nonsteady effects have not been considered.

CONCLUSIONS

A logarithmic tensile singularity in the mean normal stress has been found for rigid-plastic flow past a growing crack of finite angle with rigid flanks under combined shear and tension. Applied to the machining problem, this result helps to explain the formation of a discontinuous chip or the precracking ahead of the tool.

The tensile singularity predicts yielding of the crack flanks. Approximate solutions for flank yielding give contradictory indications. A tendency to form a cusp has been found from an order-of-magnitude analysis on the quasi-steady integral of the extended near tip HRR singular field. That result indicates decreasing strain behind the crack tip and hence overestimates any cusp. From non-hardening solutions with flank yielding for bending and tension of doubly grooved specimens there is an increasing crack opening angle near the tip. Furthermore, the strains for any cusp would be dominated by the elastic-plastic singularity which gives a blunt tip. Thus there is a need for an exact solution of a crack growing with deforming flanks into strain-hardening material.

REFERENCES

1. McCLINTOCK F.A. and SLOCUM A.H., "Predicting Fully Plastic Mode II Crack Growth from an Asymmetric Defect", *Int.J.Fract.*, 27,

- 49-62 (1985).
2. CHRISTOPHERSON D.G., OXLEY P.L. and PALMER W.S., "Orthogonal Cutting of a Work-hardening Material", *Engineering*, 16, 113-116 (1958).
 3. SHIH C.F., "Small Scale Yielding Analysis of Mixed Mode Plane Strain Crack Problems", *ASTM STP 560*, pp. 187-210 (1974).
 4. HUTCHINSON J.W., "Singular behaviour at the end of a Tensile Crack in a hardening Material", *J. Mech. Phys. Sol.*, 16, 13-31 (1968).
 5. RICE J.R. and ROSENGREN G.F. "Plane Strain Deformation near a Crack Tip in a Power-law hardening Material", *J. Mech. Phys. Sol.*, 16, 1-12 (1968).
 6. McCLINTOCK F.A., "Plasticity Aspects of Fracture", in "*Fracture*" (edited by H. Liebowitz), Vol. 3, pp. 47-225, Academic Press, New York (1971).
 7. HILL R. "On the Limits set by Plastic Yielding to the Intensities of Singularities in Stress", *J. Mech. Phys. Sol.*, 2, 278-285 (1954).
 8. McCLINTOCK F.A., "Local Criteria for Ductile Fracture", *Int. J. Fract. Mech.*, 4, 101-129 (1968).
 9. BANNERJEE J. and PALMER W.B., "Metal Cutting with a Discontinuous Chip", *Proc. 6th M.T.D.R. Conf.*, 405-415, Pergamon Press (1965).
 10. RICE J.R. "Elastic-Plastic Crack Growth" in *Mechanics of Solids*, Pergamon Press, Oxford, pp.539-562 (1982).

APPENDIX

Taking an example from machining (Fig. 4) for $\gamma_u = 1.3$, $\theta_l = 40^\circ$, $\theta_u = 50^\circ$ we find by using equations (28) - (34):

$$\omega = 59^\circ, V_u/V_l = 0.73, d\gamma_{r\theta}/d\theta = 7.44$$

and, for θ in radians,

$$F(\theta)/V_l = 0.59 \cos(2.9\theta) - 0.459 \sin(2.9\theta) .$$

A streamline, resulting from (1) for this particular example, has been sketched in Fig.

4. The velocity triangle shown in Fig. 2a defines a "slip" angle θ_s :

$$\theta_s = \sin^{-1} \left[\frac{(V_u/V_l)\sin\omega}{[(V_u/V_l)^2 + 1 - 2(V_u/V_l)\cos\omega]^{1/2}} \right] . \quad (49)$$

For this particular example $\theta_s = 45.06^\circ$.

A second example of a growing crack with $\gamma_u = 0.25$, $\theta_l = 30^\circ$, $\theta_u = 40^\circ$, gives

$$\omega = 5^\circ, \theta_s = 35.2^\circ, V_u/V_l = 0.88, d\gamma_{r\theta}/d\theta = 1.43$$

and

$$F(\theta)/V_l = 0.0623 \cos(1.55\theta) - 0.744 \sin(1.55\theta) .$$

Finally, the rotation of the material element relative to that of the stress field is important in hole growth and thus is worth considering. The rotation of the element is

$$\phi_m = \frac{1}{2} \left(\frac{\partial \dot{u}_\theta}{\partial r} + \frac{\dot{u}_\theta}{r} - \frac{1}{r} \frac{\partial \dot{u}_r}{\partial \theta} \right) . \quad (50)$$

and from (2) and (3)

$$\phi_m = -\frac{1}{2r} (F + F'') . \quad (51)$$

while that of the stress field is

$$\phi_r = \frac{\dot{u}_\theta}{r} = -\frac{F}{r} . \quad (52)$$

giving a relative rotation

$$\phi_{rel} = \frac{1}{2r} (F - F'') . \quad (53)$$

For $F(\theta)$ given by (23) and since $k > 1$ by (22), it is found that rotation and shear

strain (given by (5)) are of different sign. The effect is to open up the holes and thus to increase the damage.

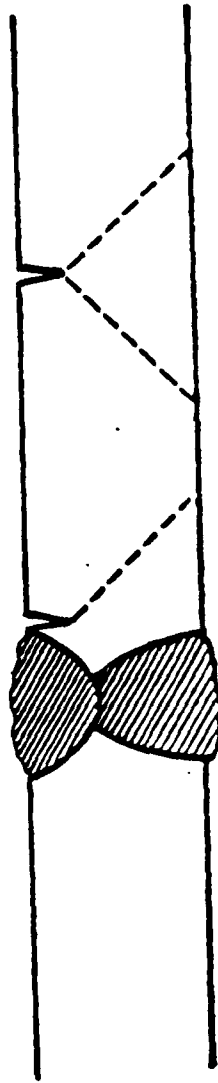


Fig. 1. Symmetric and asymmetric shear from cracks in a plate.

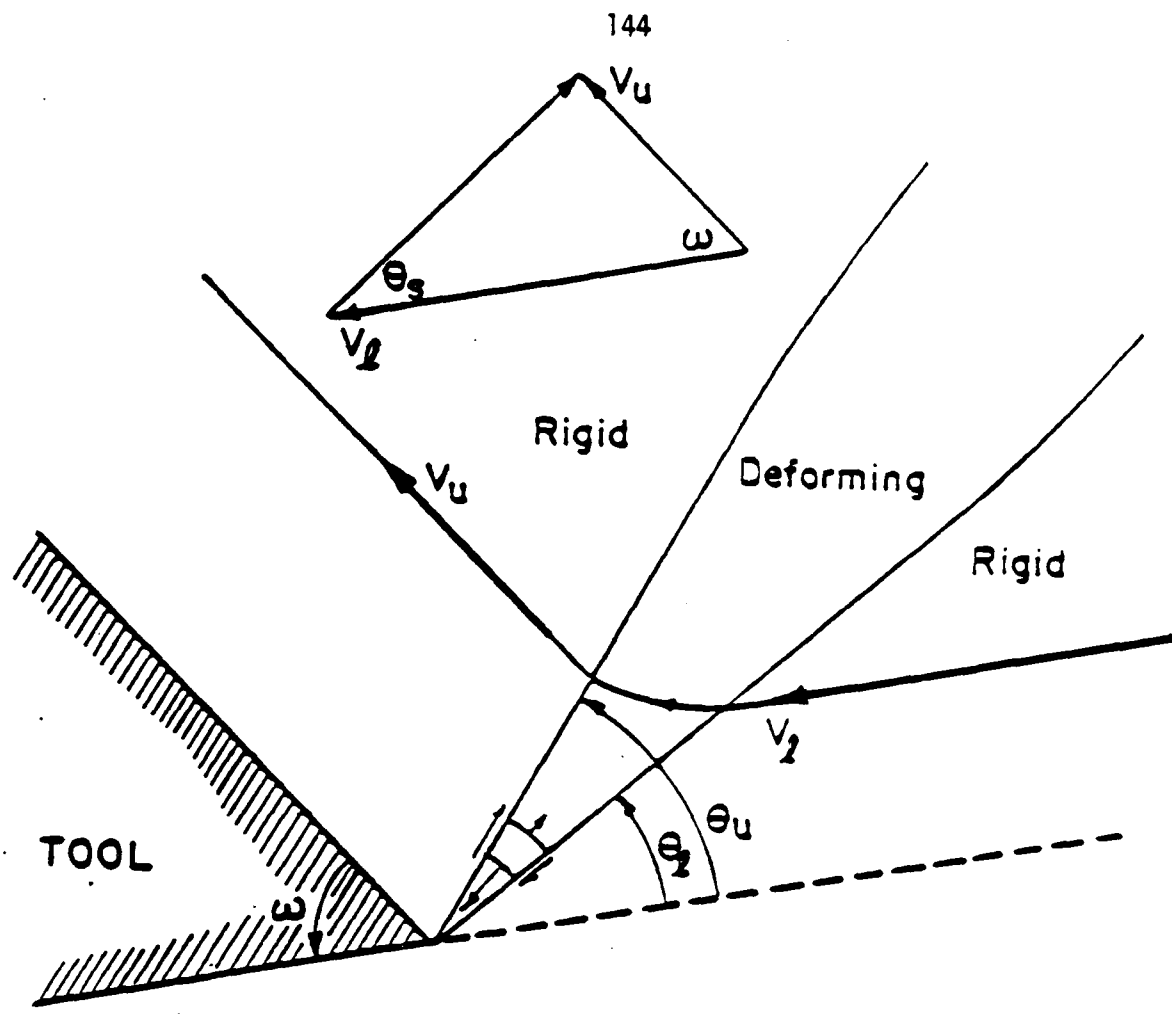


Fig. 2a. The flow field for tension in the band. The machining case is illustrated; otherwise ω is the crack opening angle.

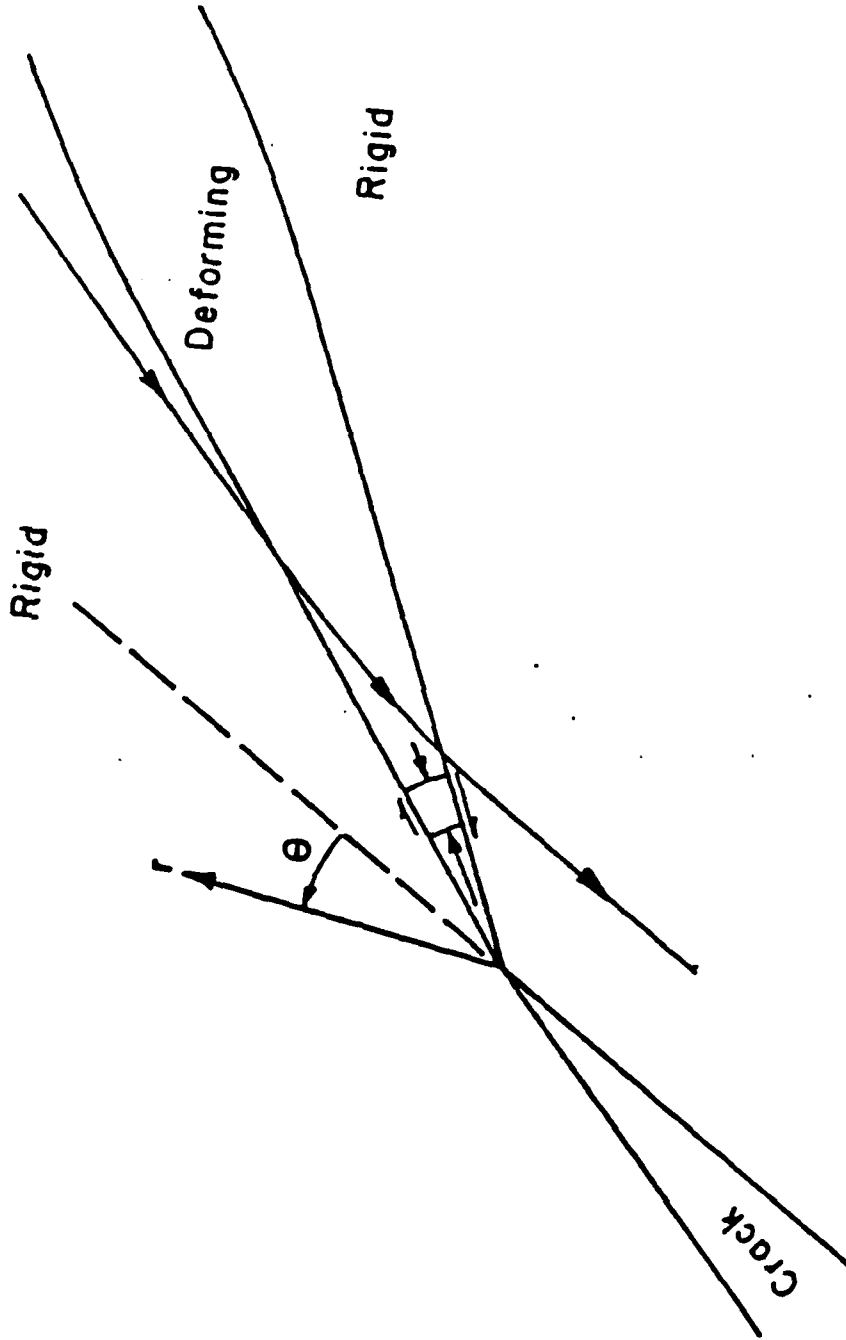


Fig.2b The field for compression in the band.

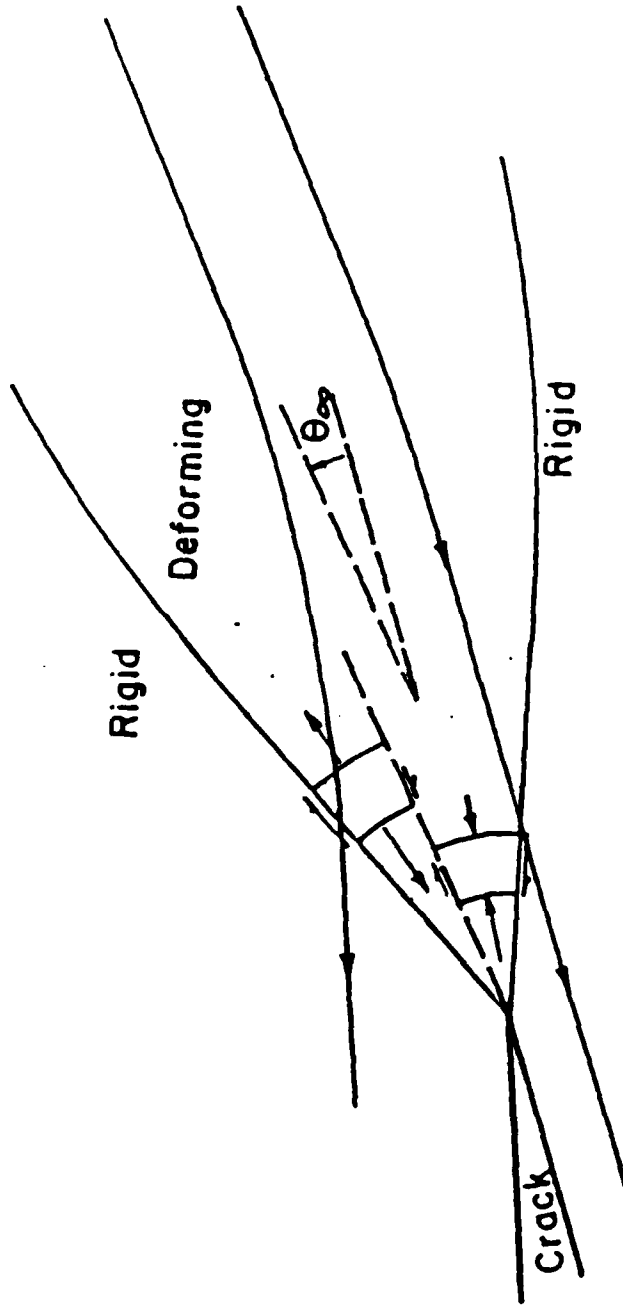


Fig.2c Field with discontinuity in stress
across $\theta = \theta_{\infty}$.

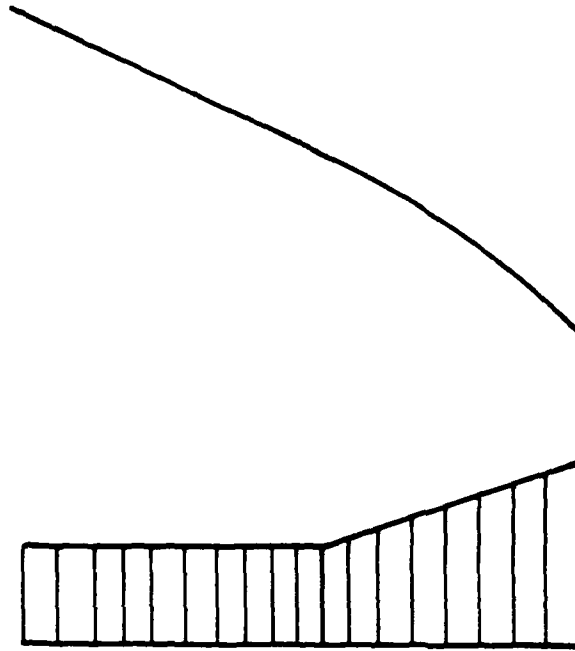


Fig. 3. Flank normal displacement increments and integrated flank shape for the doubly grooved specimen.

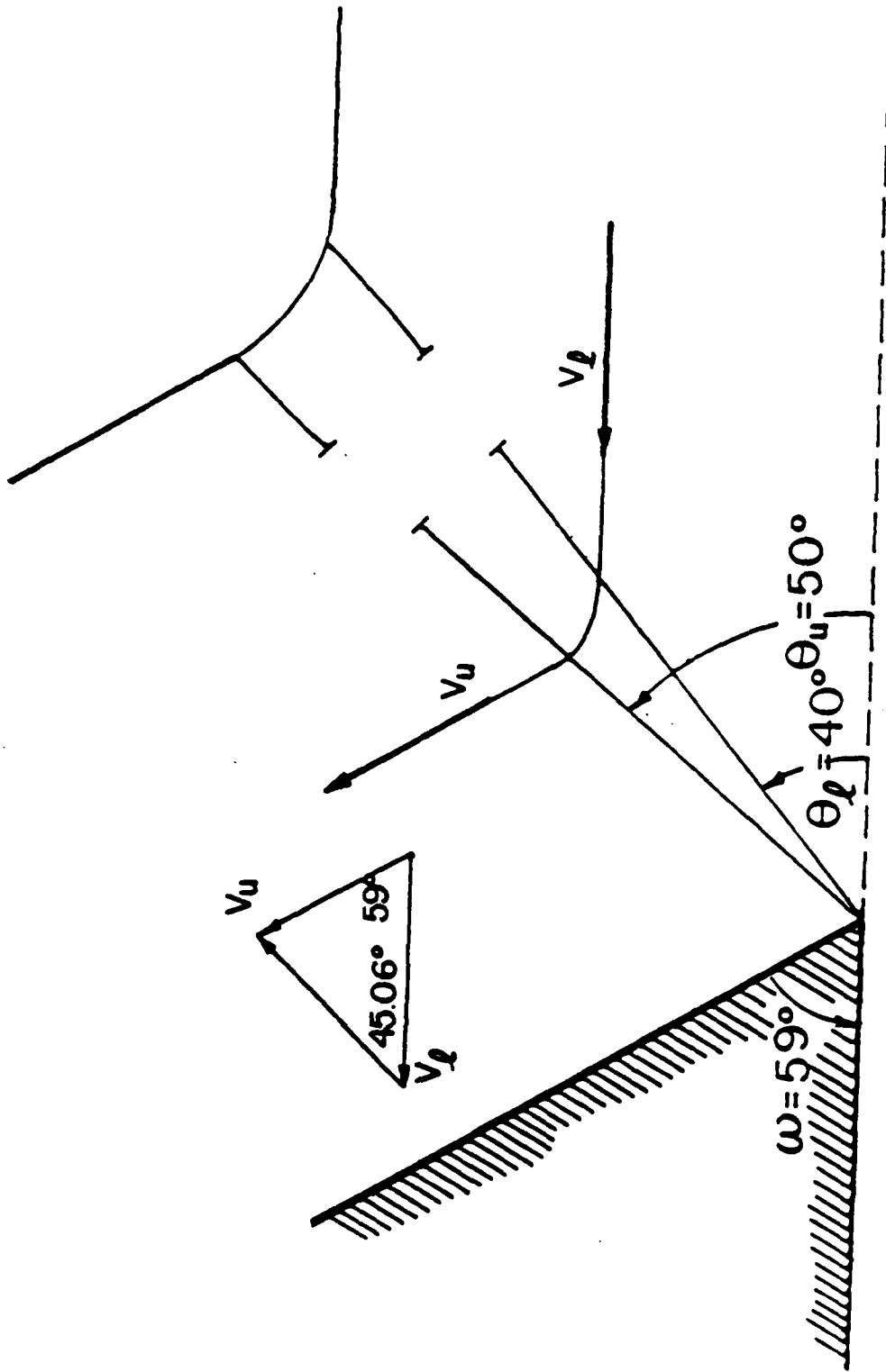


Fig. 4. A typical streamline predicted by the stream function (1) for the singular region in machining.

CHAPTER SEVEN

THE ASYMMETRIC (MIXED MODE I AND II)
FULLY PLASTIC FRACTURE - OVERVIEW

TABLE OF SYMBOLS

COA	crack opening angle
D_g	crack ductility (eq. 1)
$D_{AC,u}$	apparent crack ductility (upper flank)
$D_{AC,l}$	apparent crack ductility (lower flank)
E	modulus of elasticity
f	amount of fracture in shear band model
J	J-integral
k	shear yield
l_0	initial ligament
l_l	projected lower flank length
l_u	projected upper flank length
M^p	mixity parameter (eq. 4)
n	strain hardening exponent
P	load
s_l	amount of slip along lower plane in shear band model
s_u	amount of slip along upper plane in shear band model
T.S.	tensile strength
T	tearing modulus
T^*	eq. 2
T^{*ASY}	eq. 2
T^{*ISY}	
u_i	idealized initiation displacement
u_i	initiation displacement
u_i	growth displacement
\vec{v}_g	total displacement vector
\vec{v}_g	growth displacement vector
ρ	mean inclusion spacing
ϕ	angle of total displacement vector from transverse
γ_c	fracture strain
θ_c	crack direction from transverse.
θ_f	fracture plane
θ_{su}, θ_{sl}	upper and lower slip plane
χ	fracture parameter ($=f/s_u$)
ξ	shearing parameter ($=s_l/s_u$)
θ_u, θ_l	upper and lower flank angle from transverse

β_u upper back angle

SUMMARY

In symmetric singly grooved tensile specimens the crack advances into the relatively undamaged region between two plastic shear zones. A crack near a weld or shoulder, loaded into the plastic range, may have only a single shear band, along which the crack grows into prestrained and damaged material with less ductility than the symmetrical unconstrained configurations. In this chapter, work that deals with the effect of asymmetry in crack propagation of unconstrained fully plastic singly grooved tensile specimens is summarized. A crack growth ductility is defined as the minimum displacement per unit crack growth. Tests of six alloys showed that, for the low-hardening alloys, the crack ductility in the asymmetric case is less than a third that of the symmetric. In the higher hardening alloys the crack ductility in the asymmetric case is smaller by a factor of 1.2 at most. A noteworthy result is the presence of a Mode I opening component even with asymmetry, as is shown by the far field displacement vector being more than 45° from the transverse direction. The crack direction is less than 45° , indicating the effect of triaxiality on cracking. A macro-mechanical model for crack advance by combined fracture and sliding off along two slip planes gives the independent physical parameters (cracking and two shear directions, relative amounts of cracking and shearing) in terms of the observable quantities of the macroscopic fracture (flank angles, flank lengths, back angle) for both the symmetric and asymmetric specimens. A finite element study of the asymmetric specimens gave a crack direction within two degrees and a far field displacement vector at initiation within three degrees of that experimentally found. Stress and strain fields indicate the presence of a Mode I component. Early growth, studied by successive removal of the most damaged element, resulted in crack

growth rate for the lower hardening case about twice that of the higher hardening one.

INTRODUCTION

In symmetric singly grooved tensile specimens the crack advances into the relatively undamaged region between two symmetric shear zones. In the fully plastic case these zones narrow into bands that traverse the section. An asymmetry, introduced through a weld fillet or a harder, heat-affected zone or a shoulder on one side of the crack (Fig. 1) suppresses one of the two shear bands that would appear in a symmetrical specimen. In that case the crack advances asymmetrically, along the remaining active slip band into previously damaged material. Thus one might expect that the ductility would be less than that of pure Mode I unconstrained symmetric case.

Near the tip of the growing crack, strain hardening will cause the deformation field to fan out. For power law creep or deformation theory plasticity and a stationary crack, the asymptotic stress and strain distribution may be found from the extended by Shih's [1] HRR [2,3] fields for the general mixed mode case. Notice, however, that such a superposition of stationary singularities does not take into account the hardening of the material left behind the growing crack. Indeed, the stress and strain fields near the tips of growing cracks in ductile materials are known to differ from the stress and strain state around stationary cracks in the same materials as is shown from asymptotic solutions [4,5,6,7], supplemented through finite element calculations [8,9]. Thus, more accurately, a solution for the distribution of strain increments of a growing mixed mode crack should be used; however such a solution is not yet available.

A test with pure shear (Mode II) loading was carried out by Chant et al. [10] of high hardening carbon manganese steel (B.S. 1501-151-430A, Y.S.=329 MN/m², T.S.= 490 MN/m²). Small specimens were subjected to both Mode II and Mode I testing but the ductility, measured by dJ/da , was practically the same although the microscopic features for the pure shear specimens are different than those observed in the Mode I specimens.

Representing ductile crack propagation has been in general based on the introduction of $d(COD)/da$ [11,12,13] and the tearing modulus T or dJ/da [14,15] concepts. Such single-parameter measures are incomplete since the triaxiality and the local distribution of strain are affected by the geometry and mode of loading. The triaxiality and strain distribution in turn strongly affect the cleavage and hole growth mechanisms of crack growth.

The objective of the current chapter is to summarize the important findings of the experimental, analytical, and numerical work that deals with the effect of an asymmetry in crack propagation of unconstrained fully plastic singly grooved tensile configurations. First, approximate solutions based on the superposition of stationary singularities are presented. Next, test results on symmetric and asymmetric specimens of six alloys are summarized, along with a method for quantifying and representing the ductility. In addition, a macro-mechanical model of crack growth by combined fracture on one plane and sliding off along two others, describes, for this idealization of the physical mechanisms, the ductile crack growth for both the asymmetric and symmetric specimens. To account for the effect of the finite width of the shear band and study the stress and strain fields at initiation, a finite element investigation of the asymmetric specimens is performed. Early growth is also studied by successive removal of the critical elements.

INTEGRATED STATIONARY SOLUTIONS

1. Pure Mode II approximation.

A formulation for the accumulation of damage directly ahead of an asymmetric crack, based on strain increments adapted from Shih's [1] analysis was developed [16]. Strain increments, following a power law relation were integrated both numerically and quasi-steadily. The crack was assumed to follow the center of a 45° shear band of infinitesimal width with the far field displacement, u , being parallel to the shear band (Fig. 2a). The critical fracture strain is determined from the fracture criterion by McClintock, Kaplan and Berg [17].

The predicted displacement to crack initiation is found $u_i = O(\rho)$, of the order of mean inclusion spacing ρ . The crack growth per unit displacement was predicted $dc/du = O[\ln(c/\rho)]$, i.e. to increase approximately as the logarithm of the total crack advance per inclusion spacing ρ . The growth rate was found to be practically unaffected by strain hardening. The increasing crack growth rate, associated with the strain distribution flattening out in front of the crack at a decreasing rate that does not reach a steady state, leads to size effects in crack growth.

2. Directional effects.

Due to the higher triaxiality on one side, there is a tendency for fracture in that direction. Thus the previous pure Mode II work was extended to include sites at several angles ahead of the crack. Far field displacement is again assumed to take place parallel to the shear band (Fig. 2b). Strain increments are approximated from the mixed mode, power-law elastic solution for a stationary crack [1] and used with the fracture criterion for hole growth in shear bands [17] to predict the critical

direction. The crack is assumed to advance in the direction that requires the minimum far field displacement to reach critical damage.

At initiation, several sites around the tip are considered. The strain and hence the required displacement for damage of unity is found. The critical direction is that which minimizes the required displacement. In growth, the accumulated damage due to initiation and prior growth is found and then the required increment in damage and hence far field displacement is determined.

For a shear band at 45^0 the crack progresses at an angle of 21^0 - 30^0 from the transverse, depending on the strain hardening, indicating the effect of higher triaxiality. The crack growth rate is about 6-15% higher than with growth along the shear band. Lower strain-hardening results in the final crack orientation being closer to the 45^0 shear band and the higher crack growth rate.

EXPERIMENTAL STUDY

Tests were performed on fatigue precracked asymmetric (Fig. 3) and symmetric (Fig. 4) specimens of six alloys: 1018 cold finished, 1018 normalized, A36 hot rolled, HY80, HY100 steel, 5086-H111 aluminum. The low-hardening alloys are the 1018 CF, HY80, HY100 steel ($n \approx 0.10$) and the high-hardening alloys are the A36 HR and 1018 normalized steel ($n \approx 0.23$). In addition to the load-displacement data, the topographies of the fracture surfaces were plotted using a metallurgical microscope with a travelling stage. A schematic of the fracture surface profile is shown in Fig. 6. These profiles allow determining the growth displacement vector \vec{v}_g , the total displacement \vec{v}_1 , and hence the initiation displacement $\vec{v}_i = \vec{v}_1 - \vec{v}_g$, as well as the geometry of the fracture (flank angles, flank lengths, crack orientation).

1. Quantifying crack initiation and growth.

Initiation. As a convenient measure of crack initiation displacement from the load-displacement curves, define the "idealized initiation displacement", u_i^I/l_0 as the normalized extension between initial elastic loading and steepest unloading lines at maximum load (Fig. 5). The normalized form is used in the plots for convenience in correlating crack growth; multiplied by l_0 it becomes analogous to the more familiar COD. The tests gave:

$$(u_i^I/l_0)_{ASY} \simeq (u_i^I/l_0)_{SY}, \quad (1)$$

and

$$(u_i^I/l_0)_{high\ n} \simeq (2-4)(u_i^I/l_0)_{low\ n}. \quad (2)$$

The axial component of the initiation displacement, as measured from the profiles of the fracture surfaces, u_i/l_0 , has the same behavior as the previously defined "idealized initiation displacement", u_i^I/l_0 , i.e., u_i/l_0 is not different between asymmetric and symmetric cases. In addition, for the high hardening alloys it is about two to four times that of the low hardening ones for both geometries. A noteworthy observation is the fair amount of blunting occurring in both geometries (more blunting with higher n). An approximate relation can also be observed:

$$(u_i^I/l_0) \simeq (1.5-2.2)(u_i/l_0). \quad (3)$$

In short, initiation displacement is almost the same same in both asymmetric and symmetric cases; strain hardening affects initiation in both symmetric and asymmetric specimens.

Growth

(i) For a measure of crack growth resistance, define the crack ductility, D_g , as the minimum displacement, du_c , per unit ligament reduction dl . The displacement du_c is associated with the crack opening stretch and consists of the gauge displacement, du , and the elastic unloading du_{unl} (Fig. 5). The ligament reduction, dl , is approximated from the relative load drop, $dl \simeq (dP/P_{max})l_0$. Notice that thinning of the ligament from the far side in fully plastic flow makes the reduction in ligament rather than crack advance the appropriate measure of load drop. Thus

$$D_g = \left(\frac{du_c/l_0}{dP/P_{max}} \right)_{min} \simeq \left(\frac{du_c}{dl} \right)_{min} \quad (4)$$

The crack ductility D_g is analogous to $d(COD)/da$ and is related to the crack opening angle (COA):

$$D_g \simeq COA/\cos^2\theta_c, \quad (5)$$

where θ_c is the crack orientation. It is also the normalized maximum axial compliance allowed for stability:

$$\text{compliance allowed} < D_g l_0 / P_{max} \quad (6)$$

Tests showed that the crack ductility of the asymmetric specimens vs. that of the symmetric ones is primarily affected by strain hardening. For example,

$$\begin{aligned} (D_g)_{SY}/(D_g)_{ASY} &= 3.37 \text{ HY-100 steel } (n=0.10) \\ &= 1.06 \text{ A36 HR steel } (n=0.24) \end{aligned}$$

In short, substantial reduction in crack growth ductility with asymmetry occurs in low hardening alloys. High hardening alloys are almost as ductile in the asymmetric configuration as in the symmetric one.

(ii) Other possible measures of growth are related to D_g . A parameter, T^* , analogous to tearing modulus, $T=(E/\sigma_0^2)(dJ/da)$, can be defined. By approximating

J by the non-hardening limit [18],

$$J_{ASY} = (T.S./\sqrt{3})u\sqrt{2}, \quad J_{SY} = 2(T.S./\sqrt{3})u, \quad (7)$$

we can define T^* in terms of D_g , the tensile strength, T.S., and the modulus of elasticity, E:

$$T^*_{ASY} = D_g(E/\sqrt{3})/T.S., \quad T^*_{SY} = D_g(2E/\sqrt{3})/T.S. \quad (8)$$

Tests gave:

$$(T^*_{ASY})_{high\ n} / (T^*_{ASY})_{low\ n} > 3$$

$$(T^*_{SY})_{high\ n} \simeq (T^*_{SY})_{low\ n}$$

In conclusion, strain hardening does not affect the ductility of symmetric specimens; it does affect the ductility of asymmetric specimens.

(iii) The growth displacement as measured from the profiles of the fracture surfaces, u_g/l_0 , has the same behavior as the crack ductility D_g : for the low hardening alloys it is smaller in the asymmetric configuration than the symmetric by a factor of more than three whereas in the high hardening alloys it is reduced by a factor of 1.2 at most.

(iv) The displacement vector in the asymmetric specimens is more axial than 45° , suggesting a Mode I component. The angle from transverse, ϕ , is between 51° for the 1018 CF steel and 63° for the 1018 normalized steel.

(v) The crack direction in the asymmetric specimens is less than 45° , indicating the effect of triaxiality. The angle θ_c is 38° - 41° from transverse, larger values for the lower hardening alloys.

In conclusion, the experiments showed that while the crack initiation displacements are similar, the growth displacement for the low hardening alloys in the asymmetric case is much less than that of the symmetric. Triaxiality on one side of the asymmetric crack diverts it from 45° to 38° - 41° while the far field displacement vector is more axial than 45° , at 51° - 63° , suggesting a Mode I component, even with asymmetry.

Table 1 compares the experimental findings with the predictions of the integrated stationary crack field solutions. The initiation displacement is an order of magnitude larger than the theoretical one, apparently due to blunting. The incremental models cannot account for the big effect of strain hardening in crack growth; notice that these models are based on a superposition of stationary singularities and thus do not take the convection of hardened material into account. The size effects in fully plastic crack growth that are predicted from the incremental pure Mode II analysis are associated with the transient behavior (increasing crack growth per unit displacement).

Finally, fractographic observations show as noteworthy features in the asymmetric specimens the "shear type" fracture, more evident in the lower hardening alloys and a larger amount of sliding off in the lower flank. The symmetric specimens, with the larger ductility, show in turn the "normal type" fracture with more equiaxed voids than the corresponding asymmetric specimens.

SHEAR BAND CHARACTERIZATION OF CRACK GROWTH

To provide a physical basis for interpreting the test data, a macro-mechanical model for crack advance by sliding off and fracture was developed. The model

assumes in the general mixed mode case sliding off along two slip planes and fracture on a third and gives the independent parameters (shear and cracking directions, relative amounts of cracking and shearing) in terms of the observable quantities of the macroscopic fracture (flank angles, flank lengths, back angle).

To describe the development of deformation, assume cycles of sliding off on an upper slip plane at θ_{su} through a distance s_u , then on a lower at θ_{sl} through s_l and finally fracture at θ_f over a distance f (Fig. 7). The limiting Mode I case with two symmetric slip planes corresponds to $\theta_{su} = -\theta_{sl}$, $\theta_f = 0^0$, $s_u = s_l$, and the limiting Mode II single slip plane case corresponds to $s_l = 0$. Thus there are 5 independent physical variables: the slip and fracture angles, θ_{su} , θ_{sl} , θ_f , the cracking ratio $\chi = f/s_u$ and the shearing ratio $\xi = s_l/s_u$. Observable quantities that allow solving for the physical variables are the flank angles, θ_p , θ_u , the flank lengths normalized with the initial ligament, l_u/l_0 , l_l/l_0 , and the back angle, β_u , defined as the angle the deformed upper back surface makes to the load axis. Closed-form expressions are given in chapter four.

Examples (HY-100 and 1018 normalized steel) are shown in Table 2.

For the asymmetric specimens the shearing ratio ξ is found to be about 0.5 indicating shearing in lower flank twice that in upper flank. SEM fractographs have confirmed that the lower flank shows indeed more "shear type" fracture than the upper one. The slip angle difference $\theta_{sl} - \theta_{su}$ is a measure of the spreading out of deformation and is found to be in the high hardening alloys 4^0-6^0 as opposed to 1^0-2^0 for the low hardening ones. The cracking ratio χ is a measure of the relative amount of fracture and sliding off on the upper surface and allows comparing with the "apparent crack ductility", D_{AC} , as observed fractographically and defined as the sliding off to total area including fracture. Thus,

$$\text{In upper flank } D_{AC,u} = s_l/(f+s_l) = 1/(\chi/\xi+1) . \quad (9)$$

$$\text{In lower flank } D_{AC,l} = s_u/(f+s_u) = 1/(\chi+1) . \quad (10)$$

A comparison with values observed from SEM fractographs (Table 3), shows that the values from the fractographs are bigger by about a factor of two. Considering the idealization of the complex hole-crack tip interaction and the difficulty in measuring D_{AC} (from the extent of void growth) in the fractographs, the agreement is encouraging, giving the right trend (low hardening alloys less ductile in the asymmetric configuration than the symmetric but high hardening alloys almost equally ductile in both geometries).

FINITE ELEMENT STUDY OF THE ASYMMETRIC SPECIMENS

For further insight, a finite element study of the asymmetric specimens is performed. This work is needed to relax the assumption of the far field displacement being parallel to shear band (as was presumed in the superposition of stationary singularities), to account for the finite width of the shear band and to allow describing the Mode I component at initiation. In this finite element work (mesh is shown in Fig. 8) blunting was neglected. Besides initiation, early growth was studied by successive removal of elements reaching unit damage. To describe the Mode I component, use the Mode I mixity parameter M^P based on stresses [1].

$$M^P = \frac{2}{\pi} \tan^{-1} \left| \lim_{r \rightarrow 0} \frac{\sigma_{\theta\theta}(r, \theta = \theta_{\text{crack}})}{\sigma_{r\theta}(r, \theta = \theta_{\text{crack}})} \right| . \quad (11)$$

Results, compared with the superposition of stationary singularities and test data are shown in Table 4. Notice the presence of a large Mode I component with the far field displacement vector not along the 45° shear band but at an angle about 68° from the transverse. In addition stress and strain fields are found consistent

with the solutions for the mixed mode extended HRR fields. Displacement to crack initiation is of the order of the fracture process zone size. The critical direction is predicted at an angle of 39° - 43° from the transverse, increasing for a lower strain hardening exponent. Finite element study of early growth resulted in extension rate for the lower hardening case about half that of the higher hardening one.

CONCLUSIONS

1) Low hardening asymmetric specimens are substantially less ductile than the symmetric ones. For the crack ductility, D_g , defined as the minimum displacement per ligament reduction,

$$(D_g)_{SY}/(D_g)_{ASY} > 3 \text{ for lower hardening alloys}$$

$$< 1.2 \text{ for higher hardening alloys}$$

Thus, there is a significant effect of strain hardening in mixed Mode I and II fully plastic crack growth.

2) The initiation displacement is insensitive to geometry; however it depends on strain hardening. Blunting of the order of 10ρ or 0.1mm occurs in both geometries.

3) The displacement vector is more axial than 45° , at 51° - 63° from transverse, suggesting a Mode I component even with asymmetry (where nonhardening solutions give pure shear).

4) The crack direction is less axial than 45° , at 38° - 41° from transverse (closer to 45° with less hardening); this indicates the effect of triaxiality.

5) A superposition of stationary singularities gives practically no effect of strain hardening; it overestimates the ductility of low hardening asymmetric specimens.

6) Finite element study of the asymmetric specimens, neglecting blunting, predicts at initiation a critical direction at about 40° , a far field displacement at about 68° , gives HRR consistent stress and strain fields and describes the Mode I component.

7) Early growth, studied by successive removal of critical elements shows an effect of strain hardening; the crack growth rate for $n=0.12$ was twice that of $n=0.24$.

8) A shear band model by fracture and sliding off on two planes describes mixed mode crack growth; provides a physical basis of interpreting results.

SIGNIFICANCE AND RECOMMENDATIONS

Although much work has been done in the elastic and elastic-plastic fracture mechanics, less is known for fracture under fully plastic conditions. In structures, fully plastic flow before fracture is desirable since large deformations help detect impending fracture as well as help stabilize it by load shifting. Most fracture tests use symmetric specimens (e.g. bend, compact tensile specimens). An asymmetric configuration, however, may arise due to a weld fillet or a harder, heat-affected zone or a shoulder on one side of the crack. The effect of asymmetry on unconstrained tensile specimens has been quantified and analyzed for several alloys. Results reported here show that asymmetric (mixed mode I and II) fully plastic configurations in low hardening alloys may be less ductile than the corresponding symmetric singly grooved tensile specimens by more than a factor of 3, increasing the stiffness requirements for fracture-stable design. In addition a standard way of representing tests and comparing the two geometries is suggested. In the fully plastic state, since geometry and mode of loading can affect the triaxiality and the local strain fields, the crack growth ductility will not be a single parameter but a set.

each referring to a certain configuration and triaxiality.

Further work should include studying the effect of triaxiality by performing constrained asymmetric tests. For example, tensile testing on doubly-grooved specimens with the asymmetry introduced through varying notch angles and positions; or laterally constrained singly-grooved tensile tests. Fully plastic fracture under high triaxiality could be studied by wedge-splitting of a doubly grooved specimen. Another extension could involve testing part-through cracks in plates with asymmetric shoulders.

On the analytical side, there is a need for an asymptotic solution of mixed mode growing cracks, coupled with finite element solutions that connect far-field and near-field parameters; and possibly finding a rigid-plastic singularity for a growing crack with deforming flanks.

REFERENCES

1. Shih C.F. "Small Scale Yielding Analysis of Mixed Mode Plane Strain Crack Problems", *Fracture Analysis, ASTM STP 560*, Am.Soc.Test.Mat., Philadelphia, 187-210 (1974).
2. Hutchinson J.W. "Singular behaviour at the end of a tensile crack in a hardening material", *J. Mech. Phys. Sol.*, 16, 13-31 (1968).
3. Rice J.R. and Rosengren G.F. "Plane Strain Deformation near a crack tip in a power-law hardening material", *J. Mech. Phys. Sol.*, 16, 1-12 (1968).
4. Rice J.R. "Elastic Plastic Crack Growth" in *Mechanics of Solids*, Pergamon Press, Oxford, pp.539-562 (1982).
5. Amazigo J.C. and Hutchinson J.W. "Crack tip fields in steady crack growth with linear strain-hardening" *J. Mech. Phys. Sol.*, 25, pp.81-97 (1977).

6. Slepyan L.I. "Deformation at the edge of a growing crack", *Mekhanika Tverdogo Tela*, Vol. 8, No. 4, pp. 139-148 (1973).
7. Slepyan L.I. "Deformation of an elastic-plastic body" *Mekhanika Tverdogo Tela*, Vol. 9, No. 1, pp. 57-67 (1974).
8. Parks D.M., Lam P.S. and McMeeking R.M. "Some effects of inelastic constitutive models on crack tip fields in steady quasistatic growth", in *Advances in Fracture Research*, D. Francois et al. eds, pp. 2607-2633, Pergamon (1981).
9. Rice J.R., Drugan J.W. and Sham T.L. "Elastic-Plastic Analysis of Growing Cracks" *ASTM STP 700*, pp. 189-221 (1980).
10. Chant M., Green G., Whatmough I.J., Williams D.C. "The first large shear specimen test" General Electricity Generating Board Report No. SSW/SSD/0250/R/83, Job No. 01-95 (1983).
11. Shih C.F., deLorenzi H.G., Andrews W.R. "Studies on Crack Initiation and Stable Crack Growth", *Elastic-Plastic Fracture*, *ASTM STP 668*, pp. 65-120 (1979).
12. Dawes M.G. "Elastic-Plastic Fracture Toughness Based on COD and J-Contour Integral Concepts", *Elastic-Plastic Fracture*, *ASTM STP 668*, pp. 307-333 (1979).
13. Chipperfield C.G., Knott J.F. and Smith R.F. "Critical Crack Opening Displacement in Low Strength Steels", Third Intern. Congress on Fracture, Munich, April 1973, paper I-233 (1973).
14. Paris P.C., Tada H., Ernst H. and Zahoor A. "Initial Experimental Investigation of Tearing Instability Theory", *Elastic-Plastic Fracture*, *ASTM STP 668*, pp. 251-265 (1979).
15. Paris P.C., Tada H., Ernst H. and Zahoor A. "The Theory of Instability of the Tearing Mode of Elastic-Plastic Crack Growth" *Elastic-Plastic Fracture*, *ASTM STP 668*, pp. 5-36 (1979).
16. McClintock F.A. and Slocum A.H. "Predicting Fully Plastic Mode II Crack Growth from an Asymmetric Defect", *Int. J. Fract. Mechanics*, 27, 49-62 (1985).
17. McClintock F.A., Kaplan S.M. and Berg C.A. "Ductile Fracture by hole growth in shear bands" *Int. J. Fract. Mech.*, 2, 614-627 (1966).
18. McClintock F.A. "Plasticity Aspects of Fracture", in *Fracture*, vol. 3, edited by H. Liebowitz, Academic Press, New York, 47-225 (1971).

TABLE 1
Asymmetric fully plastic cracks

<u>Approximate</u> <u>Mode II soln.</u>	<u>Superposition</u> <u>of Shih soln.</u>	<u>Tests</u>
Initiation displacement:		
$u_i = (0.8-0.6)\rho$	$u_i = (0.6-0.4)\rho$	$u_i = (8-39)\rho$ due to blunting
Crack direction:		
$\theta_c = 45^0$ (assumed)	$\theta_c = 21^0-30^0$ $\theta_c \uparrow$ with $n \downarrow$	$\theta_c = 38^0-41^0$ $\theta_c \uparrow$ with $n \downarrow$
Growth Ductility ($D_g = du_c/dl$):		
0.190-0.200 no effect of n	0.180-0.170 little effect of n	0.215-0.072 strong effect of n
Size effects in fully plastic growth:		
1.5in. dia. specimens vs. 0.5in. dia. specimens:		
$(D_g)_{0.5in} / (D_g)_{1.5in} = 1.20$		$(D_g)_{0.5in} / (D_g)_{1.5in} = 1.04$

TABLE 2
Deformation of singly-grooved
asymmetric and symmetric specimens

<u>Alloy:</u>	HY-100		1018 normalized	
	n=0.10		n=0.24	
<u>Observations</u>	Asy	Sy	Asy	Sy
Length ratio, l_u/l_0	0.820	0.780	0.750	0.740
Length ratio, l_l/l_0	0.900	0.780	0.870	0.740
Flank angle, θ_u	39^0	-14^0	36^0	-12^0
Flank angle, θ_l	41^0	14^0	42^0	12^0
Back angle, β_u	14^0	(13^0)	13^0	(16^0)
<u>Corresponding slip and fracture parameters</u>				
Slip angle, θ_{sl}	53^0	-41^0	52^0	-31^0
Slip angle, θ_{su}	54^0	41^0	58^0	31^0
Cracking angle, θ_f	37^0	0^0	31^0	0^0
Shearing ratio, ξ	0.536	1.00	0.445	1.00
Cracking ratio, χ	2.912	1.907	1.518	1.579

TABLE 3
Apparent crack ductility

		<u>Shear band</u>	<u>fractographs</u>
		<u>model</u>	
HY100 steel			
Asy	$D_{AC,l}$	0.26	0.51
	$D_{AC,u}$	0.16	0.37
Sy	$D_{AC,l}$	0.34	0.64
	$D_{AC,u}$	0.34	0.64
1018 normalized steel			
Asy	$D_{AC,l}$	0.40	0.68
	$D_{AC,u}$	0.23	0.52
Sy	$D_{AC,l}$	0.39	0.67
	$D_{AC,u}$	0.39	0.67

TABLE 4
Comparing with the finite element results.

<u>Finite Element</u> (blunting neglected)	<u>Superposition</u> <u>of Shih soln.</u>	<u>Tests</u>
Initiation displacement:		
$u_i = (0.5-0.6)\rho$	$u_i = (0.6-0.4)\rho$	$u_i = (8-39)\rho$ due to blunting
Mode I component at initiation, M^P : relative to initial crack direction		
$\simeq 0.93$	$\simeq 0.50$	
relative to final crack direction		
$\simeq 0.71$	$\simeq 0.25$	
Displacement vector at initiation:		
$\phi \simeq 68^0$	$\phi = 45^0$ (assumed)	$\phi \simeq 69^0-58^0$
Crack direction:		
$\theta_c = 39^0-43^0$ $\theta_c \uparrow$ with $n \downarrow$	$\theta_c = 21^0-30^0$ $\theta_c \uparrow$ with $n \downarrow$	$\theta_c = 38^0-41^0$ $\theta_c \uparrow$ with $n \downarrow$
Gauge extension rate		
0.158-0.075 (Early growth) strong effect of n	(0.180-0.170) _{min} little effect of n	(0.153-0.060) _{min} strong effect of n

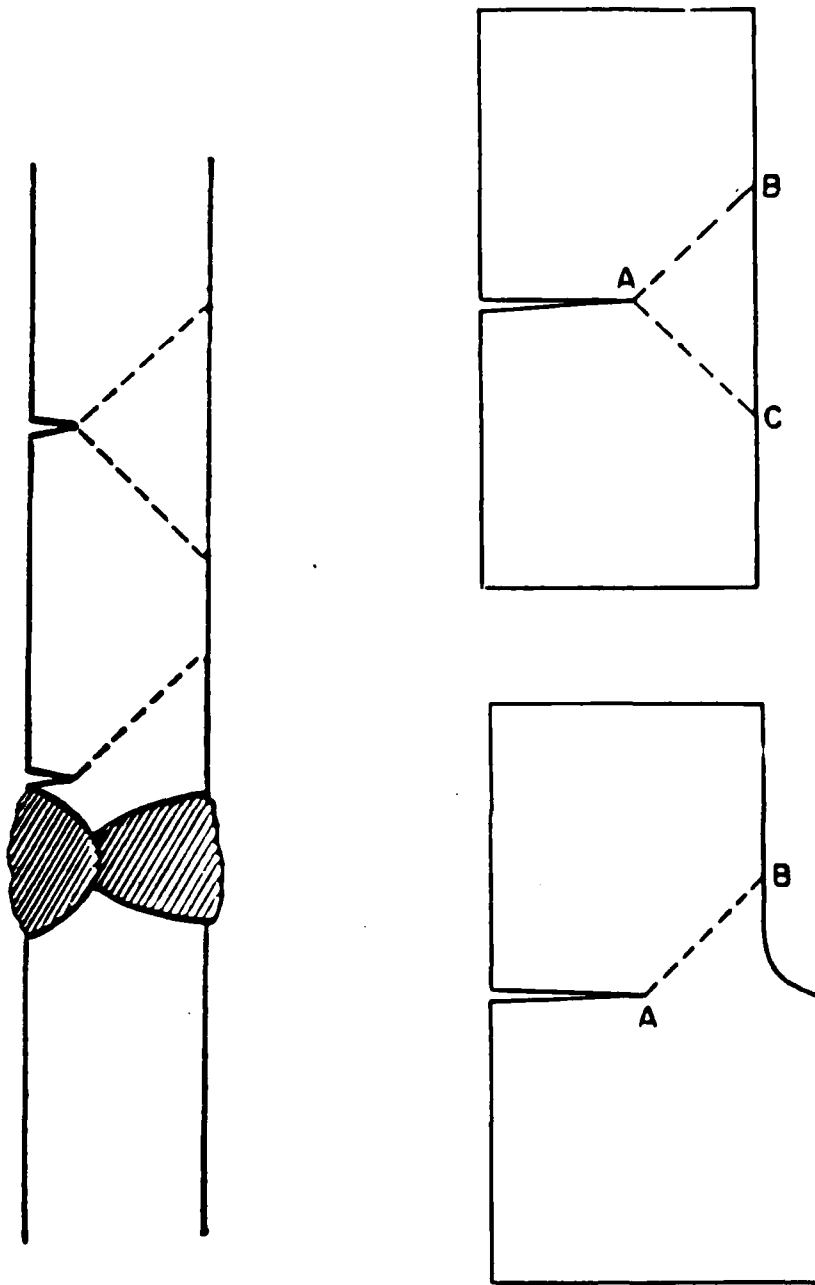


Figure 1. Asymmetric crack from a defect near a weld or a shoulder, the symmetric case is shown above.

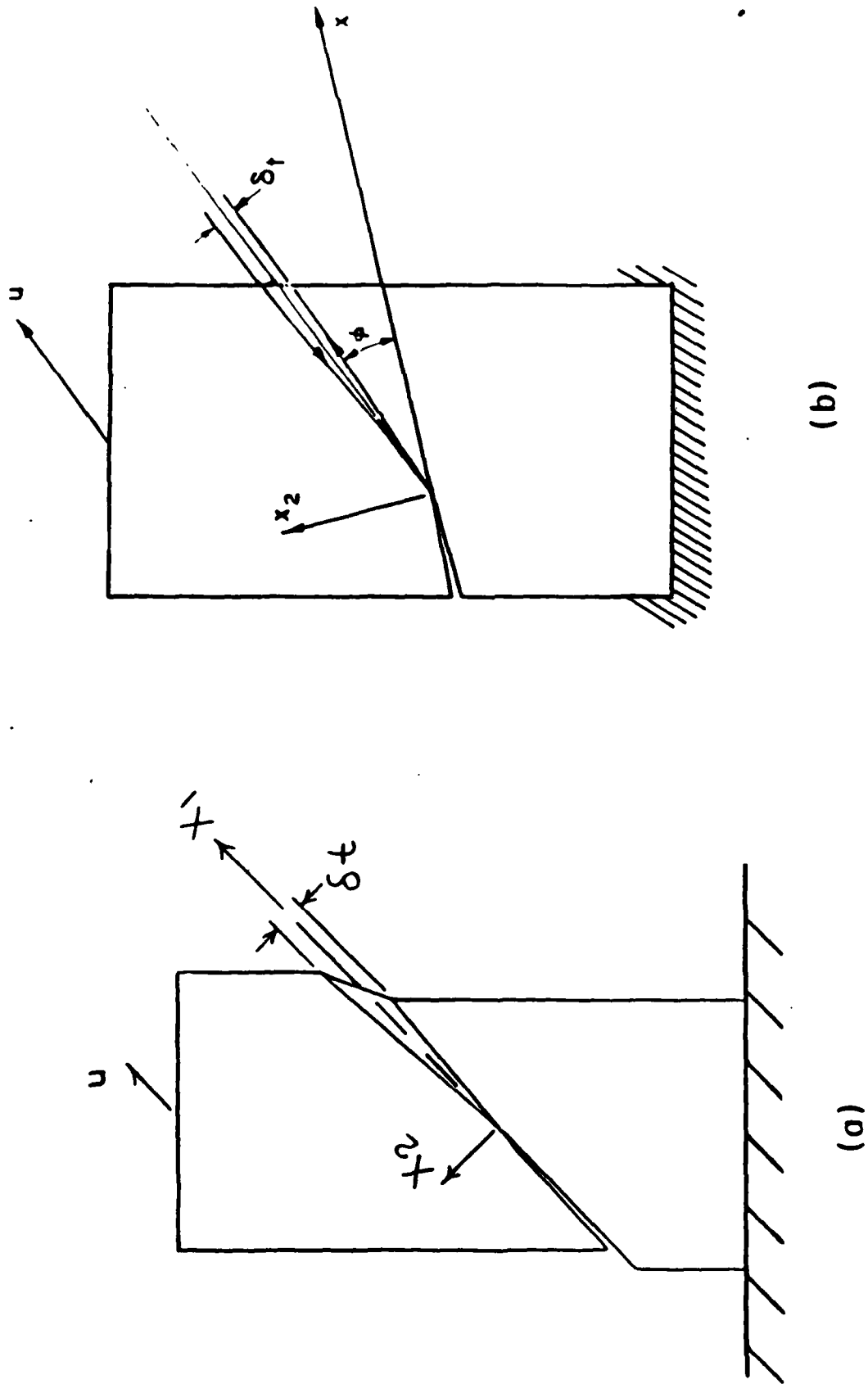


Figure 2. (a) Pure Mode II case.
 (b) Crack at an angle to the shear band.

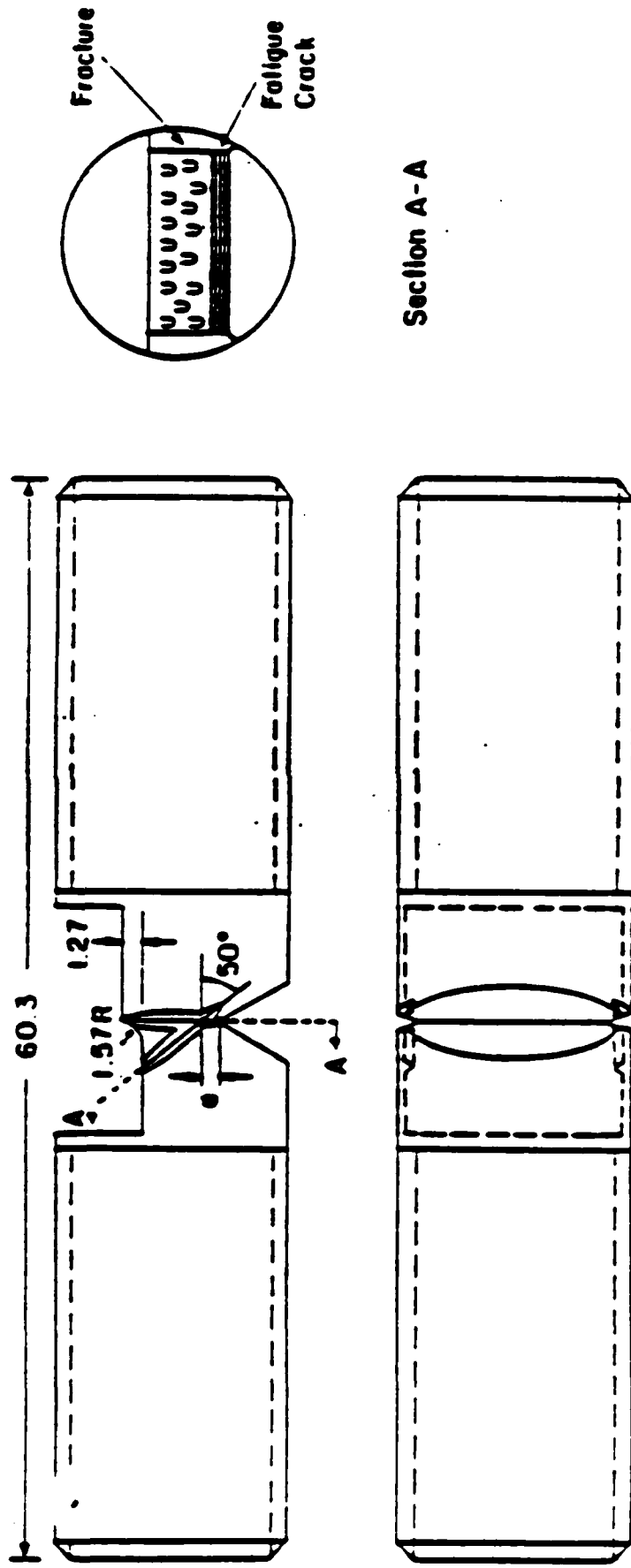


Figure 3. Second machining (after fatigue precracking) for the asymmetric specimens; a is the fatigue precrack.

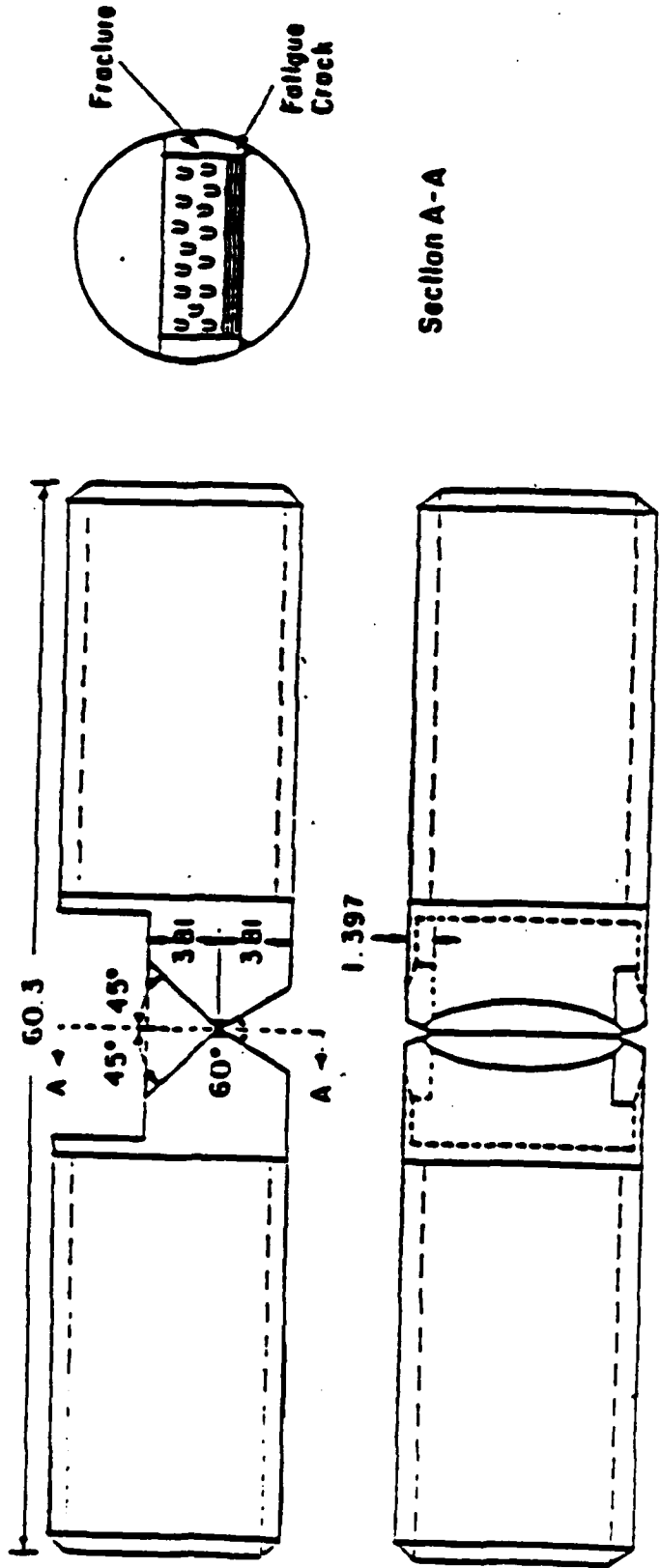


Figure 4. Second machining (after fatigue precracking) for the symmetric specimens; a is the fatigue precrack

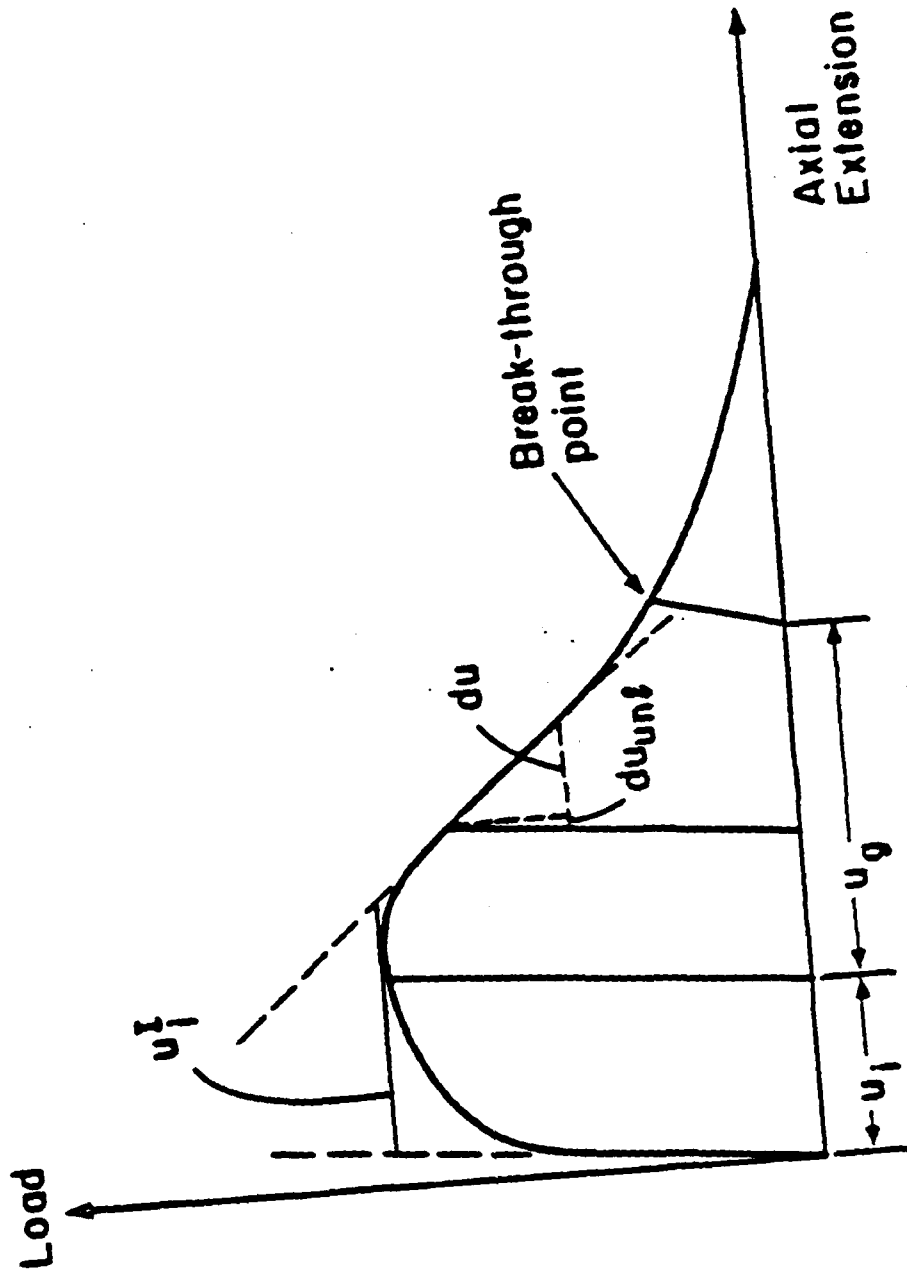


Figure 5. Schematic of the load vs. axial gauge-point displacement curve. The displacements u_g and u_i are measured after fracture.

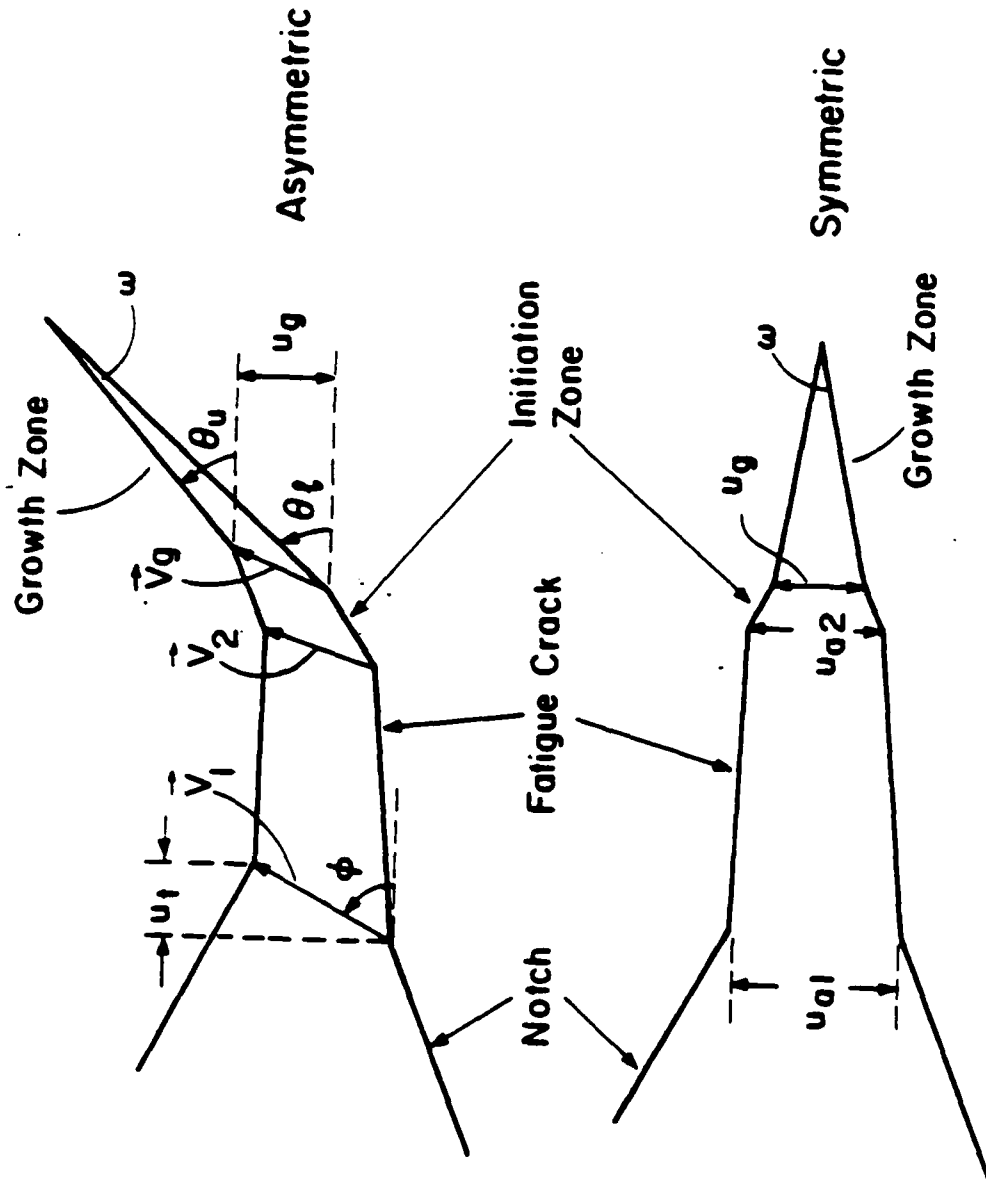


Figure 6 Schematic of the Fracture Surface Profile of the Asymmetric and Symmetric specimens

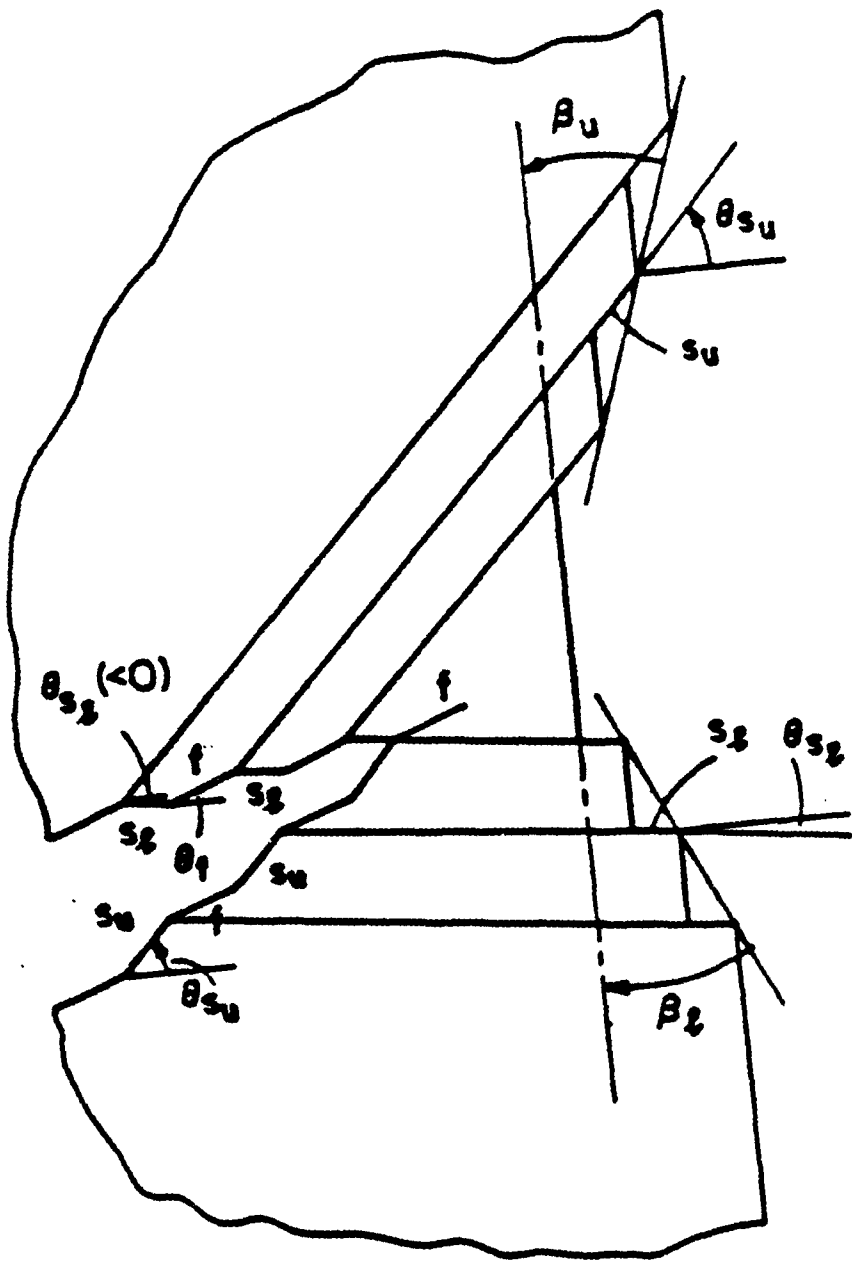


Figure 7. Development of deformation for the two-slip plane model

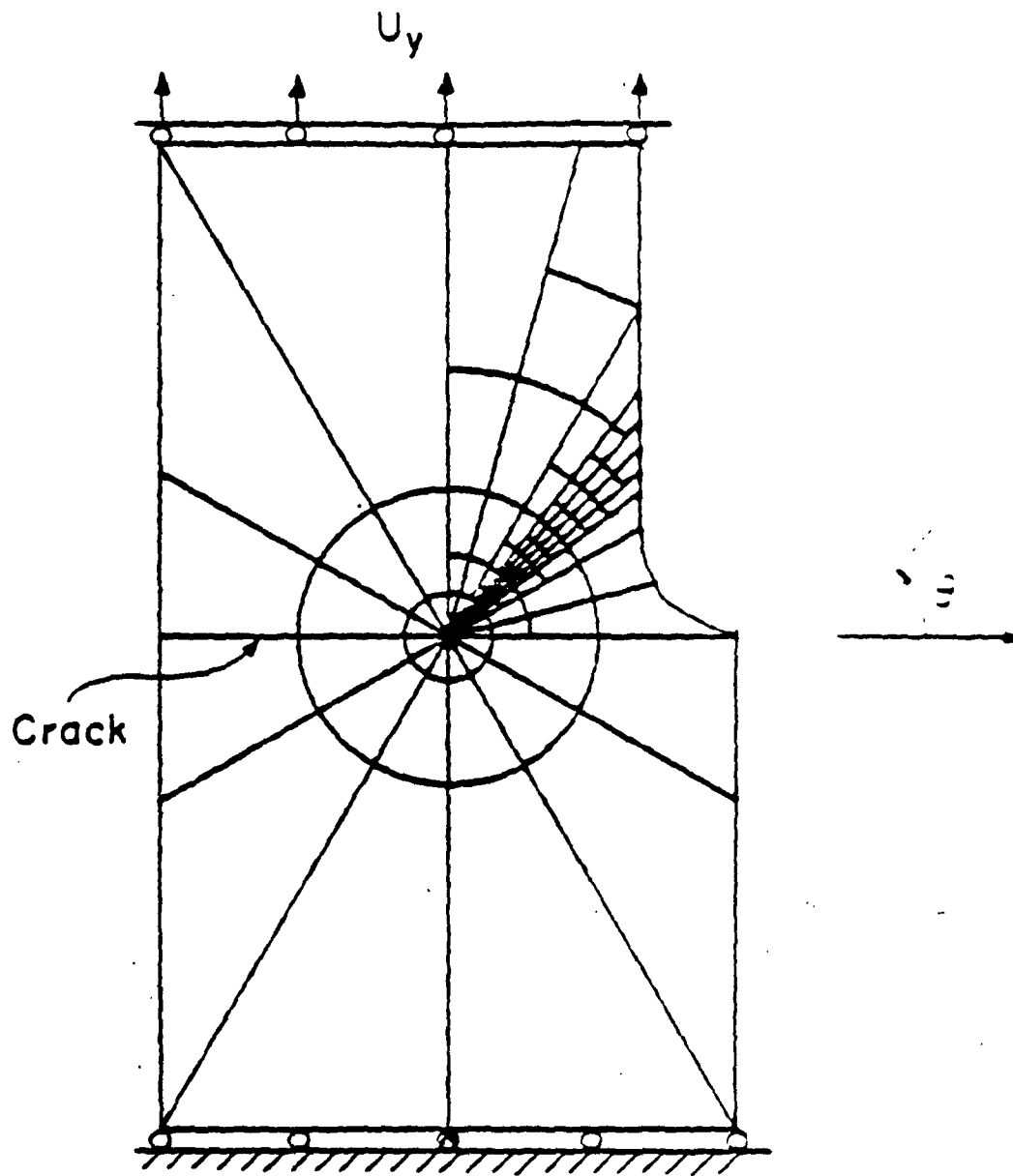


Figure 8. The finite element mesh.

APPENDIX A - Experimental Techniques

In this section the experimental techniques used (tensile testing and extensometer connections, microscopic surface topography mapping, fatigue-precracking) are described.

1. TENSILE TESTS WITH MTS, 50 METRIC TON MACHINE

Preliminary

Set Console Power switch On (Master Control Panel 413).

Set Hydraulic Pump switch in Room 1-014 ON.

Check that Feedback Selector (Model 440-32 behind the 442 Controller Panel) is in LOCAL.

Set switch in PDP-11 behind the panel under the disk drives to OUTPUT.

410 - Digital Function Generator

Set to LOCAL (to start by pressing START - if set to REMOTE then you must start from RUN in 413).

Select rates of loading and unloading, e.g.

For 20 mm stroke range,

Rate 1 = $2.4E3$ sec. means 2400 secs for 20 mm loading

Rate 2 = $2.4E2$ sec. means 240 secs for 20 mm unloading

For 50 mm stroke range, same rates of loading and unloading require

Rate 1 = $6E3$ sec.,

Rate 2 = $6E2$ sec.

PRESS RAMP, DUAL SLOPE for monotonic loading and unloading.

Set BREAKPOINT to NORMAL and BRKPNT PERCENT to 100.

442 - Controller

Press STROKE (for stroke control).

Set STROKE range as desired (e.g. ± 20 mm) by turning the RANGE knob behind the panel.

Set LOAD Range e.g. to 10K by turning the RANGE knob on stroke module behind the panel; 10K means 10V output correspond to 10,000 kgf=22,000 lb

Set SPAN 1 to 100%

Zero load indication (see digital indicator channel 1 in 430 panel) before inserting specimen by turning the ZERO knob on Load module (Model 440.21) behind the 442 panel.

Press RETURN TO ZERO (in 410) to zero out any pre-existing function generator signal.

Set METER at DC ERROR. Zero out error by turning SET POINT right if pointer is right; left if pointer is left. If whole range is not enough, use ZERO knob on stroke module behind 442 panel.

Press INTERLOCK RESET.

413 - Master Control Panel

Press RESET.

Press HYDRAULIC PRESSURE LOW, then HIGH.

Put SET POINT in 442 to 5.0 - Ram will move. (Digital indicator channel 3 should read 0.0). To further move the ram use ZERO knob on stroke module (Model 440.21) behind 442 (Controller) panel.

Notes: 1. Ram moves DOWN when turning SET POINT right,
2. to increase stiffness move ram up.

As you tighten the locknuts use SET POINT to relieve any compression: watch digital indicator channel 1 for load (channel 3 is stroke).

Press START in 410.

End of Test

TO STOP: Press HYDRAULIC PRESSURE LOW then HYD OFF on 413.

To LEAVE: Set Hydraulic Pump switch in Room 1-014 OFF.

Set Console Power OFF on 413.

Intermediate Manual Unloading and Reloading

To UNLOAD: Press HOLD in 410 (holds the test), then turn SET POINT in 442 left to unload.

TO RELOAD: Turn SET POINT right.

To CONTINUE with preset rate: Press HOLD once more.

Moving Crosshead

Press HYDRAULIC LOW, then HIGH on 413.

Set switch behind the MTS to UNLOCK.

Move crosshead by turning the UP or DOWN handle as you wish.

Set switch behind the MTS to LOCK.

Press RESET on 413.

MTS Plotter

3 channels, X, Y1 and Y2. Y1 not working

e.g. Using X channel for stroke, selecting 5% of range/in with 20 mm stroke range corresponds to 1 mm/in on the plot.

Using Y2 channel for load, selecting 20% of range/in with 10K load range corresponds to 2000 kgf/in on the plot.

Stiffness Data of the MTS.

Load Cell 33.0E6 lb/in

Load Frame 6.0E6 lb/in

2. EXTENSOMETER CONNECTIONS WITH THE VISHAY AMPLIFIER/CONDITIONER

Wiring Correspondence

AXIAL Extensometer - Full Bridge

Extens.		Vishay
A	RED	D out +
B	GREEN	C exc -
C	YELLOW	A out -
D	BLUE	B exc +
E	BLACK	F ground

CAL A corresponds to 0.0275 in. (0.6985 mm)

TRANSVERSE extensometer - Half Bridge

Extens.	Vishay
A	A out +
B	C exc - , out -
D	B exc +
E	F ground

CAL A corresponds to 0.055 in. (1.397 mm)

3. SURFACE TOPOGRAPHY MAPPING WITH THE BAUSCH AND LOMB TRAVELLING MICROSCOPE.

The apparatus consists of the microscope, linear potentiometers, stage extension bar and assorted rubber bands and C-clamps for fixing the potentiometers on the microscope. One potentiometer is clamped to the side of the microscope and one to the travelling stage.

Rubber bands are used to secure the stage extension bar to the microscope knee. Note that some of the rubber bands go around the back of the microscope. They serve two purposes; they keep the stage extension bar firmly against the microscope and they act to offset its weight.

Adjust the potentiometer and the stage extension bar so that the points of the potentiometer are reasonably centered on the bottom of the cap screws in the stage extension bar. Use rubber bands to secure the potentiometer ends on the stage extension bar screws.

The electric circuit employs a $V_0=3V$ battery and a balancing 10-turn potentiometer for each linear pot. The two green wires from the linear pot go to the battery terminals hooked with the balancing pot as in Fig. 1. The blue wire from the linear pot and the remaining wire from the balancing pot go to the plotter.

Solving the circuit gives

$$V_1 - V_2 = \left(\frac{R_2}{R_1 + R_2} - \frac{R_4}{R_3 + R_4} \right) V_0.$$

Zero the output $V_1 - V_2$ at the starting point by using the balancing 10-turn potentiometer (i.e. adjust R_4 so that $V_1 - V_2 = 0$).

To plot the topography use the 10x power on the microscope. The higher magnifications require the objective to be quite close to the surface of the specimen and one could easily hit the objective on a peak of the viewed surface when trying to focus into a valley. Move slowly your specimen along the horizontal axis and get the corresponding vertical coordinate by having the centerline of the specimen always in focus. Notice that the vertical fine scale on the microscope is $10 \text{ rev} = 1 \text{ mm}$.

4. FATIGUE PRE-CRACKING

Specimen precracking was done on the SF-1 Fatigue Machine, which is a fixed frequency (3600 rpm) rotating mass machine. It was used with the bending fixtures. The specimens were subjected to four-point bending. A uniform bending moment M is applied across the span of the specimen, given in terms of the load moment arm R (distance between rocker bearings, $R = 3$ or 6 inches) and the total applied force P from

$$M = PR/2 \quad (1)$$

The nominal alternating stress σ_a can be found by using the moment of inertia $I = bh^3/12$ (b , h are specimen width, and thickness) from

$$\sigma_a = \frac{M(h/2)}{I} = \frac{3PR}{bh^2} = \frac{M}{bh^2/6} \quad (2)$$

Notice that σ_a does not depend on the specimen length. In terms of the specimen length between grips, L , ($L = 3, 5, 6$ or 8 inches) and the modulus of elasticity of the specimen, E , the amplitude of the vibrating platen Y is

$$Y = R \frac{ML}{2EI} = \frac{3PR^2L}{Ebh^3} \quad (3)$$

The following restrictions apply

Maximum applied force, $P = 1,000$ lb

Maximum amplitude of reciprocating platen $Y = 0.4$ inches

As a rough approximation assume $\sigma_a \approx T.S.$ Then from (2) find the necessary $M = (T.S.)bh^2/6$. For a chosen R find the required P from (1), $P = 2M/R$. Next, for the chosen specimen length L check that the resulting Y from (3) is less than 0.4 inches. Notice that P should be less than $1,000$ lb.

Indicative data for fatigue pre-cracking on the SF-1 with $R=3$ inches are:

1018 CF steel (HBN=157) 0.50" dia. needs about 10,000 cycles with $P=90$ lb to grow 0.050" fatigue crack.

A36 steel (HBN=105) 0.50" dia. needs about 7,000 cycles, $P=80$ lb to grow 0.050" fatigue crack

5086-H111 aluminum (HBN=70) 1.50" dia. needs about 12,000 cycles, $P=1,000$ lb to grow 0.150" fatigue crack.

To operate the machine (for details see instruction manual):

Turn the CONTROLLER POWER switch to STANDBY.

Turn on main power switch on wall behind machine. Wait for at least half hour to allow warmup.

Attach tuning weights to the studs on either side of the orange cage.

Set the oscillating load P .

Check that knob of variable transformer is at zero.

Press START button. Gradually turn knob of variable transformer, increasing the motor speed to the extreme 100 position. This should take from 20 to 80 sec.

Turn CONTROLLER POWER switch ON.

To STOP press the STOP button and turn the variable transformer back to zero.

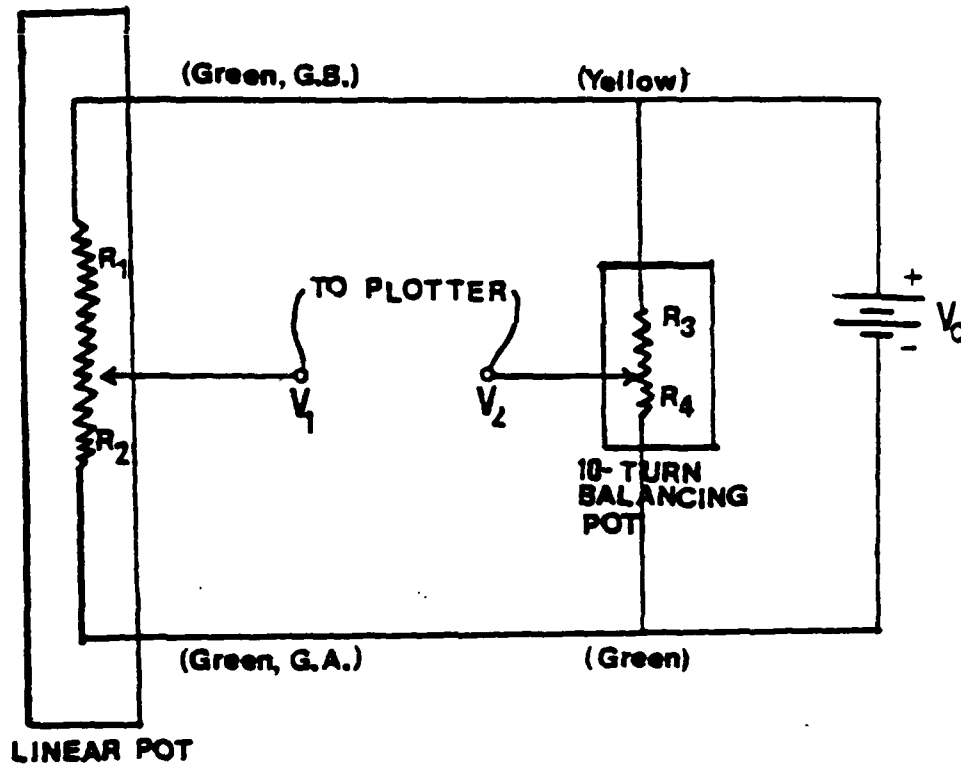
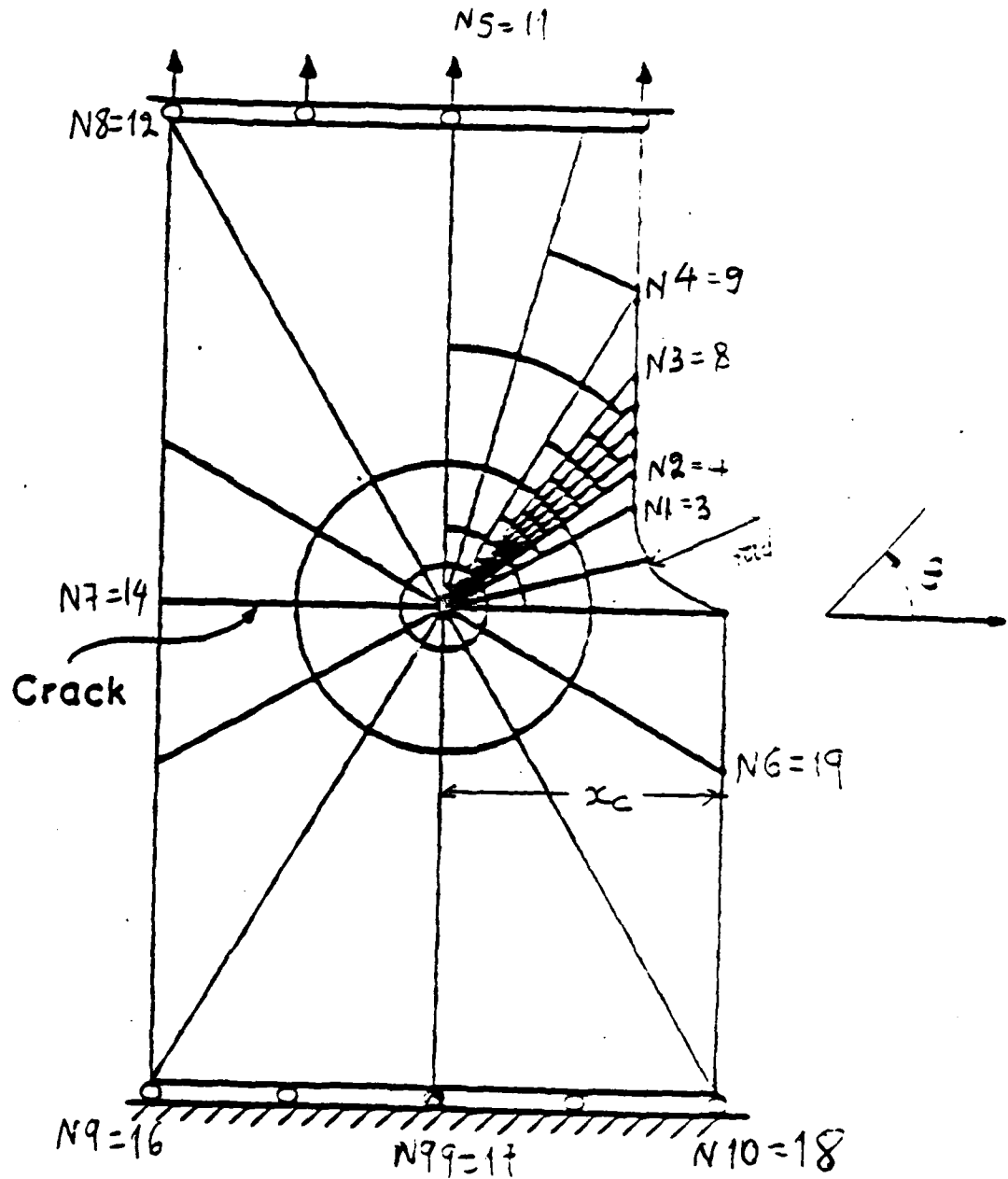


Figure 1. Surface topography mapping circuit.

APPENDIX B - MESH GENERATOR

The following FORTRAN program generates the finite element mesh for the asymmetric specimens for any desirable radial size ratio and angular spacings. Bar denotes user input.



C This program creates the node nos., element nos., and
 C the corresponding MPC constraints for the fan.
 C We have maximum Nr segments radially and N6 radial lines
 C around; here Nr=32 and N6=19.
 C RO=10 microns (one inclusion spacing) = 0.01 mm
 C s is the size ratio in the log circular mesh=1.155
 C Angular spacings are (larger to smaller) thet, thet1, thet2,
 C thet3; here thet=30, thet1=15, thet2=7.5, thet3=3.75 deg.
 C L is the node no. with coords x(L), y(L); M is the element no.
 C with nodes Nod1(M), Nod2(M), ..., Nod8(M).
 C File no. 15 contains the nodes, no. 16 contains the element data
 C and no. 17 contains the MPC constraints.

```

    DIMENSION x(15000), y(15000), Nod1(15000), phi(100),
    -         Nod2(15000), Nod3(15000), Nod4(15000), Rc(100),
    -         Nod5(15000), Nod6(15000), Nod7(15000), Nod8(15000)
    Nr = 32
  
```

c Note: Nr should be a multiple of 8 (so that the minimum no.
 c of segments radially, corresp. to the largest angle, is Nr/8)
 c Rmax = RO*(s**Nr-1)/(s-1)

Note: Bars
 denote
 user
 input

```

    RO = 0.01
    s = 1.155
    pi = 3.14159
    thet = 30.*pi/180.
    thet1 = 15.*pi/180.
    thet2 = 7.5*pi/180.
    thet3 = 3.75*pi/180.
    R30 = RO*(1+s+s**2+s**3+s**4+s**5+s**6+s**7)
    s30 = s**8
    N30 = Nr/8
    R15 = RO*(1+s+s**2+s**3)
    s15 = s**4
    N15 = Nr/4
    R75 = RO*(1+s)
    s75 = s**2
    N75 = Nr/2
  
```

```
1001 FORMAT(I5,F10.7,F10.7)
```

c Dtheta for radial lines 1-N1 is 15 deg.; N1-N2: 7.5 deg.;
 c N2-N3: 3.75 deg.; N3-N4: 7.5 deg.;
 c N4-N5: 15 deg.; N5-N6: 30 deg.; N7: crack flank.

```

    N1 = 3
    N2 = 4
    N3 = 8
    N4 = 9
    N5 = 11
    N6 = 19
    N7 = 14
  
```

c Input Nodes for the 15 deg. sectors

```

    DO 90 I=1, N1-1
      phia = (I-1)*thet1
      phi(I) = phia
      DO 100 J=1, N75
        R1 = R75*(s75**J - 1)/(s75-1)
        L = 500*I + 4*J
        x(L) = R1*cos(phia)
        y(L) = R1*sin(phia)
        WRITE(15,1001) L, x(L), y(L)
      100 CONTINUE
    90 CONTINUE
  
```

```
100
90
```

```

    CONTINUE
    DO 911 I=1, N1-1
  
```



```

    phia = (I-1)*thet1 + thet1/2.
    DO 922 J=1, N15
      R1 = R15*( s15**J - 1 )/(s15-1)
      L = 500*I + 200 + 8*J
      x(L) = R1*cos(phia)
      y(L) = R1*sin(phia)
      WRITE(15, 1001) L, x(L), y(L)
922   CONTINUE
911   CONTINUE
c   Input Nodes for the 7.5 deg. sector
    DO 82 I=N1, N2-1
      phia = (N1-1)*thet1 + (I-N1)*thet2
      phi(I) = phia
      DO 101 J=1, Nr
        R1 = R0*( s**J - 1 )/(s-1)
        L = 500*I + 2*J
        x(L) = R1*cos(phia)
        y(L) = R1*sin(phia)
        WRITE(15,1001) L, x(L), y(L)
101   CONTINUE
82    CONTINUE
    DO 912 I=N1, N2-1
      phia = (N1-1)*thet1 + (I-N1)*thet2 + thet2/2.
      DO 923 J=1, N75
        R1 = R75*( s75**J - 1 )/(s75-1)
        L = 500*I + 200 +4*J
        x(L) = R1*cos(phia)
        y(L) = R1*sin(phia)
        WRITE(15, 1001) L, x(L), y(L)
923   CONTINUE
912   CONTINUE
c   Input nodes for the 3.75 deg. sectors
    DO 83 I=N2, N3
      phia = (N1-1)*thet1 + (N2-N1)*thet2 + (I-N2)*thet3
      phi(I) = phia
      Rip = 0.
      DO 132 J=1, Nr
        R1 = R0*( s**J - 1 )/(s-1)
        L = 500*I + 2*J
        x(L) = R1*cos(phia)
        y(L) = R1*sin(phia)
        WRITE(15,1001) L, x(L), y(L)
        L = 500*I + (2*J-1)
        R2 = (R1+R1p)/2.
        x(L) = R2*cos(phia)
        y(L) = R2*sin(phia)
        WRITE(15, 1001) L, x(L), y(L)
        Rip = R1
132   CONTINUE
83    CONTINUE
    DO 913 I=N2, N3-1
      phia = (N1-1)*thet1 + (N2-N1)*thet2
      -   + (I-N2)*thet3 + thet3/2.
      DO 924 J=1, Nr
        R1 = R0*( s**J - 1 )/(s-1)
        L = 500*I + 200 +2*J
        x(L) = R1*cos(phia)
        y(L) = R1*sin(phia)
        WRITE(15, 1001) L, x(L), y(L)
924   CONTINUE

```

```

913 CONTINUE
c Input nodes for the 7.5 deg sector
DO 84 I=N3+1, N4
  phia = (N1-1)*thet1 + (N2-N1)*thet2
  -      + (N3-N2)*thet3 + (I-N3)*thet2
  phi(I) = phia
DO 133 J=1, Nr
  R1 = R0*( s**J - 1 )/(s-1)
  L = 500*I + 2*J
  x(L) = R1*cos(phia)
  y(L) = R1*sin(phia)
  WRITE(15,1001) L, x(L), y(L)
133 CONTINUE
84 CONTINUE
DO 914 I=N3, N4-1
  phia = (N1-1)*thet1 + (N2-N1)*thet2
  -      + (N3-N2)*thet3 + (I-N3)*thet2 + thet2/2.
DO 925 J=1, N75
  R1 = R75*( s75**J - 1 )/(s75-1)
  L = 500*I + 200 + 4*J
  x(L) = R1*cos(phia)
  y(L) = R1*sin(phia)
  WRITE(15, 1001) L, x(L), y(L)
925 CONTINUE
914 CONTINUE
c Input nodes for the 15 deg. sectors
DO 85 I=N4+1, N5
  phia = (N1-1)*thet1 + (N2-N1)*thet2
  -      + (N3-N2)*thet3 + (N4-N3)*thet2 + (I-N4)*thet1
  phi(I) = phia
DO 134 J=1, N75
  R1 = R75*( s75**J - 1 )/(s75-1)
  L = 500*I + 4*J
  x(L) = R1*cos(phia)
  y(L) = R1*sin(phia)
  WRITE(15,1001) L, x(L), y(L)
134 CONTINUE
85 CONTINUE
DO 915 I=N4, N5-1
  phia = (N1-1)*thet1 + (N2-N1)*thet2
  -      + (N3-N2)*thet3 + (N4-N3)*thet2 + (I-N4)*thet1 + thet1/2.
DO 926 J=1, N15
  R1 = R15*( s15**J - 1 )/(s15-1)
  L = 500*I + 200 + 8*J
  x(L) = R1*cos(phia)
  y(L) = R1*sin(phia)
  WRITE(15, 1001) L, x(L), y(L)
926 CONTINUE
915 CONTINUE
c Input nodes for the 30 deg. sectors
DO 86 I=N5+1, N6
  phia = (N1-1)*thet1 + (N2-N1)*thet2 + (N3-N2)*thet3
  -      + (N4-N3)*thet2 + (N5-N4)*thet1 + (I-N5)*thet
  phi(I) = phia
DO 135 J=1, N15
  R1 = R15*( s15**J - 1 )/(s15-1)
  L = 500*I + 8*J
  x(L) = R1*cos(phia)
  y(L) = R1*sin(phia)
  WRITE(15,1001) L, x(L), y(L)

```

```

135     CONTINUE
86     CONTINUE
      DO 916 I=N5, N6
      phia = (N1-1)*thet1 + (N2-N1)*thet2
      -      + (N3-N2)*thet3 + (N4-N3)*thet2
      -      + (N5-N4)*thet1 + (I-N5)*thet + thet/2.
      DO 927 J=1, N30
      R1 = R30*( s30**J - 1 )/(s30-1)
      L = 500*I + 200 + 15*J
      x(L) = R1*cos(phia)
      y(L) = R1*sin(phia)
      WRITE(15, 1001) L, x(L), y(L)
927     CONTINUE
916     CONTINUE
c Nodes for crack flank
      I=N7
      phia = pi
      phi(I) = phia
      DO 11 J=1, N15
      R1 = R15*( s15**J - 1 )/(s15-1)
      L = 500*I + 100 + 8*J
      x(L) = R1*cos(phia)
      y(L) = R1*sin(phia)
      WRITE(15,1001) L, x(L), y(L)
11     CONTINUE
c Nodes for crack tip
      DO 87 I=1, N6
      L = 500*I
      x(L) = 0.
      y(L) = 0.
      WRITE (15,1001) L, x(L), y(L)
      L = 500*I + 200
      x(L) = 0.
      y(L) = 0.
      WRITE (15,1001) L, x(L), y(L)
87     CONTINUE
      L = 500*N7 + 100
      x(L) = 0.
      y(L) = 0.
      WRITE (15,1001) L, x(L), y(L)

c
c Elements - M is the element no.
1002  FORMAT(15, 815)
c
      N8 = 12
      N9 = 16
      N99 = 17
      N10 = 18
      xc = 3.81
      phia = (N7-N8)*thet
      Rcy = 3.81/cos(phia)
      yc = Rcy*sin(phia)
c Notice: Epr the shoulder, the following constraint
c should be fullfilled:
c (xc1 + rad - xc)**2 + dy**2 = rad**2
c with dy=xc1*tan(thet)
      rad = 1.49
      alpha = 1. + tan(thet)*tan(thet)
      beta = xc - rad
      gamma = (xc-rad)*(xc-rad) - rad*rad

```

```

delta = beta*beta - alpha*gamma
xc1 = ( beta + SQRT(delta) ) / alpha
dy = xc1*tan(thet)
Nadd = 2*(Nr+1)
Nad1 = 2*Nr+1
c In each sector, first determine boundary nodes
c and then input elements
DO 151 I=N1, N2-1
  Rc(I) = xc1/cos(phi(I))
  arg = ( Rc(I)*(s75-1)/R75 ) + 1
  Nri = NINT( LOG(arg)/LOG(s75) )
  L1 = 500*I + Nadd
  x(L1) = xc1
  y(L1) = Rc(I)*sin(phi(I))
  WRITE(15,1001) L1, x(L1), y(L1)
  L2 = 500*(I+1) + Nadd
  Rc(I+1) = xc1/cos(phi(I+1))
  x(L2) = xc1
  y(L2) = Rc(I+1)*sin(phi(I+1))
  WRITE(15,1001) L2, x(L2), y(L2)
  L3 = L1 + 200
  x(L3) = ( x(L1) + x(L2) )/2.
  y(L3) = ( y(L1) + y(L2) )/2.
  WRITE(15,1001) L3, x(L3), y(L3)
DO 141 J=1, Nri-1
  M = 100*J + I
  Nod1(M) = 500*I + 4*(J-1)
  Nod2(M) = 500*I + 4*J
  Nod3(M) = 500*(I+1) + 4*J
  Nod4(M) = 500*(I+1) + 4*(J-1)
  Nod5(M) = 500*I + 2*(2*J-1)
  Nod6(M) = 500*I + 200 + 4*J
  Nod7(M) = 500*(I+1) + 2*(2*J-1)
  Nod8(M) = 500*I + 200 + 4*(J-1)
  WRITE(16,1002) M, Nod1(M), Nod2(M), Nod3(M),
- Nod4(M), Nod5(M), Nod6(M), Nod7(M), Nod8(M)
141 CONTINUE
  J = Nri
  L1 = 500*I + 4*(J-1)
  L2 = 500*I + Nadd
  L3 = 500*(I+1) + Nadd
  L4 = 500*(I+1) + 4*(J-1)
  L12 = 500*I + Nad1
  x(L12) = ( x(L1) + x(L2) ) / 2.
  y(L12) = ( y(L1) + y(L2) ) / 2.
  WRITE(15,1001) L12, x(L12), y(L12)
  L34 = 500*(I+1) + Nad1
  x(L34) = ( x(L3) + x(L4) ) / 2.
  y(L34) = ( y(L3) + y(L4) ) / 2.
  WRITE(15,1001) L34, x(L34), y(L34)
  M = 100*J + I
  Nod1(M) = L1
  Nod2(M) = L2
  Nod3(M) = L3
  Nod4(M) = L4
  Nod5(M) = L12
  Nod6(M) = 500*I + 200 + Nadd
  Nod7(M) = L34
  Nod8(M) = 500*I + 200 + 4*(J-1)
  WRITE(16,1002) M, Nod1(M), Nod2(M), Nod3(M),

```

AD-A162 100

MIXED MODE I AND II FULLY PLASTIC CRACK GROWTH FROM
SIMULATED WELD DEFECTS(U) MASSACHUSETTS INST OF TECH
CAMBRIDGE DEPT OF MECHANICAL ENGIN. . G A KARDOMATERS
23 OCT 85 N00014-82-K-0025 F/G 13/8

3/3

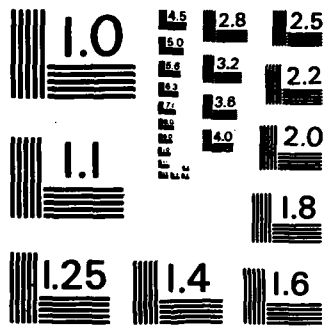
UNCLASSIFIED

NL

END

FILED

DTIC



MICROCOPY RESOLUTION TEST CHART
NATIONAL BUREAU OF STANDARDS-1963-A

```

-      Nod4(M) , Nod5(M) , Nod6(M) , Nod7(M) , Nod8(M)
151  CONTINUE
      DO 152 I=N2, N3-1
      Rc(I) = xc1/cos(phi(I))
      arg = ( Rc(I)*(s-1)/R0 ) + 1
      Nr1 = NINT( LOG(arg)/LOG(s) )
      L1 = 500*I + Nadd
      x(L1) = xc1
      y(L1) = Rc(I)*sin(phi(I))
      WRITE(15,1001) L1, x(L1), y(L1)
      L2 = 500*(I+1) + Nadd
      Rc(I+1) = xc1/cos(phi(I+1))
      x(L2) = xc1
      y(L2) = Rc(I+1)*sin(phi(I+1))
      WRITE(15,1001) L2, x(L2), y(L2)
      L3 = L1 + 200
      x(L3) = ( x(L1) + x(L2) )/2.
      y(L3) = ( y(L1) + y(L2) )/2.
      WRITE(15,1001) L3, x(L3), y(L3)
      DO 142 J=1, Nr1-1
      M = 100*J + I
      Nod1(M) = 500*I + 2*(J-1)
      Nod2(M) = 500*I + 2*J
      Nod3(M) = 500*(I+1) + 2*J
      Nod4(M) = 500*(I+1) + 2*(J-1)
      Nod5(M) = 500*I + (2*J-1)
      Nod6(M) = 500*I + 200 + 2*J
      Nod7(M) = 500*(I+1) + (2*J-1)
      Nod8(M) = 500*I + 200 + 2*(J-1)
      WRITE(16,1002) M, Nod1(M), Nod2(M), Nod3(M),
-      Nod4(M), Nod5(M), Nod6(M), Nod7(M), Nod8(M)
142  CONTINUE
      J = Nr1
      L1 = 500*I + 2*(J-1)
      L2 = 500*I + Nadd
      L3 = 500*(I+1) + Nadd
      L4 = 500*(I+1) + 2*(J-1)
      L12 = 500*I + Nad1
      x(L12) = ( x(L1) + x(L2) ) / 2.
      y(L12) = ( y(L1) + y(L2) ) / 2.
      WRITE(15,1001) L12, x(L12), y(L12)
      L34 = 500*(I+1) + Nad1
      x(L34) = ( x(L3) + x(L4) ) / 2.
      y(L34) = ( y(L3) + y(L4) ) / 2.
      WRITE(15,1001) L34, x(L34), y(L34)
      M = 100*J + I
      Nod1(M) = L1
      Nod2(M) = L2
      Nod3(M) = L3
      Nod4(M) = L4
      Nod5(M) = L12
      Nod6(M) = 500*I + 200 + Nadd
      Nod7(M) = L34
      Nod8(M) = 500*I + 200 + 2*(J-1)
      WRITE(16,1002) M, Nod1(M), Nod2(M), Nod3(M),
-      Nod4(M), Nod5(M), Nod6(M), Nod7(M), Nod8(M)
152  CONTINUE
      DO 153 I=N3, N4-1
      Rc(I) = xc1/cos(phi(I))
      arg = ( Rc(I)*(s75-1)/R75 ) + 1

```

```

      Nr1 = NINT( LOG(arg)/LOG(s75) )
      L1 = 500*I + Nadd
      x(L1) = xcl
      y(L1) = Rc(I)*sin(phi(I))
      WRITE(15,1001) L1, x(L1), y(L1)
      L2 = 500*(I+1) + Nadd
      Rc(I+1) = xcl/cos(phi(I+1))
      x(L2) = xcl
      y(L2) = Rc(I+1)*sin(phi(I+1))
      WRITE(15,1001) L2, x(L2), y(L2)
      L3 = L1 + 200
      x(L3) = ( x(L1) + x(L2) )/2.
      y(L3) = ( y(L1) + y(L2) )/2.
      WRITE(15,1001) L3, x(L3), y(L3)
DO 143 J=1, Nr1-1
      M = 100*J + I
      Nod1(M) = 500*I + 4*(J-1)
      Nod2(M) = 500*I + 4*J
      Nod3(M) = 500*(I+1) + 4*J
      Nod4(M) = 500*(I+1) + 4*(J-1)
      Nod5(M) = 500*I + 2*(2*J-1)
      Nod6(M) = 500*I + 200 + 4*J
      Nod7(M) = 500*(I+1) + 2*(2*J-1)
      Nod8(M) = 500*I + 200 + 4*(J-1)
      WRITE(16,1002) M, Nod1(M), Nod2(M), Nod3(M),
-      Nod4(M), Nod5(M), Nod6(M), Nod7(M), Nod8(M)
143 CONTINUE
      J = Nr1
      L1 = 500*I + 4*(J-1)
      L2 = 500*I + Nadd
      L3 = 500*(I+1) + Nadd
      L4 = 500*(I+1) + 4*(J-1)
      L12 = 500*I + Nadd1
      x(L12) = ( x(L1) + x(L2) ) / 2.
      y(L12) = ( y(L1) + y(L2) ) / 2.
      WRITE(15,1001) L12, x(L12), y(L12)
      L34 = 500*(I+1) + Nadd1
      x(L34) = ( x(L3) + x(L4) ) / 2.
      y(L34) = ( y(L3) + y(L4) ) / 2.
      WRITE(15,1001) L34, x(L34), y(L34)
      M = 100*J + I
      Nod1(M) = L1
      Nod2(M) = L2
      Nod3(M) = L3
      Nod4(M) = L4
      Nod5(M) = L12
      Nod6(M) = 500*I + 200 + Nadd
      Nod7(M) = L34
      Nod8(M) = 500*I + 200 + 4*(J-1)
      WRITE(16,1002) M, Nod1(M), Nod2(M), Nod3(M),
-      Nod4(M), Nod5(M), Nod6(M), Nod7(M), Nod8(M)
153 CONTINUE
DO 154 I=NS, N8-1
      Rc(I) = yc/sin(phi(I))
      arg = ( Rc(I)*(s30-1)/R30 ) + 1
      Nr1 = NINT( LOG(arg)/LOG(s30) )
      L1 = 500*I + Nadd
      x(L1) = Rc(I)*cos(phi(I))
      y(L1) = yc
      WRITE(15,1001) L1, x(L1), y(L1)

```



```

L2 = 500*(I+1) + Nadd
Rc(I+1) = yc/sin(phi(I+1))
x(L2) = Rc(I+1)*cos(phi(I+1))
y(L2) = yc
WRITE(15,1001) L2, x(L2), y(L2)
L3 = L1 + 200
x(L3) = ( x(L1) + x(L2) )/2.
y(L3) = ( y(L1) + y(L2) )/2.
WRITE(15,1001) L3, x(L3), y(L3)
DO 144 J=1, Nri-1
M = 100*J + I
Nod1(M) = 500*I + 16*(J-1)
Nod2(M) = 500*I + 16*J
Nod3(M) = 500*(I+1) + 16*J
Nod4(M) = 500*(I+1) + 16*(J-1)
Nod5(M) = 500*I + 8*(2*J-1)
Nod6(M) = 500*I + 200 + 16*J
Nod7(M) = 500*(I+1) + 8*(2*J-1)
Nod8(M) = 500*I + 200 + 16*(J-1)
WRITE(16,1002) M, Nod1(M), Nod2(M), Nod3(M),
- Nod4(M), Nod5(M), Nod6(M), Nod7(M), Nod8(M)
144 CONTINUE
J = Nri
L1 = 500*I + 16*(J-1)
L2 = 500*I + Nadd
L3 = 500*(I+1) + Nadd
L4 = 500*(I+1) + 16*(J-1)
L12 = 500*I + Nadd1
x(L12) = ( x(L1) + x(L2) ) / 2.
y(L12) = ( y(L1) + y(L2) ) / 2.
WRITE(15,1001) L12, x(L12), y(L12)
L34 = 500*(I+1) + Nadd1
x(L34) = ( x(L3) + x(L4) ) / 2.
y(L34) = ( y(L3) + y(L4) ) / 2.
WRITE(15,1001) L34, x(L34), y(L34)
M = 100*J + I
Nod1(M) = L1
Nod2(M) = L2
Nod3(M) = L3
Nod4(M) = L4
Nod5(M) = L12
Nod6(M) = 500*I + 200 + Nadd
Nod7(M) = L34
Nod8(M) = 500*I + 200 + 16*(J-1)
WRITE(16,1002) M, Nod1(M), Nod2(M), Nod3(M),
- Nod4(M), Nod5(M), Nod6(M), Nod7(M), Nod8(M)
154 CONTINUE
DO 155 I=N8, N7-1
Rc(I+1) = -xc/cos(phi(I+1))
arg = ( Rc(I+1)*(s30-1)/R30 ) + 1
Nri = NINT( LOG(arg)/LOG(s30) )
L1 = 500*(I+1) + Nadd
x(L1) = -xc
y(L1) = Rc(I+1)*sin(phi(I+1))
WRITE(15,1001) L1, x(L1), y(L1)
L2 = 500*I + Nadd
Rc(I) = -xc/cos(phi(I))
x(L2) = -xc
y(L2) = Rc(I)*sin(phi(I))
WRITE(15,1001) L2, x(L2), y(L2)

```

```

      L3 = L2 + 200
      x(L3) = ( x(L1) + x(L2) )/2.
      y(L3) = ( y(L1) + y(L2) )/2.
      WRITE(15,1001) L3, x(L3), y(L3)
DO 145 J=1, Nr1-1
      M = 100*J + I
      Nod1(M) = 500*I + 16*(J-1)
      Nod2(M) = 500*I + 16*J
      Nod3(M) = 500*(I+1) + 16*J
      Nod4(M) = 500*(I+1) + 16*(J-1)
      Nod5(M) = 500*I + 8*(2*J-1)
      Nod6(M) = 500*I + 200 + 16*J
      Nod7(M) = 500*(I+1) + 8*(2*J-1)
      Nod8(M) = 500*I + 200 + 16*(J-1)
      WRITE(16,1002) M, Nod1(M), Nod2(M), Nod3(M),
-      Nod4(M), Nod5(M), Nod6(M), Nod7(M), Nod8(M)
145 CONTINUE
      J = Nr1
      L1 = 500*I + 16*(J-1)
      L2 = 500*I + Nadd
      L3 = 500*(I+1) + Nadd
      L4 = 500*(I+1) + 16*(J-1)
      L12 = 500*I + Nad1
      x(L12) = ( x(L1) + x(L2) ) / 2.
      y(L12) = ( y(L1) + y(L2) ) / 2.
      WRITE(15,1001) L12, x(L12), y(L12)
      L34 = 500*(I+1) + Nad1
      x(L34) = ( x(L3) + x(L4) ) / 2.
      y(L34) = ( y(L3) + y(L4) ) / 2.
      WRITE(15,1001) L34, x(L34), y(L34)
      M = 100*J + I
      Nod1(M) = L1
      Nod2(M) = L2
      Nod3(M) = L3
      Nod4(M) = L4
      Nod5(M) = L12
      Nod6(M) = 500*I + 200 + Nadd
      Nod7(M) = L34
      Nod8(M) = 500*I + 200 + 16*(J-1)
      WRITE(16,1002) M, Nod1(M), Nod2(M), Nod3(M),
-      Nod4(M), Nod5(M), Nod6(M), Nod7(M), Nod8(M)
155 CONTINUE
DO 156 I=N7+1, N9-1
      Rc(I) = -xc/cos(phi(I))
      arg = ( Rc(I)*(s30-1)/R30 ) + 1
      Nr1 = NINT( LOG(arg)/LOG(s30) )
      L1 = 500*I + Nadd
      x(L1) = -xc
      y(L1) = Rc(I)*sin(phi(I))
      WRITE(15,1001) L1, x(L1), y(L1)
      L2 = 500*(I+1) + Nadd
      Rc(I+1) = -xc/cos(phi(I+1))
      x(L2) = -xc
      y(L2) = Rc(I+1)*sin(phi(I+1))
      WRITE(15,1001) L2, x(L2), y(L2)
      L3 = L1 + 200
      x(L3) = ( x(L1) + x(L2) )/2.
      y(L3) = ( y(L1) + y(L2) )/2.
      WRITE(15,1001) L3, x(L3), y(L3)
DO 146 J=1, Nr1-1

```

```

M = 100*J + I
Nod1(M) = 500*I + 16*(J-1)
Nod2(M) = 500*I + 16*J
Nod3(M) = 500*(I+1) + 16*J
Nod4(M) = 500*(I+1) + 16*(J-1)
Nod5(M) = 500*I + 8*(2*J-1)
Nod6(M) = 500*I + 200 + 16*J
Nod7(M) = 500*(I+1) + 8*(2*J-1)
Nod8(M) = 500*I + 200 + 16*(J-1)
WRITE(16,1002) M, Nod1(M), Nod2(M), Nod3(M),
- Nod4(M), Nod5(M), Nod6(M), Nod7(M), Nod8(M)
146 CONTINUE
J = Nr1
L1 = 500*I + 16*(J-1)
L2 = 500*I + Nadd
L3 = 500*(I+1) + Nadd
L4 = 500*(I+1) + 16*(J-1)
L12 = 500*I + Nad1
x(L12) = ( x(L1) + x(L2) ) / 2.
y(L12) = ( y(L1) + y(L2) ) / 2.
WRITE(15,1001) L12, x(L12), y(L12)
L34 = 500*(I+1) + Nad1
x(L34) = ( x(L3) + x(L4) ) / 2.
y(L34) = ( y(L3) + y(L4) ) / 2.
WRITE(15,1001) L34, x(L34), y(L34)
M = 100*J + I
Nod1(M) = L1
Nod2(M) = L2
Nod3(M) = L3
Nod4(M) = L4
Nod5(M) = L12
Nod6(M) = 500*I + 200 + Nadd
Nod7(M) = L34
Nod8(M) = 500*I + 200 + 16*(J-1)
WRITE(16,1002) M, Nod1(M), Nod2(M), Nod3(M),
- Nod4(M), Nod5(M), Nod6(M), Nod7(M), Nod8(M)
156 CONTINUE
DO 157 I=N9, N99-1
Rc(I+1) = -yc/sin(phi(I+1))
arg = ( Rc(I+1)*(s30-1)/R30 ) + 1
Nr1 = NINT( LOG(arg)/LOG(s30) )
L1 = 500*(I+1) + Nadd
x(L1) = Rc(I+1)*cos(phi(I+1))
y(L1) = -yc
WRITE(15,1001) L1, x(L1), y(L1)
L2 = 500*I + Nadd
Rc(I) = -yc/sin(phi(I))
x(L2) = Rc(I)*cos(phi(I))
y(L2) = -yc
WRITE(15,1001) L2, x(L2), y(L2)
L3 = L2 + 200
x(L3) = ( x(L1) + x(L2) )/2.
y(L3) = ( y(L1) + y(L2) )/2.
WRITE(15,1001) L3, x(L3), y(L3)
DO 147 J=1, Nr1-1
M = 100*J + I
Nod1(M) = 500*I + 16*(J-1)
Nod2(M) = 500*I + 16*J
Nod3(M) = 500*(I+1) + 16*J
Nod4(M) = 500*(I+1) + 16*(J-1)

```

```

Nod5(M) = 500*I + 8*(2*J-1)
Nod6(M) = 500*I + 200 + 16*J
Nod7(M) = 500*(I+1) + 8*(2*J-1)
Nod8(M) = 500*I + 200 + 16*(J-1)
WRITE(16,1002) M, Nod1(M), Nod2(M), Nod3(M),
- Nod4(M), Nod5(M), Nod6(M), Nod7(M), Nod8(M)
147 CONTINUE
J = Nr1
L1 = 500*I + 16*(J-1)
L2 = 500*I + Nadd
L3 = 500*(I+1) + Nadd
L4 = 500*(I+1) + 16*(J-1)
L12 = 500*I + Nad1
x(L12) = ( x(L1) + x(L2) ) / 2.
y(L12) = ( y(L1) + y(L2) ) / 2.
WRITE(15,1001) L12, x(L12), y(L12)
L34 = 500*(I+1) + Nad1
x(L34) = ( x(L3) + x(L4) ) / 2.
y(L34) = ( y(L3) + y(L4) ) / 2.
WRITE(15,1001) L34, x(L34), y(L34)
M = 100*J + I
Nod1(M) = L1
Nod2(M) = L2
Nod3(M) = L3
Nod4(M) = L4
Nod5(M) = L12
Nod6(M) = 500*I + 200 + Nadd
Nod7(M) = L34
Nod8(M) = 500*I + 200 + 16*(J-1)
WRITE(16,1002) M, Nod1(M), Nod2(M), Nod3(M),
- Nod4(M), Nod5(M), Nod6(M), Nod7(M), Nod8(M)
157 CONTINUE
DO 158 I=N99, N10-1
Rc(I) = -yc/sin(phi(I))
arg = ( Rc(I)*(s30-1)/R30 ) + 1
Nr1 = NINT( LOG(arg)/LOG(s30) )
L1 = 500*I + Nadd
x(L1) = Rc(I)*cos(phi(I))
y(L1) = -yc
WRITE(15,1001) L1, x(L1), y(L1)
L2 = 500*(I+1) + Nadd
Rc(I+1) = -yc/sin(phi(I+1))
x(L2) = Rc(I+1)*cos(phi(I+1))
y(L2) = -yc
WRITE(15,1001) L2, x(L2), y(L2)
L3 = L1 + 200
x(L3) = ( x(L1) + x(L2) )/2.
y(L3) = ( y(L1) + y(L2) )/2.
WRITE(15,1001) L3, x(L3), y(L3)
DO 148 J=1, Nr1-1
M = 100*J + I
Nod1(M) = 500*I + 16*(J-1)
Nod2(M) = 500*I + 16*J
Nod3(M) = 500*(I+1) + 16*J
Nod4(M) = 500*(I+1) + 16*(J-1)
Nod5(M) = 500*I + 8*(2*J-1)
Nod6(M) = 500*I + 200 + 16*J
Nod7(M) = 500*(I+1) + 8*(2*J-1)
Nod8(M) = 500*I + 200 + 16*(J-1)
WRITE(16,1002) M, Nod1(M), Nod2(M), Nod3(M),

```

```

-          Nod4(M) , Nod5(M) , Nod6(M) , Nod7(M) , Nod8(M)
148  CONTINUE
      J = Nr1
      L1 = 500*I + 16*(J-1)
      L2 = 500*I + Nadd
      L3 = 500*(I+1) + Nadd
      L4 = 500*(I+1) + 16*(J-1)
      L12 = 500*I + Nad1
      x(L12) = ( x(L1) + x(L2) ) / 2.
      y(L12) = ( y(L1) + y(L2) ) / 2.
      WRITE(15,1001) L12, x(L12), y(L12)
      L34 = 500*(I+1) + Nad1
      x(L34) = ( x(L3) + x(L4) ) / 2.
      y(L34) = ( y(L3) + y(L4) ) / 2.
      WRITE(15,1001) L34, x(L34), y(L34)
      M = 100*J + I
      Nod1(M) = L1
      Nod2(M) = L2
      Nod3(M) = L3
      Nod4(M) = L4
      Nod5(M) = L12
      Nod6(M) = 500*I + 200 + Nadd
      Nod7(M) = L34
      Nod8(M) = 500*I + 200 + 16*(J-1)
      WRITE(16,1002) M, Nod1(M) , Nod2(M) , Nod3(M) ,
-          Nod4(M) , Nod5(M) , Nod6(M) , Nod7(M) , Nod8(M)
158  CONTINUE
      DO 159 I=N10, N6-1
      Rc(I+1) = xc/cos(phi(I+1))
      arg = ( Rc(I+1)*(s30-1)/R30 ) + 1
      Nr1 = NINT( LOG(arg)/LOG(s30) )
      L1 = 500*(I+1) + Nadd
      x(L1) = xc
      y(L1) = Rc(I+1)*sin(phi(I+1))
      WRITE(15,1001) L1, x(L1), y(L1)
      L2 = 500*I + Nadd
      Rc(I) = xc/cos(phi(I))
      x(L2) = xc
      y(L2) = Rc(I)*sin(phi(I))
      WRITE(15,1001) L2, x(L2), y(L2)
      L3 = L2 + 200
      x(L3) = ( x(L1) + x(L2) )/2.
      y(L3) = ( y(L1) + y(L2) )/2.
      WRITE(15,1001) L3, x(L3), y(L3)
      DO 149 J=1, Nr1-1
      M = 100*J + I
      Nod1(M) = 500*I + 16*(J-1)
      Nod2(M) = 500*I + 16*J
      Nod3(M) = 500*(I+1) + 16*J
      Nod4(M) = 500*(I+1) + 16*(J-1)
      Nod5(M) = 500*I + 8*(2*J-1)
      Nod6(M) = 500*I + 200 + 16*J
      Nod7(M) = 500*(I+1) + 8*(2*J-1)
      Nod8(M) = 500*I + 200 + 16*(J-1)
      WRITE(16,1002) M, Nod1(M) , Nod2(M) , Nod3(M) ,
-          Nod4(M) , Nod5(M) , Nod6(M) , Nod7(M) , Nod8(M)
149  CONTINUE
      J = Nr1
      L1 = 500*I + 16*(J-1)
      L2 = 500*I + Nadd

```

```

L3 = 500*(I+1) + Nadd
L4 = 500*(I+1) + 16*(J-1)
L12 = 500*I + Nad1
x(L12) = ( x(L1) + x(L2) ) / 2.
y(L12) = ( y(L1) + y(L2) ) / 2.
WRITE(15,1001) L12, x(L12), y(L12)
L34 = 500*(I+1) + Nad1
x(L34) = ( x(L3) + x(L4) ) / 2.
y(L34) = ( y(L3) + y(L4) ) / 2.
WRITE(15,1001) L34, x(L34), y(L34)
M = 100*J + I
Nod1(M) = L1
Nod2(M) = L2
Nod3(M) = L3
Nod4(M) = L4
Nod5(M) = L12
Nod6(M) = 500*I + 200 + Nadd
Nod7(M) = L34
Nod8(M) = 500*I + 200 + 16*(J-1)
WRITE(16,1002) M, Nod1(M), Nod2(M), Nod3(M),
- Nod4(M), Nod5(M), Nod6(M), Nod7(M), Nod8(M)
159 CONTINUE
I=N7
Rc(I) = -xc/cos(phi(I))
arg = ( Rc(I)*(s30-1)/R30 ) + 1
Nr1 = NINT( LOG(arg)/LOG(s30) )
L1 = 500*I + 100 + Nadd
x(L1) = -xc
y(L1) = Rc(I)*sin(phi(I))
WRITE(15,1001) L1, x(L1), y(L1)
L2 = 500*(I+1) + Nadd
Rc(I+1) = -xc/cos(phi(I+1))
x(L2) = -xc
y(L2) = Rc(I+1)*sin(phi(I+1))
WRITE(15,1001) L2, x(L2), y(L2)
L3 = 500*I + 200 + Nadd
x(L3) = ( x(L1) + x(L2) )/2.
y(L3) = ( y(L1) + y(L2) )/2.
WRITE(15,1001) L3, x(L3), y(L3)
DO 161 J=1, Nr1-1
M = 100*J + I
Nod1(M) = 500*I + 100 + 16*(J-1)
Nod2(M) = 500*I + 100 + 16*J
Nod3(M) = 500*(I+1) + 16*J
Nod4(M) = 500*(I+1) + 16*(J-1)
Nod5(M) = 500*I + 100 + 8*(2*J-1)
Nod6(M) = 500*I + 200 + 16*J
Nod7(M) = 500*(I+1) + 8*(2*J-1)
Nod8(M) = 500*I + 200 + 16*(J-1)
WRITE(16,1002) M, Nod1(M), Nod2(M), Nod3(M),
- Nod4(M), Nod5(M), Nod6(M), Nod7(M), Nod8(M)
161 CONTINUE
J = Nr1
L1 = 500*I + 100 + 16*(J-1)
L2 = 500*I + 100 + Nadd
L3 = 500*(I+1) + Nadd
L4 = 500*(I+1) + 16*(J-1)
L12 = 500*I + 100 + Nad1
x(L12) = ( x(L1) + x(L2) ) / 2.
y(L12) = ( y(L1) + y(L2) ) / 2.

```

```

WRITE(15,1001) L12, x(L12), y(L12)
L34 = 500*(I+1) + Nadd1
x(L34) = ( x(L3) + x(L4) ) / 2.
y(L34) = ( y(L3) + y(L4) ) / 2.
WRITE(15,1001) L34, x(L34), y(L34)
M = 100*J + I
Nod1(M) = L1
Nod2(M) = L2
Nod3(M) = L3
Nod4(M) = L4
Nod5(M) = L12
Nod6(M) = 500*I + 200 + Nadd
Nod7(M) = L34
Nod8(M) = 500*I + 200 + 16*(J-1)
WRITE(16,1002) M, Nod1(M), Nod2(M), Nod3(M),
- Nod4(M), Nod5(M), Nod6(M), Nod7(M), Nod8(M)
I=N6
Rc(1) = xc/cos(phi(1))
arg = ( Rc(1)*(s30-1)/R30 ) + 1
Nri = NINT( LOG(arg)/LOG(s30) )
L1 = 500*1 + Nadd
x(L1) = xc
y(L1) = Rc(1)*sin(phi(1))
WRITE(15,1001) L1, x(L1), y(L1)
L2 = 500*I + Nadd
Rc(I) = xc/cos(phi(I))
x(L2) = xc
y(L2) = Rc(I)*sin(phi(I))
WRITE(15,1001) L2, x(L2), y(L2)
L3 = L2 + 200
x(L3) = ( x(L1) + x(L2) )/2.
y(L3) = ( y(L1) + y(L2) )/2.
WRITE(15,1001) L3, x(L3), y(L3)
DO 162 J=1, Nri-1
M = 100*J + I
Nod1(M) = 500*I + 16*(J-1)
Nod2(M) = 500*I + 16*J
Nod3(M) = 500*1 + 16*J
Nod4(M) = 500*1 + 16*(J-1)
Nod5(M) = 500*I + 8*(2*J-1)
Nod6(M) = 500*I + 200 + 16*J
Nod7(M) = 500*1 + 8*(2*J-1)
Nod8(M) = 500*I + 200 + 16*(J-1)
WRITE(16,1002) M, Nod1(M), Nod2(M), Nod3(M),
- Nod4(M), Nod5(M), Nod6(M), Nod7(M), Nod8(M)
162 CONTINUE
J = Nri
L1 = 500*I + 16*(J-1)
L2 = 500*I + Nadd
L3 = 500*1 + Nadd
L4 = 500*1 + 16*(J-1)
L12 = 500*I + Nadd1
x(L12) = ( x(L1) + x(L2) ) / 2.
y(L12) = ( y(L1) + y(L2) ) / 2.
WRITE(15,1001) L12, x(L12), y(L12)
L34 = 500*1 + Nadd1
x(L34) = ( x(L3) + x(L4) ) / 2.
y(L34) = ( y(L3) + y(L4) ) / 2.
WRITE(15,1001) L34, x(L34), y(L34)
M = 100*J + I

```

```

Nod1(M) = L1
Nod2(M) = L2
Nod3(M) = L3
Nod4(M) = L4
Nod5(M) = L12
Nod6(M) = 500*I + 200 + Nadd
Nod7(M) = L34
Nod8(M) = 500*I + 200 + 16*(J-1)
WRITE(16,1002) M, Nod1(M), Nod2(M), Nod3(M),
-   Nod4(M), Nod5(M), Nod6(M), Nod7(M), Nod8(M)
I=N5-1
Rc(I) = yc/sin(phi(I))
arg = ( Rc(I)*(s15-1)/R15 ) + 1
Nr1 = NINT( LOG(arg)/LOG(s15) )
L1 = 500*I + Nadd
x(L1) = Rc(I)*cos(phi(I))
y(L1) = yc
WRITE(15,1001) L1, x(L1), y(L1)
Rc(I+1) = yc/sin(phi(I+1))
L2 = 500*(I+1) + Nadd
x(L2) = Rc(I+1)*cos(phi(I+1))
y(L2) = yc
WRITE(15,1001) L2, x(L2), y(L2)
L3 = L1 + 200
x(L3) = ( x(L1) + x(L2) )/2.
y(L3) = ( y(L1) + y(L2) )/2.
WRITE(15,1001) L3, x(L3), y(L3)
DO 163 J=1, Nr1-1
M = 100*J + I
Nod1(M) = 500*I + 8*(J-1)
Nod2(M) = 500*I + 8*J
Nod3(M) = 500*(I+1) + 8*J
Nod4(M) = 500*(I+1) + 8*(J-1)
Nod5(M) = 500*I + 4*(2*J-1)
Nod6(M) = 500*I + 200 + 8*J
Nod7(M) = 500*(I+1) + 4*(2*J-1)
Nod8(M) = 500*I + 200 + 8*(J-1)
WRITE(16,1002) M, Nod1(M), Nod2(M), Nod3(M),
-   Nod4(M), Nod5(M), Nod6(M), Nod7(M), Nod8(M)
163 CONTINUE
J = Nr1
L1 = 500*I + 8*(J-1)
L2 = 500*I + Nadd
L3 = 500*(I+1) + Nadd
L4 = 500*(I+1) + 8*(J-1)
L12 = 500*I + Nad1
x(L12) = ( x(L1) + x(L2) ) / 2.
y(L12) = ( y(L1) + y(L2) ) / 2.
WRITE(15,1001) L12, x(L12), y(L12)
L34 = 500*(I+1) + Nad1
x(L34) = ( x(L3) + x(L4) ) / 2.
y(L34) = ( y(L3) + y(L4) ) / 2.
WRITE(15,1001) L34, x(L34), y(L34)
M = 100*J + I
Nod1(M) = L1
Nod2(M) = L2
Nod3(M) = L3
Nod4(M) = L4
Nod5(M) = L12
Nod6(M) = 500*I + 200 + Nadd

```



```

Nod7(M) = L34
Nod8(M) = 500*I + 200 + 8*(J-1)
WRITE(16,1002) M, Nod1(M), Nod2(M), Nod3(M),
-   Nod4(M), Nod5(M), Nod6(M), Nod7(M), Nod8(M)
I=N4
Rc(I) = xc1/cos(phi(I))
arg = ( Rc(I)*(s15-1)/R15 ) + 1
Nr1 = NINT( LOG(arg)/LOG(s15) )
L1 = 500*I + Nadd
x(L1) = xc1
y(L1) = Rc(I)*sin(phi(I))
WRITE(15,1001) L1, x(L1), y(L1)
L2 = 500*(I+1) + 8*Nr1
x(L2) = Rc(I)*cos(phi(I+1))
y(L2) = Rc(I)*sin(phi(I+1))
WRITE(15,1001) L2, x(L2), y(L2)
L3 = L1 + 200
x(L3) = ( x(L1) + x(L2) )/2.
y(L3) = ( y(L1) + y(L2) )/2.
WRITE(15,1001) L3, x(L3), y(L3)
L4 = 500*I + 2*(Nr+3)
x(L4) = xc1
y(L4) = yc
WRITE(15,1001) L4, x(L4), y(L4)
L5 = 500*(I+1) + Nadd
L6 = L4 + 1
x(L6) = ( x(L4) + x(L1) )/2.
y(L6) = ( y(L4) + y(L1) )/2.
WRITE(15,1001) L6, x(L6), y(L6)
L7 = L4 + 2
x(L7) = ( x(L4) + x(L5) )/2.
y(L7) = ( y(L4) + y(L5) )/2.
WRITE(15,1001) L7, x(L7), y(L7)
L8 = L2 + 8
x(L8) = ( x(L2) + x(L5) )/2.
y(L8) = ( y(L2) + y(L5) )/2.
WRITE(15,1001) L8, x(L8), y(L8)
DO 166 J=1, Nr1-1
M = 100*J + I
Nod1(M) = 500*I + 8*(J-1)
Nod2(M) = 500*I + 8*J
Nod3(M) = 500*(I+1) + 8*J
Nod4(M) = 500*(I+1) + 8*(J-1)
Nod5(M) = 500*I + 4*(2*J-1)
Nod6(M) = 500*I + 200 + 8*J
Nod7(M) = 500*(I+1) + 4*(2*J-1)
Nod8(M) = 500*I + 200 + 8*(J-1)
WRITE(16,1002) M, Nod1(M), Nod2(M), Nod3(M),
-   Nod4(M), Nod5(M), Nod6(M), Nod7(M), Nod8(M)
166 CONTINUE
J = Nr1
M = 100*J + I
Nod1(M) = 500*I + 8*(J-1)
Nod2(M) = 500*I + Nadd
Nod3(M) = 500*(I+1) + 8*J
Nod4(M) = 500*(I+1) + 8*(J-1)
Nod5(M) = 500*I + 4*(2*J-1)
Nod6(M) = 500*I + 200 + Nadd
Nod7(M) = 500*(I+1) + 4*(2*J-1)
Nod8(M) = 500*I + 200 + 8*(J-1)

```

```

WRITE (16,1002) M, Nod1(M), Nod2(M), Nod3(M),
-   Nod4(M), Nod5(M), Nod6(M), Nod7(M), Nod8(M)
J = Nr1 + 1
M = 100*J + I
Nod1(M) = L2
Nod2(M) = L1
Nod3(M) = L4
Nod4(M) = L5
Nod5(M) = L3
Nod6(M) = L6
Nod7(M) = L7
Nod8(M) = L8
WRITE (16,1002) M, Nod1(M), Nod2(M), Nod3(M),
-   Nod4(M), Nod5(M), Nod6(M), Nod7(M), Nod8(M)
DO 164 I=1, N1-1
beta = (xc1+rad)*cos(phi(I+1)) + dy*sin(phi(I+1))
gamma = (xc1+rad)*(xc1+rad) + dy*dy - rad*rad
Rc(I+1) = beta - SQRT(beta*beta-gamma)
arg = ( Rc(I+1)*(s15-1)/R15 ) + 1
Nr1 = NINT( LOG(arg)/LOG(s15) )
L1 = 500*(I+1) + Nadd
x(L1) = Rc(I+1)*cos(phi(I+1))
y(L1) = Rc(I+1)*sin(phi(I+1))
WRITE(15,1001) L1, x(L1), y(L1)
L2 = 500*I + Nadd
phi3 = ( phi(I) + phi(I+1) ) / 2.
beta = (xc1+rad)*cos(phi3) + dy*sin(phi3)
gamma = (xc1+rad)*(xc1+rad) + dy*dy - rad*rad
Rc3 = beta - SQRT(beta*beta-gamma)
L3 = L2 + 200
x(L3) = Rc3*cos(phi3)
y(L3) = Rc3*sin(phi3)
WRITE(15,1001) L3, x(L3), y(L3)
DO 165 J=1, Nr1-1
M = 100*J + I
Nod1(M) = 500*I + 8*(J-1)
Nod2(M) = 500*I + 8*J
Nod3(M) = 500*(I+1) + 8*J
Nod4(M) = 500*(I+1) + 8*(J-1)
Nod5(M) = 500*I + 4*(2*J-1)
Nod6(M) = 500*I + 200 + 8*J
Nod7(M) = 500*(I+1) + 4*(2*J-1)
Nod8(M) = 500*I + 200 + 8*(J-1)
WRITE (16,1002) M, Nod1(M), Nod2(M), Nod3(M),
-   Nod4(M), Nod5(M), Nod6(M), Nod7(M), Nod8(M)
165 CONTINUE
J = Nr1
L1 = 500*I + 8*(J-1)
L2 = 500*I + Nadd
L3 = 500*(I+1) + Nadd
L4 = 500*(I+1) + 8*(J-1)
L12 = 500*I + Nad1
x(L12) = ( x(L1) + x(L2) ) / 2.
y(L12) = ( y(L1) + y(L2) ) / 2.
WRITE(15,1001) L12, x(L12), y(L12)
L34 = 500*(I+1) + Nad1
x(L34) = ( x(L3) + x(L4) ) / 2.
y(L34) = ( y(L3) + y(L4) ) / 2.
WRITE(15,1001) L34, x(L34), y(L34)
M = 100*J + I

```

```

Nod1(M) = L1
Nod2(M) = L2
Nod3(M) = L3
Nod4(M) = L4
Nod5(M) = L12
Nod6(M) = 500*I + 200 + Nadd
Nod7(M) = L34
Nod8(M) = 500*I + 200 + 8*(J-1)
WRITE(16,1002) M, Nod1(M), Nod2(M), Nod3(M),
- Nod4(M), Nod5(M), Nod6(M), Nod7(M), Nod8(M)
164 CONTINUE
c
c This portion of the program creates the MPC constraints
2001 FORMAT(5I5)
L = 2
c
c 15-30 interface
c Nri refers to the 30 i.e. 4 elements
I = 11
Nri = 4
DO 111 J=1, Nri-1
L1 = 500*I + 4*(4*J-3)
L11 = 500*I + 4*(4*J-1)
L2 = 500*I + 16*(J-1)
L3 = 500*I + 16*J
L4 = 500*I + 8*(2*J-1)
WRITE(17,2001) L, L1, L2, L3, L4
WRITE(17,2001) L, L11, L2, L3, L4
111 CONTINUE
I = 1
Nri = 4
DO 12 J=1, Nri-1
L1 = 500*I + 4*(4*J-3)
L11 = 500*I + 4*(4*J-1)
L2 = 500*I + 16*(J-1)
L3 = 500*I + 16*J
L4 = 500*I + 8*(2*J-1)
WRITE(17,2001) L, L1, L2, L3, L4
WRITE(17,2001) L, L11, L2, L3, L4
12 CONTINUE
c
c 7.5-15 interface
c Nri refers to the 15 i.e. 7 elements
I = 3
Nri = 7
DO 13 J=1, Nri-1
L1 = 500*I + 2*(4*J-3)
L11 = 500*I + 2*(4*J-1)
L2 = 500*I + 8*(J-1)
L3 = 500*I + 8*J
L4 = 500*I + 4*(2*J-1)
WRITE(17,2001) L, L1, L2, L3, L4
WRITE(17,2001) L, L11, L2, L3, L4
13 CONTINUE
I = 9
Nri = 8
DO 14 J=1, Nri-1
L1 = 500*I + 2*(4*J-3)
L11 = 500*I + 2*(4*J-1)
L2 = 500*I + 8*(J-1)

```

```
L3 = 500*I + 8*J
L4 = 500*I + 4*(2*J-1)
WRITE(17,2001) L, L1, L2, L3, L4
WRITE(17,2001) L, L1, L2, L3, L4
14 CONTINUE
C
c 3.75-7.5 interface
c Nri refers to the 7.5 i.e. 13 elements
I = 4
Nri = 13
DO 15 J=1, Nri-1
  L1 = 500*I + (4*J-3)
  L11 = 500*I + (4*J-1)
  L2 = 500*I + 4*(J-1)
  L3 = 500*I + 4*J
  L4 = 500*I + 2*(2*J-1)
  WRITE(17,2001) L, L1, L2, L3, L4
  WRITE(17,2001) L, L11, L2, L3, L4
15 CONTINUE
I = 8
Nri = 15
DO 16 J=1, Nri-1
  L1 = 500*I + (4*J-3)
  L11 = 500*I + (4*J-1)
  L2 = 500*I + 4*(J-1)
  L3 = 500*I + 4*J
  L4 = 500*I + 2*(2*J-1)
  WRITE(17,2001) L, L1, L2, L3, L4
  WRITE(17,2001) L, L11, L2, L3, L4
16 CONTINUE
STOP
END
```

END

FILMED

1-86

DTIC